ISSN: 2408-2384 (Online)
ISSN: 1686-5456 (Print)

Environment and Natural Resources Journal

Volume 18, Number 2, April - June 2020

Environment and Natural Resources Journal (EnNRJ)

Volume 18, Number 2, April-June 2020

ISSN: 1686-5456 (Print)

ISSN: 2408-2384 (Online)

AIMS AND SCOPE

The Environment and Natural Resources Journal is a peer-reviewed journal, which provides insight scientific knowledge into the diverse dimensions of integrated environmental and natural resource management. The journal aims to provide a platform for exchange and distribution of the knowledge and cutting-edge research in the fields of environmental science and natural resource management to academicians, scientists and researchers. The journal accepts a varied array of manuscripts on all aspects of environmental science and natural resource management. The journal scope covers the integration of multidisciplinary sciences for prevention, control, treatment, environmental clean-up and restoration. The study of the existing or emerging problems of environment and natural resources in the region of Southeast Asia and the creation of novel knowledge and/or recommendations of mitigation measures for sustainable development policies are emphasized.

The subject areas are diverse, but specific topics of interest include:

- Biodiversity
- Climate change
- Detection and monitoring of polluted sources e.g., industry, mining
- Disaster e.g., forest fire, flooding, earthquake, tsunami, or tidal wave
- Ecological/Environmental modelling
- Emerging contaminants/hazardous wastes investigation and remediation
- Environmental dynamics e.g., coastal erosion, sea level rise
- Environmental assessment tools, policy and management e.g., GIS, remote sensing, Environmental Management System (EMS)
- Environmental pollution and other novel solutions to pollution
- Remediation technology of contaminated environments
- Transboundary pollution
- Waste and wastewater treatments and disposal technology

Schedule

Environment and Natural Resources Journal (EnNRJ) is a quarterly published journal in January-March, April-June, July-September and October-December.

Publication Fees

There is no cost of the article-processing and publication.

Ethics in publishing

EnNRJ follows closely a set of guidelines and recommendations published by Committee on Publication Ethics (COPE) (http://publicationethics.org/).

Editorial Office Address
Research and Academic Services Section,
Faculty of Environment and Resource Studies, Mahidol University
999, Phutthamonthon Sai 4 Road, Salaya, Phutthamonthon, Nakhon Pathom, Thailand, 73170
Phone +662 441 5000 ext. 2108 Fax. +662 441 9509-10
Website: https://www.tci-thaijo.org/index.php/ennrj/index
E-mail: ennrjournal@gmail.com

Environment and Natural Resources Journal (EnNRJ)

Volume 18, Number 2, April-June 2020

ISSN: 1686-5456 (Print)

ISSN: 2408-2384 (Online)

Environment and Natural Resources Journal (EnNRJ)

Volume 18, Number 2, April-June 2020

ISSN: 1686-5456 (Print)

ISSN: 2408-2384 (Online)

CONTENT

A GIS-based Spatial Multi-criteria Approach for Flash Flood Risk Assessment in the Ngan Sau-Ngan Pho Mountainous River Basin, North Central of Vietnam

Van Dai Hoang[1*], Hong Thai Tran[2], and Thanh Tien Nguyen[3]

[1]*Vietnam Institute of Meteorology, Hydrology and Climate change, Hanoi 100000, Vietnam*
[2]*Vietnam Meteorological and Hydrological Administration, Hanoi 100000, Vietnam*
[3]*Faculty of Surveying, Mapping and Geographic Information, Hanoi University of Natural Resources and Environment, Hanoi 100000, Vietnam*

ARTICLE INFO

Received: 23 Jul 2019
Received in revised: 8 Oct 2019
Accepted: 22 Oct 2019
Published online: 6 Dec 2019
DOI: 10.32526/ennrj.18.2.2020.11

Keywords:
Flash flood risk assessment/ GIS/ Spatial multi-criteria approach/ Ngan Sau-Ngan Pho mountainous river basin (north central of Vietnam)

*** Corresponding author:**
E-mail: daihydro2003@gmail.com

ABSTRACT

Flash flood risks in the Ngan Sau-Ngan Pho mountainous river basin (north central of Vietnam) were examined based on GIS and a spatial multi-criteria approach. A set of indicators were firstly proposed for the assessment of hazard, exposure and vulnerability. Analytic hierarchy process (AHP) technique and Iyengar and Sudarshan's method were then applied for calculating weights of hazard and vulnerability indicators, respectively. Flash flood risks were assessed by means of the “risk triangle” approach and were finally validated using past flood records. It was found that flash flood hazard was mainly at medium and low levels, with a very high hazard area of 178.6 ha accounting for 0.1% of the total river basin. Exposure at high and very high levels was mainly detected in the economic center of the basin. The high and very high vulnerability areas accounting for 98.2% of the total area were mainly concentrated in mountainous areas. The largest area was low risk totaling 219,083.1 ha (accounting for 68.6% of the basin area), followed by 67,148.6 ha (very low risk: 21%), 27,181 ha (medium risk: 9%), 5,909.7 ha (high and very high risks: 1.8%). These results demonstrate the proposed set of indicators, GIS and spatial multi-criteria analysis allow for effective flash flood risk assessment in mountains.

1. INTRODUCTION

Floods and/or flash floods are among the most common of all environmental hazards in the world causing the largest amount of deaths and property damage (CEOS, 2003). The main factors contributing to flooding problems are topography, geomorphology, drainage, engineering structures, and climate (Youssef et al., 2011). Most floods are caused by convective or frontal storms combined with the intensity and duration of the rain. In addition, there are other interrelated factors influencing flash flood severity including rainfall characteristics, water loss (evaporation and infiltration), drainage networks, drainage orders, drainage characteristics, and environmental and human processes (Saleh, 1989). Heavy rains, land-use change in basin areas and various engineering applications also contribute to the magnitude and frequency of flood events (Youssef et al., 2011). Floods can influence many aspects of human life due to their destructive effects and create significant expenses on mitigation efforts (Youssef et al., 2011). Smith (2003) indicated flooding regularly claims over 20,000 lives per year and adversely affects around 75 million people world-wide. Situated in the tropical monsoon zone close to the typhoon centre of the western pacific, Vietnam is one of the most disaster prone countries in the Mekong region and aproximately 70% of the people in Vietnam live in disaster-prone areas, with the majority of the people in the Central region (Shaw, 2006), especially in the Ngan Pho-Ngan Sau river basin (see section 2.1 for a more detailed discussion). Therefore, flash flood risk assessment

Citation: Hoang VD, Tran HT, Nguyen TT. A GIS-based spatial multi-criteria approach for flash flood risk assessment in the Ngan Sau-Ngan Pho Mountainous River Basin, North Central of Vietnam. Environ. Nat. Resour. J. 2020;18(2):110-123. DOI: 10.32526/ennrj.18.2.2020.11

plays a vital role in reducing flood inundation risk in this area.

During the past few years, many models have been proposed to assess flood hazard and risk. Prediction of flood hazard has been conventionally achieved by applying hydrologic and hydraulic models (Booij, 2005; Myronidis et al., 2009). However, the main limitation of these models is the unavailability of large-scale data. By setting up a framework by means of which the different processes of flood management can be classified, Plate (2002) defined a procedure for handling risks due to natural, environmental or man-made hazards, of which floods are representative. Based on this framework, many studies have employed remote sensing and GIS to map flood hazard and risk. Typically, using probabilistic methods, radar remote sensing data have been extensively used for flood monitoring in many basins such as Johor river (Malaysia) (Kia et al., 2012), Severn river (UK) (Matgen et al., 2011), Basilicata region (Southern Italy) (Refice et al., 2014), Europe (Sanders et al., 2005) and Dee River in Wales (UK) (Schumann and Di Baldassarre, 2010). Flood susceptibility mapping using hydrological, hydrodynamic and stochastic rainfall models has been successfully employed in the Upper Tiber River (central Italy) (Brocca et al., 2011), three mesoscale catchments in northern Germany (Haberlandt and Radtke, 2014), three raingauge sites (Ghana) (Unami et al., 2010) and along Malaysia's east coast (Pradhan, 2010; Unami et al., 2010). In addition, flood susceptibility mapping has been applied in various case studies with the help of GIS (Kia et al., 2012; Lee et al., 2012; Pradhan, 2010), neural network methods (Kia et al., 2012) and support vector machine models (Tehrany et al., 2014; Tehrany et al., 2015). Alternatively, several studies have successfully unitilzed multicriteria analysis methods to assess flood hazard in Tucumán Province (Argentina) (Fernández and Lutz, 2010), Dongting Lake region, Hunan, Central China (Wang et al., 2011) and Yasooj region (Iran) (Rahmati et al., 2016). Recently, many studies have used AHP with the help of GIS to assess flood hazard (Kazakis et al., 2015; Rahmati et al., 2016) and risk (Chen et al., 2011; Meyer et al., 2009). Furthermore, recent studies by Schumann and Di Baldassarre (2010) and Wang et al. (2011) have successfully combined AHP with fuzzy logic and genetic algorithms to incorporate the possible changes (climate change, land use change) over years into the assessment of flood hazard and management of water resources. Although all the above-discussed methods have proven successful in flood risk assessment in terms of their effectiveness and also in terms of their efficiency in many studies, they fail to take into account the indicators associated with the social-economic factors in mountains when assessing flood risks in a mountainous river basin. It is therefore, with the main objective of assessing flash flood risks by considering a wide range of climatic, natural and social-economic conditions, this study provides new insights into these factors with the help of GIS and spatial multi-criteria approach in assessing flash flood risks in a mountainous river basin.

2. METHODOLOGY

2.1 Description of study area

Ngan Sau-Ngan Pho river basin is located in Ha Tinh province (north central of Vietnam), consisting of Huong Son, Duc Tho, Vu Quang and Huong Khe Districts (Figure 1). It's geographic location extends latitudinally from 17°50′00″N to 18°37′58″N and longitudinally from 105°07′00″E to 106°56′00′E. Ngan Pho River originates from small streams in the Giang Man mountainous area, in the areas of Son Hong, Son Kim 1 and Son Kim communes of Huong Son District at an altitude of about 700 m above the mean sea level. Its maximum length, average height and slope range from 71 km to 72 km, 331 m, 25.2%, relatively. The area of Ngan Pho basin is 1,060 km² with river and stream density of 0.91 km/km². Its total volume of water is 1.40 km³ corresponding to the average flow of 45.6 m³/s. Whereas, Ngan Sau river system is the second largest tributary of Ca river extending 135 km and covering a basin area of 3,214 km².

Situated in the north central Vietnam, Ha Tinh province is often hardest hit by floods (Anh et al., 2014; Luu et al., 2019; Nguyen and Ha, 2017; Schad et al., 2012; Thao et al., 2014), especially in the Ngan Sau-Ngan Pho river basin (Kha et al., 2018; Long and Dung, 2009; Nguyen and Ha, 2017; Nguyen et al., 2017b; Trung, 2015). A flash flood in upstream Ngan Pho River occurred in September 1989 caused 10 deaths, 96 injuries, 16,200 households flooded, 177 houses washed away, and 5,026 ha of winter-spring rice damaged. Another historic flood in September 18-22nd 2002 in the upstream area of Ngan Pho and in the Central Region and Central Highlands of Vietnam river caused 77 deaths, hundreds of injuries, and 70,694 houses flooded (Figure 2(a)). The floodwaters of Ngan Sau in October 15-18nd 2010 overtook the 2002 historical flood causing all communes of Vu Quang District to be flooded and isolated (Figure 2(b)). Especially, floodwaters swept away and caused landslides of 1,520 households in 6 communes in the downstream of the Ngan Sau River. Most recently, a flood in October 2017 (Figure 2(c)-(d)) broke 28 km of the dam at the Co Chau Reservoir in Ha Tinh damaging 145 ha of rice, 2 ha of orchards and over 11,600 ha of other crops (NDO, 2017).

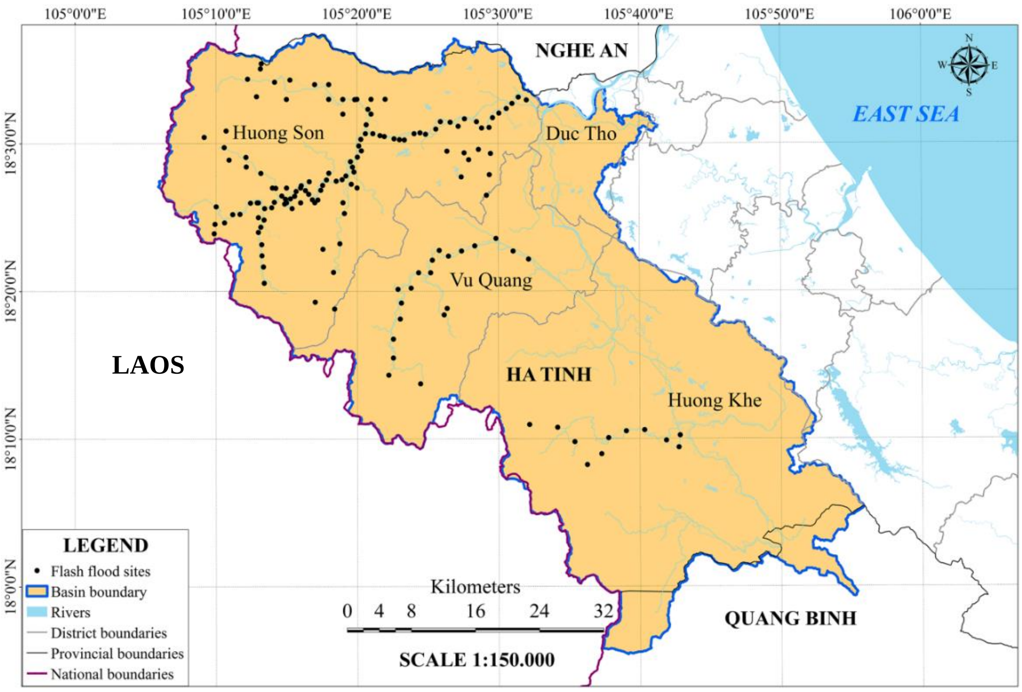

Figure 1. Study area of Ngan Pho-Ngan Sau river basin, North Central of Vietnam.

2.2 Data used

In this study, reports of flash flood status in Ngan Sau and Ngan Pho rivers were collected. Data used for risk assessment include hydro-meteorological data, land use map, topographic map, data from the statistical yearbook of the General Statistics Office in 2016, annual reports of Department of Agriculture and Rural Development, Department of Natural Resources and Environment, Steering Committee for Disaster Prevention and Search and rescue of Ha Tinh (Vietnam). In addition, field survey data collected in Ngan Pho, Ngan Sau river basin including 3,860 questionnaires from the people, district and commune officials was used as input data for flash flood risk assessment, whereas a total of 350 flash flood sites recorded in the past were used for the validation of flash flood risks in the study area.

2.3 GIS and spatial multi-criteria approach based flash flood assessment

A region's flood risk can be calculated by the "risk triangle" approach proposed by Crichton (1999) whose sides are represented by the amplitude of hazard (H), exposure (E) and vulnerability (V) as given in equation (1). If any of the sides increases, the area of the triangle, i.e., the amount of risk, increases also. Hence, risk is the result of the interaction of these three elements (Barredo and Engelen, 2010). The workflow of flood assessment is shown in Figure 3.

Hazard assessment: recent studies have indicated the cause of flash flood formation is divided into two groups of fast- (H_1) and low- (H_2) changing factors. Flood hazard is assessed as shown in Figure 4 using the following equation:

$$H = f(H_1, H_2)$$

Where, H_1 takes into account rainfall and flow surface, whereas H_2 is related to soil types, slope, density of rivers and streams, distance to rivers and land-use types.

$$R = f(H, E, V) \quad (1)$$

Figure 2. Flash floods in the study area: (a) a historic flood in September 2002 in the Ngan Pho basin; (b) in Huong Khe in October 2017, and (c and d) in Huong Khe in October 2017.

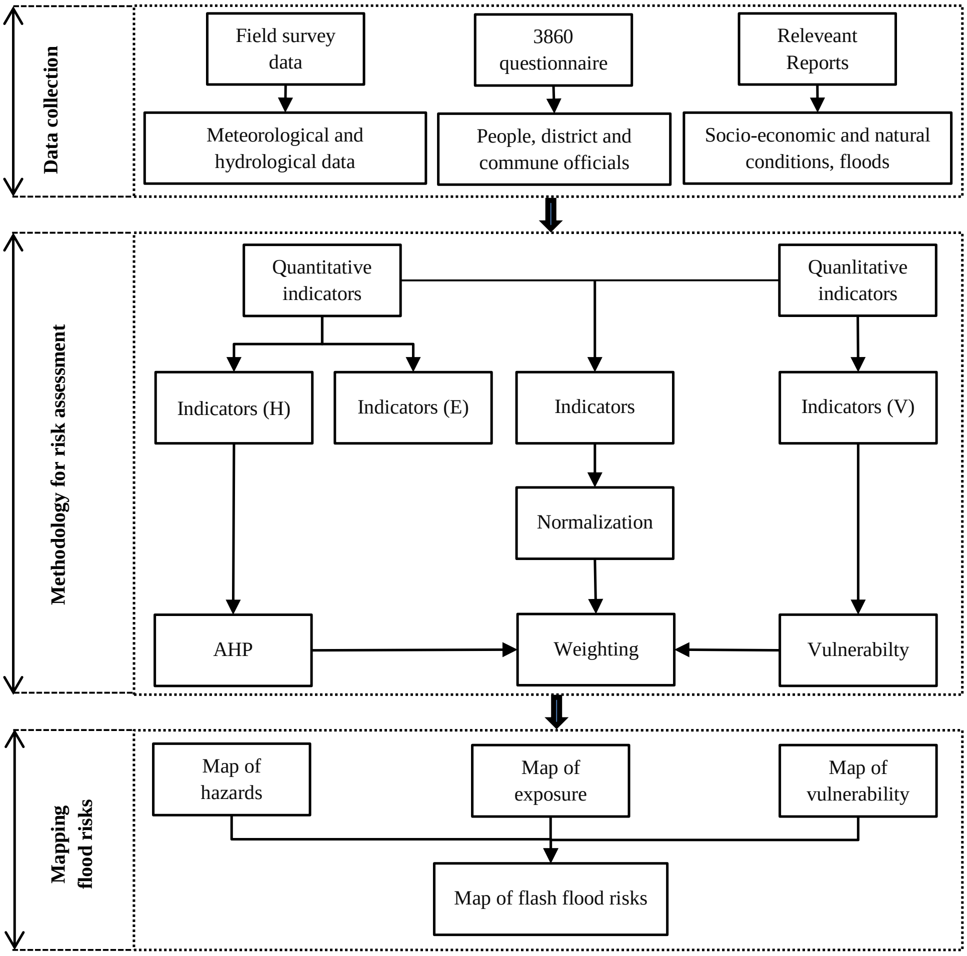

Figure 3. The workflow of flash flood assessment based on GIS and multi-criteria analysis.

Exposure assessment: exposure (E) is employed to refer to the presence (location) of people, livelihoods, environmental services and resources, infrastructure, or economic, social, or cultural assets in places that could be adversely affected by physical events and which, thereby, are subject to potential future harm, loss, or damage (Field et al., 2012). Exposure indicators used in this study is land-use types. Based on the importance of land-use types and to the level of flash flood disaster risk, five types of land use will be assigned a value determined from 1 to 5: traffic housing (5); agricultural land (4); forestry land and bamboo (3); evergreen broadleaf forest (2); and bare land and rocky mountains (1).

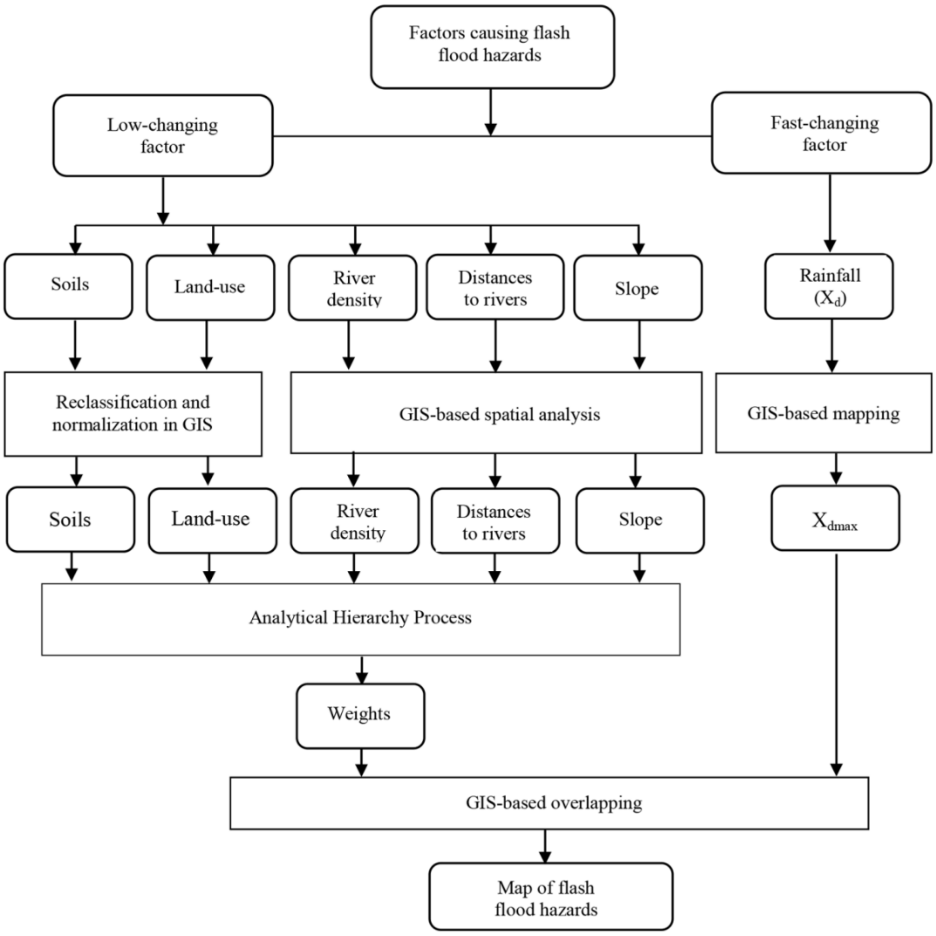

Figure 4. Flood hazard assessment using GIS and AHP.

Vulnerability assessment: according to the IPCC definition of vulnerability, vulnerability to climate change and variability is represented by three elements: exposure, sensitivity, and adaptive capacity (Bernstein et al., 2008). In this study, the social factors are clearly emphasized. Vulnerability assessment focuses on human capacity to resist, deal with flash floods and promptly recover damages and losses, so socio-economic factors were reviewed and analysed. Vulnerability indicators are identified based on a combination of two main indicators: sensitivity (S) and adaptive capacity (AC). Indicators of sensitivity (S) include people, jobs, health and education, infrastructure, agriculture (cultivation-livestock), forestry, seafood (30 sub-indicators), whereas indicators of adaptive capacity include self-recovery ability, social policies, infrastructure, awareness and communication (23 sub-indicators). These (sub-) indicators are summarised in Table 1. The vulnerability index is calculated using equation (2):

$$V = \sum_{j=1}^{n} S_i \times W_S + \sum_{j=1}^{m} AC_i \times W_{AC} \qquad (2)$$

Where, V is vulnerability index; S_i is sensitivity indicators; AC_i is adaptive capacity indicators; and W_s and W_{ac} are weights of sensitivity and adaptive capacity indicators, respectively; n and m are number of sub-indicators; and V is the vulnerability index which lies between 0 and 1, with 1 indicating maximum vulnerability and 0 indicating no vulnerability at all.

2.3.1 Normalization of indicators

Each indicator is measured in different scales and units. Therefore, they need to be normalized to values between 0 and 1 to ensure that they are comparable. Where, 1 being the highest value and 0 with being the least vulnerable area for the indicators with positive relationship with vulnerability to climate changes. This was important to identify the two possible types of functional relationship between the indicators and vulnerability. In addition, it is ensured that the index values are always in positive correlation with vulnerability and that higher value means higher vulnerability and vice versa (Žurovec et al., 2017). If vulnerability increases with an increase in the value of the indicator (positive correlation), and therefore has a positive functional relationship with vulnerability. Normalization of indicators was carried out by using the the methodology developed for the calculation of the Human Development Index (UNDP, 2006) as shown in equation (3),

$$x_{ij} = \frac{X_{ij} - \mathrm{Min}(X_{ij})}{\mathrm{Max}(X_{ij}) - \mathrm{Min}(X_{ij})} \quad (3)$$

Where, X is the separated value in the distribution, $\mathrm{Min}(X_{ij})$ is the minimum value in the distribution; $\mathrm{Max}(X_{ij})$ is the maximum value of the mean of the distribution i is the sub-city; and j is number of indicators. If the indicators are assumed to have a negative relationship with vulnerability, the above formula will be changed to the following as described in equation (4):

$$y_{ij} = \frac{\mathrm{Max}(X_{ij}) - X_{ij}}{\mathrm{Max}(X_{ij}) - \mathrm{Min}(X_{ij})} \quad (4)$$

2.3.2 Weighting methods

The next step after normalization of indicators was to summarize indicators into composite indices and assign weights based on their degree of influence on hazard and vulnerability. In this study, the weights of hazard and vulnerability components were calculated using AHP and weighting method proposed by Iyengar and Sudarshan (1982), respectively.

The weights of hazard components were obtained using the AHP technique which was proposed by Saaty (1977) and Saaty (1990). Using this method, the relative weight of each factor was estimated. The comparative scale consists of integer numbers from 1 to 9, where 1 means that the factors are equally important and 9, that a factor is extremely more important than another (Saaty, 1977; Saaty, 1990; Saaty and Vargas, 1984). The discordances between the pairwise comparisons and the reliability of the obtained weights were checked using the consistency ratio (CR) in equation (5). The consistency is used to build a matrix and is expressed by a consistency ratio, which must be less than 0.1 so as to be accepted. Otherwise, it is necessary to recalculate the weights (Saaty and Vargas, 2012).

$$\mathrm{CR} = \frac{\mathrm{CI}}{\mathrm{RI}} \quad (5)$$

Where, RI is the random index and CI represents the consistency index computing according:

$$\mathrm{CI} = \frac{\lambda_{max} - n}{n-1} \quad (6)$$

Where, λ_{max} represents the sum of the products between the sum of each column of the comparison matrix and the relative weights and n represents the size of the matrix.

The weights of land-use types were 0.33 (traffic housing), 0.27 (agricultural land), 0.2 (forestry land and bamboo), 0.13 (evergreen broadleaf forest) and 0.07 (bare land and rocky mountains) with the derived consistency ratio (CR) value of 0.08 (less than 0.1). The obtained weights of sub-indicators and indicators of hazard component, and their corresponding CR values are shown in Table 1. Data in Table 1 illustrates that the value of of CR was smaller than 0.1, therefore, these derived weights are considered reliable.

The weights of vulnerability component were obtained using method of Iyengar and Sudarshan (1982). This method was introduced to work-out a composite index from multivariate data and to rank the districts in terms of their economic performance. It is statistically sound and well suited for the development of composite index of vulnerability to climate change also (Hiremath and Shiyani, 2012). In this method, it is assumed that there are M regions/districts, *K* indicators of vulnerability and X_{ij} (i=1,2…, M; j=1,2,..., K) is the normalized score. The level of risk of i^{th} zone R_i, is assumed to be a linear sum of x_{ij} as:

$$R_i = \sum_{j=1}^{K} w_i x_{ij} \ (0 < x_{ij} < 1 \text{ and } \sum_{j=1}^{K} w_i = 1) \quad (7)$$

Table 1. Summary table of weights of hazard and vulnerability indicators

(a) – Weights of hazard indicators

Indicators	Weight	Sub-indicators	Weight
Fast-changing factor	0.25	Maximum daily rainfall	1
Low-changing factor	0.75	Types of soils	0.306
		Slope	0.295
		Density of rivers and streams	0.194
		Distance to rivers	0.148
		Types of land-use	0.057
CR = 0.03 (< 0.1)		CR = 0.07 (< 0.1)	

(b) – Weights of sensitivity indicators

Indicators	Weight	Sub-indicators	Weight
People	0.094	Rate of population growth (5 years of population)	0.027
		Percentage of elderly >60 years old	0.038
		Percentage of children <15 years	0.034
		Percentage of Women	0.033
		Percentage of poor people	0.032
		Percentage of ethnic minorities	0.060
Job	0.114	Average income per capita	0.027
		Main occupations of households (civil servants, service, industry, agriculture)	0.040
		Number of poor households	0.034
Medical	0.155	Number of patients attending hospital and commune health stations	0.043
		Average distance from commune health station/Commune People's Committee to the hospital, health center, nearest polyclinic	0.031
		Disease phenomenon after flash flood	0.033
Education	0.234	Number of pupils (preschool, primary, secondary, high school)	0.030
Infrastructure	0.136	Type of local roads	0.022
		Damage to social infrastructure facilities (schools, hospitals, clinics, cultural houses)	0.024
		Number of water wells for domestic use	0.029
		Number of households using water from dug wells and ponds for domestic use	0.024
Agriculture (cultivation-livestock)	0.076	Area of agricultural land	0.034
		Agricultural labor force	0.029
		Number of agricultural households	0.027
		Agricultural production and crop losses after flash floods	0.024

(b) – Weights of sensitivity indicators (cont.)

Indicators	Weight	Sub-indicators	Weight
Forestry	0.103	Area of forestry land	0.039
		Number of forestry households	0.053
		Forestry labor force	0.029
Seafood	0.088	Area of aquaculture	0.053
		Aquaculture water surface area affected by flash flood	0.019
		Damage to aquatic products of all kinds	0.025
		Number of aquaculture households	0.054
		Fisheries workforce	0.053

(c) – Weights of adaptive capacity indicators

Indicators	Weight	Sub-indicators	Weight
Self-recovery ability	0.436	Number of people in working age	0.044
		Life stabilization time after flash flood	0.043
Social policies	0.247	Households supported to build and repair houses	0.053
		Reserve of essentials for flash flood prevention	0.041
		Temporary relocation plans	0.028
Infrastructure	0.153	Number of local health facilities (stations, hospitals)	0.074
		Number of medical doctors	0.085
		Percentage of rural residents participating in health insurance (%)	0.032
		Type of housing	0.037
		Number of water pumping stations serving production and aquaculture in the commune	0.028
		Length of irrigation canals in the commune (km)	0.051
		Number of households using water from concentrated domestic water supply works	0.035
		Current status of local flood prevention works	0.055
Awareness and communication	0.164	Number of teachers	0.052
		Number of schools (preschool, primary, secondary, high school)	0.041
		Number of loudspeakers	0.047
		Percentage of households with radio and television	0.022
		Phone subscription number	0.048
		Number of computers with internet connection	0.054
		Ability to access to flash flood warning information	0.025
		Understanding of flash flood and prevention approaches	0.025
		Propaganda and training on natural disaster prevention and mitigation	0.033
		Early monitoring/warning system	0.047

In the method of Iyengar and Sudarshan (1982), the weights are assumed to vary inversely with the variance over the regions in the respective indicators of vulnerability. The weight w_i can be determined as:

$$w_i = \frac{c}{\sqrt{var(x_{ij})}} \tag{8}$$

Where, c is a normalizing constant and can be obtained as below:

$$c = \left[\sum_{j=1}^{j=K} \frac{1}{var(x_{ij})}\right]^{-1} \tag{9}$$

2.3.3 Identification of flood risk levels

A meaningful characterization of the vulnerability profiles should be in terms of a fractile classification based on an assumed distribution of R_i (Iyengar and Sudarshan, 1982). It is assumed that R_i follows a Beta distribution in the range (0, 1) which is skewed and relevant to characterize positive valued random variables (Bucaram et al., 2016). This distribution has the probability density as follows:

$$f(z) = \frac{z^{a-1}(1-z)^{b-1}dx}{B(a,b)}, 0 < z < 1 \text{ and } a, b > 0 \tag{10}$$

Where:

$$B(a,b) = \int_0^1 x^{a-1}(1-z)^{b-1}dx \tag{11}$$

The parameters a and b can be estimated by solving the following two simultaneous equations:

$$\begin{gathered}(1-y)a - yb = 0 \\ (y-m)a - mb = m - y\end{gathered} \tag{12}$$

Where, y is the overall mean of the localities indicators and m is defined as:

$$m = s_y^2 + y^2 \tag{13}$$

Where, s_y^2 is the variance of the indicator by locality. Let $(0, z_1)$, (z_1, z_2), (z_2, z_3), (z_3, z_4), (z_4, z_5) be the linear intervals such that each one has the same probability weight of 20%. Five classes of risks are obtained and districts were ranked accordingly: (i) less risk, if $0<y_i< z_1$; (ii) moderately risk, if $z_1<y_i< z_2$; (iii) risk, if $z_2<y_i< z_3$ (iv) highly risk, if $z_3<y_i< z_4$ and (v) very high risk, if $z_4<y_i< 1$.

3. RESULTS AND DISCUSSION

3.1 Assessment of hazard

From data in Table 2 we can see that flash flood hazards in the Ngan Pho-Ngan Sau basin were mainly low and medium, covering areas of 81,636.7 ha and 220,246.5 ha, accounting for 25.5% and 68.8% of total area, respectively. A very low hazard area of 4,643.8 ha accounting for 1.5% was measured in northeast of the basin, whereas, high and very high hazard areas of 13,274.2 ha and 178.6 ha accounting for 4.1% and 0.1% were also detected near rivers and streams (Figure 5) with high slopes and poor structures such as Son Kim 1, Tay Son, Son Hong and Su Diem communes of Huong Son District; Huong Tho, Duc Bong and Duc Giang communes of Vu Quang District; Duc Lang and Duc Dong communes of Duc Tho District (Thao et al. 2014); Phu Gia, Hoa Hai, Huong Lam and Huong Lien communes of Huong Khe District (Nguyen and Ha, 2017; Nguyen et al., 2017b).

Table 2. Summary table of areas of hazard, exposure, vulnerability and flash flood risks.

Levels	Hazard		Exposure		Vulnerability		Flash flood risks	
	Area (ha)	Percent (%)	Area (ha)	Percent (%)	Area (ha)	Percent (%)	Area (ha)	Percent (%)
Very low	4643.8	1.5	393.5	0.1	1102.4	0.3	67148.6	21.0
Low	81636.7	25.6	172769.0	54.1	336.6	0.1	219083.1	68.6
Medium	219589.3	68.8	72854.4	22.8	4310.0	1.3	27181.1	8.5
High	13274.2	4.2	52487.3	16.4	96060.4	30.1	5809.5	1.8
Very high	178.6	0.1	20818.4	6.5	217513.1	68.1	100.2	0.0
Total	319322.5	100.0	319322.5	100.0	319322.5	100.0	319322.5	100.0

3.2 Assessment of exposure

The exposure to flash flood risk in Ngan Pho-Ngan Sau river basin in Table 2 shows that areas with high and very high exposures were mainly concentrated in the economic center of the basin where densely populated areas, agricultural and non-agricultural economic activities are located. The high and very high exposure covered an area of about 73,305.7 ha, accounting for 22.9% of the basin area and were mainly concentrated in northeast and north of the basin (Figure 6). The exposure was at medium level with an area of 72,854.4 ha, accounting for 22.8%, whereas, the level of exposure was at low and very low levels corresponding to areas of 173,047.9 ha and 393.5 ha, accounting for 54.1% and only 0.1% of the total area, respectively.

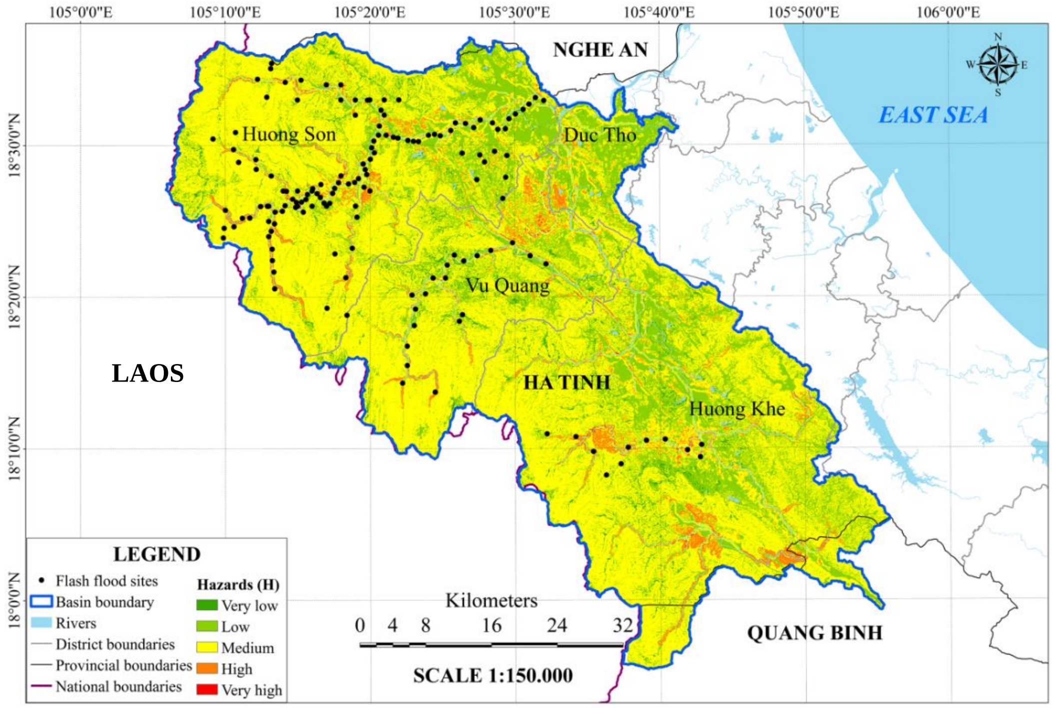

Figure 5. Map of flash flood hazard of the Ngan Pho-Ngan Sau river basin.

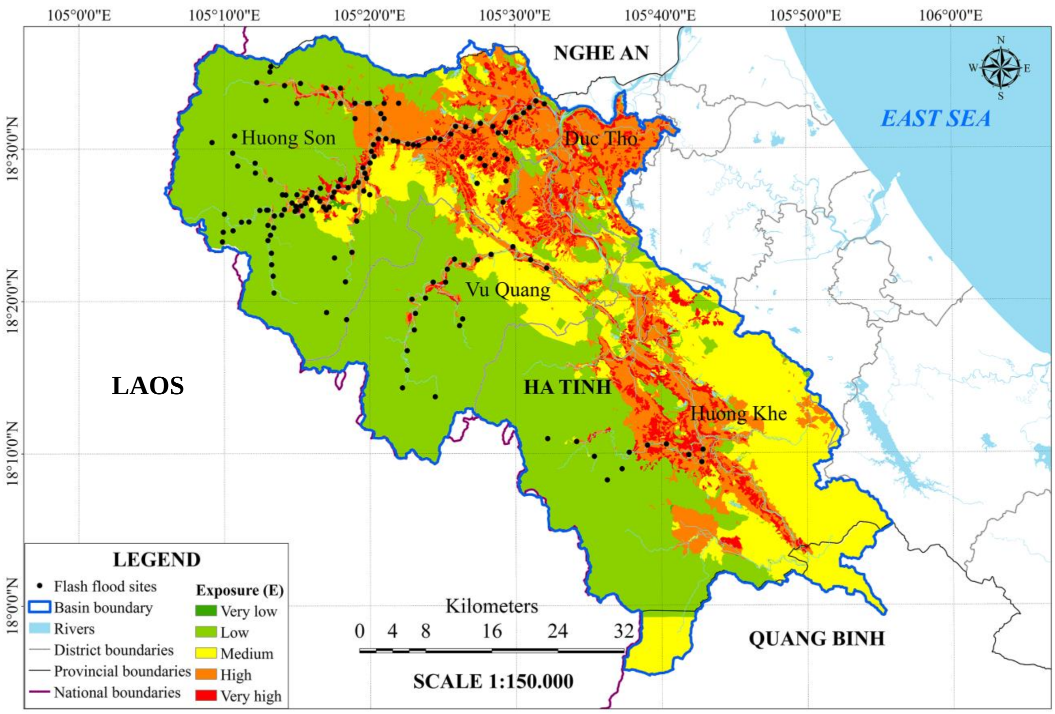

Figure 6. Map of flash flood exposure of the Ngan Pho-Ngan Sau river basin.

3.3 Asessment of vulnerability

Data in Table 2 demonstrated that the flash flood vulnerability of the Ngan Pho-Ngan Sau river basin the vulnerability was mainly at high and very high levels. In particular, the vulnerability at a very high level had an area of 219,000.1 ha (accounting for

68.3% of the basin area), followed by 96,060.4 ha of high level (accounting for 29.9%), 4,310.0 ha of medium level (accounting for 1.3%), and a relatively small area of low and very low levels with an area of 1,439.0 ha (accounting for only 0.4%). It is shown in Figure 7 that the areas of high and very high vulnerability were concentrated mainly in mountainous areas which were affected by flash floods annually, such as in the Son Kim 1, Son Kim 2, Son Hong, Son Linh communes of Huong Son District; Huong Quang, Huong Minh and Huong Tho communes of Vu Quang District; and Phu Gia, Huong Lam and Huong Lien communes of Huong Khe District (Nguyen and Ha, 2017; Nguyen et al., 2017b).

3.4 Assessment of flash flood risks

A total of 350 past-recorded flood sites were used as verification sites to validate the generated flash flood risks. Data from Figure 8 shows that most of verification sites were strongly correlated with flood risks at high and very high levels, especially in Huong Son, Duc Tho and Vu Quang Districts. A total of 303 generated risk sites at high and very high levels were detected at verification sites presenting an occupancy rate of 86.6%. This result suggests that the proposed method is very useful for accurate and reliable flash flood risk mapping. Data in Figure 8 also shows that the largest area was at low risk level covering an area of 219,083.1 ha (accounting for 68.6% of the basin area), followed by 67,148.6 ha of very low risk (21%), 27,181.1 ha of medium risk (8.5%), 5,809.5 ha of high risk and 100.2 ha of very high risk. The risks of flash floods at high and very high levels were concentrated in areas of high densities of rivers and streams (Figure 8). Specifically, high and very high flash flood risk areas were detected which accounts for 42%, 26.5%, 22.9% and 8.6% of Huong Khe, Huong Son, Duc Tho, and Vu Quang Districts, respectively. This finding is similar to flash flood records ussually reported annually in Huong Khe (Nguyen and Ha, 2017; Nguyen et al., 2011; Nguyen et al., 2017b; Thuy and Mui, 2018), Huong Son (Nguyen et al., 2017a), Duc Tho (Thao et al., 2014) and Vu Quang (Nguyen et al., 2011). Most of these areas were located in Son Hong, Son Tay, Son Ha, Son Kim 1 and Son Kim 2 communes of Huong Son District; Duc Dong and Duc Lang communes of Duc Tho District; Duc Giang, Duc Linh and Duc Bong communes of Vu Quang District; and Hoa Hai, Loc An, Phu Gia and Huong Lam communes of Huong Khe District.

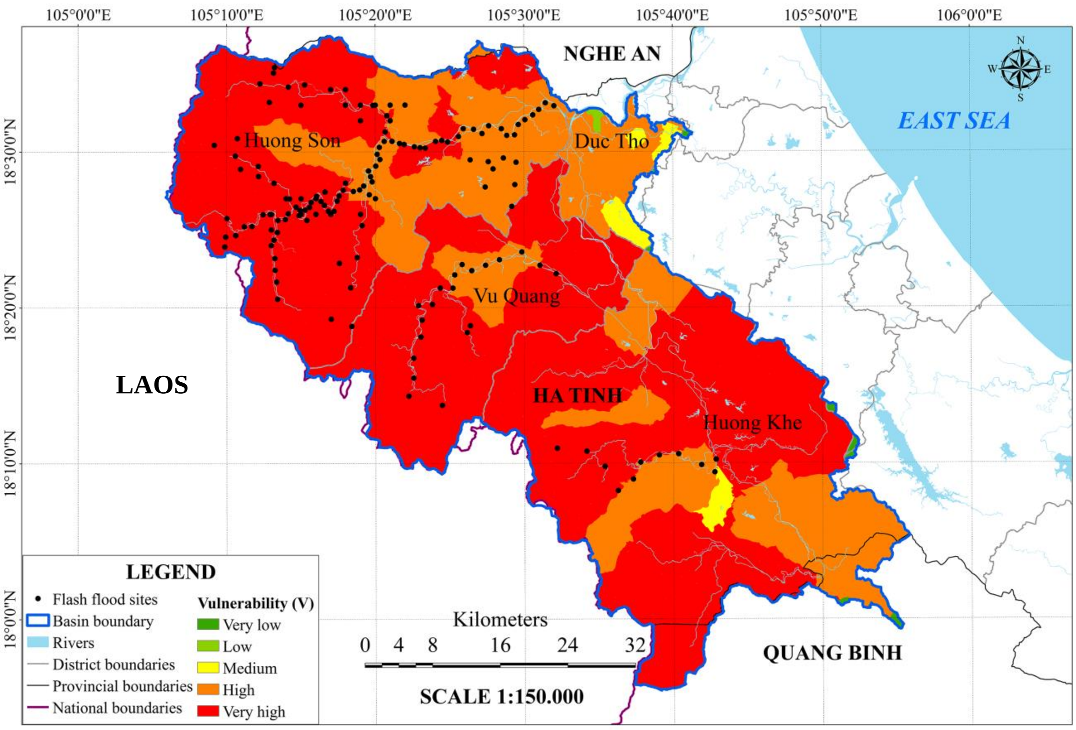

Figure 7. Map of flash flood vulnerability of Ngan Pho-Ngan Sau river basin.

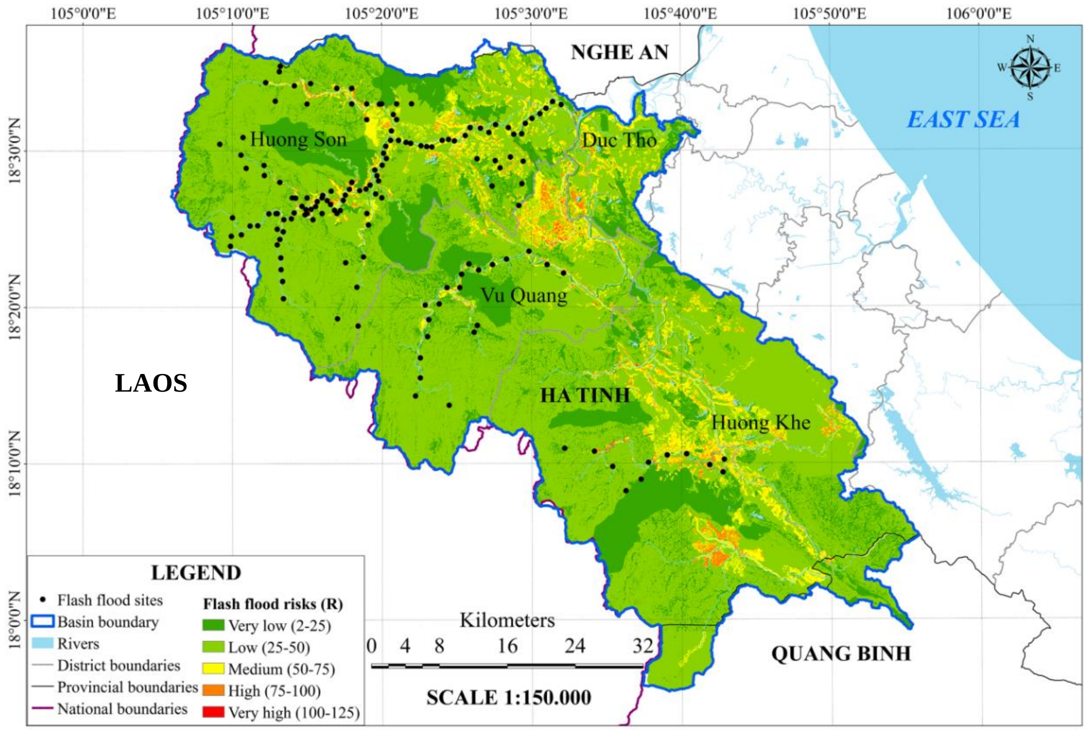

Figure 8. Map of flash flood risks of Ngan Pho-Ngan Sau river basin.

Huong Khe District: the total area of low risk was 90,928 ha accounting for 68.1.8% of the district area, followed by 21.1% (very low risk), 8.9% (medium risk), and 1.9% (high and very high risk). The total area of high and very high risk was 2,540 ha and was mainly concentrated in Huong Lam commune (741 ha), followed by Loc Yen, Phu Gia and Hoa Hai and other communes (from 14.04 ha to 97 ha). Whereas, very high risk areas were 23.9 ha and occured in seven communes of Phu Gia, Hoa Hai, Loc Yen, Huong Lien, Gia Pho, Huong Do and Phuc Dong. This result shows a good conformity with those reported by Nguyen and Ha (2017). In addition, a study of Nguyen et al. (2017b) indicated that rainfall duration and intensity in the period of 1990-2012 caused floods in 2002, 2007 and 2010 in this area. The high risk area was 2,516 ha and was mainly detected in Huong Lam commune (740.94 ha), several areas of Phuc Trach commune (14 ha) Floods were also reported in these districts in 2017 (Nguyen, 2017) and 2016 (PSN, 2016), respectively. The medium risk area was 11,904 ha and was evenly distributed in the communes. Low risk area of 90,928 ha was mainly detected in Hoa Hai commune (12,673 ha), and some of Huong Khe town, whereas a very low risk area of 28,182 ha was mainly found in Huong Vinh commune (5,538 ha and Huong Khe town (8.6 ha).

Huong Son District: the largest area of risk was at low level detected in Huong Son District with an area of 23,899.3 ha accounting for 69% of the district area, followed by 23,899 ha of very low risk, 8,361 ha of medium risk, 1,474 ha of high risk and 128 ha of very high risk. The total area of flash flood risks at high and very high levels was 1,602 ha, accounting for only 1.5% of study area and occured mainly in four communes of Son Hong, Son Kim 1, Son Kim 2 and Son Tay. Particularly, very high risks were found in Son Giang, Son Hong, Tay Son, Son Ha, Son Giang, Son Kim 1, Son Kim 2, Son Diem communes. A serious flood in Son Kim 1 and Son Kim 2 in October 2013 was also reported by Hong (2014). The flood destroyed hundreds of houses and civil works in the areas of Son Kim 1 and Son Kim 2 communes. In addition, about 300 households had all assets swept away, 57,100 houses flooded, 366 houses roofed in Huong Son. The areas of medium risks at medium level were mainly detected in Son Linh commune with an area of 1,015 ha and in Son An commune (34 ha). Low risk areas of 20,788 ha and 136 ha were found in Son Kim 1 commune and Pho Chau town, respectively. The risk area at the very low level occured mostly in Son Tay commune (9,363 ha) and some areas of Son An commune (2.6 ha).

Duc Tho District: the total area of flash flood risk at low level accounts for 55.4% of the district area, followed by 24.7% (very low level), 16.4% (medium level), 3.6% (high level). No risk at very high level was detected. The total area of high risk was 519 ha mainly concentrated in Duc Dong (146 ha) and Duc Lang (123 ha) communes. This result is similar to a flood reported in Duc Dong in 2017 (Thien, 2017) and in Duc Lang in 2016 (Group, 2016). The medimum risk areas were mainly detected in Duc Bong, Tung Anh, Duc An, Duc Lang and Duc Lac communes and some areas of Thai Yen and Duc Thanh communes (only 0.3 ha). Low risks were unevenly distributed across the district, and mostly occured in Duc Bong, Tan Huong, Duc Long, Duc Lang and Duc Hoa and in some areas of Duc Thanh commune with an area of 71 ha. A very low risk area of 3,541 ha was identified, mainly in communes of Tan Huong (907 ha), Duc Lang (602 ha).

Vu Quang District: the total low risk area accounts for 72.8% of the district area, followed by 17.3% (very low level), 7.7% (medium level), 2.2% (1,387 ha of high and very high risk area). The high risk area was mainly identified in Duc Bong commune with an area of 20.34 ha, followed by Duc Linh, Huong Tho, Duc Giang, Huong Quang, Huong Minh communes and Vu Quang town (only 0.09 ha). Four of six communes including Duc Bong, Duc Linh, Duc Giang and Huong Minh were devastated by a flood in 2011 (Minh Thu and Chau, 2011). In adition, about 300 households in Duc Bong were also isolated in a flood in 2017 (Tien, 2017). Medium risk was mostly concentrated in Duc Linh commune with an area of 1,104 ha, followed by Duc Giang, Duc Huong, Duc Bong, Huong Quang Huong Dien commune (84.7 ha). Low risk was detected in Huong Quang commune (26,632 ha) and Duc Giang commune (277.47 ha). The very low risk area was 10,767 ha, of which the largest area was found in Huong Dien commune (2,432 ha) whereas the smallest area was detected in Duc Giang commune (12 ha).

4. CONCLUSION

In this study, flash flood risk was assessed based on GIS and spatial multi-criteria approach. A set of indicators were firstly proposed for hazard, exposure and vulnerability components in mountains. An AHP technique and weighting method proposed by Iyengar and Sudarshan were then applied for calculating weights of hazard and vulnerability indicators, respectively. Flash flood risks were finally assessed using the “risk triangle” approach. The results showed that: (i) Flash flood hazard was mainly at medium and low levels. The very high hazard area was 178.6 ha, accounting for 0.1% of the total river basin; (ii) High and very high exposure was detected and mainly concentrated in the economic center of the basin; (iii) The areas of high and very high vulnerability were dominant in the basin, accounting for 98.2% of total area and were concentrated mainly in mountainous areas; (iv) The largest area of low risk was 219,083.1 ha (accounting for 68.6% of the basin area), followed by 67,148.6 ha (very low risk: 21%), 27,181.1 ha (medium risk: 9%), and 5,909.7 ha (high and very high risks: 1.8%). These results demonstrated the proposed GIS-based spatial multi-criteria approach is effective for flash flood risk assessment in mountainous river basin.

ACKNOWLEDGEMENTS

This work is sponsored and financed by the Ministry-level Scientific and Technological Key Programs of Ministry of Natural Resources and Environment of Vietnam under the project “Flash flood assessment for natural prevention and risk reduction in mountains, a case study of Ngan Pho-Ngan Sau river basin” (grant number: TNMT.2016.05.12).

REFERENCES

Anh TN, Kha DD, Duc DD, Son NT. Hydraulic modelling for flood vulnerability assessment. Case study in river basins in North Central Vietnam. Proceedings of the Conference on Integrated Water Resource Management, Management Policy and Decision Making Support. Jaques Cartier, HCMC: Vietnam; 2014.

Barredo JI, Engelen G. Land use scenario modeling for flood risk mitigation. Sustainability 2010;2(5):1327-44.

Bernstein L, Bosch P, Canziani O, Chen Z, Christ R, Riahi K. IPCC, 2007: Climate Change 2007: Synthesis Report. Geneva, Switzerland: IPCC; 2008.

Booij MJ. Impact of climate change on river flooding assessed with different spatial model resolutions. Journal of Hydrology 2005;303(1-4):176-98.

Brocca L, Melone F, Moramarco T. Distributed rainfall-runoff modelling for flood frequency estimation and flood forecasting. Hydrological Processes 2011;25(18):2801-13.

Bucaram S, Fernández MA, Renteria W. Assessing local vulnerability to climate change in Rio de la Plata Basin, Uruguay. Compendium: Cuadernos de Economía y Administración 2016;3(6):1-19.

Chen Y-R, Yeh C-H, Yu B. Integrated application of the analytic hierarchy process and the geographic information system for flood risk assessment and flood plain management in Taiwan. Natural Hazards 2011;59(3):1261-76.

Committee of Earth Observation Satellite (CEOS). The use of earth observing satellites for hazard support: Assessments and scenarios. Final report of the CEOS disaster management support group (DMSG). Ann Arbor, USA: University of Michigan; 2003.

Crichton D. The risk triangle. Natural Disaster Management 1999;102:103.

Fernández D, Lutz M. Urban flood hazard zoning in Tucumán Province, Argentina, using GIS and multicriteria decision analysis. Engineering Geology 2010;111(1-4):90-8.

Field CB, Barros V, Stocker TF, Dahe Q. Managing the Risks of Extreme Events and Disasters to Advance Climate Change Adaptation: Special Report of the Intergovernmental Panel on Climate Change. NewYork, USA: Cambridge University Press; 2012.

Group B. Golden heart fund relieved flood victims in Ha Tinh province. Bitexco Group. [Internet]. 2016 [cited 2019 July 29]. Available from: http://bitexco.com.vn/newdetail/golden-heart-fund-relieved-flood-victims-in-ha-tinh-province-115.html.

Haberlandt U, Radtke I. Hydrological model calibration for derived flood frequency analysis using stochastic rainfall and probability distributions of peak flows. Hydrology and Earth System Sciences 2014;18(1):353-65.

Hiremath DB, Shiyani R. Evaluating regional vulnerability to climate change: A case of Saurashtra. Indian Journal of Agricultural Economics 2012;67(3):334-44.

Hong VT. Emergency response to flood in Huong Son, Ha Tinh. [Internet]. 2014 [cited 2019 July 29]. Available from: https://www.oxfamblogs.org/vietnam/2014/01/29/emergency-response-to-flood-in-huong-son-ha-tinh/.

Iyengar NS, Sudarshan P. A method of classifying regions from multivariate data. Economic and Political Weekly 1982; 2047-52.

Kazakis N, Kougias I, Patsialis T. Assessment of flood hazard areas at a regional scale using an index-based approach and Analytical Hierarchy Process: Application in Rhodope-Evros region, Greece. Science of the Total Environment 2015;538:555-63.

Kha DD, Nhu NY, Anh TN. An approach for flow forecasting in ungauged catchments: A case study for Ho Ho reservoir catchment, Ngan Sau river, central Vietnam. Journal of Ecological Engineering 2018;19(3):74-9.

Kia MB, Pirasteh S, Pradhan B, Mahmud AR, Sulaiman WNA, Moradi A. An artificial neural network model for flood simulation using GIS: Johor River Basin, Malaysia. Environmental Earth Sciences 2012;67(1):251-64.

Lee MJ, Kang JE, Jeon S. Application of frequency ratio model and validation for predictive flooded area susceptibility mapping using GIS. Proceedings of the Geoscience and Remote Sensing Symposium (IGARSS), 2012 IEEE International. International Congress Center, Munich: Germany; 2012.

Long B, Dung PT. Flash floods, hydrometeorological forecasting and warning systems in Viet Nam. Proceedings of the 7th Annual Mekong Flood Forum: Integrated Flood Risk Management in the Mekong River Basin; 2009.

Luu C, von Meding J, Mojtahedi M. Analyzing Vietnam's national disaster loss database for flood risk assessment using multiple linear regression-TOPSIS. International Journal of Disaster Risk Reduction 2019;40:101153.

Matgen P, Hostache R, Schumann G, Pfister L, Hoffmann L, Savenije H. Towards an automated SAR-based flood monitoring system: Lessons learned from two case studies. Physics and Chemistry of the Earth, Parts A/B/C 2011;36(7-8):241-52.

Meyer V, Scheuer S, Haase D. A multicriteria approach for flood risk mapping exemplified at the Mulde River. Germany Natural Hazards 2009;48(1):17-39.

Minh Thu, Chau T. Spring buds after floods. [Internet]. 2011 [cited 2019 July 29]. Available from: https://en.nhandan.org.vn/society/item/1665802-.html.

Myronidis D, Emmanouloudis D, Stathis D, Stefanidis P. Integrated flood hazard mapping in the framework of the EU Directive on the assessment and management of flood risks. Fresenius Environmental Bulletin 2009;18(1):102-11.

Nhan Dan Online (NDO). Floods cause severe damage in northern and central localities. [Internet]. 2017 [cited 2019 July 29]. Available from: https://en.nhandan.org.vn/society/item/5564302-floods-cause-severe-damage-in-northern-and-central-localities.html.

Nguyen DTM, Ha HQ. Flash floods potential area mapping at Huong Khe District, Ha Tinh prov. Science and Technology Development Journal-Natural Sciences 2017;1(T4):249-54.

Nguyen H. Thousands of households violated by a flood in Ha Tinh province. [Internet]. 2017 [cited 2019 July 29]. Available from: http://daidoanket.vn/xa-hoi/ha-tinh-hang-nghin-ho-dan-bi-ngap-lut-tintuc382249.

Nguyen H, Hien HM, Shaw R, Thi TTM, Osti R, Miyake K. Community Based Disaster Risk Management in Vietnam. Nova Science Publishers, New York, USA; 2011.

Nguyen NY, Ichikawa Y, Ishidaira H. Establishing flood damage functions for agricultural crops using estimated inundation depth and flood disaster statistics in data-scarce regions. Hydrological Research Letters 2017a;11(1):12-8.

Nguyen VL, Le QD, Dong TV, Pham LH, Le TT. Study on the frequency of heavy rainfall in Huong Khe District, Ha Tinh province. VNU Journal of Science: Earth and Environmental Sciences 2017b;33(2):48-59.

Plate EJ. Flood risk and flood management. Journal of Hydrology 2002;267:2-11.

Pradhan B. Flood susceptible mapping and risk area delineation using logistic regression, GIS and remote sensing. Journal of Spatial Hydrology 2010;9(2):1-18.

Public Security News (PSN). People's Police College 5 supports people in flood-hit localities. [Internet]. 2016 [cited 2019 July 29]. Available from: http://en.cand.com.vn/Public-security-forces/People-s-Police-College-5-supports-people-in-flood-hit-localities-414865/.

Rahmati O, Zeinivand H, Besharat M. Flood hazard zoning in Yasooj region, Iran, using GIS and multi-criteria decision analysis. Geomatics, Natural Hazards and Risk 2016; 7(3):1000-17.

Refice A, Capolongo D, Pasquariello G, D'Addabbo A, Bovenga F. SAR and InSAR for flood monitoring: Examples with COSMO-SkyMed data. IEEE Journal of Selected Topics in Applied Earth Observations and Remote Sensing 2014; 7(7):2711-22.

Saaty TL. A scaling method for priorities in hierarchical structures. Journal of Mathematical Psychology 1977;15(3): 234-81.

Saaty TL. How to make a decision: the analytic hierarchy process. European Journal of Operational Research 1990;48(1):9-26.

Saaty TL, Vargas LG. Inconsistency and rank preservation. Journal of Mathematical Psychology 1984;28(2):205-14.

Saaty TL, Vargas LG. Models, Methods, Concepts and Applications of the Analytic Hierarchy Process (Vol. 175). New York, USA: Springer Science and Business Media; 2012.

Saleh A. Flash floods in deserts. A geomorphic study of desert Wadis. Institute of Arab Research, Special Studies Series 1989;51:1-93.

Sanders R, Shaw F, MacKay H, Galy H, Foote M. National flood modelling for insurance purposes: Using IFSAR for flood risk estimation in Europe. Hydrology and Earth System Sciences Discussions 2005;9(4):449-56.

Schad I, Schmitter P, Saint-Macary C, Neef A, Lamers M, Nguyen L, Hoffmann V. Why do people not learn from flood disasters? Evidence from Vietnam's northwestern mountains. Natural Hazards 2012;62(2):221-41.

Schumann G, Di Baldassarre G. The direct use of radar satellites for event-specific flood risk mapping. Remote Sensing Letters 2010;1(2):75-84.

Shaw R. Critical issues of community based flood mitigation: Examples from Bangladesh and Vietnam. Science and Culture 2006;72(1/2):62-79.

Smith K. Environmental Hazards: Assessing Risk and Reducing Disaster. Routledge; 2003.

Tehrany MS, Pradhan B, Jebur MN. Flood susceptibility mapping using a novel ensemble weights-of-evidence and support vector machine models in GIS. Journal of hydrology 2014;512:332-43.

Tehrany MS, Pradhan B, Mansor S, Ahmad N. Flood susceptibility assessment using GIS-based support vector machine model with different kernel types. Catena 2015;125:91-101.

Thao N, Thanh N, Huy M. Adaptive capacity to flood of communities in northcentral Vietnam: case studies in Yen Ho commune, Duc Tho District, Ha Tinh Province and Hung Nhan commune, Hung Nguyen District, Nghe An Province. Proceedings of the 2014 International Conference: SEAGA. Paradise Hotel, Siem Riep: Cambodia; 2014.

Thien D. Flash flood in Duc Tho distric, Ha Tinh province. [Internet]. 2017 [cited 2019 July 29]. Available from: https://baohatinh.vn/xa-hoi/hung-lu-thuong-nguon-ve-vung-ngoai-de-duc-tho-ngap-bang/141928.htm.

Thuy HLT, Mui TT. Climate Change Vulnerability Assessment Fortourism Sector in Ha Tinh Province. VNU Journal of Science: Earth and Environmental Sciences 2018;34(1):104-11.

Tien D. Police forces help people overcome floods. [Internet]. 2017 [cited 2019 July 29]. Available from: http://en.bocongan.gov.vn/articles/police-forces-help-people-overcome-floods-t4209.html.

Trung LD. Economic and welfare impacts of disasters in East Asia and policy responses: The case of Vietnamese communities. Resilience and Recovery in Asian Disasters: Community Ties, Market Mechanisms, and Governance 2015;51-73.

Unami K, Abagale FK, Yangyuoru M, Alam AHMB, Kranjac-Berisavljevic G. A stochastic differential equation model for assessing drought and flood risks. Stochastic Environmental Research and Risk Assessment 2010;24(5):725-33.

United Nations Development Programme (UNDP). Human Development Report 2006-Beyond Scarcity: Power, Poverty and the Global Water Crisis. New York, USA: UNDP; 2006.

Wang Y, Li Z, Tang Z, Zeng G. A GIS-based spatial multi-criteria approach for flood risk assessment in the Dongting lake region, Hunan, central China. Water Resources Management 2011;25(13):3465-84.

Youssef AM, Pradhan B, Hassan AM. Flash flood risk estimation along the St. Katherine road, southern Sinai, Egypt using GIS based morphometry and satellite imagery. Environmental Earth Sciences 2011;62(3):611-23.

Žurovec O, Čadro S, Sitaula B. Quantitative assessment of vulnerability to climate change in rural municipalities of Bosnia and Herzegovina. Sustainability 2017;9(7):1208.

Recent Analysis of Carbon, Nitrogen, and Lignin Phenol Compositions in the Suspended Particulate Matters at Spermonde Archipelago, South Sulawesi, Indonesia

Waode Rustiah[1*], Alfian Noor[1], Maming[1], Muhammad Lukman[2], and Nurfadilah[3]

[1]*Department of Chemistry, Faculty Mathematic and Natural Science, University of Hasanuddin, Jl. Perintis Kemerdekaan 90245, Makassar, Indonesia*

[2]*Marine Science Department, Faculty of Marine Science and Fisheries, Hasanuddin University, South Sulawesi, Indonesia*

[3]*Marine Science Department, Faculty of Fisheries and Marine Science, Mulawarman of University, East Kalimantan, Indonesia*

ARTICLE INFO

Received: 12 May 2019
Received in revised: 20 Oct 2019
Accepted: 30 Oct 2019
Published online: 27 Nov 2019
DOI: 10.32526/ennrj.18.2.2020.12

Keywords:
Spermonde/ Tallo-Makassar/ Pangkep/ Lignin phenol/ Suspended particulate matter

*** Corresponding author:**
E-mail:
waoderustiah79@gmail.com

ABSTRACT

This study analyzed the composition of monomer lignin phenols and its derivatives at the Spermonde Archipelago, South Sulawesi-Indonesia. Water samples were collected in the dry season (June 2017) and the rainy season (January 2018) from the river estuaries of Tallo-Makassar, and Pangkep. Analysis of carbon and nitrogen contents was conducted by EA-IRMS (elemental analyzer-isotope ratio mass spectrometry), while lignin phenol was analyzed by Chromatography Gas-Mass Spectroscopy (GC-MS). Spatially, the six lignin phenols (Λ*)* content in the Tallo river estuary into several outermost islands is higher than of the Pangkep river mouth. Λ values in the rainy season were higher (0.92-2.30) than in the dry season (0.62-2.07). In the dry season, the range of values for ratios of syringyl/vanillyl and cinnamyl/vanillyl was 0.35 to 1.12 and 0.39 to 0.57 indicating a low contribution of angiosperm plant tissue. In the rainy season, the values of ratios for syringyl/vanillyl and cinnamyl/vanillyl ranged from 0.37 to 1.18 and 0.32 to 0.62. The syringyl/vanillyl ratio indicates the contribution of plant tissue to angiosperms. The cinnamyl/vanillyl value is greater than 0.1, indicating a significant contribution of non-woody plant tissue. Spatially, the range of syringyl/vanillyl and cinnamyl/vanillyl ratios at the estuary of the Tallo river (0.37 to 1.12 and 0.32 to 0.57) were higher than at the Pangkep river estuary (0.35 to 1.18 and 0.39 to 0.62).

1. INTRODUCTION

The waters of the Spermonde Islands are located in the southwest of Sulawesi Province at 118°90'0"- 119°30'0" E and 5°10'0"- 5°50'0" S. These areas have an important economical and ecological role because it has a vast expanse of coral reefs, various types of sponges and enormous fisheries potential. Currently, the region received considerable pressure from a variety of activities (industry, logging and agricultural activities, and household activities) that occur in the mainland city of Makassar and Pangkep Regency (Nurdin et al., 2016). The magnitude of the land activity's effect on the waters of the Spermonde islands can be done through organic matter analysis.

The composition of organic matter along coastal and marine areas is affected by solid materials which have undergone weathering, seasonal changes, and increased erosion (Louchouarn et al., 2010; Bayram et al., 2013; Qu and Kroeze, 2012). The organic materials in waters will be overhauled by essential nutrients through the process of decomposition. Organic materials are supplied by plants from land and water plants such as the production of phytoplankton, seaweed, and other marine organisms (Xing et al., 2011; Hedges and Oades, 1997; Li et al., 2015; Lagbas et al., 2017). The changing process of organic matter that occurs in the ocean can be identified through the stable isotopes of carbon ($\delta^{13}C$), nitrogen ($\delta^{15}N$), and the molecular

Citation: Rustiah W, Noor A, Maming, Lukman M, Nurfadilah. Recent analysis of carbon, nitrogen, and lignin phenol compositions in the suspended particulate matters at Spermonde Archipelago, South Sulawesi, Indonesia. Environ. Nat. Resour. J. 2020;18(2):124-133. DOI: 10.32526/ennrj.18.2.2020.12

properties of sedimentary organic matter (SOM) (Onstad et al., 2000; Opsahl et al., 2001).

The ocean is the final destination for all activities on land and sea, naturally assimilating all foreign materials it receives. The ocean will lose the assimilation ability and pressure the ecosystem with pollution when the speed of assimilation is slower than the supply of the material. Input loads of dissolved and suspended materials that affect coastal and marine aquatic environments can cause eutrophication (cultural eutrophication) (Garnier et al., 2010), the possibility of the emergence of dangerous microalgae species (Gypens et al., 2009), and damage to coral reef ecosystems and biodiversity (Costa et al., 2008).

The characteristics of overflow from land in coastal waters can be determined by using the lignin biomarker method. Total lignin is the amount of vanillyl phenol, syringyl (S) and cinnamyl (C). In the angiosperm plants, the lignin content consists of syringyl and vanillyl phenols. Whereas gymnosperm tissue only produces vanillyl phenol, while only non-wood tissue produces cinnamyl phenol. Therefore, the S/V and C/V ratios are used to distinguish the source of angiosperms between wood and non-wood and gymnosperm plant tissue (Hansell and Carlson, 2001; Hedges and Oades, 1997). The ratio of vanillic acid to vanillyl $(Ad/Al)_v$, and syringic acid for syringaldehyde $(Ad/Al)_s$ are indicators from diagenesis lignin. The ratio of vanillic acid to vanillyl $(Ad/Al)_v$ and syringic acid to syringaldehyde $(Ad/Al)_s$ can be indicators of lignin diagenesis. Lignin biomarker has provided accurate predictions about water in the Amazon river system (Aufdenkampe et al., 2007), Bekanbeushi Moor, Northern Japan (Nagao et al., 2010) and Kapuas River, West Kalimantan (Loh et al., 2012).

Based on literature studies, until now, there has been no comprehensive research on the effects of organic runoff in the waters of the Spermonde Islands. The results of this study can be part of the pattern of development of coastal areas in the city of Makassar and Pangkep Regency that contribute to the waters of the Spermonde. This pattern of development will improve the quality of waters in spermonde and reduce damage to the diversity of animals and plants that exist around these waters. This study determined the effect of runoff of organic material from the mainland city of Makassar and Pangkep Regency into the waters of the Spermonde Islands using the composition of monomer lignin phenols.

2. METHODOLOGY

2.1 Site of study

The research was conducted in the dry season (June 2017) and the rainy season (January 2018). Spatially, the study location at the Tallo and Pangkep coastal waters areas were chosen perpendicular to the mainland. Determining the position/point of research stations during observations was done using Global Positioning System based on distance (Figure 1). This area was chosen because it is a productive area, in which there are mangrove ecosystems, seagrass beds and coral reefs (Spermonde Islands). The ecosystems are very important in sustaining the economic life of coastal communities and food security.

2.2 Methods

2.2.1 Samples preparation

Five liters of water were collected using a sample bottle at a depth of 1-2 m. The water samples were refrigerated and transported to the laboratory where they were passed through pre-weighed Whatman filter GF/F 0.7 µm assisted by vacuum pump (200 mmHg). The filters were dried (60 ^{o}C,~ 24 h) and re-weighed, yielding 500 mg of SPM.

2.2.2 Measurement of oceanographic parameters

Measurement of oceanographic parameter pH was determined by pH meter Orion 3 Star, temperature and dissolved oxygen were determined by dissolved oxygen meter YSI 550A, currents were determined by the current meter, salinity was determined by instrument WTW Multi 340itness, and brightness carried out by Secchi Disk.

2.2.3 Organic carbon content, nitrogen content, C/N ratio, stable isotope ($\delta^{13}C$ and $\delta^{15}N$) analysis

Aliquots of powdered suspended particulate matter were assayed using a carbon analyzer. Stable isotope analyzes (δ^{13}C and δ^{15}N) were carried out using mass spectrometer (Delta V Advantage, IRMS) connected to the elements analysis (NA-2500, CE Instruments) with a percentage correction of 0.15 ‰. Stable isotope ratio values using conventional standards using the equation (Hoefs, 2009):

$$\delta^{13}C \text{ and } \delta^{15}N = (R_{sample}/R_{standard} - 1) \times 1000 \ (‰)$$

Where, R_{sample} is the elements ratio of ^{13}C and ^{15}N, while the $R_{standard}$ is a ratio of ^{12}C and ^{14}N based on Pee Dee Belemnite (PDB). Carbon standards ($\delta^{13}C$ and $\delta^{15}N$ came from PDB, while nitrogen $\delta^{15}N$ used standard N2 atmospheric gas.

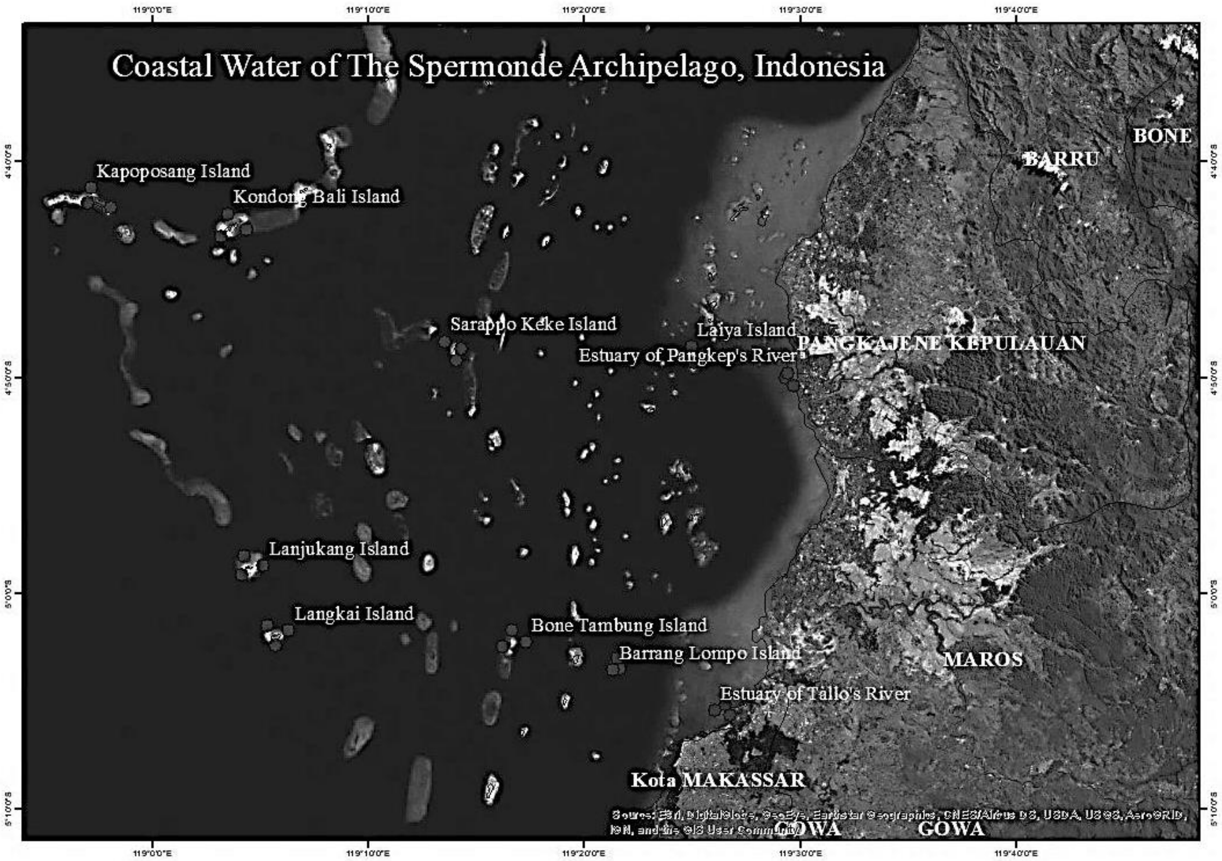

Figure 1. Sampling location (◯: sampling site)

2.2.4 Lignin phenol analysis

SPM Samples were composed of as much as 0.5 g of sediment, 1.0 g of CuO (99.9%, Sigma-Aldrich) powder was added together with 3 mL of 2 N NaOH into a mini bomb, and 10-15 mg of glucose (99.5%, Sigma-Aldrich) was added to eliminate the super oxidation effect. Samples were heated at room temperature to 175 °C with a ramping rate of 4.1°C/min, and allowed to continue at 175 °C for 3 h and manually shaken every hour. The oxidation product was cooled, then transferred by adding 10 mL of 1 N NaOH and centrifuged at 3,000 rpm for 10 min. The supernatant was collected from the centrifuge, acidified to pH 1 with 6 N. HCl. Then extracted three times by using 10 mL hexane (95%, Merck) (with 100 µL ethyl vanillin (98%, Merck) 0.5 mg/mL added as an internal standard). The excess solvent extract was evaporated by flowing N_2, until a dry residue was obtained, then stored in a desiccator at 4 °C. Then a silylation method was carried out where the dry residue was diluted with 300 µL of standard pyridine (99.8%, Merck and 150 µL of silylating bis-trimethylsilyl trifluoroacetamide (BSTFA) (99%, Merck) solvent with trimethyl-chlorosilane (TMCS) (1%, Merck) (as a catalyst). Then the samples were derivatized by heating at 90 °C for 30 min in a closed glass bottle, allowed to cool, then concentrated by evaporation. The last step was analysis by Chromatography Gas-Mass Spectroscopy (GC-MS) (Shimadzu 2010 QP Ultra) on a 30 m DB-5 capillary column (0.25 µm i.d.) with a linear temperature program (Louchouarn et al., 2010; Juarez et al., 2011; Loh et al., 2012). The correlation between the parameters was tested by using t-test.

3. RESULTS AND DISCUSSION

3.1 Aquatic conditions

Oceanographic parameters are pH(c): pH at coastal, pH(s): pH at sea, Temp(c): temperature at coastal, Temp(s): temperature at sea, Curr.(c): current at coastal, Curr.(s): current at sea, Salinity, Dissolved

Oxygen, and Brightness shown in Figure 2. The waters pH ranged from 7.36-7.76 during sampling in June 2017 (dry season) at the coast of the Tallo river estuary and the Makassar sea; temperatures ranged between 30.1-32.7 °C; the current speed range was 5.23-9.86 cm/s; the salinity range was 11.9-20.2‰; the dissolved oxygen range was between 5.51-5.97 mg/L, and the brightness range was 31.7-62.7%. While at the site estuary and seacoast in the area Pangkep have a pH range was 7.18 to 7.51; temperature range 29.7-32.1 °C; current range 6.97-8.87 cm/s; salinity range 11.2-17.2‰; dissolved oxygen ranged from 4.92 to 5.76 mg/L and the brightness ranged from 31.6 to 72.4%.

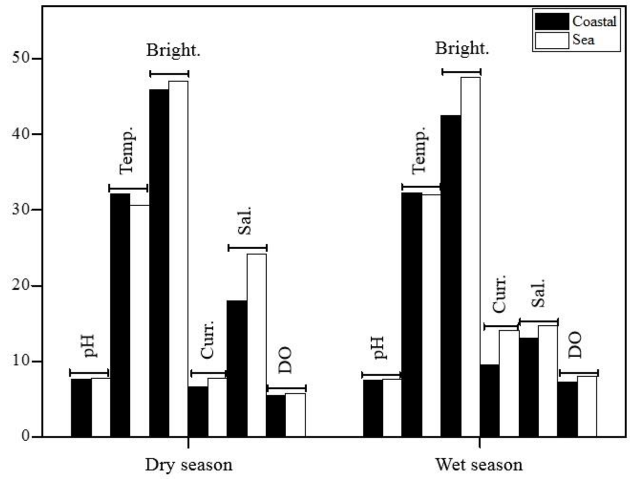

Figure 2. The oceanographic parameters values

Meanwhile, the oceanographic parameters range values in January 2018 (wet season) on the coastal estuary of the Tallo river and the Makassar sea, shows a pH range between 6.98-7.21; temperature range of 27.20-30.8 °C; current speed range 7.07-18.07 cm/s; salinity range 17.70-31.90‰; the dissolved oxygen range was 7.26-7.98 mg/L, and the brightness range was 18.40-65.40%. Observations for the coastal estuary of the Pangkep river and the sea, pH ranges from 6.89-7.18; temperature range of 27.5-30.5 °C; current speed range 11.15-16.22 cm/s; salinity range 14.8-24.5‰; the dissolved oxygen range was 7.14-7.26 mg/L, and the brightness range was 27.6-55.2%. Water quality parameters in all coastal observation seasons in the public domain and agricultural domains show the maximum pH and salinity range in the dry season due to the tendency of the conditions in the dry season to get the water from the land and rainwater to increase the salinity and pH range. DO and brightness obtained maximum values in the rainy season. The DO parameter value in the rainy season is higher than the dry season due to the mixing of seawater with fresh water which will increase DO value (Wulandari, 2008).

3.2 Elemental and isotopic composition

Analysis of organic matter source and biogeochemical changes can be done using element markers [Total Organic Carbon (TOC), Total Nitrogen (TN), and stable isotopes (δ^{13}C and δ^{15}N)]. The results of TOC measurements, TN magnitude, and C/N ratio of suspended particle material are shown in Table 1. The TOC was higher than TN and higher from the river rather than the sea area, showing low primary productivity and also reflecting the situation of most stored terrestrial organic materials before meeting the sea (Aufdenkampe et al., 2011). The magnitude and speed of runoff from land are strongly influenced by the seasons which have implications for TOC and TN. This result was due to an increase in organic production. TOC and TN values on the Tallo coast are 1.21-2.69% and 0.04-0.12% during the dry season: 0.68-1.87% and 0.04-0.11% respectively in the rainy season. TOC and TN value the Pangkep coastal 1.16-3.01% in the dry season, and 0.86-3.62% during the rainy season. The change in presentation is diminishing towards the sea, especially at a distance more than 11.46 km from the coast of Tallo and a distance more than 8.75 km on the coast of Pangkep (Figure 3).

Table 1. Composition of the organic matter in suspended particle material (Triplication).

Sampling sites	TOC (%)	TN (%)	[C/N]mol Ratio	δ^{13}C (‰)	δ^{15}N (‰)
Dry season (June sampling)					
Tallo River Estuary	2.69	0.12	22.28	-25.84	2.68
Barrang Lompo Island	1.78	0.08	20.83	-26.69	2.06
Bone Tambung Island	1.62	0.08	18.85	-21.85	3.38
Langkai Island	1.21	0.06	20.71	-24.88	2.22
Lanjukang Island	1.35	0.04	35.30	-23.66	2.06

Table 1. Composition of the organic matter in suspended particle material (Triplication) (cont.).

Sampling sites	TOC (%)	TN (%)	[C/N]mol Ratio	$\delta^{13}C$ (‰)	$\delta^{15}N$ (‰)
Pangkep River Estuary	3.01	0.16	18.31	-25.98	2.62
Laiya Island	1.79	0.08	21.25	-22.88	2.46
Sarappo Keke Island	1.39	0.05	28.73	-24.29	2.32
Kondong Bali Island	1.21	0.04	28.80	-21.87	4.38
Kapoposang Island	1.16	0.11	10.09	-25.82	3.52
Rainy season (January sampling)					
Tallo River Estuary	1.25	0.08	14.07	-26.06	4.01
Barrang Lompo Island	0.81	0.06	12.52	-25.29	3.56
Bone Tambung Island	0.68	0.05	13.34	-22.33	3.38
Langkai Island	0.72	0.04	15.14	-27.11	3.54
Lanjukang Island	1.87	0.11	16.75	-23.34	2.64
Pangkep River Estuary	1.52	0.11	21.79	-23.04	2.75
Laiya Island	1.31	0.02	69.79	-22.92	2.99
Sarappo Keke Island	0.86	0.05	16.67	-22.12	2.61
Kondong Bali Island	2.93	0.15	19.11	-23.56	4.86
Kapoposang Island	3.62	0.27	13.27	-23.81	4.56

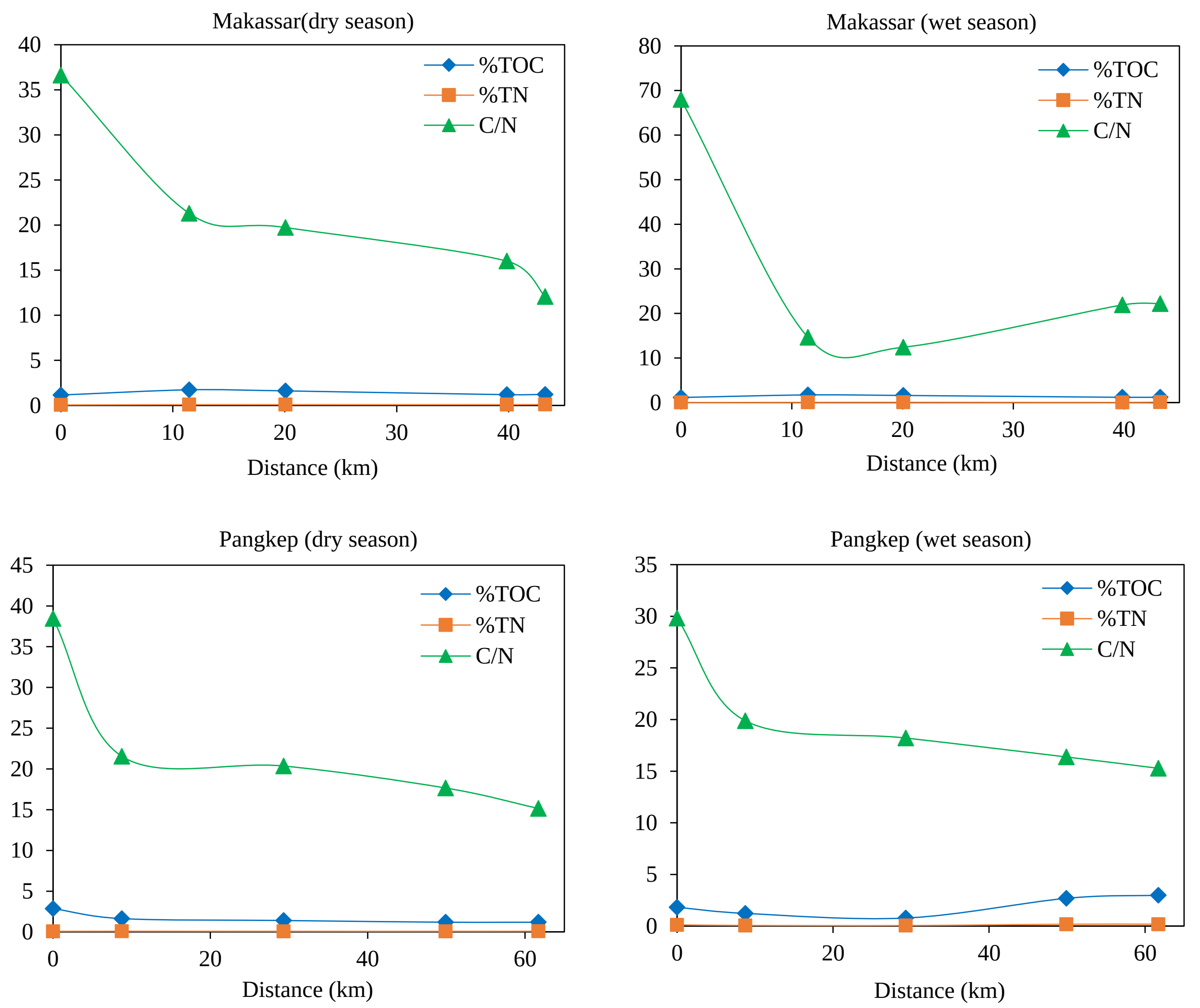

Figure 3. %TOC, %TN, and C/N ratio value (Makassar dry season, Pangkep dry season); (Makassar rainy season, Pangkep rainy season)

Figure 3 shows that the C/N ratio value on the coast of Tallo and Pangkep decreased from terrestrial to the sea (on the dry season). While in the rainy season, there is an increase in the value of the C/N ratio at various sampling points, on the Tallo coast the value of the C/N ratio near the land (at a distance of 20.07 km) is lower than the point of the sea location in front of it. The value of the ratio increases at a distance of 39.85 km, then, the ratio value decreases at a distance of 43.27 km. On the other hand, on the coast of Pangkep, there has been a decline from terrestrial to sea. The value of the C/N ratio varies with the runoff distance from land-to-sea in the dry season and rain with a range of 15-68. The C/N ratio change is strongly influenced by the amount of runoff and the spread of anthropogenic inputs, local hydrographic, hydrodynamic regimes, and other environmental features (Horiuchi et al., 2000; Schubert and Calvert, 2001; Tani et al., 2002; Shen et al., 2005; Sutapa et al., 2018a, Wahab et al., 2019).

The average isotopic values and other chemical and environmental variables in the waters off the west coast of South Sulawesi from the two seasons of data collection are shown in Figure 4. Changes in the values of $\delta^{13}C$ showed a systematic increase in the relative proportions of organic matter derived from C_3 and C_4 plants ($\delta^{13}C$ in the dry season ranging from -27.22‰ to -20.37‰ and the rainy season ranged from -27.11‰ to -21.84‰). However, the corresponding C/N ratio value does not show a systematic increase in the relative proportions of organic carbon derived from C_3 plants. Thus, the variation of the values of $\delta^{13}C$ observed is mostly due to thinning at ^{13}C during primary production as a result of increased rainfall (Guo and Xie, 2006).

Figure 4 shows the change in the value of $\delta^{15}N$ from 2.020‰ to 5.110‰ in the rainy season and 1.580‰ to 4.580‰ in the dry season. These results indicate differences of the value of $\delta^{15}N$ in the rainy season and dry season. This is due to high rainfall in the rainy season changing biological production not only in coastal and marine waters but also on land. Therefore the supply of nutrients to coastal and marine waters is very high (Onstad et al., 2000; Ménot and Burns, 2001; Sharma et al., 2005; Kitagawa et al., 2007; Bianchi et al., 2011).

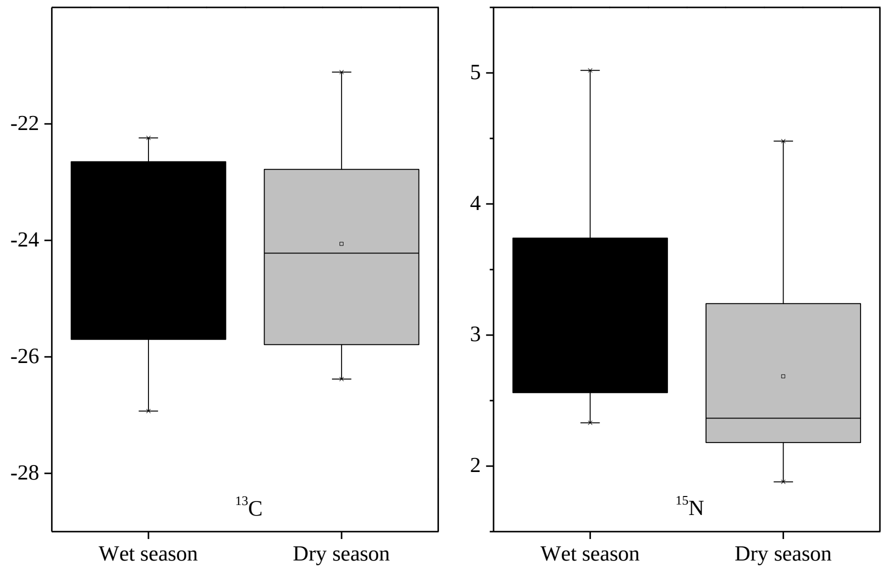

Figure 4. $\delta^{13}C$ and $\delta^{15}N$ range values based on the season

3.3 Lignin phenols composition

The composition profile of the lignin phenol contained in the SPM sample is shown in Figure 5. Based on the results, the SPM contained vanillin, vanillic acid, cynnamic acid, acetovanilins, syringic acid, syringaldhedyde, and acetonsiringone.

Based on these results, further analysis was carried out to determine Λ, S/V, C/V, $(Ad/Al)_v$, and $(Ad/Al)_s$ as shown in Table 2. Table 2 shows the range of the Λ values (value of the normalized carbon of lignin/100 mg organic carbon) in the rainy season in all locations (0.92 to 2.30) are higher than in the dry season (0.62 to 2.07 (mg/100 mg OC). In addition, temporally, lignin phenol in the rainy season in Tallo waters is higher than in Pangkep waters, but the lignin phenol composition into the sea is getting smaller. Effect of seasonal factors on the composition of lignin phenol is very significant ($p<0.05$) (Figure 6), while spatially is not significant (p>0.05) (Figure 7). The condition caused by the flow of freshwater along the watershed has brought various materials from the land which causes the magnitude of nutrient in the estuary to fluctuate (Grizzetti et al., 2012).

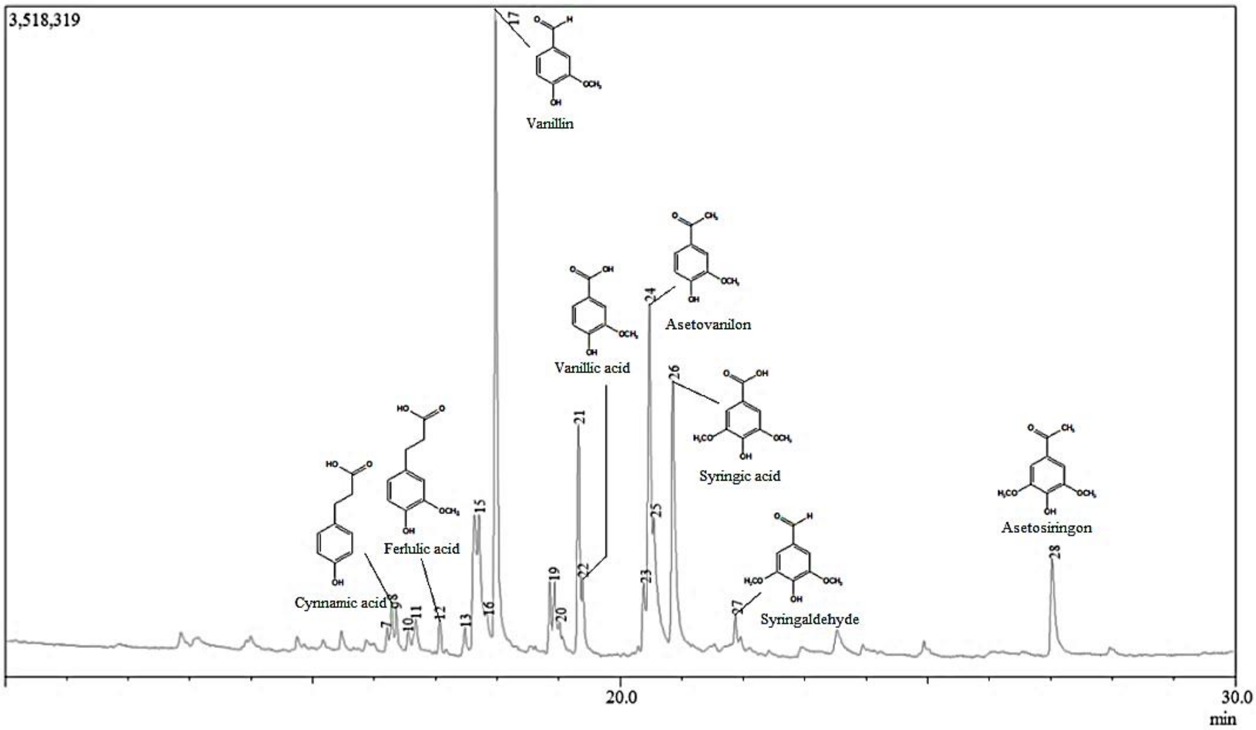

Figure 5. GC-MS analysis profile of lignin phenol

Table 2. Composition of lignin phenol from river inputs to ocean (Three time replication).

Sampling sites	Λ (mg/100 mg OC)	S/V	C/V	(Ad/Al)v	(Ad/Al)s
Dry season (June sampling)					
Tallo River Estuary	2.07	1.12	0.57	1.08	1.25
Barrang Lompo Island	1.38	0.80	0.52	0.82	0.80
Bone Tambung Island	1.15	0.71	0.52	0.83	0.74
Langkai Island	0.94	0.62	0.48	0.76	0.72
Lanjukang Island	0.72	0.45	-	0.62	0.43
Pangkep River Estuary	1.94	0.87	0.55	0.82	0.87
Laiya Island	1.46	0.72	0.45	0.80	0.73
Sarappo Keke Island	1.11	0.69	0.41	0.72	0.68
Kondong Bali Island	1.05	0.62	0.39	0.34	0.18
Kapoposang Island	0.62	0.35	-	0.20	0.10
Rainy season (February sampling)					
Tallo River Estuary	2.30	0.84	0.43	1.40	1.27
Barrang Lompo Island	1.59	0.50	0.39	0.98	0.81
Bone Tambung Island	1.53	0.80	0.42	0.72	0.87
Langkai Island	1.15	0.61	0.32	0.65	0.74
Lanjukang Island	0.92	0.37	0.46	0.92	0.71
Pangkep River Estuary	1.95	1.18	0.62	1.19	1.30
Laiya Island	1.87	0.87	0.48	1.01	1.18
Sarappo Keke Island	1.76	0.62	0.39	1.04	0.97
Kondong Bali Island	1.69	0.43	0.43	0.82	0.78
Kapoposang Island	1.46	0.38	-	0.33	0.71

Based on Figure 5, reviewed by season (temporal), the S/V and C/V ratios range from 0.35 to 1.12 and 0.39 to 0.57, respectively, in the dry season sampling. These results indicate a low contribution of angiospermic plant tissue. While in the rainy season, the S/V and C/V ratios range from 0.37 to 1.18 and 0.32 to 0.62. This S/V value indicates the contribution of plant tissue to angiosperms, while the C/V value is greater than 0.1, indicating a significant contribution of non-woody plant tissue. The value of the S/V and C/V ratios based on the season shows that during the rainy season it is higher than the dry season, this is due to rainfall factors which accelerate the entry of runoff from the mainland into the river mouth and Spermonde sea waters. The difference of the runoff character is an implication of runoff along with the river flow. The activity along the Tallo river flow (urban and industrial) differs from activity along with the Pangkep river flow (aquaculture and agriculture) (Costa et al., 2008).

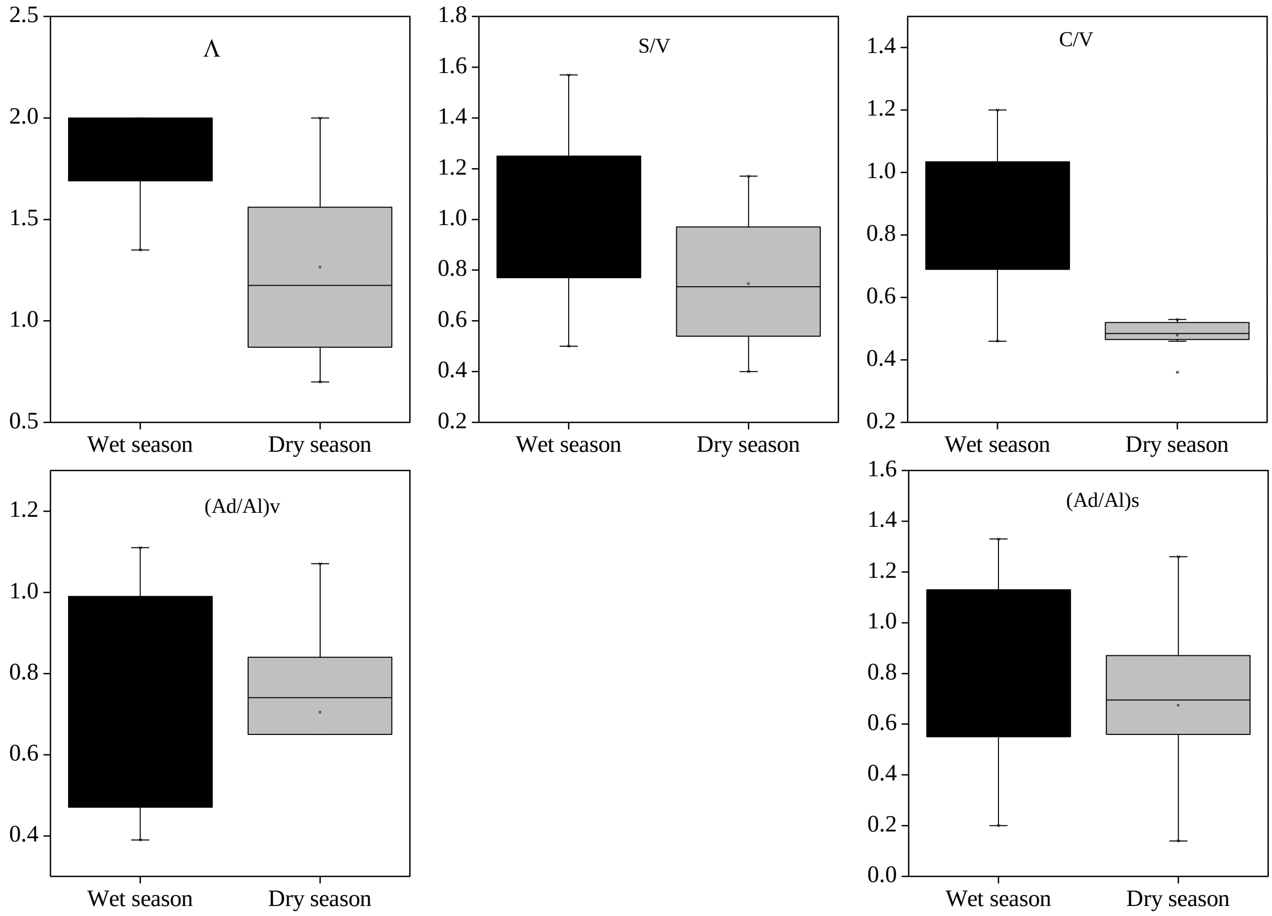

Figure 6. Box plots of the minimum and maximum values base on season

Spatially, S/V and C/V values were found to be relatively high at the estuary of the Tallo river (0.37 to 1.12 and 0.32 to 0.57) and the Pangkep river estuary (0.35 to 1.18 and 0.39 to 0.62) (Figure 6). A downward trend occurs when heading towards the outer islands. The C/V value in the dry season is not detected on Lanjukang Island and Kapoposang Island which is the outermost island and the farthest distance from the mainland, whereas in the rainy season it is not detected on Kapoposang Island. This shows that the presence of organic material in waters originating from three different types of plant tissue, including angiosperms, gymnosperms and non-woody gymnosperms is highly dependent on the speed of water flow carrying the material to deep waters (Dittmar and Lara, 2001). Furthermore, the ratio of S/V, C/V, vanillic acid to vanillin $(Ad/Al)_v$ and syringic acid to syringaldehyde $(Ad/Al)_s$ based on sampling location is shown in Figure 7.

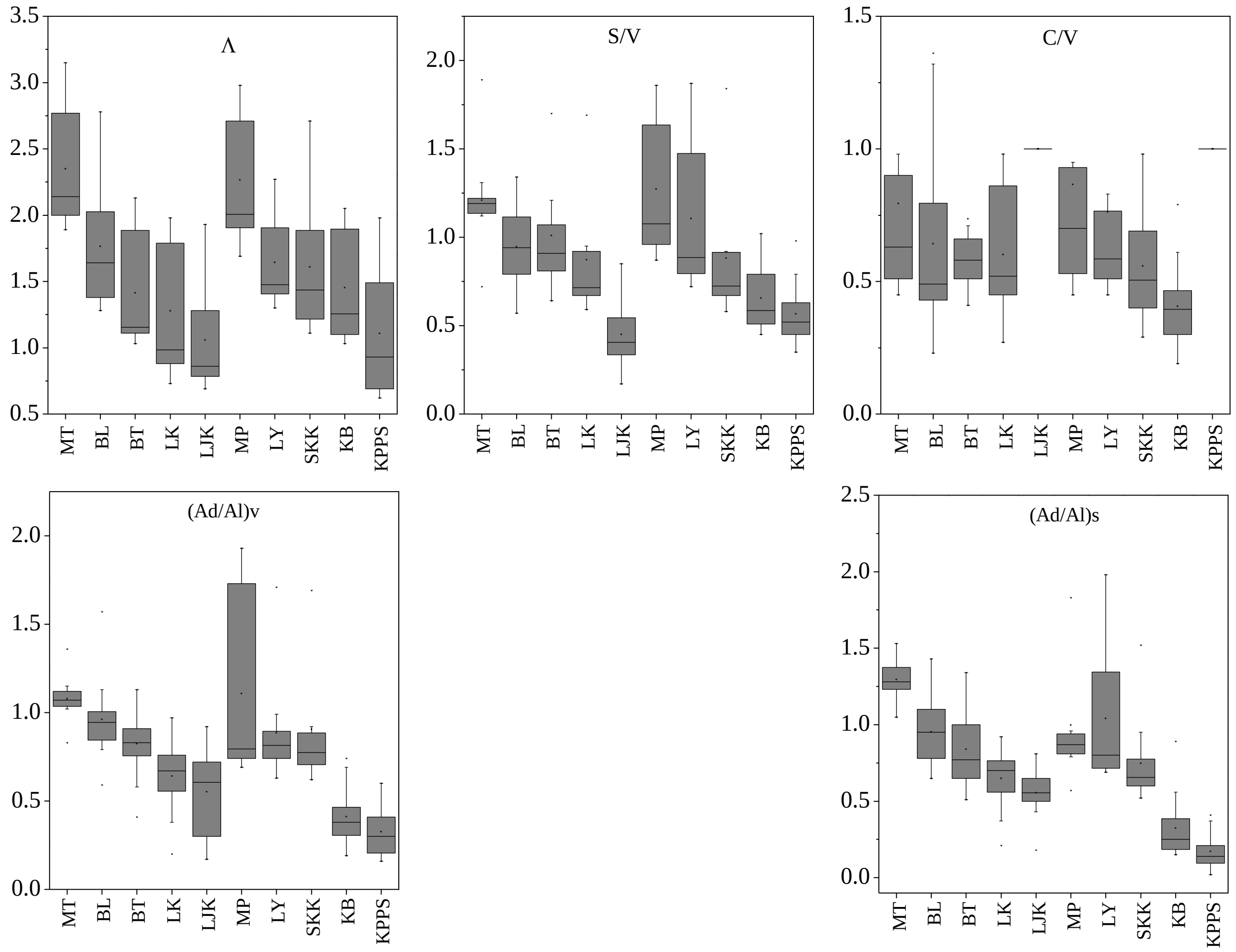

Figure 7. Box plots of the minimum and maximum values based on location

Spatially, the ratio value of $(Ad/Al)_v$ at the location of the Tallo and Pangkep river mouths up to several outermost islands ranged from 0.62 to 1.40 and 0.20 to 1.19 respectively. While the value of the ratio $(Ad/Al)_s$ in the estuary of the Tallo and Pangkep rivers ranges from 0.43 to 1.27 and 0.10 to 1.30. These results indicate that lignin (the most abundant content of humic acid) has undergone oxidative degradation and is associated with mineral from the soil (Goñi et al., 2000; Sutapa et al., 2018b).

4. CONCLUSION

The study shows the difference of the lignin phenol composition in Spermonde water (Makassar waters and Pangkep area) are influenced by seasonal factors. Makassar waters contain a higher average lignin phenol compared to Pangkep waters. Although the composition of lignin phenol content was greater in Makassar waters, the ratio of C/V lignin phenol not detected at the location of the outermost island sampling which was 43.27 km from the estuary of the Tallo river and 61.71 km from the Pangkep estuary. This condition explains that lignin has been degraded to several outermost islands.

ACKNOWLEDGEMENTS

This research was financed by the Grant of Doctoral Dissertation of the Ministry of Research and Technology in 2018. The authors would like to thank to all those helped this research.

REFERENCES

Aufdenkampe AK, Mayorga E, Hedges JI, Lerena C, Quay PD, Gudeman J, Krusche AV, Richey JE. Organic matter in the Peruvian headwaters of the Amazon: compositional evolution from the Andes to the lowland Amazon mainstem. Organic Geochemistry 2007;38:337-64.

Aufdenkampe AK, Mayorga E, Raymond PA, Melack JM, Doney SC, Alin SR. Riverine coupling of biogeochemical cycles between land, oceans, and atmosphere. Frontiers Ecology and the Environmental 2011;9:53-60.

Bayram A, Onsoy H, Bulut VN, Akinci G. Influences of urban wasterwaters on the stream water quality: a case study from Gumushane province, Turkey. Environmental Monitoring and Assessment 2013;185:1285-303.

Bianchi TS, Wysocki LA, Schreiner KM, Filley TR, Corbett DR, Kolker AS. Sources of terrestrial organic carbon in the

Mississippi Plume Region: Evidence for the importance of coastal marsh inputs. Aquatic Geochemistry 2011;17:431-56.

Costa Jr OS, Nimmo M, Cordier E. Coastal nutrifiction in Brazil: A review of the role of nutrient excess on coral reef demise. Journal of South American Earth Science 2008;25(2):257-70.

Dittmar T, Lara RJ. Molecular evidence for lignin degradation in sulphatereducing mangrove sediments (Amazonia, Brazil). Geochimica et Cosmochimica Acta 2001;65:1417-28.

Garnier J, Beusen A, Thieu V, Billen G, Bouwman L. N:P:Si Nutrient export ratios and ecological consequences in coastal seas evaluated by the ICEP approach. Global Biogeochemical Cycles 2010;24(4):1-12.

Goñi MA, Montgomery, S. Alkaline CuO oxidation with a microwave digestion system: lignin analyses of geochemical samples. Analytical Chemistry 2000;72:3116-21.

Grizzetti B, Bouraoui F, Aaloe A. Changes of nitrogen and phosphorus loads to European Seas. Global Change Biology 2012;18:769-82.

Guo G, Xie G. The relationship between plant stable carbon isotope composition, precipitation and satellite data, Tibet Plateau, China. Quaternary International 2006;144:68-71.

Gypens N, Borges AV, Lancelot C. Effect of eutrophication on air-SSa CO_2 fluxes in the coastal Southern North Sea: A model study of the past 50 years. Global Change Biology 2009;15:1040-56.

Hansell AD, Carlson CA. Biogeochemistry of total organic carbon and nitrogen in the Sargasso Sea: Control by convective overtuum. Deep-Sea Research 2001;48;1649-67.

Hedges JI, Oades JM. Comparative organic geochemistries of soils and marine sediments. Organic Geochemistry 1997;27(7-8);319-61.

Hoefs J. Stable Isotope Geochemistry. 6th ed. Springer: Berlin Heidelberg; 2009.

Horiuchi K, Minoura K, Hoshino K, Oda T, Nakamura T, Kawai T. Palaeoenvironmental history of Lake Baikal during the last 23000 years. Palaeogeography, Palaeoclimatology, Palaeo-ecology 2000;157;95-108.

Juarez S, Rumpel C, Mchunu C, Chaplot V. Carbon mineralization and lignin content of eroded sediments from a grazed watershed of South-Africa. Geoderma 2011;(167-168):247-53.

Kitagawa H, Tareq SM, Matsuzaki H, Inoue N, Tanoue E, Yasuda Y. Radiocarbon concentration of lake sediment cellulose from Lake Erhai in southwest China. Nuclear Instruments and Methods in Physics Research Section B: Beam Interactions with Materials and Atoms 2007;259:526-9.

Lagbas AJ, Salvaleon JAM, V. Ruyeras JJN. Zooplankton and white goby (*Glossogobius giuris* Hamilton 1822): Correlation and fishers' perception in selected sites in Laguna de bay, Luzon island, Philippines. Environment and Natural Resources Journal 2017;15(1):1-18.

Li W, Fujibayashi M, Nomura M, Nishimura O, Li X. Predominance of terrestrial organic matter in sediments from a cyanobacteria-blooming hypereutrophic lake. Ecological Indicators 2015;(50):35-43.

Loh PS, Chen CA, Anshari GZ, Wang JT, Lou JY, Wang SL. A comprehensive survey of lignin geochemistry in the sedimentary organic matter along the Kapuas River (west kalimantan, Indonesia). Journal of Asian Earth Sciences 2012;43(1):118-29.

Louchouarn P, Amon RMW, Duana S, Pondell C, Seward SM, White N. Analysis of lignin-derived phenols in standard references materials and ocean dissolved organic matter by gas chromatography/tandem mass spectrometry. Marine Chemistry 2010;118(1-2):85-97.

Ménot G, Burns S. Carbon isotopes in embryogenic peat bog plants as climatic indicators: Calibration from an altitudinal transect in Switzerland. Organic Geochemistry 2001;32:233-45.

Nagao S, Takafumi A, Osamu S, Masao, Yasuyuki S. Carbon Isotopes and Lignin composition of POC in a small river in Bekanbeushi Moor, northern Japan. Nuclear Instruments and Methods in Physics Research B 2010;268:1098-101.

Nurdin N, Amri K, Djalil AR, Akbar AS M, Jaya I, Agus. Shallow water cover dynamic on small islands, Spermonde Archipelago. Majalah Ilmiah Globe 2016;17(2):105-12.

Onstad GD, Canfield DE, Quay PD, Hedges JI. Sources of particulate organic matter in rivers from the continental USA: lignin phenol and stable carbon isotope compositions. Geochimica et Cosmochimica Acta 2000;64:3539-46.

Opsahl S, Zepp RG. Photochemically-induced alteration of stable isotope ratios ($\delta^{13}C$) in terrigenous dissolved organic carbon. Geophysical Research Letters 2001;28(12):2417-20.

Qu HJ, Kroeze C. Nutrient export by rivers to the coastal waters of China: Management strategies and future trends. Regional Environmental Change 2012;12(1):153-67.

Schubert CJ, Calvert SE. Nitrogen and carbon isotopic composition of marine and terrestrial OM in Arctic Ocean sediments: Implication for nutrient utilization and OM composition. Deep-Sea Research 2001;48:789-810.

Shen J, Xingqi L, Sumin W, Matsumoto R. Palaeoclimatic changes in the Qinghai Lake area during the last 18,000 years. Quaternary International 2005;136:131-40.

Sharma S, Mora G, Johnston JW, Thompson TA. Stable isotope ratios in swale sequences of Lake Superior as indicators of climate and lake level fluctuations during the Late Holocene. Quaternary Science Reviews 2005;(24):1941-51.

Sutapa IW, Wahab AW, Taba P, Nafie NL. Synthesis and structural profile analysis of the MgO nanoparticles produced through the sol-gel method followed by annealing process. Oriental Journal of Chemistry 2018a;34(2):1016-25.

Sutapa IW, Wahab AW, Taba P, Nafie NL. Dislocation, crystallite size distribution and lattice strain of magnesium oxide nanoparticles. Journal of Physics: Conference Series 2018b; 979(012021):1-9.

Tani Y, Kurihara K, Nara F, Itoh N, Soma M, Soma Y, Tanaka A, Yoneda M, Hirota M, Shibata Y. Temporal changes in the phytoplankton community of the southern basin of Lake Baikal over the last 24,000 years recorded by photosynthetic pigments in a sediment core. Organic Geochemistry 2002; 33:1621-34.

Wahab AW, Karim A, Nafie NL, Satrimafitrah P, Triana, Sutapa IW. Production of the nanoparticles using leaf of *Muntingia calabura* L. as bioreductor and potential as a blood sugar nanosensor. Journal of Physics: Conference Series 2019;1242(012004):1-9.

Wulandari L. Analysis of macrozoobenthos pollution and community structure in the Kahayan river, Palangka Raya city. Journal of Oceanography 2008;5(2):110-30.

Xing L, Hailong Z, Zineng Y, Yao S, Meixun Z. Terrestrial and marine biomarker estimates of organic matter sources and distributions in surface sediments from the East China Sea shelf. Continental Shelf Research 2011;31(10):1106-15.

Revision of Vajiralongkorn Dam's Reservoir Characteristic Curves Using NDWI Derived from Landsat 8 Data

Yutthana Phankamolsil[1] and Ekasit Kositsakulchai[2*]

[1]*Environmental Engineering and Disaster Management Program, Mahidol University, Kanchanaburi Campus, Saiyok, Kanchanaburi 71150, Thailand*
[2]*Department of Irrigation Engineering, Faculty of Engineering at Kamphaeng Saen, Kasetsart University, Nakhon Pathom 73140, Thailand*

ARTICLE INFO

Received: 17 Aug 2019
Received in revised: 20 Oct 2019
Accepted: 6 Nov 2019
Published online: 6 Dec 2019
DOI: 10.32526/ennrj.18.2.2020.13

Keywords:
Reservoir/ Storage capacity curve/ Remote sensing/ Landsat/ NDWI

*** Corresponding author:**
E-mail: ekasit.k@ku.th

ABSTRACT

Reservoir characteristics are the essential information for water management planning and reservoir operation. Regular monitoring and assessment of the reservoir characteristics can reduce risks associated with the reservoir operation. This research assessed the reservoir characteristics (water surface, volume) of Vajiralongkorn Dam using remote sensing. Reservoir water surface was classified using the Normalized Difference Water Index (NDWI) derived from the Landsat 8 data, and validated using the streamline matching rate (SMR) and the streamline matching error (SME) techniques for shoreline accuracy assessment. The volume between two water levels was calculated using the prismatic equation. The storage capacity curve was constructed from the reservoir water level and cumulative volume. The accuracy of NDWI technique was satisfactory in identifying reservoir water surface with a good accuracy of shoreline delineation (SMR>95% and SME=11.7 m). The water surface has decreased on the average of 8.2 km^2 (2.8%) compared with the original data in 1980. The storage capacity has decreased 495.3 million m^3 (MCM) over 38 years from 1980 to 2018, an annual capacity loss of 13 MCM. Finally, sustainable service of the reservoir needs better knowledge of the effects of storage loss, the erosion and sediment-transport processes, and conservation measures.

1. INTRODUCTION

The Vajiralongkorn (VJK) dam, located in the western Thailand has a large and important water storage reservoir. The dam was constructed in 1980 across the Kwai Noi River. The crossed construction in a river inevitably effects the sediment transport and accumulation. For this reason, the change in the sediment transport system leads to sediment accumulation problems resulting in the reduction of storage capacity and lifespan of reservoir (Morris and Fan, 1998; Fan and Morris, 1992a; Fan and Morris, 1992b). The reservoir characteristics (surface area and storage) are vital parameters in reservoir operation. Over the long period of operation, the reservoir characteristics changed due to morphology and human activity effects, such as sedimentation, land-use change or reclamation (Cesare et al., 2001). Therefore, it is essential to regularly survey and assess the reservoir characteristic curves. However, the financial cost has a great influence on the frequency of reservoirs survey (MacPheson et al., 2011).

There are two approaches commonly used to conduct the revision of reservoir characteristic curves. The first approach is bathymetric survey (Ortt et al., 2000; Odhiambo and Boss, 2004; Su et al., 2008; Grin, 2014). It relies on measuring the actual depths of water in the reservoir to calculate volume, in addition to bed-mapping the reservoir. For example, MacPheson et al. (2011) conducted bathymetric and topographic surveys to determine the water storage capacity, and the loss of capacity owing to sedimentation in Loch Lomond reservoir in Santa Cruz County, California. Other researchers including Su et al. (2008), Grin (2014), and Odhiambo and Boss

Citation: Phankamolsil Y, Kositsakulchai E. Revision of Vajiralongkorn Dam's reservoir characteristic curves using NDWI derived from Landsat 8 Data. Environ. Nat. Resour. J. 2020;18(2):134-145. DOI: 10.32526/ennrj.18.2.2020.13

(2004) likewise employed this approach. However, the approach requires time-consuming measurements, and needs several survey lines for generating a bed map. The second approach is an indirect method, which relies on a remote sensing technique (Pandey et al., 2016; Cui et al., 2013; Jain et al., 2002). Peng et al. (2006) estimated a new reservoir storage curve of Fengman reservoir in China using remote sensing. The NDWI technique was used to extract water body from Landsat TM images and compared with the observed data. The result showed that reservoir storage curve estimation is reasonable and has relatively high precision. Foteh et al. (2018) revised the live storage capacity and the total loss of Jayskwadi reservoir capacity due to the sediment deposition in India using Landsat 8 OLI/TIRS satellite data. The previous studies demonstrated the potential of remote sensing technique in assessing the reservoir sedimentation and analyzing its spatio-temporal variation. One of the common data source was the Landsat image (Avisse et al., 2017; Du et al., 2014; Rodrigues et al., 2012; Gupta and Banerji, 1985), especially for estimating reservoir storage loss (Zhang et al., 2018; El-Shazli and Hoermann, 2016; Ran and Lu, 2012).

This research investigated the remote sensing method for assessing water surface and volume of VJK reservoir. The specific objectives were to identify the water surface of VJK reservoir using the NDWI derived from the Landsat 8 data, and to estimate the VJK storage loss using the revised storage capacity curve.

2. METHODOLOGY

The overall methodology comprised four steps (Figure 1). Landsat image acquisition and preprocessing, reservoir surface water extraction, shoreline accuracy assessment, and storage capacity estimation.

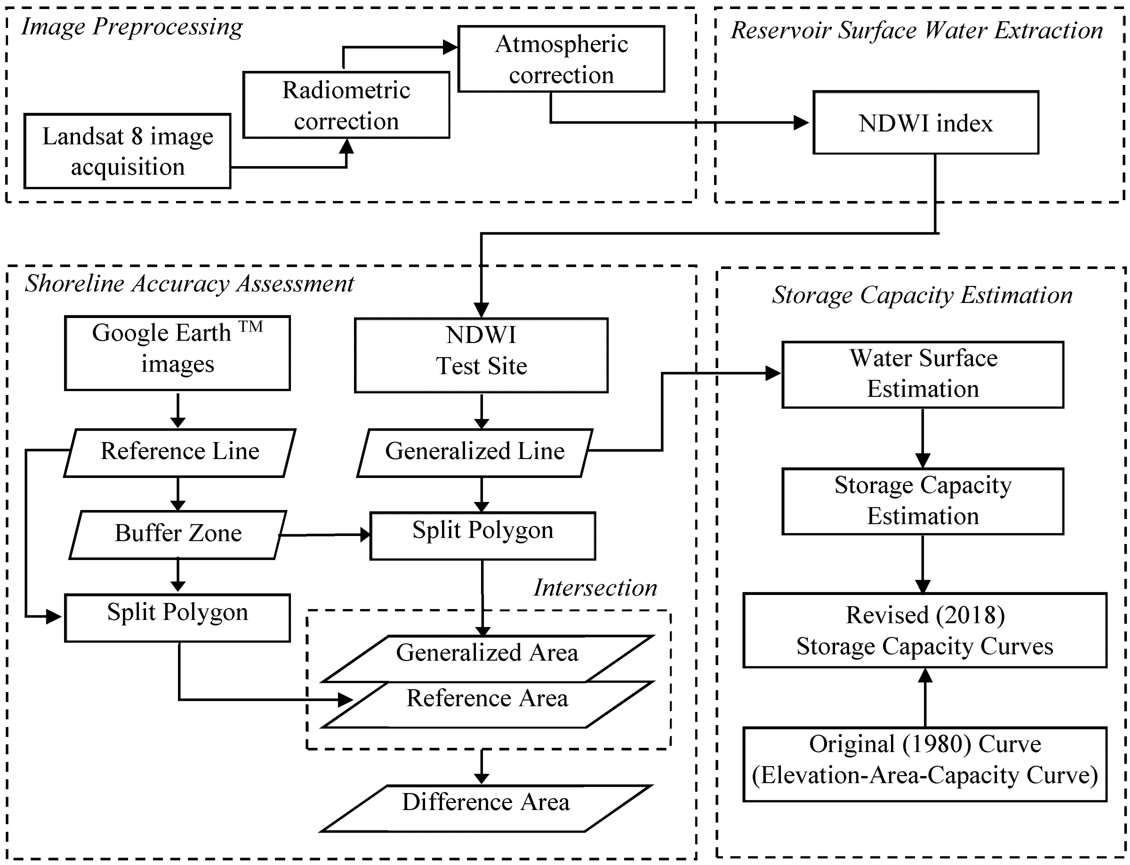

Figure 1. Overall methodology

2.1 Study site

The Vajiralongkorn (VJK) dam is located in Kanchanaburi province (about 150 km from the city center), in western Thailand (Figure 2). The dam is across the Kwai Noi River where the topography is mountainous. It is a rock-fill dam with a concrete facing slab that was constructed in 1980 and started operating in 1984. The reservoir was equipped to provide storage and release of water for multipurpose uses such as irrigation, flood control, hydropower generation, navigation, ecosystem, fishing and tourism. The reservoir has a surface area of 3,720 km^2 and length of 1.1 km; the height of the dam is 92 m above the river bed. The maximum pool level, the normal pool level, and the minimum pool level are respectively +160.5 m.a.s.l. (11,000 MCM), +155.0 m.a.s.l. (8,860 MCM), and +135.0 m.a.s.l. (3,012 MCM). The active storage is 5,848 MCM (difference between the normal and the minimum pool levels). Figure 2(e) shows the storage zones.

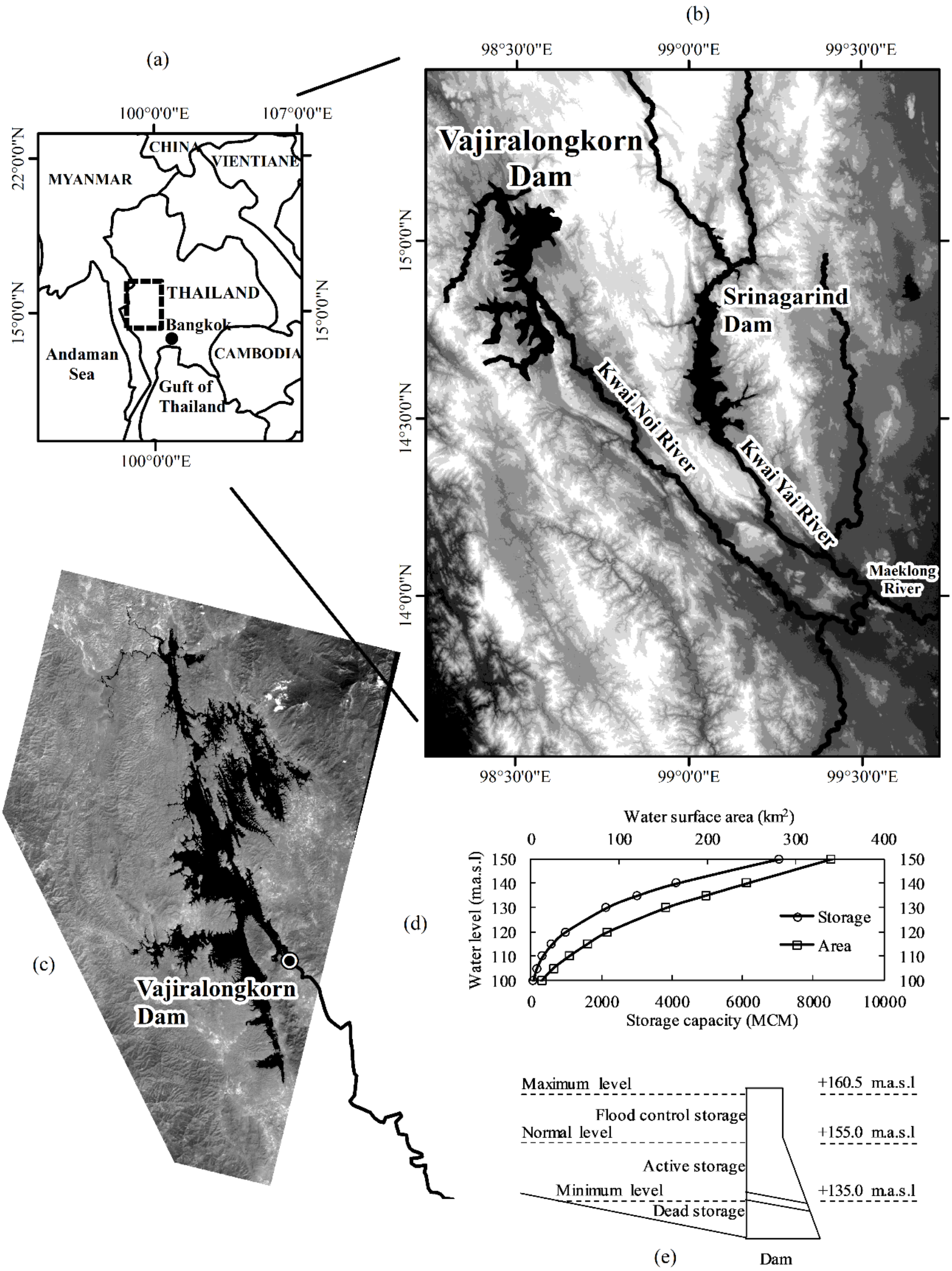

Figure 2. Location of the Vajiralongkorn (VJK) dam and reservoir characteristics: (a) regional map, (b) the Digital Elevation Model (DEM), (c) VJK reservoir from Landsat 8 false composite image, (d) VJK reservoir characteristic curves, and (e) VJK reservoir storage zoning.

2.2 Landsat 8 image

2.2.1 Data acquisition

The Landsat 8 satellite launched in February 2013, is the eighth American Earth observation (EO) satellite under the Landsat program, which is a collaboration between the National Aeronautics and Space Administration (NASA) and the United States Geological Survey (USGS). The Landsat 8 satellite collects the EO images with a 16-day repeat cycle (Scheffers and Kelletat, 2016). The Earth Explorer (http://earthexplorer.usgs.gov/) is the primary search interface for accessing images held in the USGS database. All images are distributed via Hypertext Transfer Protocol Secure (HTTPS), which are available to users at no cost. The image's data are stored in Geographic Tagged Image File Format (GeoTIFF) with Universal Transverse Mercator (UTM) projection and WGS84 datum. Twelve scenes (path 131, row 50) covering the entire VJK reservoir from 2013 to 2018 were selected (Table 1). The selection criteria were based on the range of reservoir water levels. Moreover, in order to avoid cloud disturbance, only the images with cloud cover less than 8% were selected.

2.2.2. Data pre-processing

Image pre-processing is an improvement of image data that maybe noisy or distorted during acquisition. The Landsat 8 OLI/TIRS images are acquired in the digital number (DN) format. Therefore, the radiometric calibration and atmospheric correction are prerequisite steps in order to generate the consistent and high-quality images, which consisted of three steps: (1) to convert DNs to the radiance based on the rescaling factors from the metadata file; (2) to convert radiance to TOA reflectance (Chander et al., 2009; Mishra et al., 2014), requiring additional information (Earth-Sun distance, solar zenith angle and exo-atmospheric irradiance); and (3) to apply atmospheric correction, requiring the atmospheric condition when the image was acquired. The atmospheric correction of Landsat images selected the Fast Line-of-Sight Atmospheric Analysis of Spectral Hypercubes (FLAASH) (Felde et al., 2003).

Table 1. Landsat 8 scene characteristics and the corresponding VJK reservoir water level

Acquisition date	Scene cloud cover (%)	Sun elevation L1 (degree)	Sun azimuth L1 (degree)	Reservoir water level (m.a.s.l.)
October 27th, 2013	1.06	56.1126559	142.6220	151.39
December 14th, 2013	1.53	46.0880237	148.7269	150.89
January 15th, 2014	0.10	45.72501243	142.9447	149.81
March 20th, 2014	7.65	59.88195648	116.8853	148.77
June 11th, 2015	2.70	64.98964157	66.1792	137.75
November 18th, 2015	1.39	51.20337824	147.3655	145.01
December 20th, 2015	2.01	45.40461047	147.7899	144.23
January 5th, 2016	0.24	44.97032311	145.1159	143.84
February 6th, 2016	0.14	48.80871324	136.1957	142.79
March 25th, 2016	2.40	61.14411182	113.2510	140.93
February 11th, 2018	0.86	49.98898489	134.2105	147.98
March 15th, 2018	3.37	58.39307113	119.6039	146.16

2.3 Estimation of reservoir characteristics

2.3.1 Reservoir surface water extraction

Reservoir shoreline was classified using the Normalized Difference Water Index (NDWI) (Deng et al., 2019; Ouma and Tateishi, 2007; Gao, 1996; McFeeters, 1996) which is a supervised classification technique applied for surface water detection with a selected suitable threshold. The NDWI designed to maximize reflectance of water by using the green wavelengths whereas water is reflected the lowest in the near-infrared band, opposite vegetation and soil which are the high reflections (Feyisa et al., 2014). The current research selected the threshold of zero to extract reservoir surface water. The NDWI is expressed as follows:

$$\mathrm{NDWI} = \frac{\mathrm{Green} - \mathrm{NIR}}{\mathrm{Green} + \mathrm{NIR}} \quad (1)$$

Where, Green is the green wavelengths (Band 3 of Landsat 8 OLI), NIR is the near-infrared band (Band 5 of Landsat 8 OLI).

2.3.2 Reservoir storage capacity estimation

The storage capacity was estimated using the prismatic equation (Equation 2) (Peng et al., 2006) that calculates from the incremental volume between any two-stage elevations and the reservoir's active storage capacity:

$$V_{i+l} = \frac{(Z_{i+l} - Z_i)}{3} \left(A_i + A_{i+l} + \sqrt{A_i \times A_{i+l}}\right) \quad (2)$$

Where, A_i and A_{i+l} are the reservoir water surface area at elevation Z_i and Z_{i+l} respectively, and V_{i+l} is the reservoir storage volume between Z_i and Z_{i+l} elevations. The storage capacity can calculate by the volume accumulation.

2.4 Accuracy assessment

2.4.1 Reference shoreline data

The high resolution images from Google Earth database were employed as the reference data for shoreline accuracy assessment. For this reason, the water surface data were not recorded by the observation data in the database of the Electricity Generating Authority of Thailand (EGAT) due to the large Vajiralongkorn dam and the water level fluctuation causing the change in water surface over time. Therefore, it is difficult to obtain the accurate ground-truth reservoir shoreline. The advantage of using Google Earth imagery is that it provides the latest imagery with high spatial resolution depending on the geographic viewed area. The reservoir shoreline can be visually seen on the image. Moreover, it provided images taken at different time periods which will be very useful for the researchers to perform the land cover change detection studies (Malarvizhi et al., 2016). However, the limitation of Google Earth imagery is that it is not possible to obtain the original multispectral band data (USGS, 2016), hence further image processing such as classification using unsupervised or supervised techniques is impracticable.

In the current study, the five sample sites (A1, A2, A3 A4, A5) surrounding the VJK reservoir were chosen for shoreline accuracy assessment by comparing the results between NDWI and Google Earth data (Figure 3). The sites were chosen based on the acquisition date of Google Earth history imagery which closely matched to the Landsat image scenes. In addition, it can represent the land cover characteristics on reservoir shoreline. It is not possible to compare the entire Vajiralongkorn shoreline since both image sources are different in acquisition time and scene size. The single Landsat scene is larger than the Google Earth image that was created using the satellite image mosaic. The Landsat acquisition information and Google Earth imagery are shown in Table 2.

2.4.2 Shoreline accuracy assessment

There are two steps in shoreline accuracy assessment: overlay analysis and streamline matching. The overlay analysis is a spatial analysis technique in GIS software**.** The on-screen digitizing and geo-referencing techniques were used for reference lines identification from the Google Earth imagery in the UTM/WGS84/zone47N projection system. Then, the buffer zone was created using the reference line offset of 30 m for error assessment; the offset distance is equal to the Landsat pixel resolution. The buffer zone was split into two sides as the "reference area". Secondly, the generalized line representing the reservoir shoreline was identified from the NDWI derived from the Landsat image. All image in raster data format was converted to vector data format using vectorization function. The buffer zone from the previous step was split using the generalized line as the "generalized area". Finally, the reference and generalized areas were overlay using the intersection function, which results in the difference area for calculating the streamline matching techniques.

The streamline matching techniques (Chen et al., 2012; Zhou, and Chen, 2011) compare the difference feature lines between the reference and generalized area (Figure 4). This approach can be divided by the streamline matching rate (SMR) and streamline matching error (SME). The SMR measures the changes rate in the length of generalized line or the shapes similarity between the reference and generalized line (Equation 3), while the SME calculates the average dispersion between the features (Equation 4):

$$SMR = \frac{L'}{L} \times 100 \quad (3)$$

$$SME = \frac{\Delta A}{L} \times 100 \quad (4)$$

Where, L is the total length of reference line, L′ is the length of generalized line within the buffer zone, and ΔA is the difference area between the reference line and generalized line within the buffer zone.

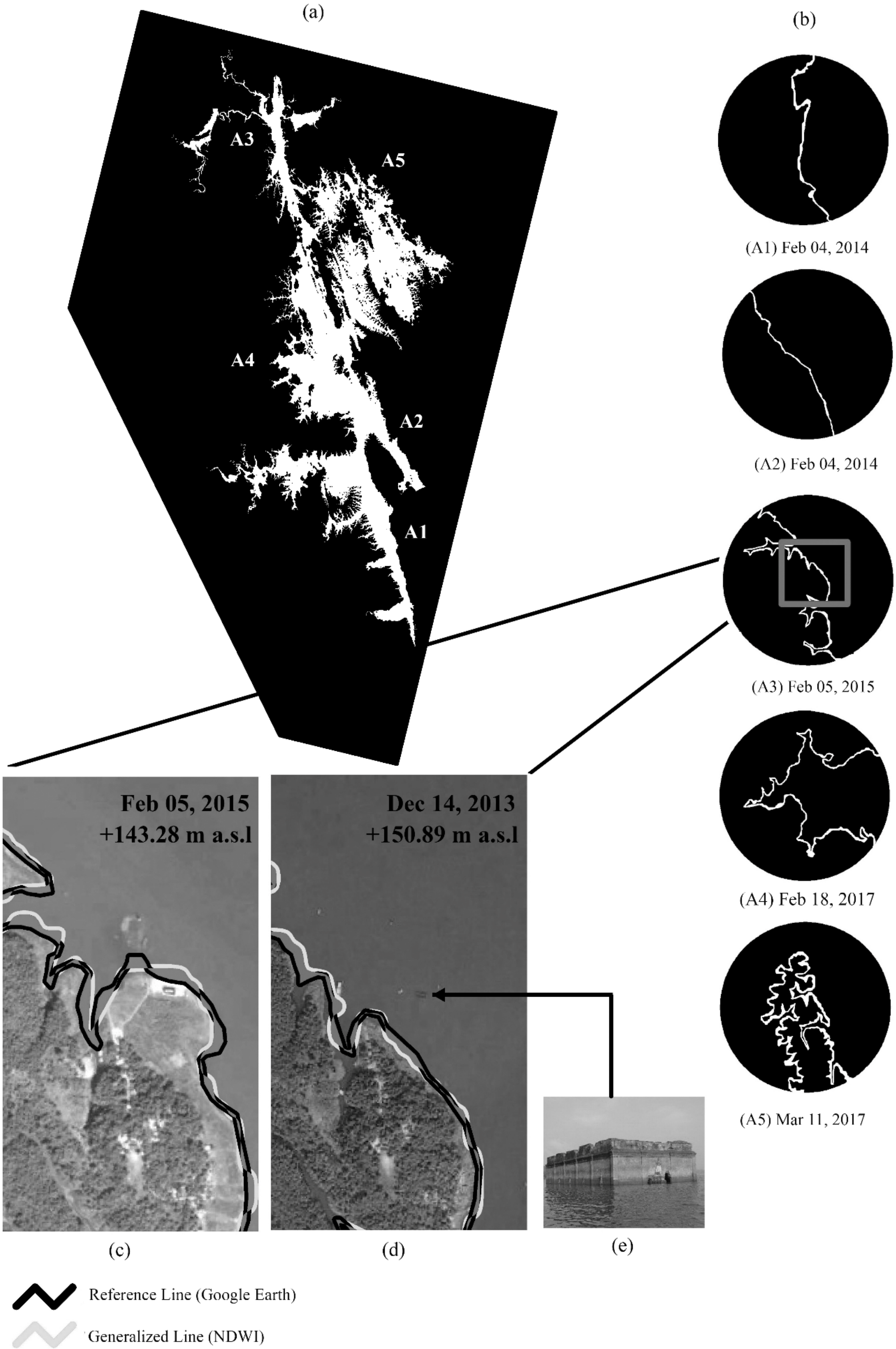

Figure 3. The shoreline sampling from high resolution images (Google Earth) as the reference lines for comparing with those derived from Landsat 8 data: (a) examples of shoreline extracted from the Google Earth high resolution images; (b) five sample locations surrounding the VJK Reservoir; (c) and (d), the sample location A3 on 5 February 2015 (c) and on 14 December 2013 (d) when reservoir water levels were respectively +143.28 m.a.s.l. and +150.89 m.a.s.l.; (e) the sunken temple as a reference location.

Table 2. Image acquisition dates of Landsat 8 scenes and Google Earth high resolution images and the corresponding VJK reservoir's water level

Location	Landsat scene		Google Earth Image	
	Date	Water level (m.a.s.l.)	Date	Water level (m.a.s.l.)
A1	Feb 09, 2014	148.28	Feb 09, 2014	148.28
	Mar 12, 2017	143.21	Mar 11, 2017	143.21
A2	Feb 09, 2014	148.28	Feb 02, 2014	148.72
	Mar 12, 2017	143.17	Mar 11, 2017	143.21
A3	Dec 14, 2013	150.89	Dec 14, 2013	150.89
	Feb 03, 2015	150.89	Feb 05, 2015	143.28
A4	Feb 09, 2014	150.89	Dec 14, 2013	150.89
	Feb 08, 2017	144.13	Dec 14, 2013	144.13
A5	Feb 09, 2014	150.89	Dec 14, 2013	150.89
	Mar 12, 2017	143.36	Feb 05, 2015	143.31

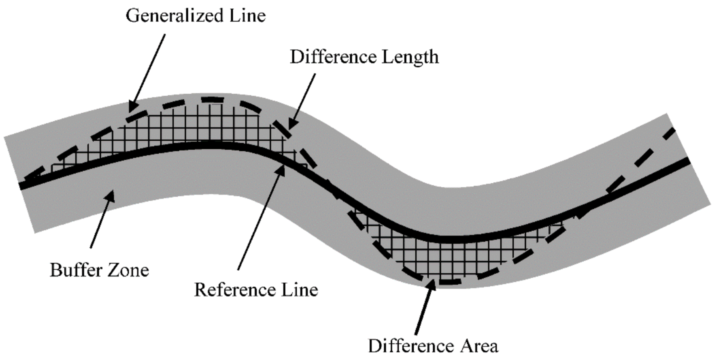

Figure 4. The streamline matching techniques: the reference line is the reservoir's shoreline that was digitized from Google Earth map; the generalized line is the water surface line identified using NDWI; the buffer zone is the tolerance zone and the distance from the reference line; the difference length is the difference length of generalized line from the reference line within buffer zone; and difference zone denotes the area that are not compatible within the buffer zone.

3. RESULTS

3.1 Reservoir water surface

The water surface of VJK reservoir identified using NDWI derived from Landsat 8 is shown in Figure 5. The water surface area was clearly discerned from the bright pixels. Table 3 shows the comparison of the water surface area between the NDWI-derived area and the original area (1980) at the water level from +137.75 m.a.s.l. to +151.39 m.a.s.l. The water surface area expands with the increasing of reservoir water level. The original data in 1980 reported the largest area of 318.8 km^2 (+151.39 m.a.s.l.) and the smallest of 201.8 km^2 (+137.75 m.a.s.l.), while the revised data using NDWI technique were respectively 310.7 km^2 and 197.4 km^2. The scatter plot (Figure 6(a)) indicated high correlation between the original area (1980) and the NDWI techniques (r^2=0.9679). There was no trend in the residual plot (Figure 6(b)). The mean of difference between the revised area and the original one was -8.2 km^2 (-2.8%) and ranged between -0.2 km^2 (-0.1%) and -25.7 (-9.7%) (Table 3).

The accuracy of VJK Reservoir's shoreline identification was assessed using the SMR and SME. The comparison of the shoreline between the generalized lines (derived from NDWI) and the reference lines (from high resolution images) which selected from five locations surrounding the shoreline of VJK reservoir (Figure 3). The result of accuracy assessment is shown in Table 4. The mean of SMR was 95.1%; the SMR indicated the proportion of the length of generalized line within the buffer zone to the total length of reference line (Equation 3). The mean of SMR error was -4.9%, while the highest and the lowest SMR errors were respectively -12.1% and + 2.0%. The mean of SME was 11.7 m; the SME estimated from the ratio of the difference area between the reference line and generalized line to the total length of reference line (Equation 4). The highest and the lowest SME are respectively 17.9 m and 6.3 m. The values of SME were lower than the resolution (30 m) of Landsat image.

Table 3. Comparison of water surface area of VJK reservoir between the original data in 1980 and the revision one from NDWI technique

Water level (m.a.s.l.)	Reservoir water surface area (km^2)		Difference from the original	
	Original (1980)	NDWI	(km^2)	(%)
137.75	201.8	197.4	-4.5	2.2
140.93	229.0	227.2	-1.8	0.8
142.79	244.9	239.2	-5.6	2.3
143.84	253.9	237.7	-16.2	6.4
144.54	259.9	247.2	-12.7	4.9
145.01	263.9	238.2	-25.7	9.7
146.16	273.8	273.6	-0.2	0.1
147.98	289.4	286.2	-3.2	1.1
148.77	296.2	295.2	-1.0	0.3
149.81	305.2	300.5	-4.7	1.5
150.89	314.5	299.5	-15.0	4.8
151.39	318.8	310.7	-8.1	2.5
Average			-8.2	2.8

Table 4. Accuracy assessment of shoreline of VJK reservoir derived from NDWI

Sample site	Acquisition date	ΔA (m^2)	L (m)	L′ (m)	SMR (%)	SMR error (%)	SME (m)
A1	Feb 09, 2014	55,920	3,135	3,240	103.3	+3.3	17.8
	Mar 12, 2017	51,399	2,882	2,942	102.0	+2.0	17.9
A2	Feb 09, 2014	15,562	2,590	2,489	96.1	-3.9	6.3
	Mar 12, 2017	17,058	2,589	2,480	95.8	-4.2	6.9
A3	Dec 14, 2013	62,402	7,601	7,155	94.1	-5.9	8.3
	Feb 03, 2015	61,043	8,032	7,060	87.9	-12.1	7.6
A4	Feb 09, 2014	147,417	8,638	7,938	91.9	-8.1	17.1
	Feb 08, 2017	77,136	8,177	7,667	93.8	-6.2	9.4
A5	Feb 09, 2014	129,374	12,265	10,802	97.8	-2.2	10.5
	Mar 12, 2017	194,786	12,242	10,808	88.3	-11.7	15.9
				Mean	95.1	-4.9	11.7

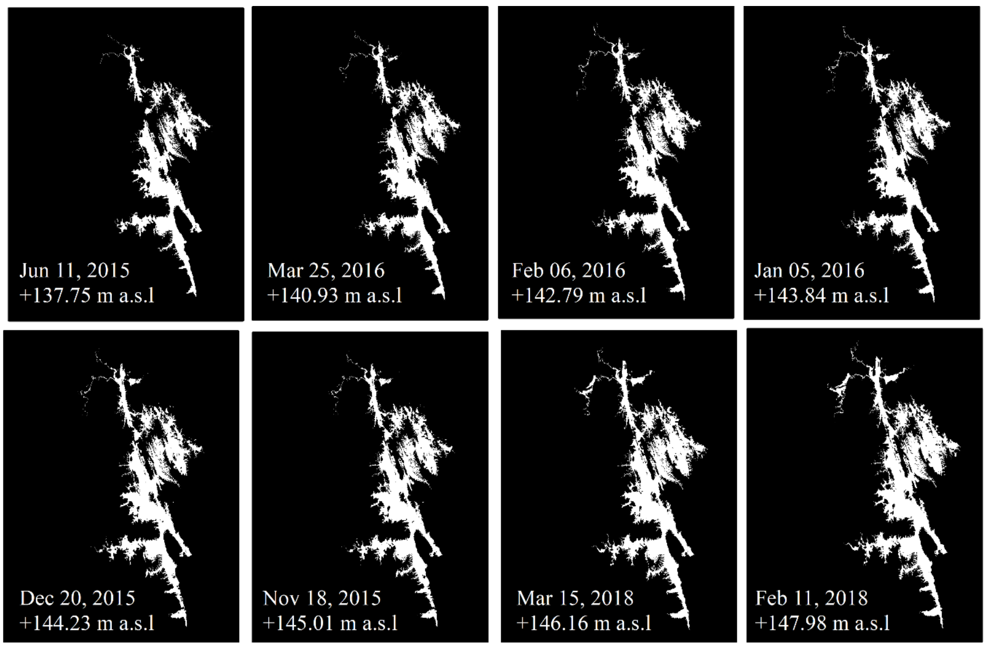

Figure 5. Water surfaces of VJK reservoir from water level of +137.75 m.a.s.l. to 151.39 m.a.s.l. identified using NDWI derived from Landsat 8 data

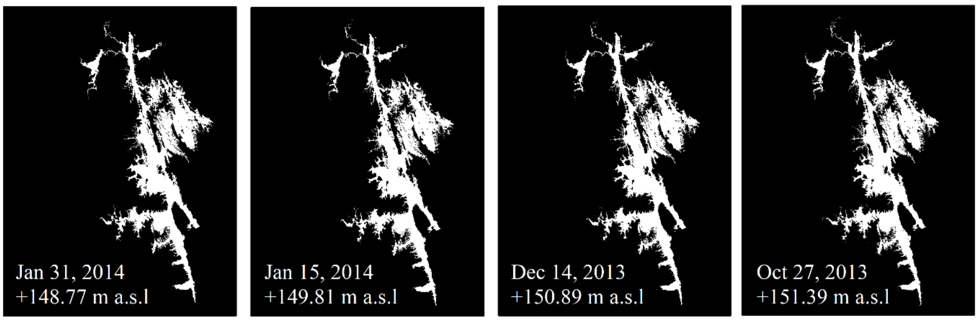

Figure 5. Water surfaces of VJK reservoir from water level of +137.75 m.a.s.l. to 151.39 m.a.s.l. identified using NDWI derived from Landsat 8 data (cont.)

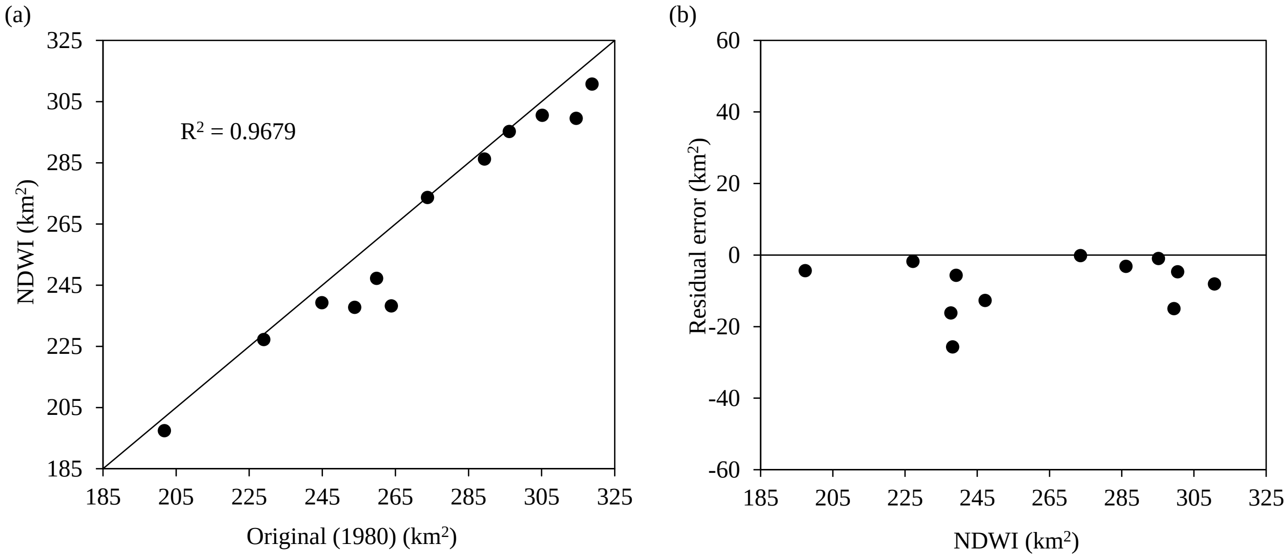

Figure 6. Comparison of the water surface areas of VJK reservoir between the original data in 1980 and the revised one using NDWI technique: (a) Scatter plot, (b) Residual errors

3.2 Reservoir storage capacity curve

The storage capacity curve was derived from the accumulated volume calculated using the prismatic equation (Equation 2). Table 5 and Figure 7 show the comparison of the reservoir storage capacity between the original curve (1980) and the revised curve (2018) at the water level from +137.75 m.a.s.l. to +151.39 m.a.s.l. The initial storage (3,006.4 MCM) was set at the minimum water level (+135.00 m.a.s.l.). The storage capacity of the revised curve arrived the maximum volume of 7,030.2 MCM at water level +151.39 m.a.s.l. Figure 7 show the comparison of cumulative curves between the original curve (1980) and revised one (2018): water level and water surface areas (Figure 7(a)), and water level and storage capacity (Figure 7(b)). The storage capacity of VJK reservoir was decreased 495.3 MCM (6.6 %) at the water level +151.39 m.a.s.l. The annual capacity loss from 1980 to 2018 was estimated at 13 MCM.

Table 5. Comparison of reservoir characteristics (water surface and volume) of the Vajiralongkorn Dam between the original data in 1980 and the revision in 2018

Water level (m.a.s.l.)	Level difference (m)	Water surface (km^2)		Incremented volume (MCM)		Cumulative volume (MCM)		Difference from original	
		Original (1980)	Revised (2018)	Original (1980)	Revised (2018)	Original (1980)	Revised (2018)	(MCM)	(%)
135.00	0.0	178.4	177.8	0.0	0.0	3,006.4	3,006.4	0.0	0.0%
137.75	2.8	201.8	197.4	581.1	525.0	3,587.5	3,531.4	-56.1	-1.6%
140.93	3.2	229.0	227.2	761.0	678.8	4,348.5	4,210.2	-138.3	-3.2%
142.79	1.9	244.9	239.2	489.4	443.0	4,837.9	4,653.3	-184.6	-3.8%
143.84	1.1	253.9	237.7	290.7	262.3	5,128.6	4,915.6	-213.0	-4.2%

Table 5. Comparison of reservoir characteristics (water surface and volume) of the Vajiralongkorn Dam between the original data in 1980 and the revision in 2018 (cont.)

Water level (m.a.s.l.)	Level difference (m)	Water surface (km^2)		Incremented volume (MCM)		Cumulative volume (MCM)		Difference from original	
		Original (1980)	Revised (2018)	Original (1980)	Revised (2018)	Original (1980)	Revised (2018)	(MCM)	(%)
144.54	0.7	259.9	247.2	199.6	169.7	5,328.2	5,085.3	-242.9	-4.6%
145.01	0.5	263.9	238.2	136.6	121.3	5,464.8	5,206.6	-258.2	-4.7%
146.16	1.2	273.8	273.6	343.0	306.8	5,807.8	5,513.5	-294.3	-5.1%
147.98	1.8	289.4	286.2	568.4	503.8	6,376.2	6,017.2	-359.0	-5.6%
148.77	0.8	296.2	295.2	256.5	232.6	6,632.7	6,249.8	-382.9	-5.8%
149.81	1.0	305.2	300.5	346.6	297.8	6,979.3	6,547.6	-431.7	-6.2%
150.89	1.1	314.5	299.5	370.8	330.0	7,350.1	6,877.6	-472.5	-6.4%
151.39	0.5	318.8	310.7	175.4	152.5	7,525.5	7,030.2	-495.3	-6.6%

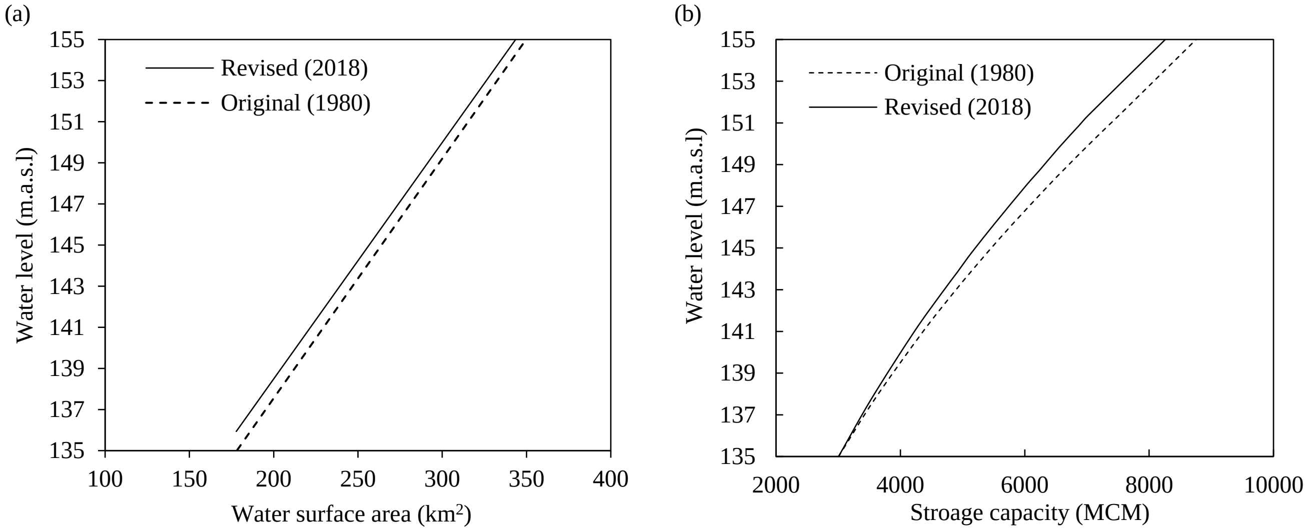

Figure 7. Comparison between original (1980) and revised (2018) reservoir characteristic curves of Vajiralongkorn Dam, (a) water level vs water surface area curve, (b) water level vs storage capacity curve

4. DISCUSSION AND CONCLUSION

The water surface area of VJK reservoir decreased on the average of 8.2 km^2 comparing with the original data in 1980, which is consistent with the reports in other studies. For example, El-Shazli and Hoermann (2016), Jeyakanthan and Sanjeevi (2011) and Fan and Morris (1992b) reported that the morphology of reservoir had changed because of sedimentation.

In conclusion, this paper investigated the assessment of water surface and volume of VJK reservoir using NDWI derived from Landsat 8 data. The accuracy of NDWI technique was satisfactory in identifying reservoir water surface. The water surface decreased on the average of -8.2 km^2 (-2.8%) comparing with the original data in 1980. The storage capacity of VJK reservoir was decreased 495.3 MCM over 38 years from 1980 to 2018 with the annual capacity loss of 13 MCM.

Remote sensing is an effective method in land and water monitoring. Landsat 8 provides a compromised option between spatial and temporal resolutions. Water surface and volume of VJK reservoir were successfully estimated using NDWI technique, however, only reservoir water levels ranged from +137.75 m.a.s.l. to 151.39 m.a.s.l. were monitored. The estimation of entire range of reservoir water level is an arduous task because it requires more satellite data. Cloud covering, especially during the rainy season makes satellite images inapplicable. In addition, the current research did not directly measured the sediment accumulation, but it is rather an indirect technique. Bathymetric survey is recommended for collecting reservoir bottom elevations particularly below the minimum water level of the VJK reservoir (+135 m.a.s.l.).

For further research, the evaluation of the effects of storage loss should be addressed both on the operation performance of the VJK dam and on the water resource management in the Mae Klong River Basin. The understanding on the erosion and sediment transport processes in the VJK watershed should be improved. Appropriate conservation measures should be studied and put into practice in the upstream forests of VJK dam.

ACKNOWLEDGEMENTS

The authors express their gratitude to the Electricity Generating Authority of Thailand (EGAT) for the Vajiralongkorn dam’s data and to the USGS for Landsat 8 data from the website (http://earthexplorer.usgs.gov/). The software licenses in this study (ArcGIS and ENVI) were provided by the Faculty of Environment and Resource Studies, Mahidol University, Thailand.

REFERENCES

Avisse N, Tilmant A, Müller MF, Zhang H. Monitoring small reservoirs' storage with satellite remote sensing in inaccessible areas. Hydrology and Earth System Sciences 2017;21(12): 6445-59.

Cesare DD, Schleiss A, Hermann F. Impact of turbidity currents on reservoir sedimentation. Journal of Hydraulic Engineering 2001;127(1):6-16.

Chander G, Markham BL, Helder DL. Summary of current radiometric calibration coefficients for Landsat MSS, TM, ETM+, and EO-1 ALI sensors. Remote Sensing of Environment 2009;113(5):893-903.

Chen Y, Wilson J, Zhu Q, Zhou Q. Comparison of drainage-constrained methods for DEM generalization. Computers and Geosciences 2012;48:41-9.

Cui L, Qiu Y, Fei T, Liu Y, Wu G. Using remotely sensed suspended sediment concentration variation to improve management of Poyang Lake, China. Lake and Reservoir Management 2013;29(1):47-60.

Deng Z, Sun Y, Zhang K, Qiu Q, Sun W. A water identification method basing on grayscale Landsat 8 OLI images. Geocarto International 2019:1-11.

Du Z, Li W, Zhou D, Tian L, Ling F, Wang H, et al. Analysis of Landsat-8 OLI imagery for land surface water mapping. Remote Sensing Letters 2014;5(7):672-81.

El-Shazli A, Hoermann G. Development of storage capacity and morphology of the Aswan High Dam Reservoir. Hydrological Sciences Journal 2016;61(14):2639-48.

Fan J, Morris GL. Reservoir sedimentation. I: delta and density current deposits. Journal of Hydraulic Engineering 1992a; 118(3):354-69.

Fan J, Morris GL. Reservoir sedimentation. II: Reservoir desiltation and long-term storage capacity. Journal of Hydraulic Engineering 1992b;118(3):370-84.

Felde GW, Anderson GP, Cooley TW, Matthew MW, Adler-Golden SM, Berk A, et al. Analysis of hyperion data with the FLAASH atmospheric correction algorithm. Proceedings of the International Geoscience and Remote Sensing Symposium (IGARSS); 2003 Jul 21-25; Toulouse, France; 2003.

Feyisa GL, Meilby H, Fensholt R, Proud SR. Automated water extraction index: A new technique for surface water mapping using Landsat imagery. Remote Sensing of Environment 2014;140:23-35.

Foteh R, Garg V, Nikam BR, Khadatare MY, Aggarwal SP, Kumar AS. Reservoir sedimentation assessment through remote sensing and hydrological modelling. Journal of the Indian Society of Remote Sensing 2018;46(11):1893-905.

Gao B-C. NDWI-A normalized difference water index for remote sensing of vegetation liquid water from space. Remote Sensing of Environment 1996;58(3):257-66.

Grin S. Geometry and water height-area-volume curves of the reservoirs in the semiarid Madalena basin in Northeast Brazil [Bachelor final project]. Enschede, University of Twente; 2014.

Gupta RP, Banerji S. Monitoring of reservoir volume using LANDSAT data. Journal of Hydrology 1985;77(1):159-70.

Jain SK, Singh P, Seth SM. Assessment of sedimentation in Bhakra Reservoir in the western Himalayan region using remotely sensed data. Hydrological Sciences Journal 2002;47(2):203-12.

Jeyakanthan VS, Sanjeevi S. Reservoir capacity estimation of Singoor reservoir, India, by per-pixel and sub-pixel processing of multi-date satellite images. Geocarto International 2011;26(4):305-20.

MacPheson KR, Freeman LA, Flint LE. Analysis of Methods to Determine Storage Capacity of, and Sedimentation in, Loch Lomond Reservoir, Santa Cruz County, California, 2009. Reston, VA: U.S. Geological Survey; 2011.

Malarvizhi K, Kumar SV, Porchelvan P. Use of high resolution Google Earth satellite imagery in landuse map preparation for urban related applications. Procedia Technology 2016; 24:1835-42.

McFeeters SK. The use of the Normalized Difference Water Index (NDWI) in the delineation of open water features. International Journal of Remote Sensing 1996;17(7):1425-32.

Mishra N, Haque M, Leigh L, Aaron D, Helder D, Markham B. Radiometric cross calibration of Landsat 8 operational land imager (OLI) and Landsat 7 Enhanced Thematic Mapper Plus (ETM+). Remote Sensing 2014;6(12):12619-38.

Morris GL, Fan J. Reservoir Sedimentation Handbook: Design and Management of Dams, Reservoirs, and Watersheds for Sustainable Use. New York, USA: McGraw-Hill; 1998.

Odhiambo BK, Boss SK. Integrated echo sounder, GPS, and GIS for reservoir sedimentation studies: Examples from two Arkansas lakes. Journal of the American Water Resources Association 2004;40(4):981-97.

Ortt RA, Kerhin RT, Wells D, Cornwell J. Bathymetric Survey and Sedimentation Analysis of Loch Raven and Prettyboy Reservoirs. Coastal and Estuarine Geology File Report. Baltimore, MD: Maryland Geological Survey; 2000.

Ouma YO, Tateishi R. Lake water body mapping with multiresolution based image analysis from medium-resolution satellite imagery. International Journal of Environmental Studies 2007;64(3):357-79.

Pandey A, Chaube UC, Mishra SK, Kumar D. Assessment of reservoir sedimentation using remote sensing and recommendations for desilting Patratu Reservoir, India. Hydrological Sciences Journal 2016;61(4):711-8.

Peng D, Guo S, Liu P, Liu T. Reservoir storage curve estimation based on remote sensing data. Journal of Hydrologic Engineering 2006;11(2):165-72.

Ran L, Lu XX. Delineation of reservoirs using remote sensing and their storage estimate: an example of the Yellow river basin, China. Hydrological Processes 2012;26(8):1215-29.

Rodrigues LN, Sano EE, Steenhuis TS, Passo DP. Estimation of small reservoir storage capacities with remote sensing in the Brazilian Savannah region. Water Resources Management 2012;26(4):873-82.

Scheffers AM, Kelletat DH. Lakes of the World with Google Earth, Understanding Our Environment. Dordrecht, the Netherlands: Springer; 2016.

Su H, Liu H, Heyman WD. Automated derivation of bathymetric information from multi-spectral satellite imagery using a non-linear inversion model. Marine Geodesy 2008;31(4):281-98.

United States Geological Survey (USGS). Landsat 8 (L8) Data User's Handbook. Sioux Falls, SD: Earth Resources Observation and Science Center; 2016.

Wu C-H, Chen C-N, Tsai C-H, Tsai C-T. Estimating sediment deposition volume in a reservoir using the physiographic soil erosion-deposition model. International Journal of Sediment Research 2012;27(3):362-77.

Zhang F, Li J, Zhang B, Shen Q, Ye H, Wang S, et al. A simple automated dynamic threshold extraction method for the classification of large water bodies from landsat-8 OLI water index images. International Journal of Remote Sensing 2018;39(11):3429-51.

Zhou Q, Chen Y. Generalization of DEM for terrain analysis using a compound method. ISPRS Journal of Photogrammetry and Remote Sensing 2011;66(1):38-45.

Environment and Natural Resources Journal 2020; 18(2): 146-155

Detection of Changes in Land Cover and Land Surface Temperature Using Multi Temporal Landsat Data

Aye Aye Myint[1*] and Myat Myat Min[2]

[1]Faculty of Computing, University of Computer Studies, Mandalay, Myanmar
[2]Faculty of Computer Science, University of Computer Studies, Mandalay, Myanmar

ARTICLE INFO

Received: 18 Jul 2019
Received in revised: 18 Oct 2019
Accepted: 19 Nov 2019
Published online: 3 Jan 2020
DOI: 10.32526/ennrj.18.2.2020.14

Keywords:
Land cover/ Land surface temperature/ Change detection/ NDVI

*** Corresponding author:**
E-mail:
ayeayemyint@ucsm.edu.mm

ABSTRACT

Land cover changes and land surface temperature have rose in the tropical regions of Myanmar especially in the surrounding areas of Magway city due to the rapid growth of urban sprawl. This study investigated the patterns of land cover and the trend of land surface temperature in Magway city area between 1989 and 2017. For this purpose, Landsat 5 TM and Landsat 8 OLI were used and land surface temperatures (LST) were calculated through thermal data with Normalized Difference Vegetation Index (NDVI). After obtaining the land cover map by using maximum likelihood algorithm for each study period, the accuracy of this map was tested using 100 ground checkpoints in an error matrix. A statistical analysis of the results showed the increase of the built-up area by 11.7% and the decline of the vegetation area by 19.7% from 1989 to 2017. Moreover, land surface temperature has risen by 4 °C during this 28 years period. Therefore, this study is intended to help the Magway city development council plan effective land cover management in the future.

1. INTRODUCTION

Land cover (LC) is defined as the earth's surface attributes captured by vegetation, water, desert, and ice and it also includes structures created only by human activities such as mine exposure and settlement (Lambin et at., 2003). Land cover represents an important factor in the geographic analysis, from physical geography to environmental analysis and spatial planning approaches. This is a dynamic variable that reflects the interaction between socio-economic activity and local environmental changes and therefore needs to be updated frequently (Rujoiu and Mihai, 2016). LC information is essential for managing natural resources and monitoring of environmental changes (Bharath et al., 2013).

Moreover, land use/land cover (LULC) changes are considered as important tools for assessing global change at different space-time scales (Lambin, 1997). It is a widespread, accelerating, and important process which is driven by human behavior and at the same time results in changes that impact human livelihood (Agarwal et al., 2002). Land cover change refers to the conversion from one category of land cover to another and/or the modifications of conditions within a category (Meyer and Turner, 1992). These changes in the LULC system have important environmental consequences of impacts on soil and water, biodiversity and microclimate (Lambin et at., 2003).

Investigation of land cover change can be performed on a temporal scale, such as a decade to assess landscape change caused by anthropogenic activities on the land (Gibson and Power, 2000). More prominently, LULC change data are significant for environmental and climate change studies and developing considerate the multifaceted relations between anthropogenic actions and global temperature change (Jung et al., 2006; Gong et al., 2013). In addition, accurate and up-to-date information on land cover changes is needed to understand and assess the environmental impact of such changes (Lambin and Geist, 2008).

Knowledge of Land Surface Temperature (LST) and its temporal and spatial variations within a city environment is most important for the study of urban climate and human-environment interactions (Singh and Grover, 2014; Alavipanah et al., 2015). LST information at the regional and global scales can

Citation: Myint AA, Min MM. Detection of changes in land cover and land surface temperature using multi temporal Landsat data. Environ. Nat. Resour. J. 2020;18(2):146-155. DOI: 10.32526/ennrj.18.2.2020.14

be detected by sensor, since most of the energy in this spectral region is directly emitted from the surface (Sobrino, 2008). LST is determined by energy fluxes between the surface and the atmosphere (Voogt and Oke, 2003). LST can be obtained from thermal images depending on the number of bands using a single infrared channel or a split window method (Pu et al., 2006). LST is one of the main variables measured using remote sensing thermal bands of various sensors such as AVHRR, MODIS, Landsat-5TM, Landsat-7ETM+ and Landsat-8TIRS (Gebrekidan, 2016).

Many studies have investigated the relationship between LULC and LST using remote-sensing imagery on regional and global climate (Chen et al., 2017; Zhang et al., 2016). The relationship between LULC and LST is very important in land management and global climate change research. Therefore, LST measurements caused by changes in LULC can provide an indication of the expansion of heat distribution associated with LULC patterns and human-related changes. In addition, LST is sensitive to various land surface features and can be used to extract various land use/cover types information (Sinha et al., 2015).

Remote sensing data provides a way to understand the changes in spatio-temporal land cover related to basic physical properties in terms of surface radiance and emissivity data. Moreover, remote sensing technology in combination with geographic information system technology is an effective technique for the observation of land cover/use and land surface temperature changes (Orhan and Yakar, 2016).

This study investigated the spatial pattern of land cover changes and LST using remote sensing Landsat data within the period of 1989-2017. The objectives of this paper are (a) to generate the land cover classification map and LST map and (b) to estimate the pattern of land cover changes and the trend of LST in Magway city and its surrounding areas between 1989 and 2017.

2. METHODOLOGY

2.1 Study area

The study area is the capital city of Magway region, located at latitude 20°09′15″ North and longitude 094°56′43″ East with an area of about 146.6443 km^2 (Figure 1). It is situated in an arid region of the central part of Myanmar. The landscape of the region (Magway) is located on a plain with few valleys and is surrounded by Ayayarwaddy River in the west and Ying Creek in the south. The climate is a dry tropical type and is characterized by summer, rain and cold seasons. The summer season begins at the end of February and ends in mid-June. The rainy season is mostly from June to October. The remaining months are called the cold season. The mean annual rainfall is about 948.7 mm while average high temperature is 46.5 °C and low temperature is 8.2 °C (based on 2017 data from the Department of Meteorology and Hydrology, Magway). The temperature is very high and hottest in April and May.

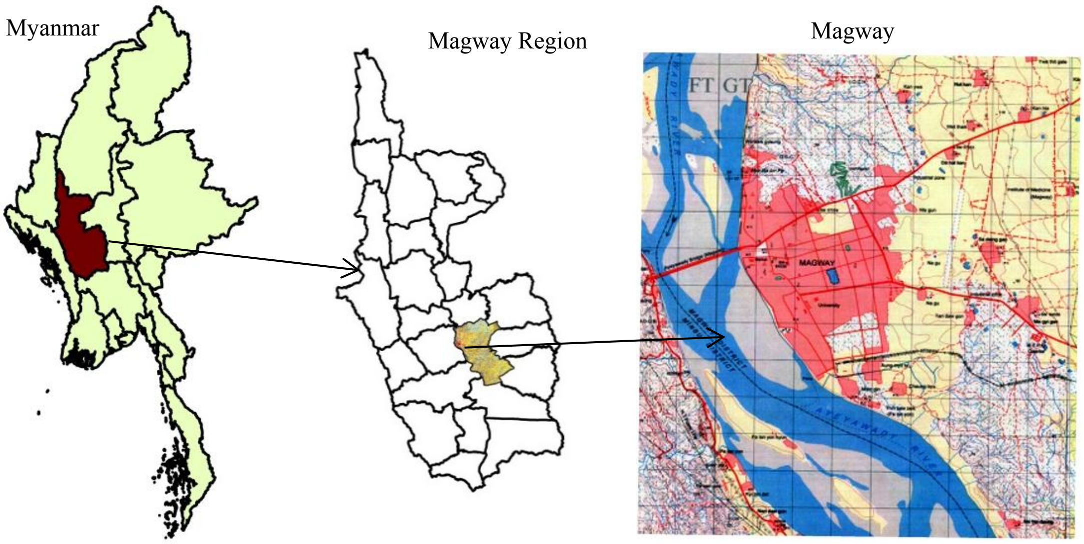

Figure 1. Location map of study area (Source – Myanmar Information Management Unit).

2.2 Landsat data

In this study, Landsat 5 TM for 1989, 2004 and Landsat 8 OLT/TIRS (path/row: 134/46) images were downloaded from US Geological Survey (http://earthexplorer.usgs.gov/). The obtained Landsat data (Level 1 Terrain Corrected (L1T) products were geometrically transformed to real world coordinates using UTM zone 46 North projections and WGS-84 datum. Meteorological data are obtained from Department of Meteorology and Hydrology, Magway. ArcGIS 10.1 and QGIS 3.0 are used for this entire study. The details of satellite data collected are shown in Table 1.

Table 1. Detail information of Landsat data

Satellite	Data acquisition	Sensors	Format
Landsat 5	21-04-1989	TM	GeoTIFF
Landsat 5	13-03-2004	TM	GeoTIFF
Landsat 8	02-04-2017	OLI/TIRS	GeoTIFF

2.3 Image preprocessing

Image preprocessing is required before image classification and extracts LST. The preprocessing step includes atmospheric correction, bands combination, and clipping the study area. Atmospheric correction is a necessary step to accurately extract quantitative information from the Landsat Data. These images were performed by Dark Object Subtraction method in QGIS 3.0. All the bands were used to produce a composite image for the purpose of land cover classification image analysis. Landsat images contain a very large area, so the study area is clipped by overlaying geo-referenced outline boundary of the study area using ArcGIS 10.1 software. The extraction of land surface temperature from thermal band images was employed in three study periods. The detailed methodology is shown in Figure 2.

2.4 Extract LST from thermal band

Thermal band 6 for Landsat 5 and band 10/11 for Landsat 8 were employed to calculate the LST from all the periods under the following phases. Meta data values are used for calculation of LST in the following Table 2.

At the first stage, the digital number was transformed into spectral radiance by using Equation 1 for Landsat 5 (Markham, 1986) and Equation 2 for Landsat 8 (Lee et al., 2012; Nichol and To, 2012).

$$L_\lambda = \left(\frac{L_{max} - L_{min}}{Qcal_{max}}\right) \times Qcal + L_{min} \quad (1)$$

$$L_\lambda = M_L \times Qcal + A_L \quad (2)$$

Where, L_λ is the spectral radiance in W/(m^2 sr µm). Qcal is the DN of each image, and $Qcal_{max}$ is the maximum DN (65535 for the 16-bit Landsat 8 and 255 for Landsat 5. L_{max} and L_{min} are the maximum and minimum top of atmospheric (TOA) radiances in W/(m^2 sr µm). M_L (0.0003342) and A_L (0.1) are band specific multiplicative and additive rescaling factors obtained from the image Meta data file.

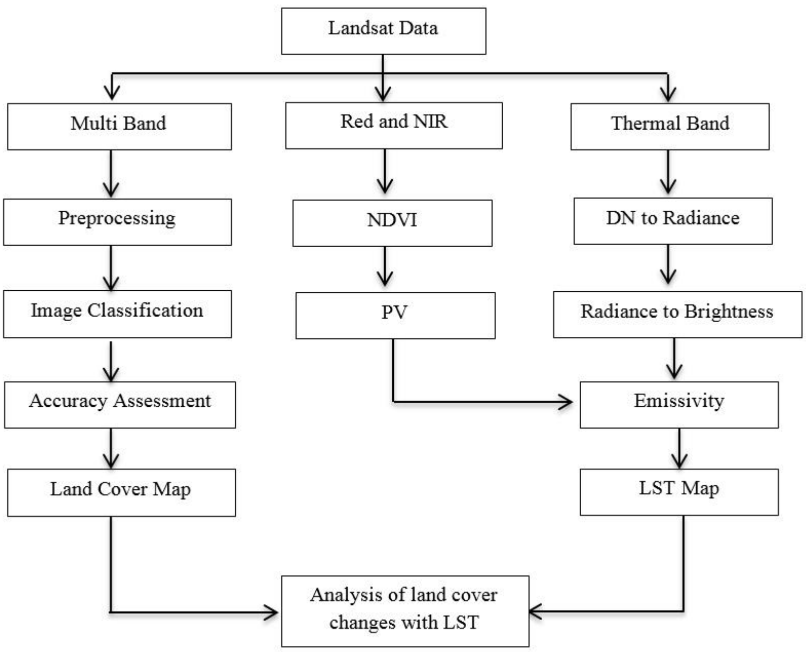

Figure 2. General work flow of methodology

At the second stage, the radiance was converted to brightness temperature in Celsius using Equation 3 (Chander and Markham, 2003).

$$T_b = \frac{K_2}{\ln\left(\frac{K_1}{L_\lambda}+1\right)} - 273.15 \quad (3)$$

Where, T_b is the at-sensor brightness temperature in Celsius unit, L_λ is the spectral radiance, and K_1 and K_2 are calibration constants of Landsat 5/8 from Meta file.

Normalized Difference Vegetation Index (NDVI) was used for determination of land surface emissivity by using Equation 4 (Tucker, 1979).

$$NDVI = (NIR - Red) / (NIR + Red) \quad (4)$$

Where, NIR is near infrared band (band 4 for Landsat 5, band 5 for Landsat 8) and Red is red band (band 3 for Landsat 5, band 4 for Landsat 8).

Table 2. Values of parameters of Landsat images from Meta data

Variable	Description	Landsat 5	Landsat 8
L_{min}	Minimum values of radiance	1.238	-
L_{max}	Maximum values of radiance	15.303	-
$Qcal_{max}$	Maximum quantize calibration	255	65535
K_1	Thermal constant	607.76	774.8853
K_2	Thermal constant	1260.56	1321.0789

After the NDVI was computed; proportional vegetation (Pv) can be extracted by using Equation 5 with NDVI values (Sobrino et al., 2004).

$$P_v = [(NDVI - NDVI_{min}) / (NDVI_{max} - NDVI_{min})]^2 \quad (5)$$

Where, Pv is proportion of vegetation, $NDVI_{min}$ is minimum values of NDVI and $NDVI_{max}$ is maximum values of NDVI.

Land surface emissivity for each thermal band was computed based on proportion of vegetation using Equation 6 (Sobrino et al., 2004).

$$\varepsilon = 0.004 \times Pv + 0.986 \quad (6)$$

Where, ε is land surface emissivity, Pv is proportion of vegetation.

At the final stage, land surface temperatures were estimated from brightness temperatures (emissivity correction) by using Equation 7 (Artis and Carnahan, 1982).

$$LST = \frac{T_b}{\left[1+\left\{\left(\frac{T_b}{\rho}\times\lambda\right)\right\}\times \ln\varepsilon\right]} \quad (7)$$

Where, LST is the land surface temperature, λ is the wavelength of emitted radiance in meters (λ=11.5 μm), ε is land surface emissivity, T_b is the brightness temperature in Celsius and $\rho = h \times c/\sigma = 1.438\times10^{-2}$ mK (σ=Boltzmann constant $=1.38\times10^{-23}$ J/K, h=Planck's constant$=6.626\times10^{-34}$ Js, c=velocity of light$=2.998\times10^{8}$ m/s).

2.5 Classification of land cover

In this research, the supervised classification (maximum likelihood algorithm) was employed mapping the land cover of the study area. For this classification, the images of study area were categorized into five classes including water body, sand bar, built up, agricultural and sparse vegetation land as shown in Table 3. Training data are collected from the field survey and use of Google Earth. Maximum Likelihood algorithm classifies a pixel taking into account the variance and the covariance of the spectral response pattern of each category. A probability density function is created for each spectral category used to classify unknown pixels by calculating the probability that the pixel belongs to each class. Pixels are assigned to classes with a higher probability. It is the greatest classification method when accurate training data is provided (Schowengerdt, 2006; Lillesand et al., 2015).

Table 3. Descriptions of land cover class

Class	Description
Water body	River, lake
Sand bar	Sandy land, bare land, wet land
Built up	Urban and rural land
Agricultural	Peanut, bean, sesame and dry farm land
Vegetation	Sparse vegetation, grass or tropical savannah , shrubs, open tropical land

2.5.1 Accuracy assessment of land cover map

In this study, 100 random points were done by using the stratified random sampling techniques to get accurate assessment of each classified image. Random points were a minimum distance of 10 m apart to avoid selecting the same pixel. These points are exported into a ".kml" file for viewing on Google Earth. Each of these points is examined to identify whether it belongs to "water" or "other" class and so on. This process is done for all of these points on the classified images from 1989 to 2017. The comparison of reference data (ground check points) and classification results was carried out statistically using error matrix. The following formulas are measured for each classification images (Lillesand et al., 2015).

$$\text{User Accuracy} = \frac{\text{Total number of correctly classified samples in each category}}{\text{Total number of classified samples in that category (row total)}} \times 100 \quad (8)$$

$$\text{Producer Accuracy} = \frac{\text{Total number of correctly classified samples in each category}}{\text{Total number of classified samples in that category (col total)}} \times 100 \quad (9)$$

$$\text{Overall Accuracy} = \frac{\text{Total number of correctly classified samples}}{\text{Total number of refferne samples}} \times 100 \quad (10)$$

$$\text{Kappa Coefficient} = \frac{[(\text{Total sum correct}) - \text{sum of all (col total} \times \text{row total)}]}{[(\text{Total sum correct})^2 - \text{sum of all (col total} \times \text{row total)}]} \quad (11)$$

3. RESULTS AND DISCUSSION

3.1 Land cover classification

Supervised classification of multiple Landsat images is an effective tool to quantify current LU / LC and detect in environmental changes (Cheruto et al., 2016). In this study, the classification images generated the five major LC features of Magway city and its surrounding area for 1989 and 2017 as shown in Figure 3. The classified images were assessed for accuracy based on 100 random reference points for each class over the study period. Accuracy assessment is an important parameter for urban growth and LST (Wang et al., 2018). Table 4 shows the overall accuracy and Kappa coefficient of 1989, 2004, and 2017 is above 86% and 0.83 of the classified images. Areas of spatial and temporal LC were calculated between 1989 and 2017.

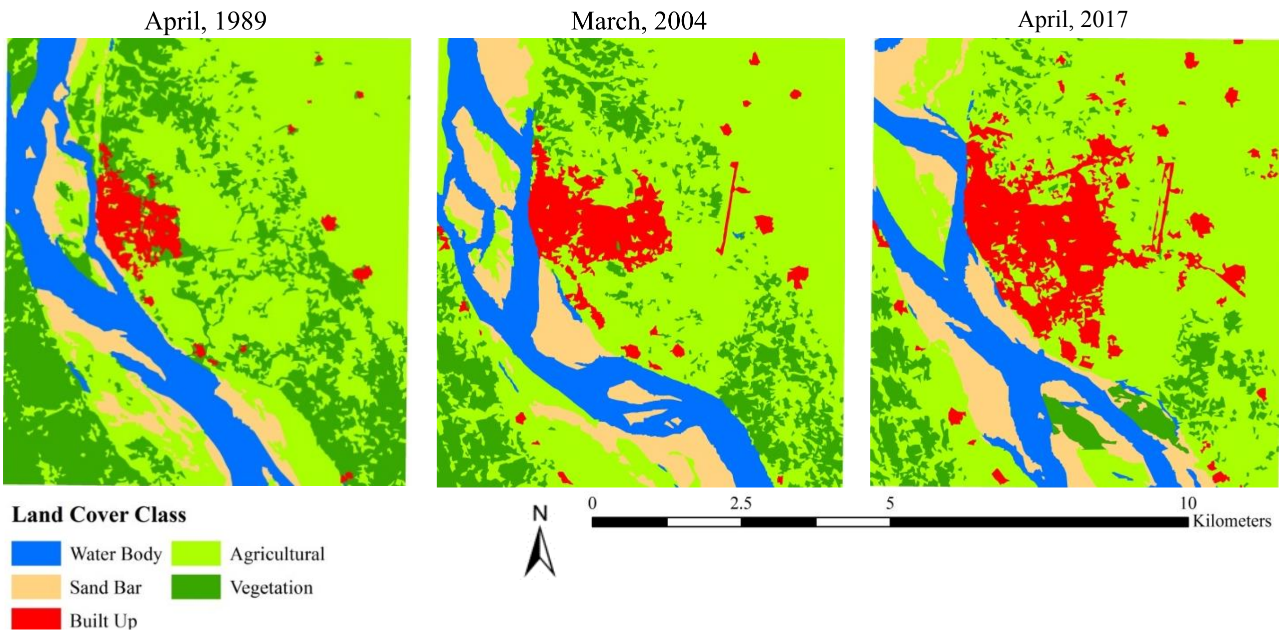

Figure 3. Land covers maps for 1989, 2004 and 2017

Table 4. Accuracy assessment of land cover from 1989 to 2017

Year	User accuracy (%)					Producer accuracy (%)					Overall	K
	Water body	Sand bar	Built up	Agriculture	Vegetation	Water body	Sand bar	Built up	Agriculture	Vegetation	Accuracy	Coefficient
1989	90	90	85	90	75	100	90	100	66.7	83.3	86%	0.83
2004	80	90	100	80	90	88.9	78.3	100	88.9	85.7	88%	0.85
2017	100	95	90	80	95	95.2	100	94.7	94.1	79.2	92%	0.9

The results of LC changes in the study area showed that built up area has dramatically expanded to occupy agriculture and vegetation areas from 4.8 km^2 in 1989, to 9.7 km^2 in 2004 and 21.9 km^2 in 2017. The area of water body slightly increased from 18.3 km^2 in 1989 to 19.9 km^2 in 2004 and decreased to 15.98 km^2 in 2017. Sand bar increased from 9.9 km^2 in 1989 to 14.6 km^2 in 2004 and slightly decreased to 12.4 km^2 in 2017. Vegetation has also decreased from 39.1 km^2 in 1989 to 21.2 km^2 in 2004 and slightly decreased to 10.4 km^2 in 2017. Agriculture increased from 73.9 km^2 in 1989 to 81.3 km^2 in 2004, and 85.95 km^2 in 2017 (Table 5).

According to the statistics results, the urbanization is rapidly increasing where most agricultural land is transformed into built up land. Vegetation land has been converted into agricultural and also into built up land. Water body has been transformed into sand bar and agricultural land. Sand bar has been transformed into water body and agricultural land during the study periods. These changes of temporal trend in the study area, mainly focused on five types, are due to the population increase and their needs for adequate food supply, secure housing and socio-economic activities. With the population increase, the built up area and agricultural area have increased from year to year.

In summary, all land cover classes except water area and sand bar showed high change rate between the study areas. The water body and sand bar have fluctuating changes over the period. Figure 4 shows the gain or loss in land cover type.

Table 5. Statistics of land cover from 1989 to 2017

Land cover	1989		2004		2017		1989-2004	2004-2017
Type	Acres	%	Acres	%	Acres	%	Change of area	Change of area
Water body	18.33	12.6	19.90	13.6	15.98	10.9	1.57	-3.92
Sand bar	9.95	6.8	14.60	10	12.37	8.4	4.65	-2.22
Built up	4.78	3.3	9.65	6.6	21.91	14.9	4.87	12.26
Agricultural	73.85	50.6	81.31	55.4	85.95	58.6	7.45	4.65
Vegetation	39.12	26.9	21.20	14.5	10.41	7.1	-17.93	-10.79

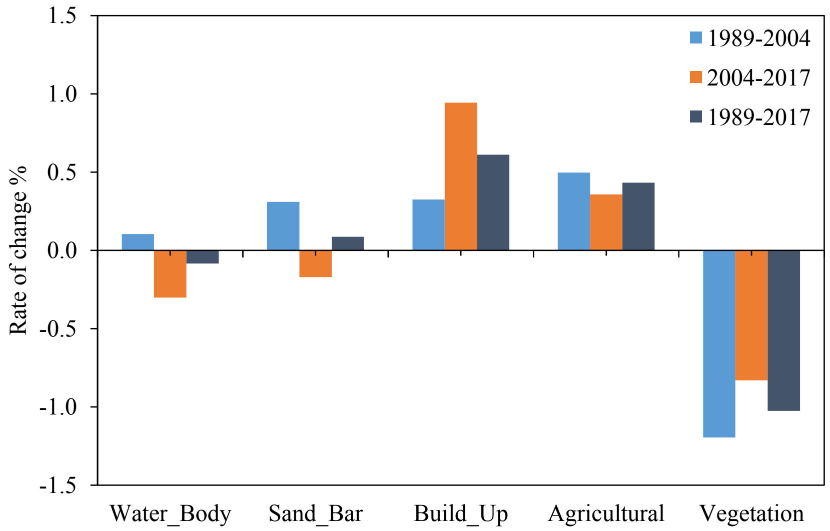

Figure 4. Change trends of land cover between 1989 and 2017

Land use/cover changes are complex and at the same time interrelated such that the expansion of one land cover type occurs at the expense of other land cover classes (Shiferaw and Singh, 2011). Cansong and Lede (2014) proposed the expansion of agricultural land is at the expense of lands with natural vegetation cover. The results of this study are consistent with the results of other studies. In our study results, the expansion of built up and agricultural land had previously been vegetation land. Agriculture is the most important sector of Myanmar's economy.

3.2 Land surface temperature

The LST map is extracted by using a single channel method from the thermal infrared band of Landsat data for 1989, 2004 and 2017 shown in Figure 5. The results of LST has been presented in Table 6, the surface temperatures were recorded in the range of 24-39 °C in 1989, the temperature ranges from 23-38 °C in 2004 and ranges from 26-43 °C in 2017, respectively. Therefore, temperature change significantly increased in 2017, the highest temperature recorded was 43 °C and lowest temperature was 26 °C. The most important indicator would be the maximum temperature. The maximum temperature change was about 1 °C decrease between 1989 and 2004 and increase of 5 °C from 2004 to 2017.

An assessment of these areas was done using a ground validation technique in order to get a better understanding of these changes. It was discovered that LST has decreased by nearly 1 °C which is probably due to the fact that the water body areas have increased by 1.6 km^2 during 1989 and 2004. The LST of study area has increased by 5 °C was growth of human activities such as industrial, residential and expanded agricultural are established from 2004 to 2017. When increasing development of built up areas, expanded agricultural and decreasing vegetation can be influenced to LST increase by 5 °C from 2004 to 2017. After 28 years, the maximum temperature increased by 4 °C which is a pointer to the change in the spatial pattern of the LST in study area. Moreover, comparison between temperatures at the Meteorological station (Magway) and surface temperature of LST map showed the estimated LST value was less than 3 °C.

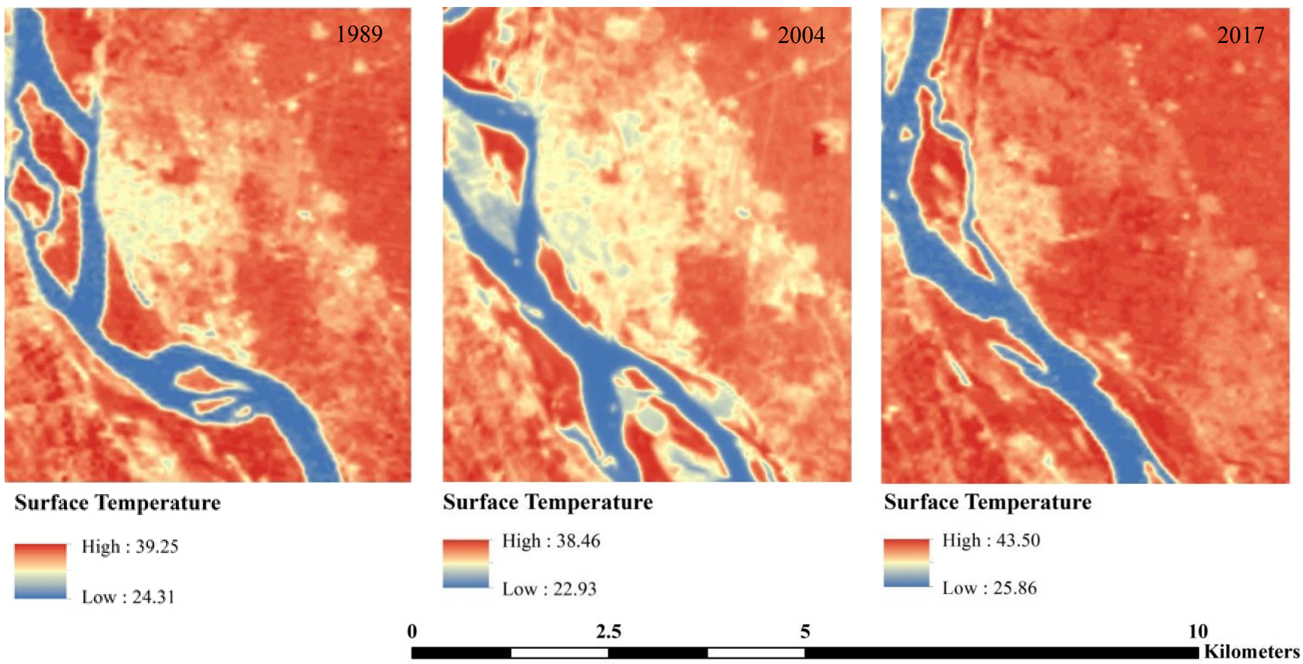

Figure 5. Land surface temperature maps extract from Landsat images for 1989, 2004, 2017

Table 6. Statistics of land surface temperature for 1989, 2004 and 2017

Year	Min	Max	Mean	Std Dev	Coefficient variation
1989	24.31	39.25	35.07	3.61	0.10
2004	22.93	38.46	33.02	3.64	0.11
2017	25.86	43.50	36.35	3.91	0.10

As shown in Figure 6, the mean surface temperature values fluctuate between 1989 and 2017. It can be concluded that the LST trend in the study area increases between the years 2004 and 2017. However, this trend has changed showing higher values since 2004. Despite the slight decrease in 2004, the overall trend of surface temperature shows an increasing trend.

Land cover has a significant impact on surface temperature. Conversion of land cover types increases the effect of surface temperature and greatly influences the number and distribution of hot spots (Tran et al., 2017).

From the analysis of this study, the relationship between LC and LST observed that the mean LST of sand bar was higher than other LC classes over the study periods. The mean LST of built up area was 33.48 °C on 1989, whereas the built up mean LST was slightly lower at 31.06 °C on 2004 and it was slightly higher at 34.86 °C on 2017 (Table 7). The agricultural land had a higher mean LST (Figure 7) due to the fact that the agricultural pixels were a mix of harvested area and unplanted bare soil. Zhang et al. (2013) revealed that agricultural area was characterized by the highest LST which is probably due to the fact that these areas consisted of mainly unplanted bare soil, as bare surfaces are usually characterized by higher LST than planted crop covers. Therefore, the agriculture trend is to shift from actively growing crops. Like agricultural, vegetation had the higher mean LST because the vegetation pixels were a mixture of the spare vegetation, tropical savannah and dried plants.

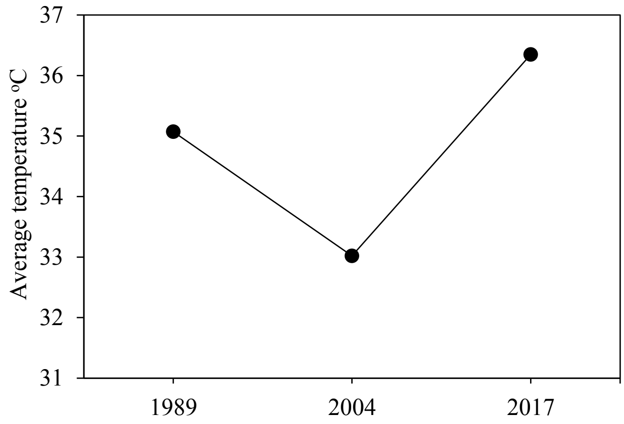

Figure 6. Mean surface temperature of the study area in 1989 - 2017

Table 7. Mean and standard deviation (STD) of LST in each LC class for 1989, 2004, 2017

Year	LST	Water body	Sand bar	Built up	Agricultural	Vegetation
1989	Mean	26.41	36.47	33.48	36.68	35.93
	STD	2.07	1.93	0.79	1.01	1.5
2004	Mean	25.19	35.38	31.06	34.31	34.67
	STD	2.21	1.77	1.00	1.66	1.22
2017	Mean	27.84	39.06	34.86	37.62	37.59
	STD	2.2	2.94	1.05	2.39	2.37

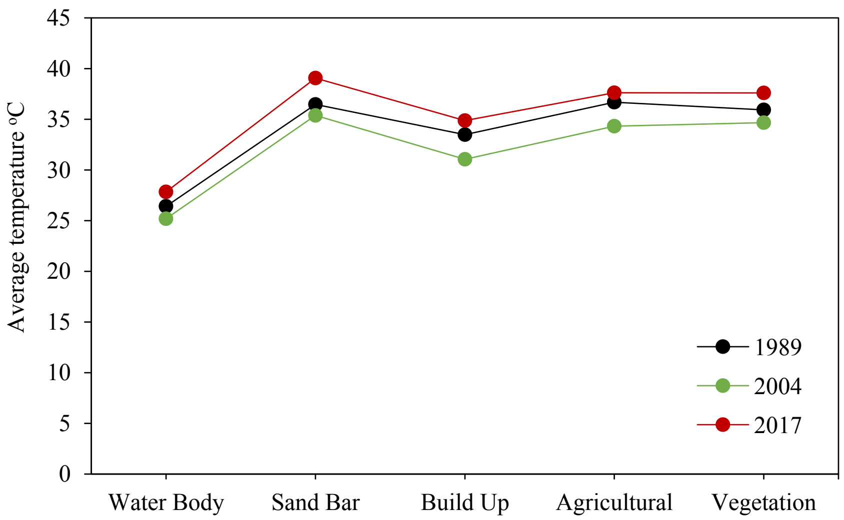

Figure 7. Mean surface temperature in each LC category for three dates

The main reason is probably due to differences in general weather conditions at the time of image acquisition and LC changes (growth in built up and agricultural, degradation of healthy vegetation) during the study dates. However, the average LST of overall area for the study observation years has increase rate 0.94 °C to 2.59 °C, it signifies effect on local and global warming; this is closely related with the rapidly expanding urban and agricultural.

4. CONCLUSION

This study has presented spatio-temporal changes of land cover and LST over a 28-year period in Magway city and its surrounding areas. Landsat satellite data were used to extract land cover information with five major categories, and LST was measured from the thermal band and then analysed for the changes and relationship of LST and LC. The land cover change was observed as the expansion of built up area due to exponential growth of population, rapidly growing infrastructure and poor land use planning. Agricultural areas were extended for higher production and to earn more income. On the other hand, vegetation area has experienced high conversion rate and decreased by an amount of -28.7 km^2 from 1989 to 2017. The analyzed trend of temperature change indicates maximum temperature change is from 39-43 °C between 1989 and 2017. Similarly, the minimum temperature change ranges from 24-26 °C between these periods. This research point out that land cover change is an important cause for rising land surface temperature. The combination of remote sensing and GIS technologies produces powerful analysis and a monitoring system for future management and planning of landscape.

REFERENCES

Agarwal C, Green GM, Grove JM, Evans TP, Schweik CM. A Review and Assessment of Land-use Change Models: Dynamics of Space, Time, and Human Choice. Newton Square, PA: USDA Forest Service; 2002.

Alavipanah S, Wegmann M, Qureshi S, Weng Q, Koellner T. The role of vegetation in mitigating urban land surface temperatures: A case study of Munich, Germany during the warm season. Sustainability 2015;7(4):4689-706.

Artis DA, Carnahan WH. Survey of emissivity variability in thermography of urban areas. Remote Sensing of Environment 1982;12(4):313-29.

Bharath S, Rajan KS, Ramachandra TV. Land surface temperature responses to land use land cover dynamics. Geoinformatics Geostatistics: An Overview. 2013;1(4):1-10.

Cansong L, Lede N. Analysis on spatial-temporal distribution patten and change characteristics of land cover in Burma based on high-resolution remote sensing image and GIS technology. Proceedings of the 7th International Conference on Intelligent Computation Technology and Automation; 2014 Oct 25-26; Changsha: China; 2014.

Chander G, Markham B. Revised Landsat-5 TM radiometric calibration procedures and postcalibration dynamic ranges. IEEE Transactions on Geoscience and Remote Sensing 2003; 41(11):2674-7.

Chen YC, Chiu HW, Su YF, Wu YC, Cheng KS. Does urbanization increase diurnal land surface temperature variation? Evidence and implications. Landscape and Urban Planning 2017;157:247-58.

Cheruto MC, Kauti MK, Kisangau DP, Kariuki PC. Assessment of land use and land cover change using GIS and remote sensing techniques: A case study of Makueni County, Kenya. Journal of Remote Sensing and GIS 2016;5:1-6.

Gebrekidan, Werku. Modeling land surface temperature from satellite data, the case of Addis Ababa. Proceedings of the United Nations Conference Centre Addis Ababa; 2016 Sep 23-24; Africa Hall, Addis Ababa: Ethiopia; 2016.

Gibson PJ, Power CH. Introductory Remote Sensing: Digital Image Processing and Applications. London, United Kingdom: Routledge; 2000.

Gong P, Wang J, Yu L, Zhao Y, Zhao Y, Liang L, Niu Z, Huang X, Fu H, Liu S, Li C. Finer resolution observation and monitoring of global land cover: First mapping results with Landsat TM and ETM+ data. International Journal of Remote Sensing 2013;34(7):2607-54.

Jiménez-Muñoz JC, Sobrino JA. Split-window coefficients for land surface temperature retrieval from low-resolution thermal infrared sensors. IEEE Geoscience and Remote Sensing Letters 2008;5(4):806-9.

Jung M, Henkel K, Herold M, Churkina G. Exploiting synergies of global land cover products for carbon cycle modeling. Remote Sensing of Environment 2006;101(4):534-53.

Lambin EF, Geist HJ, Lepers E. Dynamics of land-use and land-cover change in tropical regions. Annual Review of Environment and Resources 2003;28(1):205-41.

Lambin EF, Geist HJ. Land-Use and Land-Cover Change: Local Processes and Global Impacts. Heidelberg, Germany: Springer; 2008.

Lambin EF. Modelling and monitoring land-cover change processes in tropical regions. Progress in Physical Geography 1997;21(3):375-93.

Lee TW, Lee JY, Wang ZH. Scaling of the urban heat island intensity using time-dependent energy balance. Urban Climate 2012;2:16-24.

Lillesand T, Kiefer RW, Chipman J. Remote Sensing and Image Interpretation. Hoboken, New Jersey, USA: John Wiley and Sons; 2015.

Markham BL. Landsat MSS and TM post-calibration dynamic ranges, exoatmospheric reflectances and at-satellite temperatures. Landsat Technical Notes 1986;1:3-8.

Meyer WB, Turner BL. Human population growth and global land-use/cover change. Annual Review of Ecology and Systematics 1992;23(1):39-61.

Nichol JE, To PH. Temporal characteristics of thermal satellite images for urban heat stress and heat island mapping. ISPRS Journal of Photogrammetry and Remote Sensing 2012;74(1):153-62.

Orhan O, Yakar M. Investigating land surface temperature changes using Landsat data in Konya, Turkey. International Archives of Photogrammetry, Remote Sensing and Spatial Information Sciences 2016;41:285-89.

Pu R, Gong P, Michishita R, Sasagawa T. Assessment of multi-resolution and multi-sensor data for urban surface temperature retrieval. Remote Sensing of Environment 2006;104(2):211-25.

Rujoiu-Mare MR, Mihai BA. Mapping land cover using remote sensing data and GIS techniques: A case study of Prahova Subcarpathians. Procedia Environmental Sciences 2016; 32:244-55.

Schowengerdt RA. Remote sensing: Models and methods for image processing. California, USA: Elsevier; 2006.

Shiferaw A, Singh KL. Evaluating the land use and land cover dynamics in Borena Woreda South Wollo Highlands, Ethiopia. Ethiopian Journal of Business and Economics (The) 2011;(2)1:69-104.

Singh R, Grover A, Zhan J. Inter-seasonal variations of surface temperature in the urbanized environment of Delhi using Landsat thermal data. Energies 2014;7(3):1811-28.

Sinha S, Sharma LK, Nathawat MS. Improved land-use/land-cover classification of semi-arid deciduous forest landscape using thermal remote sensing. Egyptian Journal of Remote Sensing and Space Science 2015;18(2):217-33.

Sobrino JA, Jimenez-Munoz JC, Paolini L. Land surface temperature retrieval from LANDSAT TM 5. Remote Sensing of environment 2004;90(4):434-40.

Tran DX, Pla F, Latorre-Carmona P, Myint SW, Caetano M, Kieu HV. Characterizing the relationship between land use land cover change and land surface temperature. ISPRS Journal of Photogrammetry and Remote Sensing 2017;124:119-32

Tucker CJ. Red and photographic infrared linear combinations for monitoring vegetation. Remote Sensing of Environment 1979;8(2):127-50.

Voogt JA, Oke TR. Thermal remote sensing of urban climates. Remote Sensing of Environment 2003;86(3):370-84.

Wang S, Ma Q, Ding H, Liang H. Detection of urban expansion and land surface temperature change using multi-temporal Landsat images. Resources, Conservation and Recycling 2018;128:526-34.

Zhang F, Tiyip T, Kung H, Johnson VC, Maimaitiyiming M, Zhou M, Wang J. Dynamics of land surface temperature (LST) in response to land use and land cover (LULC) changes in the Weigan and Kuqa river oasis, Xinjiang, China. Arabian Journal of Geosciences 2016;9(7):499.

Zhang Y, Odeh IO, Ramadan E. Assessment of land surface temperature in relation to landscape metrics and fractional vegetation cover in an urban/peri-urban region using Landsat data. International Journal of Remote Sensing 2013;34(1): 168-89.

Microbubble Application to Enhance Hydrogenotrophic Denitrification for Groundwater Treatment

Rawintra Eamrat[1*], Yuya Tsutsumi[2], Tatsuru Kamei[3], Wilawan Khanichaidecha[4], Tsukasa Ito[5], and Futaba Kazama[3]

[1]*Faculty of Environmental Science, Ramkhamheng University, Thailand*
[2]*Interdisciplinary Graduate School of Medicine and Engineering, University of Yamanashi, Japan*
[3]*Faculty of Life and Environmental Sciences, University of Yamanashi, Japan*
[4]*Faculty of Engineering, Naresuan University, Thailand*
[5]*Department of Environmental Engineering Science, Gunma University, Japan*

ARTICLE INFO

Received: 30 May 2019
Received in revised: 31 Oct 2019
Accepted: 20 Nov 2019
Published online: 22 Jan 2020
DOI: 10.32526/ennrj.18.2.2020.15

Keywords:
Millibubble/ Microbubbles/ Mass transfer/ Hydrogenotrophic denitrification/ Nitrogen removal/ Bacteria community

*** Corresponding author:**
E-mail: rawintra.e@gmail.com

ABSTRACT

The physicochemical and biological characteristics of milli-microbubbles were compared to evaluate their performance on hydrogenotrophic denitrification (HD) for groundwater treatment in remote areas. The hydrogen supply was controlled at 1.14 L/d with 40 mgN/L of NO_3-N. The microbial community structure in two bubble reactors was investigated by high throughput sequencing. Microbubbles enhanced biodegradation in the HD system, providing a maximum nitrogen removal efficiency of 99%. Approximately 50% of total hydrogen was utilized for biological nitrate removal with the highest hydrogen effectiveness achieved at 1.21 g N/g H_2. In contrast, millibubbles achieved less than 10% efficiency and 9.9% of total hydrogen was consumed for biological nitrogen removal. *Thauera* spp., *Hydrogenophaga* spp. and *Rhodocyclaceae* of Proteobacteria phylum were the dominant bacteria in the microbubble reactor, whereas *Methyloversatilis* spp. was dominant in the millibubble reactor, in which a relatively low amount of hydrogen (0.6 mg/L) was dissolved. The differences can be attributed to the higher hydrogen transfer efficiency (45×10^{-3} s^{-1}) and lower rising velocity (0.31 mm/s) of the microbubbles system than the millibubbles system (2×10^{-3} s^{-1} and 480 mm/s). The micro-hydrogen bubble technology affords increased hydrogen effectiveness, reduced energy consumption, and modified system design. Therefore, it is more appropriate for enhancing HD.

1. INTRODUCTION

Groundwater is an important water resource in several developing countries including Nepal, the Philippines, Vietnam, and Thailand, and most residents, especially in remote areas, consume groundwater directly without any treatment (Khatlwada et al., 2002; Tirado, 2007). Therefore, nitrate contamination of groundwater is a serious environmental issue in the above mentioned countries. According to the WHO standard, nitrate-nitrogen (NO_3-N) concentration should not exceed 11 mg/L and nitrite-nitrogen (NO_2-N) should be less than 0.9 mg/L (WHO, 2011), but nitrate contamination ranges from 12 to 60 mg-N/L in these countries. Three significant causes of nitrate contamination are the extensive use of fertilizers, discharge of domestic wastewater, and unsanitary disposal of sewage waste (Khatlwada et al., 2002; Pathak et al., 2009). Moreover, rapid urbanization in recent decades have led to increases in nitrate contamination in terms of concentration values and contaminated areas. The negative effects of nitrate consumption have been manifested in infants and pregnant women as blue baby syndrome (methemoglobinemia). In addition, nitrate can transform to potential carcinogens such as nitrosamines (via nitrite) (Bouchard et al., 1992). Methods of remediating nitrate contamination of groundwater are categorized into physicochemical and biological technologies. Physicochemical methods include chemical precipitation, membrane

Citation: Eamrat R, Tsutsumi Y, Kamei T, Khanichaidecha W, Ito T, Kazama F. Microbubble application to enhance hydrogenotrophic denitrification for groundwater treatment. Environ. Nat. Resour. J. 2020;18(2):156-165. DOI: 10.32526/ennrj.18.2.2020.15

filtration, electro-dialysis, and catalysis. However, limitations of waste treatment, construction cost, and facility maintenance are not conductive to their application in remote areas (Shrimali and Singh, 2001). In contrast, biological methods have advantages of low cost and simple management (Nuclear, 2012). Therefore, they may be applicable to improving groundwater quality in remote areas. Among biological technologies, hydrogenotrophic denitrification (HD) is the most well-known process that leaves no residual organic carbon in the treated water (Karanasios et al., 2010). HD is an autotrophic denitrification process in which hydrogen acts as an electron donor and bicarbonates as carbon source under anoxic conditions. The stoichiometric expression of the HD reaction is shown in Equation (1).

$$NO_3^- + 3.03\ H_2 + H^+ + 0.229\ HCO_3^- \rightarrow 0.48\ N_2 + 3.60\ H_2O + 0.0458\ C_5H_7O_2N \quad (1)$$

However, low solubility, low gas-liquid mass transfer, and high cost of hydrogen gas limit its widespread application. Therefore, advanced technologies such as hollow fiber membranes and gas permeation membranes are applied to the HD system to generate small hydrogen bubbles, increase hydrogen utilization, and eliminate sludge wash-out (Mansell and Edward, 2002). However, membranes are expensive and require frequent cleaning and operation by skillful technicians. Another factor of concern in remote areas is the intermittent supply of electricity. Another means of increasing the efficiency of the HD system and hydrogen gas utilization is to use a gas diffuser to increase the amount of total hydrogen gas supply and concentration of dissolved hydrogen (DH). Various excellent gas diffusers have been used in laboratory and actual wastewater treatment systems. In recent years, the HD system with air stone as hydrogen bubbling diffuser was extensively proposed for nitrate removal. Vasiliadou (2009). developed a packed bed reactor with air stone as gas diffuser to treat an initial nitrate concentration of 80 mg/L, achieving a removal efficiency of 90% and a maximum removal capacity of 2.26 $kgNO_3\text{-}N/m^3{\cdot}d$ (Vasiliadou et al., 2009). Similarly, a system proposed by Khanitchaidecha (2012) achieved 96% efficiency under operating conditions of 70 mL/min hydrogen flow by an air stone diffuser (Khanitchaidecha et al., 2012). Therefore, the air stone is a reliable diffuser appropriate for HD systems in rural areas. However, a large volume of hydrogen gas supply is required to achieve high system performance, which is a drawback of the HD system. The effectiveness of hydrogen gas can be increased by increasing the surface area of bubbles and bubble dynamics through the generation of microbubbles. However, only a few studies have been conducted on the application of microbubbles to enhance the performance of simple HD systems, physicochemical properties, and the bacterial community structure of microbubble systems. In this study, a microbubble generator incorporating an oscillating mesh (named MiBos) was used. This microbubble generator was developed by one of the co-authors of this study, Ito T (Gunma University, Japan). The significant advantage of MiBos is stable generation of microbubbles even with low doses of gas, providing small bubbles that do not negatively affect bacterial cells.

The objective of this study is to investigate the applicability of the micro-hydrogen bubble technology to enhancing HD performance, and consequently develop a simple operative, cost effective, and highly effective hydrogen system for groundwater treatment. Micro-hydrogen bubbles produced with the MiBos diffuser were compared with milli-hydrogen bubbles generated by the air stone. The nitrogen removal performance, effluent quality (NO_3-N and NO_2-N concentration), hydrogen effectiveness, biological hydrogen consumption and microbial community in the two systems were investigated. Lastly, the hydrogen gas rate transfer coefficient (K_La) and rising velocity of the hydrogen bubbles were compared to explain the difference in the two hydrogen bubble processes for nitrate removal from groundwater via HD.

2. METHODOLOGY

2.1 Diffuser characteristic

Two types of hydrogen-bubble diffusers were used in this study: an air stone (STARPET, Japan) of 15×30 mm diameter was used to produce hydrogen gas in the first HD reactor, and a microbubble generator incorporated with an oscillating mesh (MiBos) was used in the second reactor. The average bubble size in the first reactor was approximately $2.20\pm0.25\times10^3$ µm, categorized as millibubbles. The average bubble size in the second reactor was about 25±13 µm, categorized as microbubbles (Takahashi, 2005). The physicochemical characteristics including total gas-liquid mass transfer coefficient (K_La) and rising velocity of hydrogen bubble were calculated using Equation (2) and Equation (3) (Stenstrom, 2007; Ghosh, 2009). Argon gas was supplied into 1 L of distilled water to remove dissolve oxygen (DO) in water and DO concentration was monitored by a DO meter until it reached lower than 0.3 mg/L. Subsequently, hydrogen gas was continuously supplied at 1 mL/min via the two diffusers. In-situ DH concentration was frequently measured by a DH meter (ENH-1000, Japan) until it reached the steady state. After that, the hydrogen gas supply was stopped immediately. The decreasing DH concentration was measured until it reached 0 mg/L. During the experiment, the temperature was controlled at 32±0.5 °C by a thermostat and liquid circulation was kept at 150 rpm using a magnetic stirrer, which was also applied to the mixed liquid. The total gas-liquid mass transfer coefficient can be determined as follows:

$$\ln\frac{(C^* - C_L)}{(C^* - C_S)} = -K_La(t - t_S) \qquad (2)$$

K_La = total gas-liquid mass transfer coefficient
C^* = dissolved hydrogen concentration at saturation concentration (mg/L)
C_L = dissolved hydrogen concentration at time (mg/L)
C_s = dissolved hydrogen concentration at start point (mg/L)
t = time (min)

$$V = \frac{1}{18} \times \frac{gd^2}{v} \qquad (3)$$

V = the rising velocity (m/s)
g = gravitational acceleration (m/s^2)
d = bubble diameter (m)
v = kinematic viscosity of water (m^2/s)

2.2 Reactor setup and operation

Two laboratory-scale cylindrical reactors were set up (height 31.4 cm, internal diameter 9 cm, working volume 2 L). One reactor used a MiBos diffuser, whereas the other used an air stone diffuser. Enriched HD sludge from a previous study was added into both reactors which was obtained from a reactor with high nitrogen removal efficiency (90% of total nitrogen removal and no nitrite accumulation) that operated for over 600 days. A nitrogen loading rate of 80 g-N/m^3/day, hydraulic retention time of 24 h, hydrogen gas flow rate of 40 mL/min, dissolved hydrogen concentration of 1.5±0.1 mg/L and temperature of 32±0.5 °C were maintained in the reactor (Eamrat et al., 2017). The enriched HD sludge was add to a reactor until the concentration of the mixed liquid suspended solid (MLSS) was 0.30±0.05 g/L. Synthetic groundwater was prepared based on the groundwater quality of Kathmandu, containing approximately 40 mg-N/L of nitrate. The chemical detail consisted of 0.24 g/L of $NaNO_3$, 0.5 g/L of $NaHCO_3$, 0.3 g/L of $MgSO_4 \cdot 7H_2O$, 0.027 g/L of KH_2PO_4, 0.18 g/L of $CaCl_2 \cdot 2H_2O$ and Trace element I and II. Moreover, the synthetic groundwater was supplied with argon gas to maintain the dissolved oxygen concentration (0.3±0.1 mg/L) before continuously fed to the reactors at 4 L/d, the hydraulic retention time was 12 h and solid retention time was 12 h. The water temperature was controlled at 32±0.5 °C. Hydrogen was supplied to the reactors with the lowest flow rate of 1 mL/min from a hydrogen gas generator (HG260, GL Science, Japan) via the two diffusers. One reactor used a MiBos as diffuser, whereas the other used an air stone as diffuser. The surfaces of the reactors were covered with plastic beads to prevent oxygen penetration from the air. During operation, the liquid and sludge inside the reactors were completely mixed by a magnetic stirrer. A schematic diagram of reactor operation is illustrated in Figure 1. To investigate the performance of the micro- and milli-hydrogen bubble reactors, nitrogen removal efficiency, biological hydrogen gas consumption by denitrifiers and hydrogen effectiveness were calculated using Equation (4)-(7).

$$\text{Nitrogen removal efficiency (\%)} = \frac{\text{Nitrogen removal rate } [g \cdot N/(m^3 \cdot d)]}{\text{Nitrogen loading rate } [g \cdot N/(m^3 \cdot d)]} \times 100 \qquad (4)$$

$$\text{Nitrogen loading rate } [g \cdot N/(m^3 \cdot d)] = \frac{\text{Influent nitrate } [g \cdot N/L] \times \text{Flow rate } [L/d]}{\text{Reactor volume } [m^3]} \qquad (5)$$

$$\text{Nitrogen removal rate } [g \cdot N/(m^3 \cdot d)] = \frac{(\text{Nitrate} + \text{Nitrite removed})[g \cdot N/L]) \times \text{Flow rate } [L/d]}{\text{Reactor volume } [m^3]} \qquad (6)$$

$$\text{Hydrogen effectiveness}\ [\text{mg}\cdot\text{N/g}\cdot\text{H}_2] = \frac{\text{Nitrogen removal rate}\ [\text{g}\cdot\text{N}/(\text{m}^3\cdot\text{d})] \times \text{Reactor volume}\ [\text{m}^3]}{\text{Total hydrogen supply volume}\ [\text{g}\cdot\text{H}_2/\text{d}]} \quad (7)$$

2.3 Analytical method

Water samples were collected from the synthetic groundwater (inlet) and treated water (outlet), then filtered through a 0.45 µm membrane filter and kept in the sampling bottles for water quality analysis. The concentrations of nitrate and nitrite were measured in accordance with the standard method for water and wastewater analysis (APHA et al, 2012). Ultraviolet spectrophotometric screening was used for nitrate measurement, and the colorimetric method was used for nitrite measurement using a UV spectrophotometer (UV-1800, Japan). In situ pH and DH were measured using a pH meter (Horiba, B712) and a DH meter (ENH-1000, Japan).

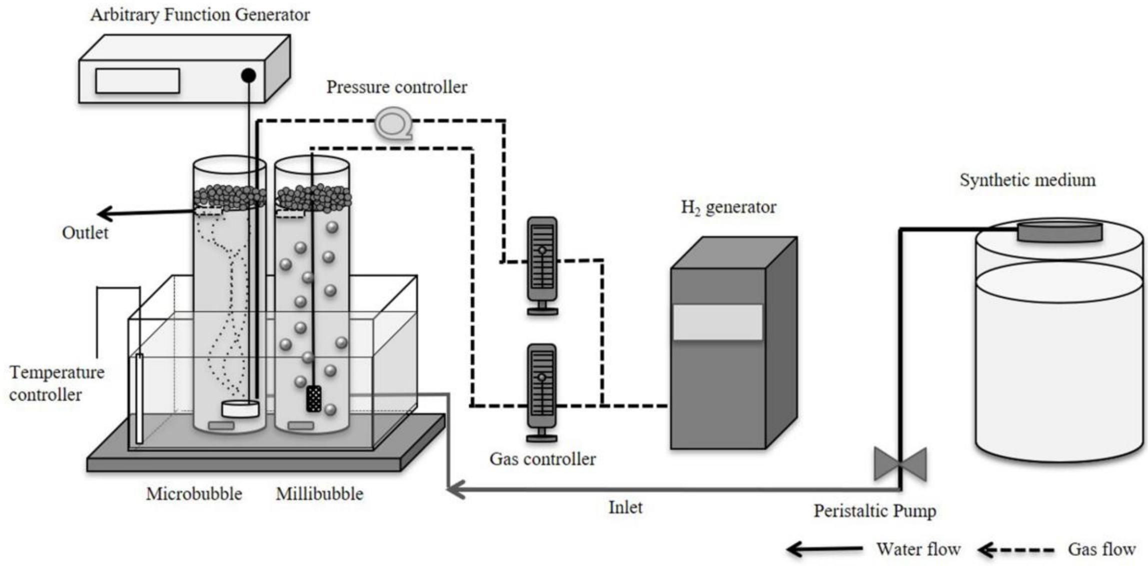

Figure 1. Layout of laboratory-scale hydrogenotrophic denitrification reactors

2.4 DNA extraction, PCR and Illumina next-generation sequencing analysis

To identify the microbial community in micro- and milli- hydrogen bubble reactors, sludge samples of about 0.1 g (wet weight) were collected and examined using the Illumina Next Generation Sequencing method. The total DNA in each sample was extracted using a FastDNA® Spin Kit for soil (MP-Biomedicals, Santa, CA, USA) according to the manufacturer's protocol. The V4 hypervariable region of the 16S rRNA gene was selected for polymerase chain reaction (PCR). The primers were the universal primer set; 515F (5′-GTGCCAGCM GCCGCGGTAA-3′) and 806R (5′-GGACTACHVG GGTWTCTAAT-3′). The 25 µL of PCR reaction mixture comprised 12.5 µL of sybrII, 0.1 µL of forward primer, 0.1 µL of reverse primer, 10.3 of water and 2 µL of DNA extracted sample. The PCR protocol consisted of denaturation at 94 °C for 30 s, followed by 40 cycles of denaturing at 94 °C for 15 s, annealing at 55 °C for 30 s, extension at 72 °C for 30 s, and the final elongation at 72 °C for 5 min. The amplicons from all samples were sent out for pyrosequencing using the Ilumina MiSeq platform of a commercial sequencing service (FASMAC Co., Ltd. Atsugi, Japan).

3. RESULTS AND DISCUSSION

3.1 Performance of the two reactors for hydrogenotrophic denitrification

Two-hydrogen bubble processes with millibubbles from the air stone and microbubbles using MiBos as diffusers were operated to evaluate the nitrogen removal performance, hydrogen effectiveness, and biological hydrogen consumption via hydrogen oxidizing denitrification. Hydrogen gas was continuously supplied into reactors and controlled at 1 mL/min (or 1.14 L/d). The in-situ dissolved hydrogen (1.4-1.5 mg/L) in the micro-reactor was similar to that in literature reporting 1.44 mg/L of hydrogen gas in water at 32 °C. DH was slightly lower than the theoretical value in the milli-reactor (1.2 mg/L). Figure 2 shows two phases of the experiments adaptation and reaction periods. During the adaptation period (0-9 days), significant fluctuations in the amounts of NO_3-N and NO_2-N were observed in the milli-reactor. Approximately 10-15 mg-N/L of nitrate in the synthetic groundwater was removed, and then converted to nitrite. The highest nitrite accumulation was found to be 10 mg/L in day four of the operation. The overall nitrogen removal efficiency was approximately zero. After adaptation periods, the nitrogen removal efficiency was increased to 20% (nitrite removal). Moreover, DH concentration was suddenly decreased from 1.2 mg/L to 0.5 mg/L, although hydrogen gas was continuously supplied to the reactor. The dropping DH concentration implies that the amount of hydrogen gas transferring to the liquid phase was lower than that consumed by denitrifying bacteria. In the micro-hydrogen bubble reactor, nitrite was also found in the effluent from nitrate conversion in the adaptation period. However, some nitrate could be completely converted to nitrogen gas and released to the air. The performance of the micro-hydrogen bubble reactor continuously increased to 99% after the adaptation period (Figure 2(b)). At peak performance, the nitrate and nitrite concentrations were less than 1 mg/L, which meet the standards for safe drinking water. Moreover, DH was found to be in the range of 1.4-1.5 mg/L during the experiment. All above results show that the micro-hydrogen bubble reactor offers effective denitrification and high DH (greater dissolution in water and longer persistence).

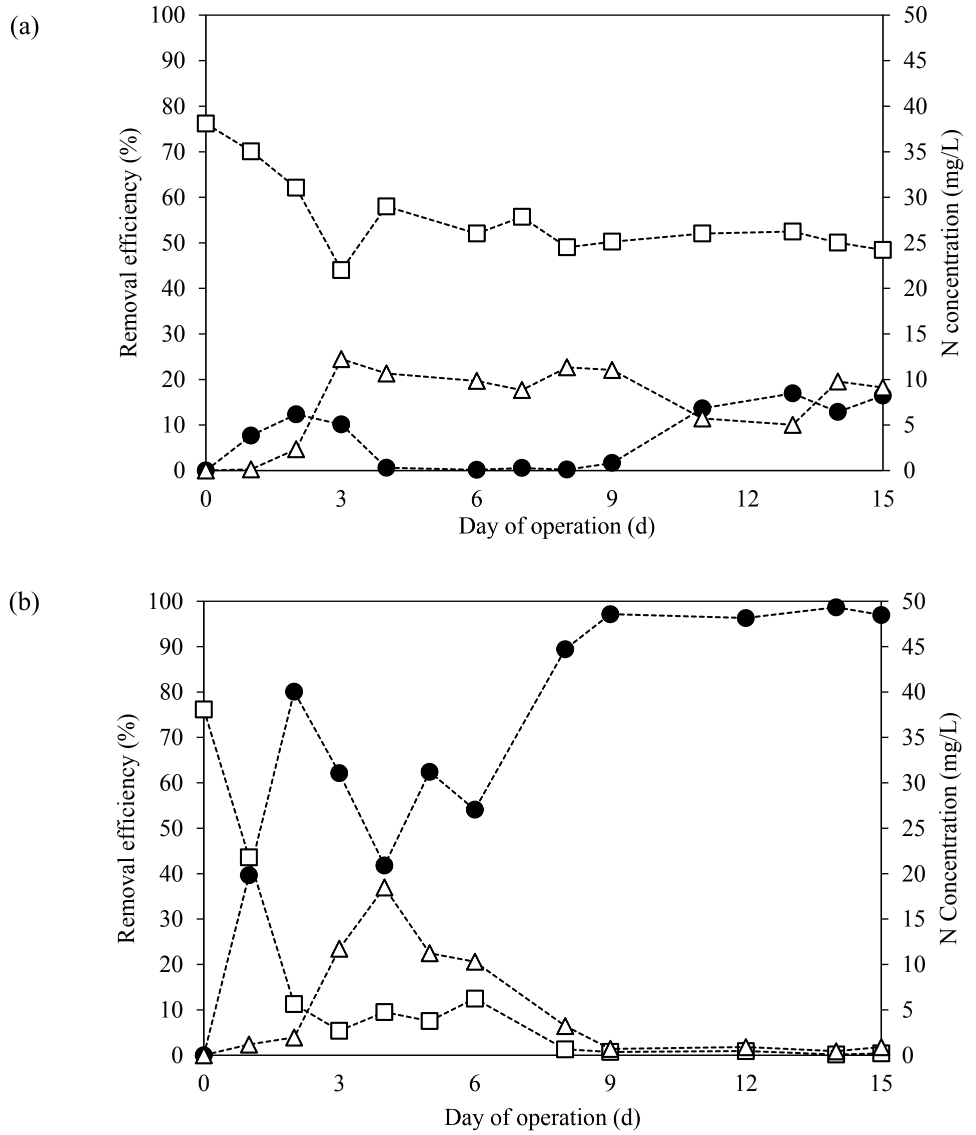

Figure 2. Performance of two systems in term of nitrogen removal efficiency and effluent concentration by (a) millibubble reactor and (b) microbubble reactor [●=Removal efficiency (%); □=NO_3-N concentration (mg/L); Δ=NO_2-N concentration (mg/L)]

According to the nitrogen removal performance, the percentage of biological hydrogen gas consumption by denitrifiers was calculated (Figure 3). The specific hydrogen consumption was calculated based on the stoichiometry of the denitrification reaction with hydrogen gas as the electron donor (Equation (1)). Here, each mole of nitrate reduces to nitrogen gas per 3.03 mole of hydrogen gas consumed. Consequently, 0.43 g of hydrogen gas was consumed in order to remove 1 g of NO_3-N. Figure 3 shows the differences between total hydrogen supply; biological hydrogen consumption was assumed to be the unused hydrogen that was released to the air. Biological hydrogen consumption was less than 10% in the milli-hydrogen bubble reactor, showing that hydrogen gas was mainly released to the air. Although, the biological denitrification consumption was low, the hydrogen effectiveness of the milli-hydrogen bubble reactor was 197 mg-N/g-H_2. On the other hand, in the micro-hydrogen bubble reactor, hydrogen consumption was found to be around 25% during the adaptation period and the value increased to around 50% after the adaptation period. These findings indicate that the effectiveness of hydrogen during operation was 1.21 g-N/g-H_2, which was higher than that of the milli-hydrogen bubble reactor by about 6 times. In summary, micro-hydrogen bubbles can enhance reactor performance for nitrogen removal and hydrogen effectiveness, leading to a low-cost treatment system that might be affordable for developing countries. The overall performance of the two suspended growth reactors in this study was also compared to that of previous studies using sequencing batch reactor, attached growth reactor, biofilm reactor and packed bed reactor. Reactor configuration and diffuser types affect nitrogen removal efficiency and hydrogen gas effectiveness. In an attached growth reactor, a packed bed reactor with air stone for hydrogen bubbling achieved high removal efficiency under short hydraulic retention time as compared with the MiBos diffuser. However, a large volume of hydrogen gas is supplied into the air stone system making the hydrogen gas effectiveness low. For the MiBos diffuser, microbubble technology can enhance the nitrogen removal efficiency and hydrogen gas effectiveness as compared to the air stone (Table 1). The micro-hydrogen bubble reactor achieved excellent efficiency of greater than 90%. Therefore, the micro-hydrogen bubble reactor offers potential for enhancing the performance of a hydrogenotrophic denitrification reactor.

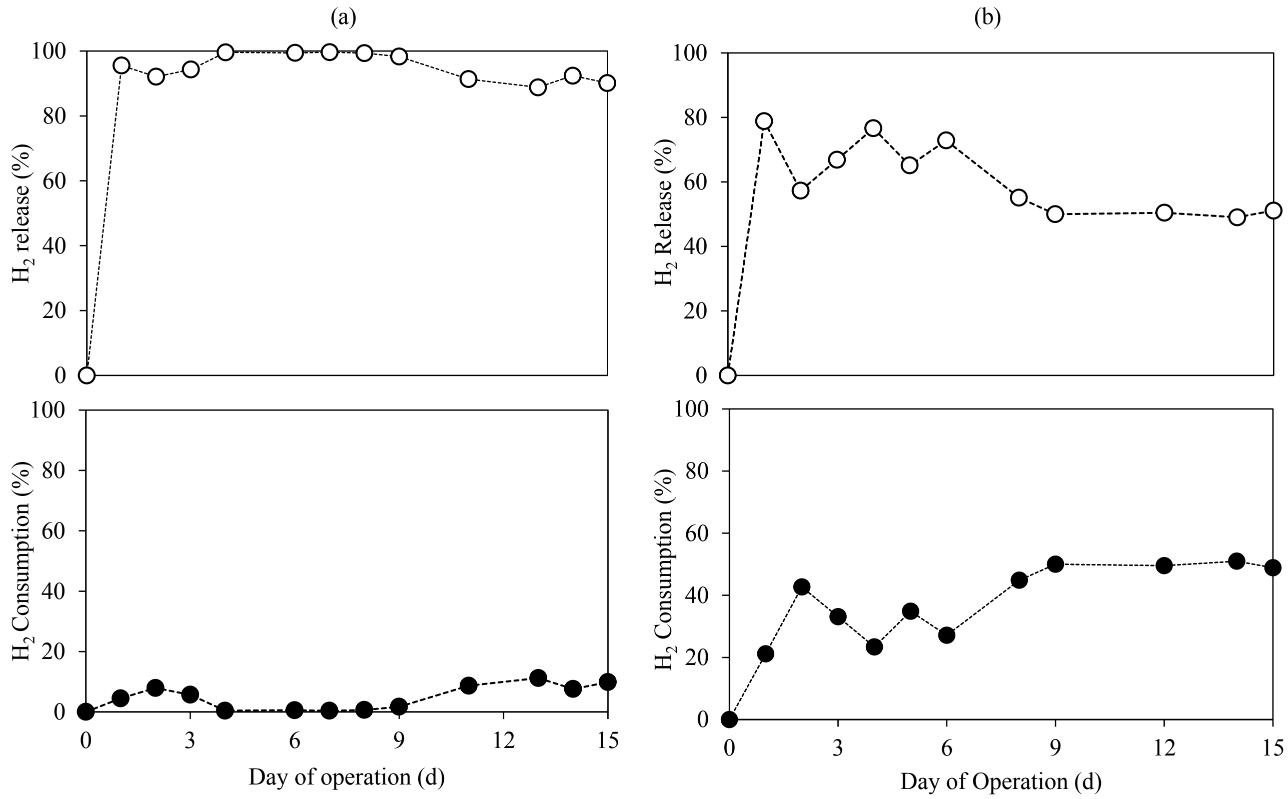

Figure 3. Percentage of biological hydrogen consumption for denitrification with two bubbles reactors; (a) millibubble reactor and (b) microbubble reactor

Table 1. Performance of HD systems in the literature

Reactors	Diffuser types	HRT (h)	H_2 supply (g/d)	Removal efficiency (%)	H_2 effectiveness (g-N/g-H_2)	References
Sequencing batch reactor	Bubble stone	480	2.14	100	0.12	Mousavi et al. (2013)
Sequencing batch reactor	Commercial bubble stone	3	1.34	100	0.01	Ghafari et al. (2009)
Attached growth reactor	Air stone	2.5	9.00	96	0.06	Khanitchaidecha et al. (2012)
Packed bed reactor	Fixed nozzles	1.0	11.57	82	0.34	Vasiliadou et al. (2009)
Packed bed reactor	Aquarium diffusing stone	2.0	12.86	80	0.04	Lee et al. (2010)
Suspended growth reactor	Air stone	12.0	0.13	16	0.20	This study
Suspended growth reactor	MiBos	12.0	0.13	98	1.21	This study

3.2 Mechanism of physical properties by micro-hydrogen bubbles

The difference in nitrogen removal efficiency and hydrogen dissolution between two reactors with milli-hydrogen bubble from Air stone and micro-hydrogen bubble from MiBos reactors is clarified in this section. Physical properties such as total gas-liquid mass transfer coefficient (K_La) and rising velocity of hydrogen bubbles generated from the two diffusers are summarized in Table 2. The increasing rate of DH concentration in the microbubble reactor was found to be faster than that in the millibubble reactor because of the transfer of most microbubbles to the surrounding liquid, large driving force, and low rising velocity. The transfer coefficient (K_La) refers to the ability to transfer hydrogen gas to the liquid phase, which depends on the size of bubble (Cruz et al., 1999; Painmanakul et al., 2009). As such, the K_La of the microbubble reactor was 45×10^{-3} s^{-1}, which is approximately 22.5 times greater than that of the millibubble reactor (2×10^{-3} s^{-1}). Micro-hydrogen gas transfer rateto dissolved hydrogen was faster than millibubble hydrogen gas. Moreover, the DH concentration arising from microbubbles persists about 10 times longer in the liquid phase than that arising from millibubbles under the same hydrogen supply amount. Therefore, microbubbles can enhance dissolved hydrogen for an extended duration, which has the potential to enhance nitrate removal via hydrogenotrophic denitrification. Moreover, the rising velocity of bubbles was found to be approximately 0.31 mm/s and 480 mm/s for the microbubble and millibubble reactors, respectively (Equation 3). Low rising velocity of microbubble caused bubbles to gradually shrink in water and ultimately disappear by dissolution. Therefore, the rate transfer of hydrogen gas to liquid phase was also related with rising velocity. Therefore, microbubbles of hydrogen were easily dissolved and consumed by microorganisms.

Table 2. Summary of the comparison of the physical properties between microbubbles and millibubbles

Diffusers	Bubble types	Flow rate (mL/min)	Total H_2 supply (mL)	Bubble diameter (µm)	K_La (s^{-1})	Rising velocity (mm/s)
Air stone	Millibubble	1	5	$2.2\pm0.25\times10^3$	2×10^{-3}	480
MiBos	Microbubble	1	5	25 ± 13	45×10^{-3}	0.31

3.3 Microbial community

After the comparison of biological and physicochemical performance of the two different bubble processes (micro-hydrogen bubble and milli-hydrogen bubble), the bacterial community was further analyzed with high throughput sequencing of 16S rRNA gene of bacteria. Sludge samples from both milli- and micro-bubbles reactors were taken on the 15th day of operation for identifying abundant microbial communities. As shown in Figure 4, the total of identified bacteria phyla for both samples were 18. *Proteobacteria* was the most predominant phylum (83%) with some *Bacteroidetes* (9%) and *Firmicutes* (3%) in the microbubble reactor (Figure 4(a)), while the milli-hydrogen bubble reactor was mainly represented by *Proteobacteria* (76%) with some *Bacteroidetes* (12%) and *Planctomycetes* (6%) as shown in Figure 4(b). Within *Proteobacteria, Betaproteobacteria* (60-71%) was the most predominant class instead of *Alphaproteobacteria* (12%) in both samples, while *Grammaproteobacteria* (4%) was found only in the milli-hydrogen bubble reactor. In a previous study, *Proteobacteria*, *Firmicutes*, *Bacteroidetes and Planctomycetes* were detected in autohydrogenotrophic denitrification and denitrification (Wang et al., 2015). Juretschko (2002) demonstrated that the phylum *Planctomycetes* was detected in nitrifying-denitrifying activated sludge from an industrial sewage treatment plant (Juretschko et al., 2002). Moreover, *Firmicutes* was reported to be predominant in autotrophic denitrification biocathode and hydrogenotrophic denitrification under thermophilic (30 °C) conditions (Wang et al., 2015; Xiao et al., 2015). *Bacteroidetes* was found to be dominant in prior nitritation and partial nitritation processes (Chen et al., 2016). From the present study, it is demonstrated that the microorganisms in both reactors were detected in the denitrification and the microorganisms could use hydrogen gas as the electron donor for nitrate removal. Conventionally, the bacterial community structures from two samples were further analysed at the family and genus levels (Figure 5). *Thauera* spp., Rhodocyclaceae, and *Hydrogenophaga* spp. belonging to Betaproteo-bacteria were highly enriched in the microbubble reactor and accounted for 29.3, 26.1, and 8.5% of the total bacteria, respectively. On the contrary, *Methyloversatilis* spp. (25.9%), *Thauera* spp. (13.8%), and *Hydrogenophaga* spp. (8.5%) were abundant in the milli-hydrogen bubble reactor. In a previous study, *Thauera* spp. and *Hydrogenophaga* spp. were detected in a hydrogenotrophic denitrification bioreactor for nitrate removal and *Thauera* spp. was found to have potential for nitrate removal under low hydrogen supply (Eamrat et al., 2017; Mao et al., 2013; Chen et al., 2015). *Methyloversatilis* spp. was recognized to enable heterotrophic denitrification, consuming organic carbon (i.e., methanol) as carbon source for nitrate removal (Sun et al., 2016). The role of *Methyloversatilis* spp. in denitrification was classified (Mustakhimov et al., 2013); the bacteria was discovered in the methylotrophy metabolic pathways during the transformation of nitrate to nitrite under anoxic conditions. Related with the reactor performance, the low dissolved hydrogen of 0.5 mg/L in the milli-hydrogen bubble reactor resulted in insufficient hydrogen for complete hydrogenotrophic denitrification, and thus heterotrophic denitrification occurred and became dominant. It can be summarized that nitrate removal in the micro-hydrogen bubble reactor occurred through hydrogenotrophic denitrifiers, whereas that in the milli-hydrogen bubble reactor was enabled by a combination of hydrogenotrophic denitrifiers and heterotrophic denitrifiers.

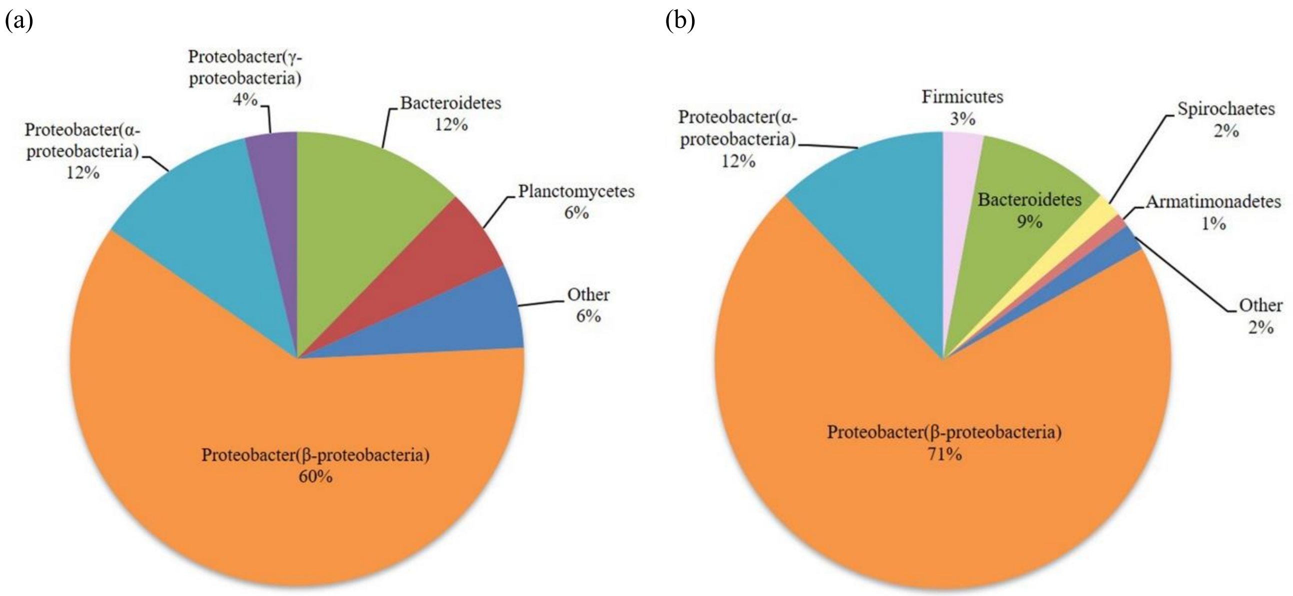

Figure 4. Relative abundance values at the phylum levels with two hydrogen-bubble systems; (a) millibubble system and (b) microbubble system.

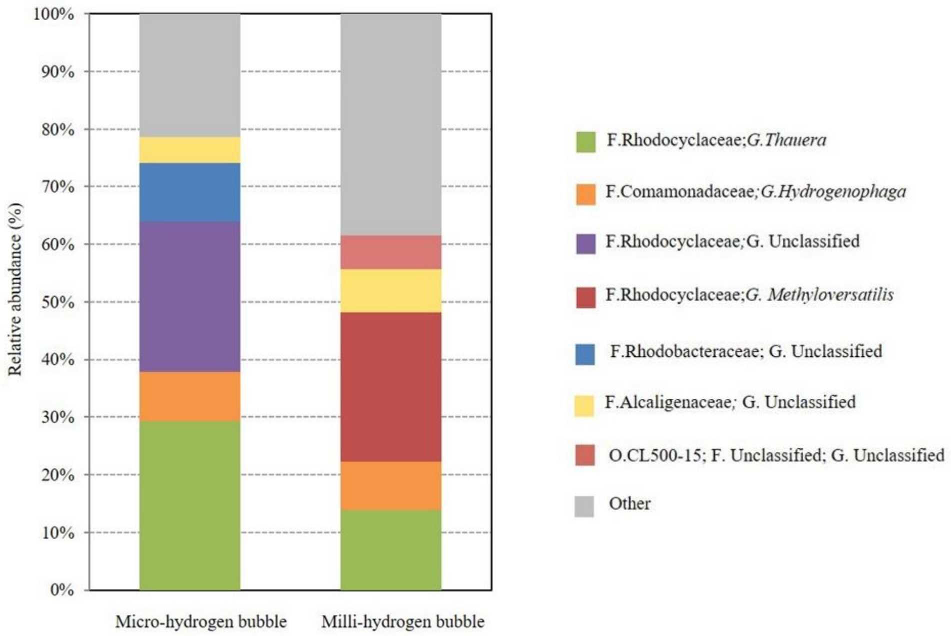

Figure 5. Relative abundance values at the family and genus levels with two hydrogen bubble systems during microbubble system and millibubble system; The abundance values lower than 5% were included in “other” group.

4. CONCLUSIONS

This research compared the performance of micro-hydrogen bubbles (mean bubble size of 25±13 μm) and milli-hydrogen bubbles (mean bubble size of $2.20\pm0.25\times10^3$ μm) generated from MiBos and Air stone for nitrate removal from groundwater. The micro-hydrogen bubble reactor performed better than the milli-hydrogen bubble reactor by achieving excellent nitrogen removal efficiency and increased hydrogen effectiveness. The nitrogen removal efficiency reaching 99 % and around 50% of total hydrogen was utilized for biological consumption, which increased the hydrogen effectiveness to reach 1.21 g-N/g-H_2. In comparison, the milli-hydrogen bubble reactor achieved less than 10% efficiency and biological consumption accounted for 9.9% of total hydrogen at the same dose of hydrogen supply with the micro-hydrogen bubble reactor. The different results demonstrate that microbubbles have high dissolution ability, faster hydrogen mass transfer efficiency (45×10^{-3} s^{-1}), and low velocity (0.31 mm/s) as compared with milli-hydrogen bubbles (2×10^{-3} s^{-1} and 480 mm/s). Physicochemical properties significantly affected the microbial community. *Thauera* spp., *Hydrogenophaga* spp. and Rhodocyclaceae belonging to Betaproteobacteria, which can use nitrate as the electron accepter and hydrogen as electron donor under anaerobic conditions, were enriched in the micro-hydrogen bubble reactor, enabling hydrogenotrophic denitrification. In the milli-hydrogen bubble reactor, insufficient hydrogen caused *Methyloversatilis* spp. to become dominant instead of *Thauera* spp., *Hydrogenophaga* spp., and Rhodo-cyclaceae, thus, both heterotrophic and hydrogenotrophic denitrification possibly occurred. However, other factors including system designs and long-term operation should be further studied before applying the HD system to the treatment of contaminated water.

5. ACKNOWLEDGEMENTS

This research was performed with partial financial assistance from the “Project for Hydro-Microbiological Approach for Water Security in Kathmandu Valley, Nepal” under the Science and Technology Research Partnership for Sustainable Development (SATREPS) program of JST and JICA, and the Japan Society for the Promotion of Science KAKENHI GRANT number 26340059.

REFERENCES

APHA, AWWA, WEF. Standard Methods for the Examination of Water and Wastewater. 22th ed. New York, USA: American Public Health Association/American Water Works Association/Water Environment Federation; 2012.

Bouchard DC, Williams MK, Surampalli RY. Nitrate contamination of groundwater; Sources and potential health effects. American Water Work Association 1992;84(9):85-90.

Chen DHW, Ji B, Li W, Yu J. A high-throughput sequencing study of bacterial communities in an autohydrogenotrophic denitrifying bio-ceramsite reactor. Process Biochemistry 2015;50(11):1904-10.

Chen DXD, Dawen C, Sha W, Xiaona H, Wenru L, Dianhai Y. Performance and microbial ecology of a nitritation sequencing batch reactor treating high-strength ammonia wastewater. Scientific Reports 2016;6(1):1-8.

Cruz AJG, Silva AS, Araujo MLGC, Giordano RC, Hokka CO. Estimation of the volumetric oxygen tranfer coefficient (K_La) from the gas balance and using a neural network technique. Brazilian Journal of Chemical Engineering 1999;16(2):179-83.

Eamrat R, Yuya T, Tatsuru T, Willawan K, Yasuhiro T, Futaba K. Optimization of hydrogenotrophic denitrification behavior using continuous and intermittent hydrogen gas supply. Journal of Water and Environment Technology 2017; 15(2):65-75.

Ghafari S, Masitah H, Mohamed KA. Effect of carbon dioxide and bicarbonate as inorganic carbon sources on growth and adaptation of autohydrogenotrophic denitrifying bacteria. Journal of Hazardous Materials 2009;162(2-3):1507-13.

Ghosh P. Coalescence of bubbles in liquid. Bubble Science, Engineering and Technology 2009;1:75-8.

Juretschko S, Alexander L, Angelika L, Michael W. The microbial community composition of a nitrifying-denitrifying activated sludge from an industrial sewage treatment plant analyzed by the full-cycle rRNA approach. Systematic and Applied Microbiology 2002;25(1):84-99.

Karanasios KA, Vasiliadou IA, Pavlou S, Vayenas DV. Hydrogenotrophic denitrification of potable water: A review. American Water Work Association 2010;180(1-3):20-37.

Khanitchaidecha W, Maneesha S, Kamei T, Futaba K. NH_4-N removal through nitrification and hydrogenotrophic denitrification in simple attached growth reactors. Water, Air, and Soil Pollution 2012;223(7):3939-53.

Khatlwada NR, Takizawa S, Tran TVN, Inoue M. Groundwater contamination assessment for sustainable water supply in Kathmandu valley, Nepal. Water Science and Technology 2002;46(9):147-54.

Lee JW, Lee KH, Park KY, Maeng SK. Hydrogenotrophic denitrification in a packed bed reactor: Effects of hydrogen-to-water flow rate ratio. Bioresource Technology 2010; 101(11):3940-6.

Mansell BO, Edward DS. Hydrogenotrophic denitrification in a microporous membrane bioreactor. Water Research 2002; 36(19):4683-90.

Mao Y, Yu X, Tong Z. Characterization of Thauera-dominated hydrogen-oxidizing autotrophic denitrifying microbial communities by using high-throughput sequencing. Bioresource Technology 2013;128:703-10.

Mousavi S, Shaliza I, Mohamed KA. Effects of operational parameters on the treatment of nitrate-rich wastewater by autohydrogenotrophic denitrifying bacteria. Water and Environment Journal 2013;28(3):556-65.

Mustakhimov I, Marina GK, Mary EL, Ludmila C. Insights into denitrification in methylotenera mobilis from denitrification pathway and methanol metabolism mutants. Journal of Bacteriology 2013;195(10):2207-11.

Nuclear L. Environmental remediation and restoration technologies in nuclear decommissioning projects. Decommissioning 2012;416-47.

Painmanakul P, Jidapa W, Marupatch J, Gilles H. Theoretical prediction of volumetric mass transfer coefficient (K_La) for designing an aeration tank. Engineering Journal 2009; 13(3):13-28.

Pathak DR, Hiratsuka A, Wata I. Assessment of nitrate contamination in groundwater of a shallow aquifer in Kathmandu, Nepal. Hydrology Science Journal 2009; 329:178-83.

Rice EW, Baird RB, Eaton AD, Clesceri LS. Standard Methods for the Examination of Water and Wastewater. 22nd ed. New York, USA: American Water Works Association; 2012.

Shrimali M, Singh KP. New methods of nitrate removal from water. Environmental Pollution 2001;112(3):351-9.

Stenstrom MK. Measurement of Oxygen Transfer in Clean Water (ASCE/EWRI 2-06). New York, USA: American Society of Civil Engineers; 2007.

Sun Y, Dandan S, Xiaoli Z, Na S, Yuan T. Microbial diversity and community structure of denitrifying biological filters operated with different carbon sources. SpringerPlus 2016;5(1):1752-60.

Takahashi M. Zeta potential of microbubbles in aqueous solutions: electrical properties of the gas-water interface. Journal of Physical Chemistry 2005;109(46):21858-64.

Tirado R. Nitrate in Drinking Water in the Philippines and Thailand. Greenpeace South East Asia; 2007.

Vasiliadou IA, Karanasios KA, Pavlou S, Vayenas DV. Hydrogenotrophic denitrification of drinking water using packed-bed reactors. Desalination 2009;248(1-3):859-68.

Wang H, Qiulai H, Dan C, Li W, Zhuocheng Z. Microbial Community in a hydrogenotrophic denitrification reactor based on pyrosequencing. Applied Microbiology and Biotechnology 2015;99:10829-37.

World Health Organization (WHO). Guidelines for Drinking Water Quality. 4th ed. Switzerland: Publication of World Health Organization; 2011.

Xiao Y, Yue Z, Song W, Zhao Y. Bacterial community structure of autotrophic denitrification biocathode by 454 pyrosequencing of the 16S rRNA gene. Environmental Microbiology 2015;492-9.

Metal Accumulation in Lichens as a Tool for Assessing Atmospheric Contamination in a Natural Park

Chaiwat Boonpeng[1*], Duangkamon Sangiamdee[2], Sutatip Noikrad[1], Santi Watthana[3], and Kansri Boonpragob[1]

[1]Lichen Research Unit, Department of Biology, Faculty of Science, Ramkhamhaeng University, Hua Mark, 10240 Bangkok, Thailand
[2]Department of Chemistry, Faculty of Science, Ramkhamhaeng University, Hua Mark, 10240 Bangkok, Thailand
[3]School of Biology, Institute of Science, Suranaree University of Technology, Mueang District, 30000 Nakhon Ratchasima, Thailand

ARTICLE INFO

Received: 24 Jul 2017
Received in revised: 11 Nov 2019
Accepted: 25 Nov 2019
Published online: 20 Jan 2020
DOI: 10.32526/ennrj.18.2.2020.16

Keywords:
Background concentration/ Bioaccumulation/ Motor vehicle/ *Parmotrema tinctorum*/ Tourism

*** Corresponding author:**
E-mail:
chaiwat.bioru@gmail.com

ABSTRACT

Motor vehicles passing through natural areas could contribute to the air pollution that most likely causes biodiversity losses and decreases air quality. This study assessed the impact of tourism on atmospheric metal pollution in Khao Yai National Park (KYNP), Thailand. Native thalli of the epiphytic lichen *Parmotrema tinctorum* were collected during the rainy period at a total of eleven sampling sites: three sites in forested (no traffic), four sites in accommodation (low-moderate traffic) and four sites in parking (moderate-high traffic) areas in KYNP. Nine traffic-related metals, including As, Cd, Cr, Cu, Fe, Pb, Sb, V and Zn, were detected using inductively coupled plasma mass spectrometry (ICP-MS). The concentrations of most metals did not show significant differences between the higher traffic intensity areas and the no traffic area, and the concentrations of the metals were in the range of their background concentrations. Only Cr and V, metals related to motor vehicles, were identified at the accommodation sites at significantly higher concentrations (Cr=3.4 μg/g, V=1.33 μg/g) than their baseline concentrations (Cr=1.4 μg/g, V=0.96 μg/g). These two metals have adverse effects on humans, plants, lichens and other organisms. Bioaccumulation ratios (B ratios) indicated that most metals at most sampling sites did not bioaccumulate. No metal demonstrated high or severe bioaccumulation. This result suggests that the impact of tourism on atmospheric metal pollution in the rainy period at the KYNP was modest. It also affirms the ability of lichen as an effective tool for assessing atmospheric contamination in natural areas.

1. INTRODUCTION

Natural parks are generally rich in biodiversity, provide increased air quality and serve as recreational sites for family vacations and tourists. Most national parks are modified to facilitate and support tourism, such as the construction of access roads, accommodations and camping sites. Motor vehicles passing through these areas could affect both biodiversity and the purity of the air (Liu et al., 2018; Nascimbene et al., 2014). Several pollutants are released from motor vehicles, such as heavy metals (Koz et al., 2010; Yemets et al., 2014; Zhao et al., 2019). They can pollute the air and are toxic to living organisms, especially sensitive species such as lichens, bryophytes and aerial plants, leading to biodiversity losses (Spellerberg, 1998). In addition, park authorities and visitors are most likely affected by their toxicity (Kampa and Castanas, 2008). The need to understand the impact of tourism on environmental quality in natural areas is crucial for sustainable tourism, organisms and ecosystems.

Lichens are symbiotic organisms of fungi and algae and/or cyanobacteria. They have no root system or waxy cuticle and rely on atmospheric water and nutrients for growth and survival. These characteristic enable them to serve as great bioaccumulators of

Citation: Boonpeng C, Sangiamdee D, Noikrad S, Watthana S, Boonpragob K. Metal accumulation in lichens as a tool for assessing atmospheric contamination in a natural park. Environ. Nat. Resour. J. 2020;18(2):166-176. DOI: 10.32526/ennrj.18.2.2020.16

atmospheric deposition (Bargagli and Mikhailova, 2002; Garty and Garty-Spitz, 2015). Unlike gaseous pollutants i.e., NO_x and SO_x, lichens are tolerant to metals. They can accumulate amounts of metals above their need. The tolerance mechanism is very complex and still not fully understood. Lichen substances or secondary metabolites (e.g., usnic acid, norstictic acid and psoromic acid) play an important role in the tolerance mechanism (Bačkor and Loppi, 2009). Pawlik-Skowrońska and Bačkor (2011) found a strongly positive correlation between the amounts of secondary metabolites and Zn/Pb accumulation in the studied lichens. Oxalates also showed a potential mechanism for extracellular metal detoxification (Pawlik-Skowrońska et al., 2006).

Biomonitoring with lichens is a cost-effective technique that is easy to implement and requires no electricity for installation and operation, allowing the technique to be used in natural/remote areas (Conti et al., 2009; Loppi, 2014) as opposed to conventional air monitoring instruments. The lichen *Parmotrema tinctorum* (Despr. ex Nyl.) Hale is a cosmopolitan species (Louwhoff and Elix, 2000). In Thailand, it is found in cool, humid, moderate-high light intensity and relatively unpolluted areas (e.g., mountain areas). Its potential to be used as a bioindicator/biomonitoring species of air quality has been tested and confirmed by several scientists (Boonpeng et al., 2018; Koch et al., 2016; Port et al., 2018). In Thailand, it was used as a biomonitor of atmospheric deposition for assessing air quality in the Map Ta Phut petrochemical complex (Boonpeng et al., 2017a; Boonpeng et al., 2017b; Boonpeng et al., 2018). In Brazil, it was used as a bioaccumulator of atmospheric pollutants in urban and forested areas in the Rio Grande do Sul (Koch et al., 2016; Port et al., 2018), and in the urban area of the Porto Alegre (Käffer et al., 2012). It was also used to monitor radionuclides around the Fukushima Dai-ichi Nuclear Power Plant in Tsukuba city, Japan (Ohmura et al., 2015).

Khao Yai National Park (KYNP) was announced as a World Heritage Site in 2005 by the United Nations Educational, Scientific and Cultural Organization (UNESCO). Due to its high biodiversity of both flora and fauna, beautiful scenic views and waterfalls, cool weather, and proximity to Bangkok, KYNP is one of the most popular tourist places in Thailand. The impacts of tourism on soil, vegetation, wildlife and water in the area were previously documented (Phumsathan, 2010), but the impact of the area on air quality has never been determined. The number of visitors in the park has sharply increased from ca. 750,000 in 2010 to 1,500,000 visitors in 2018 (2 fold increase); similarly, the number of motor vehicles (cars and motorcycles) has steadily increased from ca. 280,000 to 380,000 vehicles (1.4 fold increase) over the last 6 years (Figure 3). The result of this study can reveal the situation of air quality in KYNP. The objectives of this study were to (i) use the lichen *P. tinctorum* to monitor the concentrations of traffic-related metals in the air in KYNP; and (ii) assess the impact of tourism on atmospheric metal pollution during the rainy season in KYNP. We hypothesized that motor vehicle traffic can contribute to the level of metal pollutants in the study area.

2. METHODOLOGY

2.1 Study area

Khao Yai National Park (KYNP) is located in the areas of Nakhon Nayok, Prachinburi, Saraburi and Nakhon Ratchasima Provinces in Thailand, covering an area of 2,169 km^2 with a complex terrain and elevations ranging from ca. 50 to 1,351 meters above sea level (m.a.s.l.), the park is approximately 170 km northeast of Bangkok (Figure 1). Climatic conditions in the area are shown in Figure 2. The annual cumulative rainfall is 2,073 mm, the rainy period occurs from April to October (7 months), and the dry period occurs from November to March (5 months) (Brockelman et al., 2017). The monthly relative humidity (RH) ranges from 68 to 90%, which is consistent with the amount of rainfall and rain events. The monthly average temperature ranges from 19 to 24 °C; April, May and June are the hottest months (>23.7 °C); and November, December and January are cool months (<21 °C). A high number of visitors and motor vehicles appear in the tourist season from October to January and especially in December and January when there are >180,000 visitors per month and >40,000 vehicles per month (Figure 3).

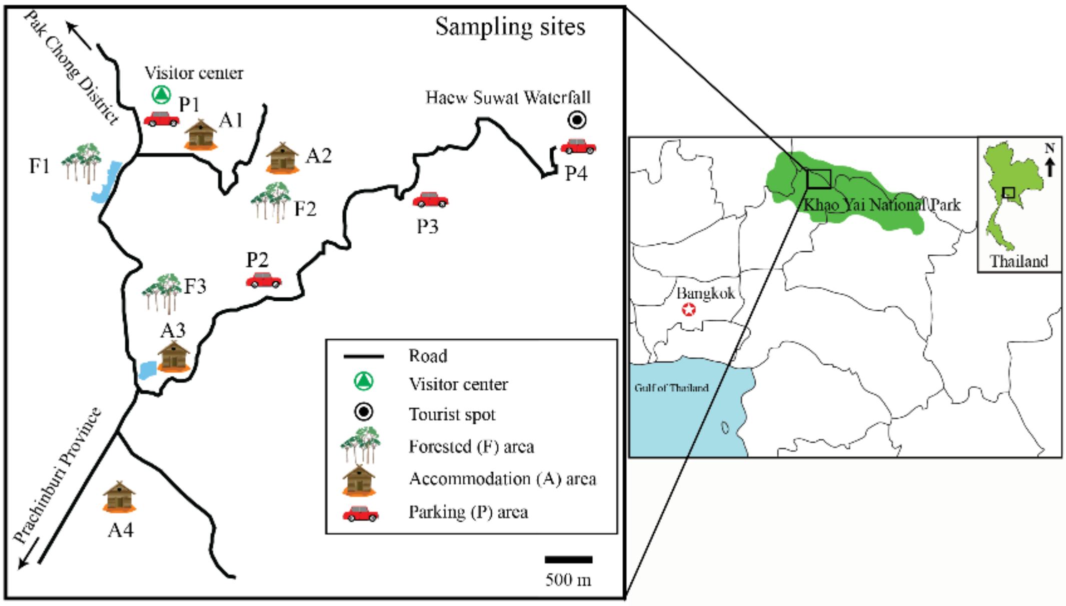

Figure 1. Location of eleven sampling sites in the forested (F), accommodation (A), and parking (P) areas in Khao Yai National Park in Thailand.

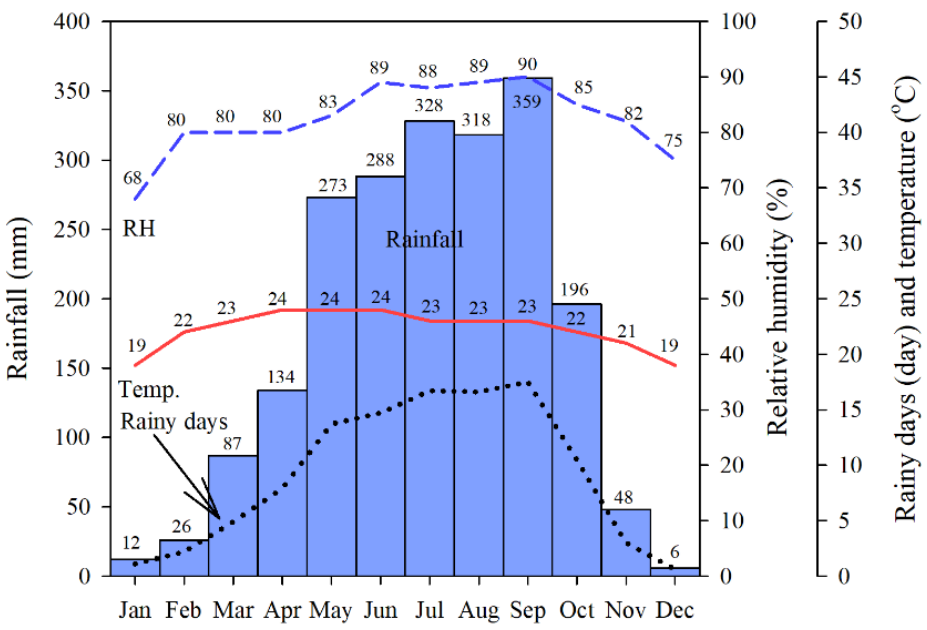

Figure 2. Monthly average climatic conditions in Khao Yai National Park include temperature (temp., solid red line), cumulative rainfall (blue bars) and rainy days (dotted black line), which were averaged from 1994 to 2014 (modified from Brockelman et al., 2017), and monthly average relative humidity (RH, dashed blue line), which was measured at the canopy of the tropical rain forest near the Khao Yai Meteorological Station from 2013 to 2014 (Mongkol Phaengphech, unpublished data).

2.2 Lichen collection and sampling sites

The native (*in situ*) thalli of the epiphytic foliose (lobe-like) lichen *P. tinctorum* (Figure 4) were collected early in the rainy season on June 2, 2018. This lichen species was selected because it was found at all sampling sites and was easy to identify and collect. The zonation of a lichen thallus probably shows different element concentrations due to different ages (Bargagli and Mikhailova, 2002); therefore, only the peripheral parts of the thalli, approximately 2-4 cm from the lobe tips, were collected. This zone corresponds to 2-3 years (Wannalux, 2014); thus, it should represent element accumulations during the last 2-3 years. Because the same tree species cannot be observed at all sampling sites, the lichen samples were then picked up from various tree species, on 3-5 trees, approximately 2-4 meters above the ground, at each of the eleven sampling sites in the forested (F1 to F3), accommodation (A1 to A4) and parking (P1 to P4) areas (Table 1, Figure 1), with 10-15 thallus fragments each (ca. 2-3 g air-dry weight, and 1-2 fragments from each thallus). Samples from each site were then divided into 5 portions for chemical analysis. These areas were chosen based on their traffic levels, which were estimated based on the intensity of motor vehicles passing through: 0 (no traffic, forested), 1 (low-moderate traffic, accommodation) and 2 (moderate-high traffic, parking). At the forested sites, the samples were collected within the forests at least 1 km from nearby roads. At the accommodation sites, the samples were taken at the roadside within the areas, and at the parking sites, the samples were picked up at the center of the areas.

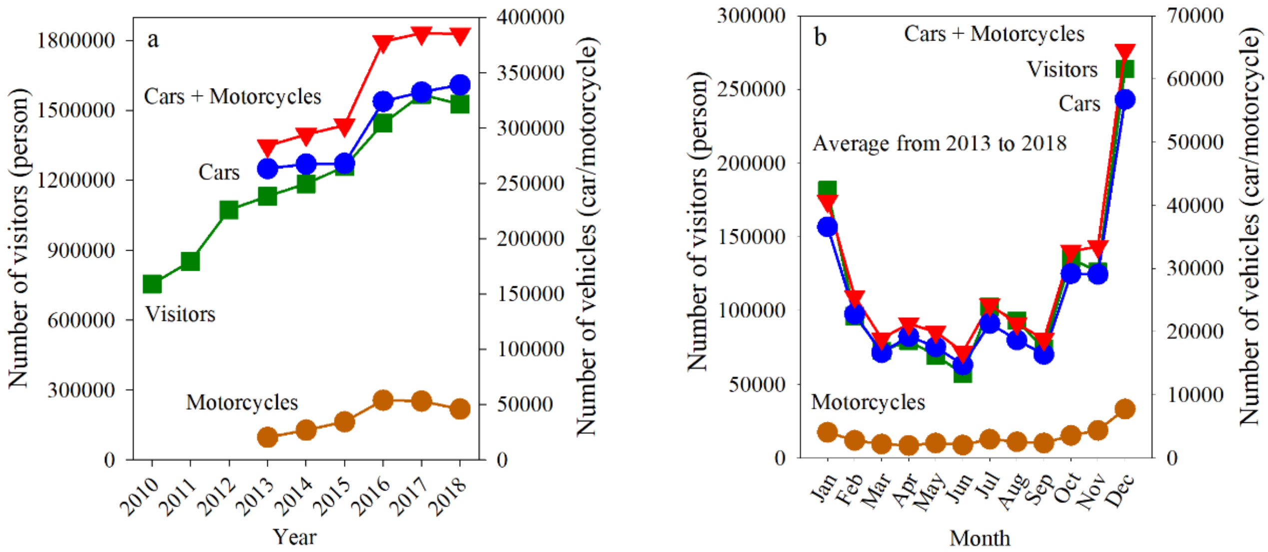

Figure 3. Annual (a) and monthly (b) number of visitors and motor vehicles in Khao Yai National Park. The brown circles represent motorcycles, the blue circles represent cars, the red triangles represent both types of vehicles, and the green squares represent visitors (Department of National Parks, Wildlife and Plant Conservation, 2019).

Figure 4. The lichen sample and sampling site. (a) the epiphytic lichen *Parmotrema tinctorum* (Despr. ex Nyl.) Hale, and (b) collecting lichen samples on a tree at a sampling site in the parking area in KYNP.

Table 1. Description of the sampling sites in Khao Yai National Park in Thailand.

Sampling mode	Sampling site	Latitude Longitude	Local name	Elevation (m.a.s.l.)	Traffic level
Forested (F)	F1	14º25´58´´N 101º21´59´´E	Mo Singto	803	0 (no traffic)
	F2	14º25´50´´N 101º23´04´´E	Golf Course	738	0
	F3	14º25´11´´N 101º22´25´´E	Nong Khing	758	0

Table 1. Description of the sampling sites in Khao Yai National Park in Thailand (cont.).

Sampling mode	Sampling site	Latitude Longitude	Local name	Elevation (m.a.s.l.)	Traffic level
Accommodation (A)	A1	14º26´01´´N 101º22´47´´E	Suratsawadee Young Camp	722	1 (low-moderate)
	A2	14º26´07´´N 101º23´04´´E	Tiewthus Zone	771	1
	A3	14º24´52´´N 101º22´29´´E	Khao Yai Training Center 2	754	1
	A4	14º24´02´´N 101º22´09´´E	Thanarat Zone	766	1
Parking (P)	P1	14º26´17´´N 101º22´20´´E	Khao Yai National Park Office	741	2 (moderate-high)
	P2	14º25´23´´N 101º23´11´´E	Lam Ta Khong Camping Ground	725	2
	P3	14º25´52´´N 101º24´01´´E	Pha Kluai Mai Camping Ground	701	2
	P4	14º26´05´´N 101º24´52´´E	Haew Suwat Waterfall	651	2

2.3 Metal analysis

Lichen samples were processed in the Analytical Chemical Laboratory at Ramkhamhaeng University and carefully cleaned to remove extraneous materials such as mosses and barks. Analytical method for metals in the lichens was based on the procedure done by Sangiamdee (2014). Unwashed lichen material was immersed in liquid nitrogen and subsequently pulverized and homogenized with a ceramic mortar and pestle. It was then separated through a 500-µm sieve plate. Approximately 200 mg of lichen powder was mineralized with 2 mL of conc. HNO_3 in a block digestion system (AIM 600, Aim Lab, Australia) at 150 °C for 150 min. The concentrations of nine traffic-related metals, including As, Cd, Cr, Cu, Fe, Pb, Sb, V and Zn, were determined using inductively coupled plasma mass spectrometry (ICP-MS, NexION 300Q, PerkinElmer, USA). The analytical quality was assessed with the certified reference material BCR-482 (lichen, *Pseudevernia furfuracea*) and spike samples. The recoveries (n=7) ranged between 92.3% (Sb) and 99.5% (Cr). The analytical precision, expressed as percent relative standard deviation (%RSD), was less than 6% (n=7) for all analyzed metals.

2.4 Data interpretation

The concentration of each metal from each sampling site was compared with its background concentration to determine the variation from its baseline concentration. The background concentrations were obtained from the same lichen species (*P. tinctorum*), which were collected on various tree species in all seasons at KYNP (Boonpeng, 2016; Boonpeng et al., 2017b). The results were subsequently interpreted using bioaccumulation ratios (B ratio) (B ratio=mean concentration of an analyzed metal in a sampling site divided by mean background concentration of that metal): ≤1.0=absence of bioaccumulation, >1.0-2.1=low bioaccumulation, >2.1-3.4=moderate bioaccumulation, >3.4-4.9=high bioaccumulation, and >4.9=severe bioaccumulation (Cecconi et al., 2019).

2.5 Statistical analysis

The amount of each metal from all the sampling sites was tested for normality using Shapiro-Wilk's test ($p<0.05$). The metals with normal distributions (Cr and Cu) were examined using one-way ANOVA with Tukey's test for post hoc comparison, whereas those with non-normal distributions (As, Cd, Fe, Pb, Sb, V, Zn) were tested using the Kruskal-Wallis test for analyzing statistically significant differences ($p<0.05$). Spearman correlation was used to test the relationship between traffic levels and metal contents in the lichen samples. All statistical analyses were performed using SPSS V. 22 (IBM Corp, NY, USA), and graphs were constructed using SigmaPlot 11.0 (Systat Software, CA, USA).

3. RESULTS AND DISCUSSION

3.1 Metal concentrations in lichens

The concentrations of the nine traffic-related metals analyzed from the native lichen *P. tinctorum* at the eleven sampling sites in KYNP are shown in Table 2 and Figure 5. The data revealed that tourism had a minor impact on the atmospheric metal pollution in the park. Concentrations of most metals were not significantly different in the higher traffic intense areas (accommodation or parking) than in the no traffic intensity area (forested). However, Cr and V had significantly higher concentrations in the accommodation and parking areas than in the forested area (Figure 5, $p<0.05$). No metal showed a significantly positive correlation with the estimated traffic intensity. In addition, 88 (89%) out of 99 mean concentrations of all metals at all sampling sites were below or in the range of the background concentrations of the metals. All means of As, Cd, Fe, Pb and Zn could be acceptable as the baseline concentrations, while 5, 2, 2 and 2 mean values of Cr, Cu, Sb and V, respectively, exceeded the range of their baseline concentrations (Table 2). The highest concentrations of Cu and Sb were observed at the forested sites, and geogenic and biomass decomposition could be sources of these metals. Chromium and vanadium, which are metals related to motor vehicles, showed peak concentrations at the accommodation sites.

3.2 Bioaccumulation ratios

The bioaccumulation ratios (B ratios) reveal variation in each metal at each sampling site compared to its background concentration (Table 3). Based on the B ratios, most metals, 77.8%, demonstrated an absence of bioaccumulation, 17.2% of the metals demonstrated low bioaccumulation, only 5% of the metals demonstrated moderate bioaccumulation (Cr, Sb), and no metal demonstrated high or severe bioaccumulation (Table 3). According to their concentrations, Cr was moderately bioaccumulated at three accommodation sites (A1, A2, A4), while Sb occurred at 2 forested sites (F1, F2).

Table 2. Means and Standard Deviations (SD) (n=5) of 9 traffic-related metals in the native lichen *Parmotrema tinctorum* collected at eleven sampling sites in the Forested (F), Accommodation (A) and Parking (P) areas in Khao Yai National Park, and the background element concentrations (BECs) obtained from previous studies (Boonpeng, 2016; Boonpeng et al., 2017b).

Sampling site	Mean±SD (µg/g dry weight)								
	As	Cd	Cr	Cu	Fe	Pb	Sb	V	Zn
F1	0.15±0.04	0.07±0.06	1.6±0.8	5.2±1.0	222±80	0.6±0.7	0.11±0.16	0.74±0.20	13±5
F2	0.12±0.02	0.05±0.03	1.8±1.6	6.6±1.1	268±159	BDL	0.15±0.17	0.76±0.13	14±6
F3	0.15±0.02	0.07±0.04	2.7±0.8	2.8±1.3	201±43	2.1±1.8	0.04±0.03	0.92±0.31	14±5
A1	0.19±0.09	0.02±0.02	3.6±0.8	2.0±1.5	271±121	1.2±1.5	0.03±0.01	1.00±0.58	9±3
A2	0.13±0.02	0.05±0.03	3.8±0.7	3.0±2.0	265±48	2.3±0.7	0.02±0.02	0.97±0.28	10±3
A3	0.24±0.07	0.09±0.06	2.9±0.3	4.4±2.4	200±26	3.6±3.6	0.04±0.01	1.35±0.37	17±14
A4	0.33±0.16	0.09±0.06	3.4±1.0	4.4±3.3	411±258	2.1±1.8	0.06±0.04	2.02±2.06	7±9
P1	0.16±0.02	BDL	0.6±0.2	1.8±1.1	234±87	1.8±1.7	0.04±0.01	0.99±0.27	20±9
P2	0.17±0.03	0.08±0.07	1.8±0.7	6.2±0.6	353±87	1.8±1.0	0.02±0.02	1.09±0.19	17±5
P3	0.15±0.02	0.02±0.02	1.2±1.0	1.9±1.1	202±56	1.6±1.6	0.03±0.01	0.99±0.25	21±8
P4	0.11±0.04	BDL	BDL	1.1±0.1	246±106	1.7±1.7	0.02±0.01	1.22±0.56	9±4
Mean BEC	0.27	0.11	1.4	3.4	340	4.1	0.04	0.96	20
Range of BEC	0.16-0.35	0.04-0.15	0.4-2.1	1.4-5.6	211-450	1.1-6.8	0.02-0.08	0.44-1.25	11-26

BDL = Below Detection Limit, Cd = 0.013 µg/g, Cr = 0.100 µg/g, Pb = 0.07 µg/g.

Table 3. Bioaccumulation ratios (B ratios) of metals in the native lichen *Parmotrema tinctorum* at eleven sampling sites in the Forested (F), Accommodation (A) and Parking (P) areas in Khao Yai National Park.

Sampling site	B ratio								
	As	Cd	Cr	Cu	Fe	Pb	Sb	V	Zn
F1	0.5	0.6	*1.2*	*1.5*	0.7	0.1	**2.4**	0.8	0.7
F2	0.4	0.4	*1.3*	*1.9*	0.8	<0.07*	**3.4**	0.8	0.7
F3	0.6	0.7	*2.0*	0.8	0.6	0.5	0.9	1.0	0.7
A1	0.7	0.2	**2.6**	0.6	0.8	0.3	0.6	1.0	0.4
A2	0.5	0.4	**2.8**	0.9	0.8	0.6	0.4	1.0	0.5
A3	0.9	0.8	*2.1*	*1.3*	0.6	0.9	0.8	*1.4*	0.8

Table 3. Bioaccumulation ratios (B ratios) of metals in the native lichen *Parmotrema tinctorum* at eleven sampling sites in the Forested (F), Accommodation (A) and Parking (P) areas in Khao Yai National Park. (cont.).

Sampling site	B ratio								
	As	Cd	Cr	Cu	Fe	Pb	Sb	V	Zn
A4	*1.2*	0.8	**2.4**	*1.3*	*1.2*	0.5	*1.3*	*2.1*	0.3
P1	0.6	<0.013*	0.4	0.5	0.7	0.5	0.9	1.0	1.0
P2	0.6	0.8	*1.3*	*1.8*	1.0	0.4	0.3	*1.1*	0.9
P3	0.6	0.2	0.9	0.5	0.6	0.4	0.6	1.0	1.0
P4	0.4	<0.013*	<0.100*	0.3	0.7	0.4	0.4	*1.3*	0.5

Bioaccumulation ratio (B ratio): ≤1.0=absence of bioaccumulation (regular), >1.0-2.1=low bioaccumulation (italic), >2.1-3.4=moderate bioaccumulation (bold), >3.4-4.9=high bioaccumulation, and >4.9=severe bioaccumulation (Cecconi et al., 2019). Asterisk (*)=the value is not B ratio; it is the method detection limit of each element in µg/g.

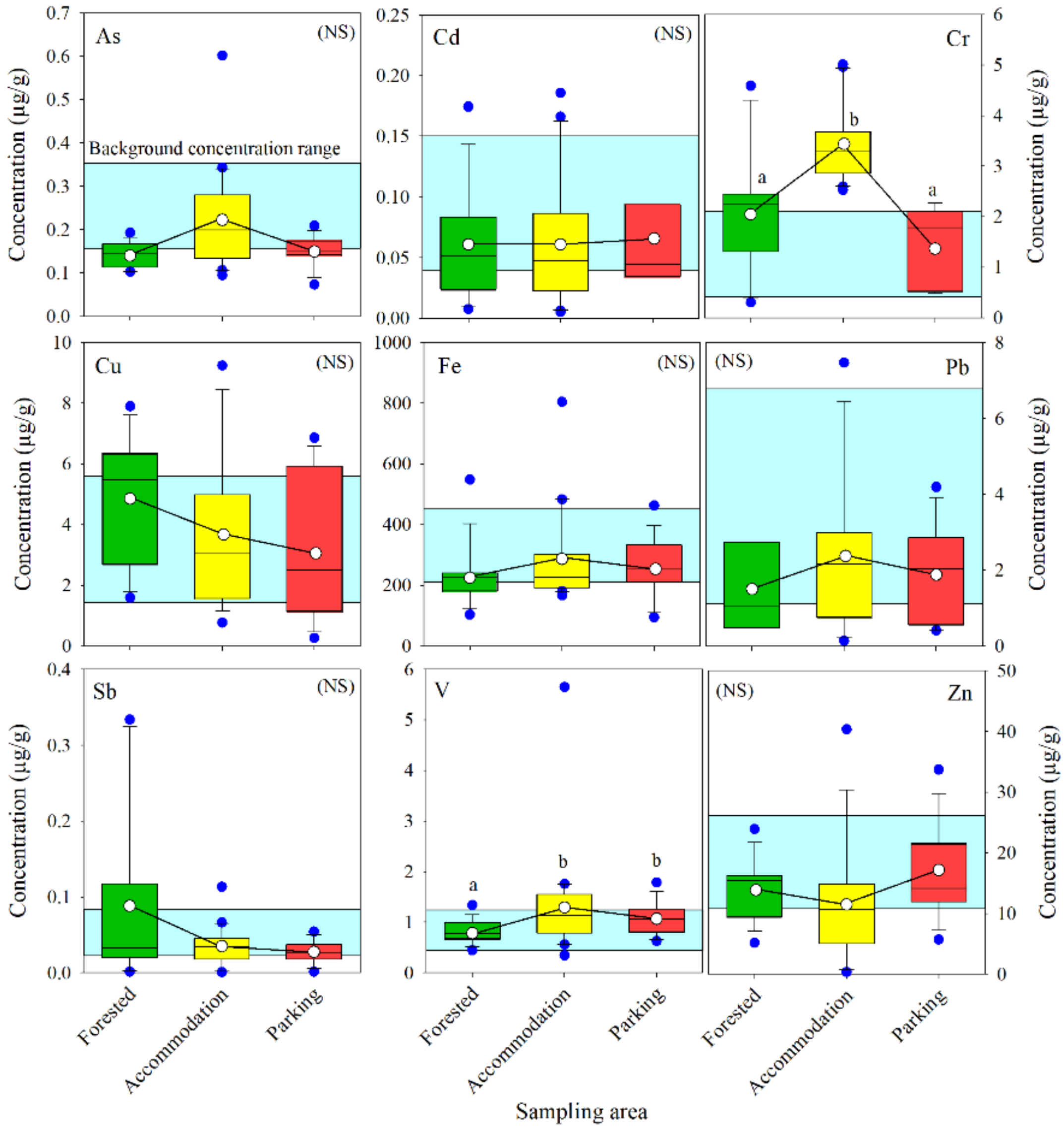

Figure 5. Box plots of metal concentrations in the lichen *Parmotrema tinctorum* in the forested (F), accommodation (A) and parking (P) areas. The horizontal bar within each box represents the median, while the empty circle with a connecting line represents the mean. The sky-blue area behind the boxes shows the range of the background concentration of each metal. Different letters on the boxes of Cr and V indicates statistically significant differences, and NS denotes nonsignificant differences among the study areas (p<0.05).

4. DISCUSSION

This study assessed the impact of tourism on atmospheric metal pollution in a natural park in Thailand. We found that the impact was modest because the concentrations of most traffic-related metals were comparable to their background concentrations. Only Cr and V seemed to be problems (pollute the air) in the park. Chromium is associated with the wearing of brakes (Liu et al., 2018; Sorbo et al., 2008). It had a significantly higher concentration in the accommodation area than in the forested area ($p<0.05$). However, the Cr content in the highest traffic intensity area (parking) was comparable to that in the lowest traffic intensity area (forested), indicating that there were additional sources of Cr in the accommodation area apart from vehicle traffic. There were reports that bark substrates can contribute to some element contents in lichen thalli growing in a forested area and the element concentrations in the barks were correlated with those in the lichens (Prussia and Killingbeck, 1991). However, amounts of the elements in the lichens were found in the range of their background concentrations. Thus, the higher Cr content in the lichen of this study than its background concentration observed at the accommodation sites was probably caused by the atmospheric composition rather than the bark differences. Regardless of the additional source of Cr, Cr has serious effects on living organisms, including humans. According to the ATSDR 2017 Substance Priority List (ATSDR, 2017), its toxicity, frequency, and potential for human exposure in the United States was ranked at no. 17. Health effects of Cr on the respiratory tract include irritation of the lining of the nose, runny nose, and breathing problems (asthma, cough, shortness of breath, and wheezing). The International Agency for Research on Cancer (IARC) has determined that Cr(VI) compounds are carcinogenic to humans. Adverse effects observed in animals following ingestion of Cr(VI) compounds occur in the stomach, small intestine (irritation and ulcer) and blood (anemia) (ATSDR, 2012a). Chromium is a highly toxic nonessential metal for microorganisms and plants. It causes deleterious effects on plant physiological processes such as photosynthesis, water relations and mineral nutrition (Shanker et al., 2005). In addition, exposure to Cr(VI) has caused a significant decline in physiological processes in the lichen *Pyxine cocoes* (Bajpai et al., 2015). Vanadium is related to fossil fuel combustion (Yemets et al., 2014) and continental dust (ATSDR, 2012b). It had a significantly higher concentration in the accommodation and parking areas than in the forested area. This metal was placed at no. 200 by ATSDR (ATSDR, 2017). Breathing air with vanadium pentoxide can result in coughing, and the IARC has determined that V is possibly carcinogenic to humans. Damage to the lungs, throat and nose, as well as a decrease in the number of red blood cells, have been observed in animals exposed to V compounds. Vanadium is a nonessential element for plants as well. It was found to retard the growth of Chinese green mustard and tomato plants (Vachirapatama et al., 2011) and induce a significant reduction in the phosphatase activity of lichens (LeSueur and Puckett, 1980). To reduce and remove these hazardous pollutants from the air, we recommend increasing tree density in the area (McDonald et al., 2016).

Several studies have reported that high quantities of metals in lichens in urban and/or industrial areas were associated to the local traffic density (Boonpeng et al., 2017b; Guidotti et al., 2009; Koz et al., 2010; Olowoyo et al., 2011; Sorbo et al., 2008). A number of studies have been carried out along highways in rural and natural areas to clarify and assess the impact of road traffic on atmospheric metal pollution (Liu et al., 2018; Yemets et al., 2014; Zhao et al., 2019). The previously mentioned study clearly suggests that motor vehicles can increase the amount of metals in areas with high traffic due to fossil fuel combustion, tire wear, brake abrasion, lubricating oils and vehicle component wear (Sorbo et al., 2008). Similar results should occur in KYNP where >300,000 cars and >45,000 motorcycles passed through yearly during the last three years. Nevertheless, only the results for Cr and V were in line with this assumption, while the results for the seven remaining metals (As, Cd, Cu, Fe, Pb, Sb, and Zn) were not. Notably, the methodology used in this study was appropriate for assessing the amounts of pollutants (metals) that were suspended in the air, and it may not be directly suitable for assessing pollutants that are on the ground or in the water. The metals As, Cd, Cu, Fe, Pb, Sb and Zn may have been released from vehicles but may have been suspended in the air for a short period of time. Tree leaves along the roads or in the sampling sites could have trapped the metals that were then leached out by rainwater, fog or dew. High and frequent rainfall in the area could help clean the air. High relative humidity does not allow metals that fall on the ground to resuspend in the air. In addition, ground level flora such as grasses and herbaceous plants act as biocovers on the ground, which could interrupt and reduce the resuspension of dust in the air.

Air pollutants clearly can be washed out of the air by rainfall; nevertheless, rainwater can both add and remove pollutants in lichen thalli (Adamo et al., 2003; Gallo et al., 2017). Because the lichens of this study were sampled in the early part of the rainy period (June), the results of this study could confirm that the impact of tourism on airborne metal concentrations in the park in the rainy period was low. However, the situation may be different in the dry period.

Based on the recently developed scales proposed by Cecconi et al. (2019), the B ratios of most metals from most of the sampling sites indicated the absence of bioaccumulation (77.8%), no B ratio of any metal indicated high or severe bioaccumulation. Although the interpretative scales were properly developed for research in Italy, they could be used in studies with lichens in other countries as well because they were based on a robust conceptual framework (Cecconi et al., 2019).

This study stated the atmospheric metal contamination in the natural park in Thailand. However, several other pollutants can be emitted from motor vehicles, such as nitrogen oxides (NO_x), sulfur oxides (SO_x) and polycyclic aromatic hydrocarbons (PAHs) (Gombert et al., 2003; Mateos and González, 2016; Nascimbene et al., 2014). Air pollution in the dry period may be different, and the impact of tourism on other environmental matrixes, i.e., pedosphere, hydrosphere and biosphere, should be assessed. Thus, periodic monitoring and an overall assessment of environmental quality for this UNESCO World Heritage Site is paramount because an increasing amount of motor vehicles have been passing through the park.

5. CONCLUSION

The impact of tourism on atmospheric metal pollution during the rainy period in KYNP was modest. Only Cr and V seemed to be problematic at some accommodation sites. The B ratios indicated that most metals at most sampling sites did not bioaccumulate. This study provides a model to assess the impact of tourism on environmental quality in natural parks. The model can be applied to other natural areas as they are also affected by tourism promotion policies.

6. ACKNOWLEDGMENTS

We would like to thank Khao Yai National Park for supporting the study and collection of lichen samples, and providing the number of visitors and vehicles. We are also thankful to graduate students at the Analytical Laboratory at the Department of Chemistry, Faculty of Science, Ramkhamhaeng University for helping with the metal analysis. This study was funded by the National Research Council of Thailand (NRCT).

REFERENCES

Adamo P, Giordano S, Vingiani S, Castaldo Cobianchi R, Violante P. Trace element accumulation by moss and lichen exposed in bags in the city of Naples (Italy). Environmental Pollution 2003;122:91-103.

Agency for Toxic Substances and Disease Registry (ATSDR). Public health statement for chromium [Internet]. 2012a [cited 2019 Jul 22]. Available from: https://www.atsdr.cdc.gov/PHS/PHS.asp?id=60&tid=17/.

Agency for Toxic Substances and Disease Registry (ATSDR). Public health statement for vanadium [Internet]. 2012b [cited 2019 Jul 22]. Available from: https://www.atsdr.cdc.gov/PHS/PHS.asp?id=274&tid=50/.

Agency for Toxic Substances and Disease Registry (ATSDR). The ATSDR 2017 substance priority list [Internet]. 2017 [cited 2019 Jul 22]. Available from: https://www.atsdr.cdc.gov/spl/index.html#2017spl/.

Bačkor M, Loppi S. Interactions of lichens with heavy metals. Biologia Plantarum 2009;53:214-22.

Bajpai R, Shukla V, Singh N, Rana TS, Upreti DK. Physiological and genetic effects of chromium (+VI) on toxitolerant lichen species, *Pyxine cocoes*. Environmental Science and Pollution Research 2015;22:3727-38.

Bargagli R, Nimis PL. Accumulation of inorganic contaminations. In: Nimis PL, Scheidegger C, Wolseley PA. editors. Monitoring with Lichens - Monitoring Lichens. The Netherlands: Kluwer Academic; 2002. p. 65-84.

Boonpeng C. The Effects of Atmospheric Deposition on Lichens for Assessing Environmental Quality at the Map Ta Phut Petrochemical Industrial Area, Thailand [dissertation]. Bangkok: Ramkhamhaeng University; 2016.

Boonpeng C, Polyiam W, Sriviboon C, Jhampasri T, Watthana S, Sangvichien E, Boonpragob K. Accumulation of inorganic pollutants and photosynthetic responses of transplanted lichens at distances away from an industrial complex. Thai Journal of Botany 2017a;9:181-91.

Boonpeng C, Polyiam W, Sriviboon C, Sangiamdee D, Watthana S, Nimis PL, Boonpragob K. Airborne trace elements near a petrochemical industrial complex in Thailand assessed by the lichen *Parmotrema tinctorum* (Despr. ex Nyl.) Hale. Environmental Science and Pollution Research 2017b;24: 12393-404.

Boonpeng C, Sriviboon C, Polyiam W, Sangiamdee D, Watthana S, Boonpragob K. Assessing atmospheric pollution in a petrochemical industrial district using a lichen-air quality index (LiAQI). Ecological Indicators 2018;95:589-94.

Brockelman WY, Nathalang A, Maxwell JF. Mo Singto Forest Dynamics Plot: Flora and Ecology. Pathum Thani, Thailand: National Science and Technology Development Agency (NSTDA); 2017.

Cecconi E, Fortuna L, Benesperi R, Bianchi E, Brunialti G, Contardo T, Nuzzo LD, et al. New interpretative scales for lichen bioaccumulation data: The Italian proposal. Atmosphere 2019;10:1-19.

Conti ME, Pino A, Botrè F, Bocca B, Alimonti A. Lichen *Usnea barbata* as biomonitor of airborne elements deposition in the Province of Tierra del Fuego (southern Patagonia, Argentina). Ecotoxicology and Environmental Safety 2009;72:1082-9.

Department of National Parks, Wildlife and Plant Conservation. Number of income, tourists and vehicles [Internet]. 2019 [cited 2019 Aug 9]. Available from: http://portal.dnp.go.th /Content/nationalpark?contentId=11191.

Gallo L, Corapi A, Apollaro C, Vespasiano G, Lucadamo L. Effect of the interaction between transplants of the epiphytic lichen *Pseudevernia furfuracea* L. (Zopf) and rainfall on the variation of element concentrations associated with the water-soluble part of atmospheric depositions. Atmospheric Pollution Research 2017;8:912-20.

Garty J, Garty-Spitz RL. Lichens and particulate matter: Inter-relations and biomonitoring with lichens. In: Upreti DK, Divakar PK, Shukla V, Bajpai R. editors. Recent Advances in Lichenology: Modern Methods and Approaches in Biomonitoring and Bioprospection. New Delhi, India: Springer; 2015. p. 47-85.

Gombert S, Asta J, Seaward MRD. Correlation between the nitrogen concentration of two epiphytic lichens and the traffic density in an urban area. Environmental Pollution 2003;123:281-90.

Guidotti M, Stella D, Dominici C, Blasi G, Owczarek M, Vitali M, Protano C. Monitoring of traffic-related pollution in a province of central Italy with transplanted lichen Pseudevernia furfuracea. Bulletin of Environmental Contamination and Toxicology 2009;83:852-8.

Käffer MI, Lemos AT, Apel MA, Rocha JV, Martins SM, Vargas VMF. Use of bioindicators to evaluate air quality and genotoxic compounds in an urban environment in Southern Brazil. Environmental Pollution 2012;163:24-31.

Kampa M, Castanas E. Human health effects of air pollution. Environmental Pollution 2008;151:362-7.

Koch NM, Branquinho C, Matos P, Pinho P, Lucheta F, Martins SM, Vargas VMF. The application of lichens as ecological surrogates of air pollution in the subtropics: A case study in South Brazil. Environmental Science and Pollution Research 2016;23:20819-34.

Koz B, Celik N, Cevik U. Biomonitoring of heavy metals by epiphytic lichen species in Black Sea region of Turkey. Ecological Indicators 2010;10:762-5.

LeSueur P, Puckett KJ. Effect of vanadium on the phosphatase activity of lichens. Canadian Journal of Botany 1980;58:502-4.

Liu R, Zhang Z, Shen J, Wang Z. Analysis of metal content and vertical stratification of epiphytic mosses along a Karst Mountain highway. Environmental Science and Pollution Research 2018;25:29605-13.

Loppi S. Lichens as sentinels for air pollution at remote alpine areas (Italy). Environmental Science and Pollution Research 2014;21:2563-71.

Louwhoff HJJS, Elix JA. The lichens of Rarotonga, Cook Islands, South Pacific Ocean II: Parmeliaceae. Lichenologist 2000;32:49-55.

Mateos AC, González CM. Physiological response and sulfur accumulation in the biomonitor Ramalina celastri in relation to the concentrations of SO_2 and NO_2 in urban environments. Microchemical Journal 2016;125:116-23.

McDonald R, Kroeger T, Boucher T, Longzhu W, Salem R, Adams J, et al. Planting Healthy Air. USA: The Nature Conservancy; 2016.

Nascimbene J, Tretiach M, Corana F, Lo Schiavo F, Kodnik D, Dainese M, Mannucci B. Patterns of traffic polycyclic aromatic hydrocarbon pollution in mountain areas can be revealed by lichen biomonitoring: A case study in the Dolomites (Eastern Italian Alps). Science of the Total Environment 2014;475:90-6.

Ohmura Y, Matsukura K, Abe J-iP, Hosaka K, Tamaoki M, Dohi T, Kakishima M, et al. 137Cs concentrations in foliose lichens within Tsukuba-city as a reflection of radioactive fallout from the Fukushima Dai-ichi Nuclear Power Plant accident. Journal of Environmental Radioactivity 2015;141:38-43.

Olowoyo J, van Heerden E, Fischer JL. Trace element concentrations from lichen transplants in Pretoria, South Africa. Environmental Science and Pollution Research 2011;18:663-68.

Pawlik-Skowrońska B, Bačkor M. Zn/Pb-tolerant lichens with higher content of secondary metabolites produce less phytochelatins than specimens living in unpolluted habitats. Environmental and Experimental Botany 2011;72:64-70.

Pawlik-Skowrońska B, Purvis OW, Pirszel J, Skowroński T. Cellular mechanisms of Cu-tolerance in the epilithic lichen Lecanora polytropa growing at a copper mine. Lichenologist 2006;38:267-75.

Phumsathan S. Environmental Impacts of Tourism in Khao Yai National Park, Thailand [dissertation]. Texas: Texas A and M University; 2010.

Port RK, Käffer MI, Schmitt JL. Morphophysiological variation and metal concentration in the thallus of *Parmotrema tinctorum* (Despr. ex Nyl.) Hale between urban and forest areas in the subtropical region of Brazil. Environmental Science and Pollution Research 2018;25:33667-77.

Prussia CM, Killingbeck KT. Concentrations of ten elements in two common foliose lichens: Leachability, seasonality, and the influence of rock and tree bark substrates. Bryologist 1991;94:135-42.

Sangiamdee D. Validation of Sample Preparation Methods for Determination of Metal Accumulation in Lichen *Parmotrema tinctorum* by Inductively Coupled Plasma Mass Spectrometry (ICP-MS) [dissertation]. Bangkok: Ramkhamhaeng University; 2014.

Shanker AK, Cervantes C, Loza-Tavera H, Avudainayagam S. Chromium toxicity in plants. Environment International 2005;31:739-53.

Sorbo S, Aprile G, Strumia S, Castaldo Cobianchi R, Leone A, Basile A. Trace element accumulation in *Pseudevernia furfuracea* (L.) Zopf exposed in Italy's so called Triangle of Death. Science of the Total Environment 2008;407:647-54.

Spellerberg IF. Ecological effects of roads and traffic: A literature review. Global Ecology and Biogeography Letters 1998;7: 317-33.

Vachirapatama N, Jirakiattikul Y, Dicinoski G, Townsend AT, Haddad PR. Effect of vanadium on plant growth and its accumulation in plant tissues. Songklanakarin Journal of Science and Technology 2011;33:255-61.

Wannalux B. The Growth and Longevity of Tropical Lichens of Khao Yai National Park [dissertation]. Bangkok: Ramkhamhaeng University; 2014.

Yemets OA, Solhaug KA, Gauslaa Y. Spatial dispersal of airborne pollutants and their effects on growth and viability of lichen transplants along a rural highway in Norway. Lichenologist 2014;46:809-23.

Zhao L, Zhang C, Jia S, Liu Q, Chen Q, Li X, Liu X, et al. Element bioaccumulation in lichens transplanted along two roads: The source and integration time of elements. Ecological Indicators 2019;99:101-7.

Landsat Time-series Images-based Urban Heat Island Analysis: The Effects of Changes in Vegetation and Built-up Land on Land Surface Temperature in Summer in the Hanoi Metropolitan Area, Vietnam

Thanh Tien Nguyen*

Faculty of Surveying, Mapping and Geographic Information, Hanoi University of Natural Resources and Environment, Hanoi, Vietnam

ARTICLE INFO

Received: 23 Sep 2019
Received in revised: 2 Dec 2019
Accepted: 27 Dec 2019
Published online: 17 Feb 2020
DOI: 10.32526/ennrj.18.2.2020.17

Keywords:
Urban heat island/ Land surface temperature/ Vegetation/ Built-up land/ Landsat images/ Hanoi (Vietnam)

*** Corresponding author:**
E-mail: tdgis_ntthanh@163.com

ABSTRACT

Rapid and unplanned urbanization leads to temperature rise, urban vegetation decrease and built-up land increase, forming an urban heat island (UHI). This study investigated the effects of changes in vegetation and built-up land on land surface temperature (LST) in summer, based on remotely sensed images. LST was first retrieved by means of the Radiative Transfer Model (RTM). Scatter-plots and an univariate linear regression model (ULRM) were first employed to independently measure the influence of NDVI on LST, and of NDBI on LST, respectively. In order to assess the effects of changes in vegetation and built-up land on LST, a multivariate linear regression model (MLRM) was finally employed to improve the accuracy of the predicted model in the identification of the joint effect of both the normalized difference vegetation index (NDVI) and the normalized difference built-up index (NDBI) on LST. The result from the case from the Hanoi Metropolitan Area (HMA), Vietnam using Landsat-5 TM and Landsat-8 OLI/TIRS time-series images during the 1996-2016 period shows that there exists a negative effect of built-up land and a positive effect of vegetation on LST. In addition, indications of intensifying UHI effects were detected in the HMA, especially tending to expand faster and wider to the parts of western, north-western and south-western HMA during the 1996-2007 period. These findings suggest that vegetation weakens the effect of UHIs, whereas, built-up land greatly strengthens the effect of UHIs in the HMA.

1. INTRODUCTION

An UHI is a metropolitan area which is defined by the huge differences between urban and suburban/rural temperatures (Liu and Zhang, 2011). Based on the spatial occurrence, UHIs were classified into two types: surface urban heat islands (SUHIs) and atmospheric urban heat islands (AUHIs) (Ranagalage et al., 2017). Estoque et al. (2017) indicated SUHIs can be detected based on LST, whereas, AUHIs can be identified through air temperature. SUHIs tend to be strongest during the day when the sun is shining (Ranagalage et al., 2017). The buildings, concrete, asphalt, industrial activities and heat from vehicles, factories and air conditioners in urban areas are the main causes of UHIs (Liu and Zhang, 2011). A few studies have discovered the main negative impacts of SUHIs on humans and environments such as the weakening of living environments and an increased mortality rate (Ranagalage et al., 2017), the adverse health effects (Tan et al., 2010), and the worsen local weather and climate (Liu and Zhang, 2011). Thus, the analysis of UHIs plays an important role in the urban environmental protection and sustainability. UHIs mainly appear around high LST areas which are governed by high surface heat fluxes and obviously affected by urbanization (Dousset and Gourmelon, 2003; Sun et al., 2010; Liu and Zhang, 2011). A higher level of exchange of these surface heat fluxes was found with more vegetated and built-up areas (Oke, 1982). Therefore, in order to understand the formation of UHIs in UHI studies, it becomes vital to explore the effects of both vegetation coverage and built-up land on LST.

Citation: Nguyen TT. Landsat time-series images-based urban heat island analysis: The effects of changes in vegetation and built-up land on land surface temperature in summer in the Hanoi metropolitan area, Vietnam. Environ. Nat. Resour. J. 2020;18(2):177-190. DOI: 10.32526/ennrj.18.2.2020.17

Traditionally, UHI analysis can be carried out based on LSTs measured at meteorological stations (Lu et al., 2009). However, the uneven distribution and limited conditions of these in situ measurements may result in the measured LSTs not fully representing the distribution of LSTs across the big region (Liu and Zhang, 2011). Another limitation of this approach is the near impossibility of capturing enough LSTs over a large area (Vu and Nguyen, 2018b). The occurrences of remote sensing technology overcome those limitations of traditional methods. Compared to LST traditional measurements, remotely sensed images have their advantages of high-resolution, wide-coverage and intensive-points, etc. (Liu and Zhang, 2011), which make UHI studies become easier. UHI studies are mainly based on the spatial distribution of LST. The first studies of UHIs based on satellite-derived LST retrieval were carried out mainly using low-resolution NOAA AVHRR images (Balling and Brazel, 1988; Gallo et al., 1993). Since remotely sensed images of high resolution thermal infrared (TIR) satellite sensors such as 120-m resolution Landsat MSS and TM, 60-m resolution ETM+, and recently 100-m resolution TIRS started to be freely distributed, these data have also been widely utilized to derive LSTs for UHI studies (Liu and Zhang, 2011; Lu et al., 2009; Ranagalage et al., 2017; Ongsomwang et al., 2018; Sanecharoen et al., 2019). With the help of geographic information systems (GIS) techniques, many previous SUHI studies have successfully estimated the effects of urban landscape composition and pattern on LST (Ranagalage et al., 2017; Bokaie et al., 2016; Estoque et al., 2017; Kikon et al., 2016; Liu and Zhang, 2011; Weng et al., 2004). NDVI and NDBI have been considered as the most commonly used landscape indices for examining the spatial and temporal variations of LST (Kumar and Shekhar, 2015; Ranagalage et al., 2017). The first studies on the relationship between LST and vegetation cover using the NDVI were carried out by Goward et al. (2002) and Weng (2001). Later, both these indices were used as land cover types (Zhang et al., 2009). Recent studies have shown that there exists a negative correlation of LST with NDVI and a positive correlation of LST with NDBI (Liu and Zhang, 2011; Ranagalage et al., 2017; Sanecharoen et al., 2019). In spite of these significant contributions, the main limitation of previous work is that the used method, the ULRM, fails to estimate the interrelationship between variables, thus, leading to low accuracy of the predicted model in the evaluation of the joint effect of both vegetation cover and built-up land on LST. In order to solve this problem, the MLRM is employed to measure the interaction effects of two variables on the dependent variable instead. Therefore, this research examined the joint impact of both vegetation and built-up land on LST by means of the MLRM instead, using Landsat time-series data acquired at three-time points in summer in the period of 1996-2016 of the HMA (Vietnam). Specific objectives of this study are: (1) to derive LST, NDVI and NDBI from Landsat TM and OLI/TIRS data and analyze their spatio-temporal variations; (2) to apply the MLRM to investigate the joint-effects of both NDVI (vegetation) and NDBI (built-up land) on LST.

2. METHODOLOGY

2.1 Description of the study area

The research was conducted in the HMA, Vietnam, which is located at 20°54'34.14"-21°6'22.69" south latitude and 105°42'16.97"-105°56'21.48" east longitude (Figure 1) with an area of 273.9 km^2. Vietnam has been experiencing dramatic economic growth since the Doi Moi Policy started in 1986 (Logan, 2005) which has greatly contributed to the rapid urbanization in Hanoi city (Tsunoda et al., 2014), particularly after Hatay province, Vinhphuc province's Melinh district and the four communes of Luongson district, Hoabinh province were merged into the metropolitan area of Hanoi from August 2008 (Hiep, 2014). Therefore, rapid urban development displaced vegetation in many areas, especially in the HMA. Hanoi is now the largest city in Vietnam with an estimated population of 8.05 million and a population density of 2,300 people for every square kilometer in 2019. It has a tropical monsoon climate with wet and dry seasons. The dry and wet seasons extend from November to April and from May to September, respectively (Garcia et al., 2006).

2.2 Data used

The remote sensing data used in the change detection should be obtained from a sensor system that acquires data at approximately the same time of day (Star et al., 1997) or at near anniversary dates to minimize inconsistencies in sun angle or phenology (Jensen, 2009). However, it is not possible to obtain extract (or near) anniversary dates in the HMA because of Landsat orbit changes and monthly average cloud cover of 72.4% (Lasko et al., 2018).

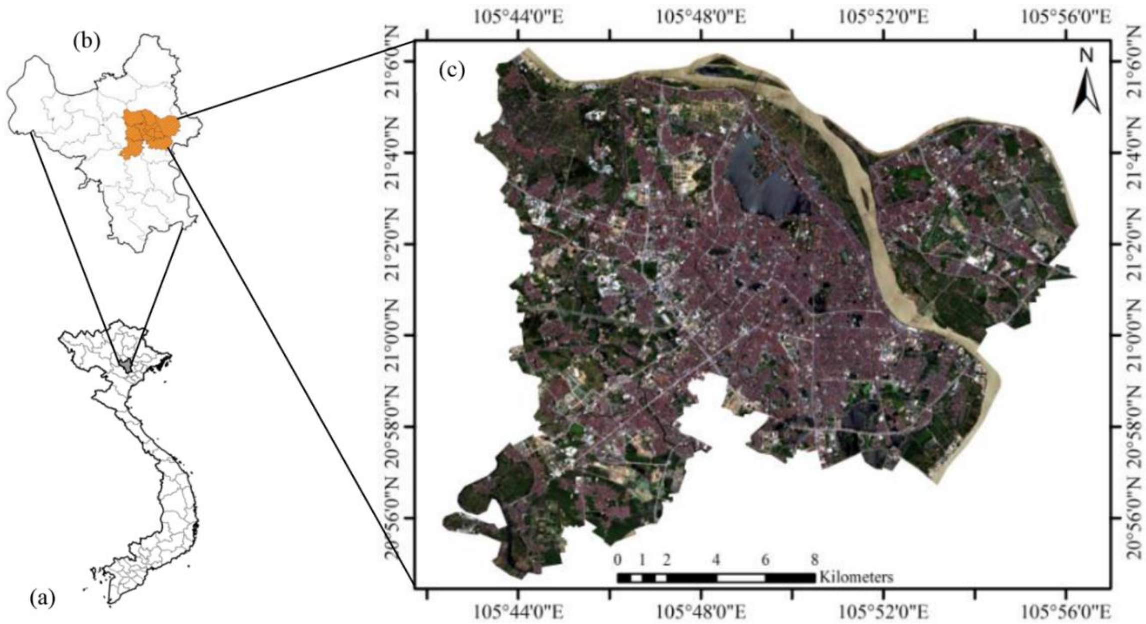

Figure 1. The study area: (a) Vietnam, (b) Hanoi city, and (c) the Hanoi metropolitan area (2016 Landsat-8 OLI true color composite)

Therefore, daytime Landsat images (path 127, row 045/046) with 30-m spatial resolution freely distributed by the U.S. Geological Survey acquired in the wet (summer) season of 1996, 2007 and 2016 were collected (Table 1) in this study. All the Landsat images projected in the UTM Zone N48 and WGS 1984 ellipsoid datum were the Precision and Terrain Correction products (Vu and Nguyen, 2018b). The multispectral bands of the Landsat-5 TM and Landsat-8 OLI data have 30-m spatial resolution, while the thermal band 6 of Landsat-5 TM and thermal bands 10 and 11 of Landsat-8 TIRS have 120-m and 100-m spatial resolution, respectively and were resampled to 30 meter pixels. In addition, reference data of a total of 400 sample points randomly selected from high resolution images in Google Earth Maps and the field survey data of nine air temperatures measured by meteorological stations (Table 2) were also collected for the accuracy assessment of built-up land and LST derived from Landsat images, respectively.

Table 1. Descriptions of Landsat-5 TM and Landsat-8 OLI/TIRS datasets

Sensor	Date of acquisition (Y-M-D)	Time of acquisition (hh:mm:ss)	Path/Row	Spatial resolution of bands (m)	Cloud cover (%)	Image quality
TM	1996-9-30	02:41:56.28	127/045	30	2.00	9/9
TM	1996-9-30	02:42:20.18	127/046	30	10.00	9/9
TM	2007-5-24	03:17:49.46	127/045	30	1.00	7/9
TM	2007-5-24	03:18:13.30	127/046	30	19.00	7/9
OLI, TIRS	2016-6-01	03:23:04.77	127/045	30	13.03	9/9
OLI, TIRS	2016-6-01	03:23:28.67	127/046	30	13.74	9/9

2.3 Identification of the relationship between LST, vegetation and built-up land

2.3.1 Image pre-processing

The image pre-processing process involves two steps. The first step involves the conversion of the DN data (Q_{cal}) to top of atmosphere (ToA) radiance ($L_{ToA,\lambda}$) using inflight sensor calibration parameters in the metadata file. The conversion of (Q_{cal})-to-($L_{ToA,\lambda}$) for Landsat-5 TM data (Chander et al., 2009; Vu and Nguyen, 2018a) and Landsat-8 OLI/TIRS data (Nguyen and Vu, 2019; Zanter, 2016) are performed using Equation (1) and (2), respectively:

$$L_{ToA,\lambda} = \left(\frac{L_{max,\lambda} - L_{min,\lambda}}{Q_{cal_{max}} - Q_{cal_{min}}}\right) \times (Q_{cal} - Q_{cal\_min}) + L_{min,\lambda} \quad (1)$$

Where; $L_{TOA,\lambda}$ is ToA spectral radiance [W/m^2·sr·µm] at the wavelength λ (µm); Q_{cal} is DN values; Q_{cal_min} and Q_{cal_max} are minimum and maximum DN values corresponding to $L_{min,\lambda}$ and $L_{max,\lambda}$, respectively; $L_{min,\lambda}$ and $L_{max,\lambda}$ are ToA spectral radiance [W/m^2·sr·µm].

$$L_{ToA,\lambda} = M_L Q_{cal} + \Delta_L \quad (2)$$

Where; $L_{ToA,\lambda}$ is ToA spectral radiance [W/(m^2·sr·µm)] at the wavelength λ (µm); M_L and Δ_L are the radiance multiplicative scaling factor and the radiance additive scaling factor for the bands, respectively; Q_{cal} is the DN value.

After the Q_{cal} -to- $L_{ToA,\lambda}$ conversion, the second step involves compensating for atmospheric effects for Landsat reflective bands using the FLAASH algorithm (Adler-Golden et al., 1999). The spectral radiance is determined using Equation (3) (Adler-Golden et al., 1998; Adler-Golden et al., 1999):

$$L^* = \left(\frac{A\rho}{1-\rho_e S}\right) + \left(\frac{B\rho_e}{1-\rho_e S}\right) + L_a^* \quad (3)$$

Where; ρ is the pixel surface reflectance; ρ_e is an average surface reflectance for the pixel and a surrounding region; S is the spherical albedo of the atmosphere; L_a^* is the radiance backscattered by the atmosphere; A and B are coefficients that depend on atmospheric and geometric conditions but not on the surface. The values of A, B, S and L_a^* are determined based on MODTRAN4 (Ahmadian et al., 2016). After the water retrieval, the spatially averaged reflectance ρ_e is estimated using Equation (4) (Adler-Golden et al., 1998; Adler-Golden et al., 1999):

$$L_e = \left(\frac{(A+B)\rho_e}{1-\rho_e S}\right) + L_a^* \quad (4)$$

2.3.2 Land surface temperature retrieval

Using the RTM-based method, LST can be retrieved from Landsat-5 using band 6 and Landsat-8 TIRS using band 10 with an accuracy of lower than 0.6 K and 1 K, respectively (Vu and Nguyen, 2018b). Therefore, in this study, this method was applied to obtain LST from Landsat-5/ Landsat-8 TIR data acquired in 2007 and 2016, respectively. LST in the TIR region can be retrieved using Equation (5) (Barsi et al., 2003; Vu and Nguyen, 2018b):

$$L_{ToA,\lambda} = \tau_\lambda\left[\varepsilon_\lambda B_{b,\lambda}(T_s) + (1-\varepsilon_\lambda)L_{atm,\lambda}^{\downarrow}\right] + L_{atm,\lambda}^{\uparrow} \quad (5)$$

Where; $L_{ToA,\lambda}$ is the TOA radiance [W/(m^2·sr·µm)] determined from Equation (1) and (2); ε_λ is the land surface emissivity (LSE); $B_{b,\lambda}(T_s)$ is the blackbody radiance [W/(m^2·sr·µm)] given by the Planck's law and T_s is the LST (Kelvin); $L_{atm,\lambda}^{\uparrow}$ is the upwelling atmospheric radiance [W/(m^2·sr·µm)]; $L_{atm,\lambda}^{\downarrow}$ is the downwelling atmospheric radiance [W/(m^2·sr·µm)] and τ_λ is the total atmospheric transmissivity between the surface and the sensor (Vu and Nguyen, 2018b).

In this study, the result of Sobrino et al. (2008) was used to estimate the LSE by means of the NDVI-based threshold approach. The LSE is calculated in three cases: (i) if NDVI<$NDVI_{soil}$ then the pixel is considered mainly covered by bare soil, and a mean value of 0.97 is assumed for the LSE of soil (ε_s) (Vu and Nguyen, 2018b); (ii) NDVI<$NDVI_{veg}$ if then the pixel corresponds to dense vegetation areas (fully vegetated), and the LSE of vegetation (ε_v) is given a value of 0.99 (Sobrino et al., 2008; Vu and Nguyen, 2018b); (iii) if $NDVI_{soil}$<NDVI<$NDVI_{veg}$ then each pixel is considered a mixing of bare soil and vegetation, and the LSE is estimated using (6):

$$\varepsilon_i = f_v \cdot \varepsilon_v + (1 - f_v) \cdot \varepsilon_s \quad (6)$$

Where; ε_i is the LSE of pixel i; ε_v and ε_s are the LSE of vegetation and soil; and f_v is the vegetation fraction retrieved from Equation (7). LST was finally retrieved using Equation (8):

$$f_v = \left(\frac{NDVI - NDVI_{soil}}{NDVI_{veg} - NDVI_{soil}}\right)^2 \quad (7)$$

Where; $NDVI_{soil}$ and $NDVI_{veg}$ are the NDVI values corresponding to bare soil and full vegetation cover, respectively.

$$T_s = \frac{K_2}{\ln\left[\frac{K_1}{B_{b,\lambda}(T_s)} + 1\right]} - 273.16 \quad (8)$$

Where; K_1 and K_2 are calibration constant 1 [W/(m^2·sr·µm)] and calibration constant 2 (Kevin), respectively; $B_\lambda(T_s)$ is the blackbody radiance [W/(m^2·sr·µm)]; and ln is the natural logarithm.

2.3.3 Vegetation coverage and built-up land estimation

The NDVI can be considered as indications of the presence of vegetation and amount or condition of vegetation on pixel basis (Orhan et al., 2014; Ranagalage et al., 2017), whereas, the NDBI is an index for extracting built-up areas (Zha et al., 2003). The positive NDBI values indicate built-up areas and those close to 0 indicate vegetation, while the negative values represent water bodies (Ranagalage et al., 2017). NDVI and NDBI are expressed as Equation (9) and (10), respectively:

$$\text{NDVI} = \frac{R_{NIR} - R_{RED}}{R_{NIR} + R_{RED}} \tag{9}$$

$$\text{NDBI} = \frac{R_{MIR} - R_{NIR}}{R_{MIR} + R_{NIR}} \tag{10}$$

Where; R_{RED}, R_{NIR}, and R_{MIR} are the surface reflectance of the red band (band 3 in Landsat-5 TM and band 4 in Landsat-8 OLI), of the near-infrared band (band 4 in Landsat-5 TM and band 5 in Landsat-8 OLI), and of the short wavelength infrared band (band 5 in Landsat-5 TM and band 6 in Landsat-8 OLI), respectively.

2.3.4 Identification of the relationship between LSTs, vegetation and built-up land

After the values of LST, NDVI, and NDBI extracted from multi-spectral Landsat-5 TM and Landsat-8 OLI/TIRS images, a total of 304,306 points converted from raster data were used for the identification of the effects of changes in vegetation and built-up land on LST in the HMA. In this process, in order to investigate these effects, scatter-plots and the ULRM were first employed to independently measure the influence of NDVI on LST, and of NDBI on LST. As discussed above, the ULRM fails at estimating the interrelationship between variables, thus, leading to low accuracy of the predicted model in the evaluation of the joint effect of both vegetation and built-up land on LST. Therefore, the MLRM was finally applied to improve the accuracy of the predicted model in the identification the joint effect of both NDVI and NDBI on LST.

3. RESULTS AND DISCUSSION

3.1 LST in 1996, 2007 and 2016

Data from Table 2 illustrates the minimum and maximum differences in values between estimated LSTs and the meteorological air temperatures (MATs) were 1.1-4.2 °C, 0.9-4.0 °C and 0.6-4.0 °C at the three time points, respectively. These positive differences are similar to those reported in previous studies of Chan et al. (2018) and Rhee and Im (2014) that the day LST is higher than air temperature. The two main metrics, root mean square error (RMSE) and mean absolute error (MAE), were determined with the values of 2.3 °C and 2.0 °C on 30 September 1996, 2.6 °C and 2.6 °C on 24 May 2007, and 2.2 °C and 1.9 °C on 01 June 2016. In addition, regression analysis between Landsat-retrieved LSTs and the MATs is shown in scatter-plots in Figure 2. Examinations of the results show that there existed significant high correlation coefficients of 0.911, 0.897 and 0.845 between LSTs and MATs corresponding with relatively high R-squared values of 0.831 in 1996, 0.714 in 2007 and 0.804 in 2016 (statistically significant at the 0.05 level). RMSE and MAE values ranged between 2.2 °C and 2.6 °C, and 1.9 °C and 2.6 °C and high correlation coefficients and R-square values for regression models indicate that these LSTs retrieved from Landsat-5/ Landsat-8 TIR images can be used for the investigation the effects of changes in vegetation and built-up land on LST in this study.

Table 2. Summary of validation results for LSTs obtained from Landsat-5/ Landsat-8 TIR data.

Station names	H (m)	Temperatures (°C)														
		1996-9-30					2007-5-24					2016-6-01				
		T_2	T_3	T_{2-42}	T_{L5}	Dif.	T_3	T_4	T_{3-18}	T_{L5}	Dif.	T_3	T_4	T_{3-23}	T_{L8}	Dif.
Bacgiang	7.501	26.5	28.4	27.8	31.1	3.3	33.1	34.2	33.4	37.1	3.7	33.5	34.3	33.8	34.4	0.6
Sondong	58.473	27.8	29.7	29.1	33.3	4.2	34.7	36.0	35.1	39.1	4.0	34.3	34.8	34.5	38.5	4.0
Lucngan	14.646	25.7	28.0	27.3	28.5	1.2	34.6	35.4	34.8	38.7	3.9	34.4	35.0	34.6	37.6	3.0
Hiephoa	20.565	27.1	28.7	28.2	30.0	1.8	32.8	34.6	33.3	35.6	2.3	34.0	35.1	34.4	37.4	3.0
Langson	257.881	25.3	27.1	26.6	27.8	1.2	32.0	32.9	32.3	35.0	2.7	32.1	32.9	32.4	35.2	2.8
Huulung	41.479	-	-	-	-	-	33.6	35.3	34.1	35.5	1.4	32.8	33.4	33.0	34.1	1.1
Thatkhe	162.452	24.1	26.8	26.0	28.1	2.1	31.8	33.2	32.2	34.1	1.9	32.7	34.3	33.3	34.0	0.7

Table 2. Summary of validation results for LSTs obtained from Landsat-5/ Landsat-8 TIR data (cont.).

Station names	H (m)	Temperatures (°C)														
		1996-9-30					2007-5-24					2016-6-01				
		T_2	T_3	$T_{2\text{-}42}$	T_{L5}	Dif.	T_3	T_4	$T_{3\text{-}18}$	T_{L5}	Dif.	T_3	T_4	$T_{3\text{-}23}$	T_{L8}	Dif.
Bacson	395.081	25.3	27.3	26.7	27.8	1.1	31.9	33.4	32.4	33.2	0.9	31.1	31.8	31.4	32.5	1.1
Dinhlap	190.645	25.3	27.8	27.1	28.3	1.3	33.1	34.0	33.4	35.7	2.3	33.0	33.6	33.2	34.5	1.3
Accuracies		RMSE =				2.3	RMSE =				2.6	RMSE =				2.2
		MAE =				2.0	MAE =				2.6	MAE =				1.9

Notes: H are heights above mean sea level of meteorological stations in meters; T_2, T_3 and T_4 are the air temperatures measured by six meteorological stations at 1.5 m above ground at 2 AM, 3 AM and 4 AM (GMT) corresponding to local times of 9 AM, 10 AM and 11 AM in Vietnam; $T_{2\text{-}42}$, $T_{3\text{-}18}$ and $T_{3\text{-}23}$ are the interpolated air temperatures on 30th September 1996 at 2:42 AM, on 24th May 2007 at 3:18 AM and on 01 June 2016 at 3:23 AM from meteorological data monitored at from 2 AM to 3 AM and at from 3 AM to 4 AM; T_{L5}, T_{L8} and Diff. are LSTs retrieved from Landsat-5/ Landsat-8 TIR data and the value differences between LSTs and interpolated MATs, respectively; - represents no available data.

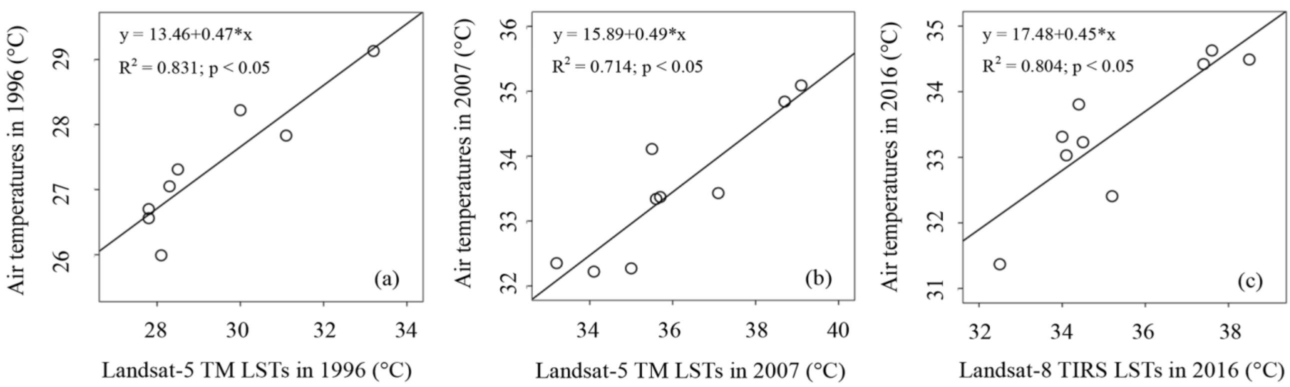

Figure 2. Scatter-plots of between meteorological air temperatures and LSTs obtained from Landsat-5/ Landsat-8 TIR images

The distribution of LSTs retrieved from TIR bands of 1996 and 2007 Landsat-5, and 2016 Landsat-8 images in the HMA is shown in Figures 3 and 4. The descriptive statistics of LSTs are summarized in Table 3. The LST in HMA ranged from 20.02 °C to 38.01 °C with a mean of 26.45 °C on 30 September 1996 (02:41:56.28 GMT). LST varied in the range of from 18.72 °C to 54.83 °C with a mean of 38.81 °C on 24 May 2007 (03:17:49.46 GMT), whereas, on 01 June 2016 (03:23:04.77 GMT), LST ranged from 26.83 °C to 66.93 °C with a mean value of 42.93 °C. In general, higher LSTs were detected mostly in the core urban areas of the HMA. Small areas of high LSTs were mostly found in the center in 1996 (Figure 3(a)). By 2007 and 2016, however, high LST areas had greatly expanded towards the western, north-western and south-western parts of the HMA. A recent study carried out by Nguyen et al. (2019) also indicated that, by 2009 and 2016, Hanoi's residential areas developed and expanded to these directions of the city. Meanwhile, the area of high LSTs was almost unchanged in the period of 2007-2016 (Figure 3(b) and (c)). Data from histograms and boxplots in Figure 4 demonstrates that the distribution of the LST was strongly right-skewed in 1996 dominated by many very high LSTs, left-skewed in 2007 and fairly balanced in 2016. LSTs were mainly concentrated in the range of 24 °C-30 °C in 1996, 30 °C-47 °C in 2007 and 36 °C-55 °C in 2016. It can be clearly seen that the high LST areas had been increasing rapidly during 1996-2016 and tends to expand towards the western, north-western and south-western parts. The increase of buildings, concrete, asphalt in residential areas in the city centre and the northwest, and newly built areas of residential housing and industrial activities in the west and southwest during 1999-2016 (Nguyen et al., 2019) may have accounted for the increasing of LSTs in these directions. In addition, the rapid increase of vehicles such as motorcycles and cars (Tuan and Shimizu, 2005) and of air conditioners from zero to 0.13 million units during 1985-2005 (Nguyen et al., 2009) also greatly contributed heat transferred to the land surface of the Earth.

Table 3. Descriptive statistics of the LST, NDVI and NDBI in the HMA.

Date	Time (GMT)	Minimum	Median	Mean	Maximum
1996-9-30	02:41:56.28	20.02	26.01	26.45	38.01
2007-5-24	03:23:04.77	18.72	39.17	38.81	54.83
2016-6-01	03:17:49.46	26.83	42.83	42.93	66.93

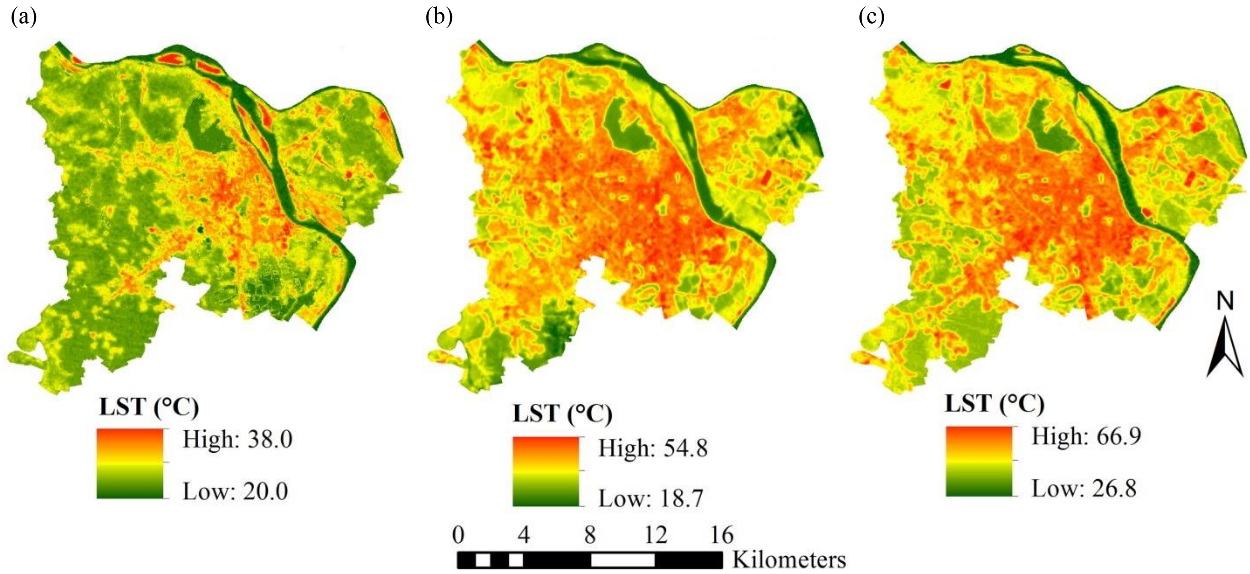

Figure 3. Land surface temperatures in 1996, 2007 and 2016

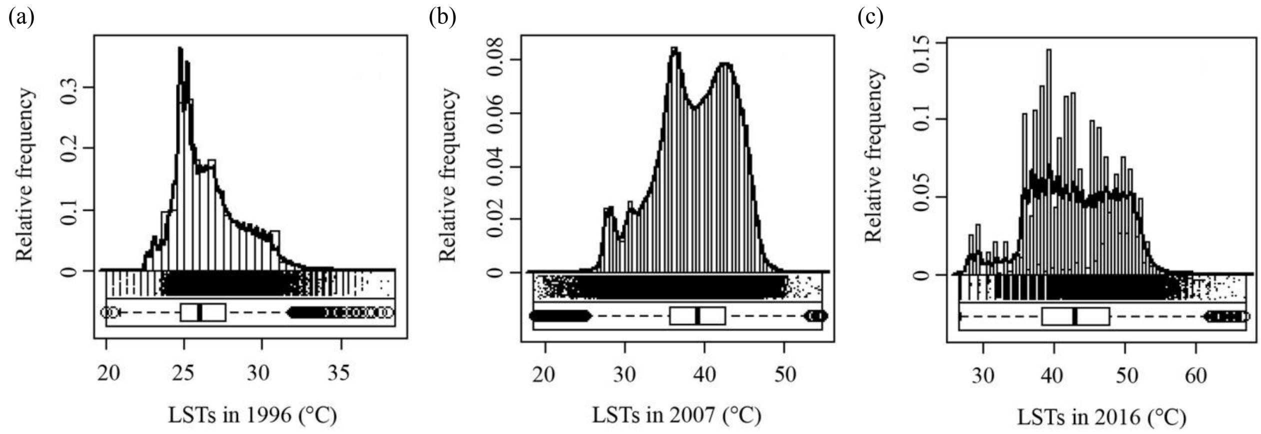

Figure 4. Histograms, density traces, 1-D scatter-plot and box-plots of LSTs retrieved in 1996, 2007 and 2016

3.2 NDVI in 1996, 2007 and 2016

The distribution of NDVI in the HMA in 1996, 2007 and 2016 are shown in Figures 5 and 6, and their statistics are summarized in Table 4. Data from Table 4 demonstrates NDVI values ranged from -1 to 1 at the three-time points. The mean values of 0.46 in 1996, 0.37 in 2007 and 0.4 in 2016, and median NDVI values of 0.5 in 1996, 0.36 in 2007 and 0.4 in 2016 proves vegetation cover decreased gradually during this period, especially from 1996 to 2007. Data from Figure 5 shows that areas of high NDVI values were mainly detected in the western, north-western and south-western parts of the HMA at these three-time points, whereas, areas of low NDVI were mainly concentrated in the core urban areas of the HMA. Data from histograms and boxplots in Figure 6 demonstrates that the distribution of the NDVI was strongly left-skewed with many low NDVI values dominating the plot. The order of the left-skewness is of NDVI in 2016, 2007 and 1996, respectively corresponding to the decrease of NDVI over the three-time points. Forests in the west and active agricultural land in the southwest and northwest of the HMA (Nguyen et al., 2019) have accounted for the higher NDVI values, whereas, the crowded residential areas in the city centre and industrial zone in suburban areas causing low density of vegetation cover (Hoang, 2016; Hoang, 2017) were the causes of low NDVI values.

Table 4. Descriptive statistics of the NDVI in the HMA

Date	Time (GMT)	Minimum	Median	Mean	Maximum
1996-9-30	02:41:56.28	-1.00	0.50	0.46	1.00
2007-5-24	03:23:04.77	-1.00	0.36	0.37	1.00
2016-6-01	03:17:49.46	-1.00	0.40	0.40	1.00

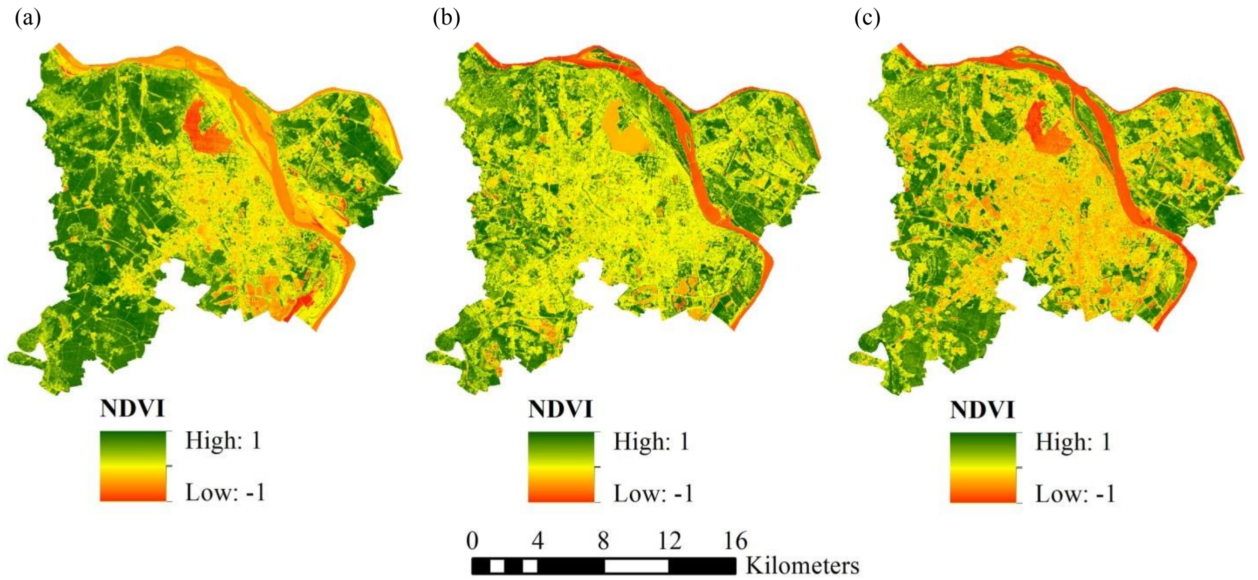

Figure 5. NDVI in 1996, 2007 and 2016

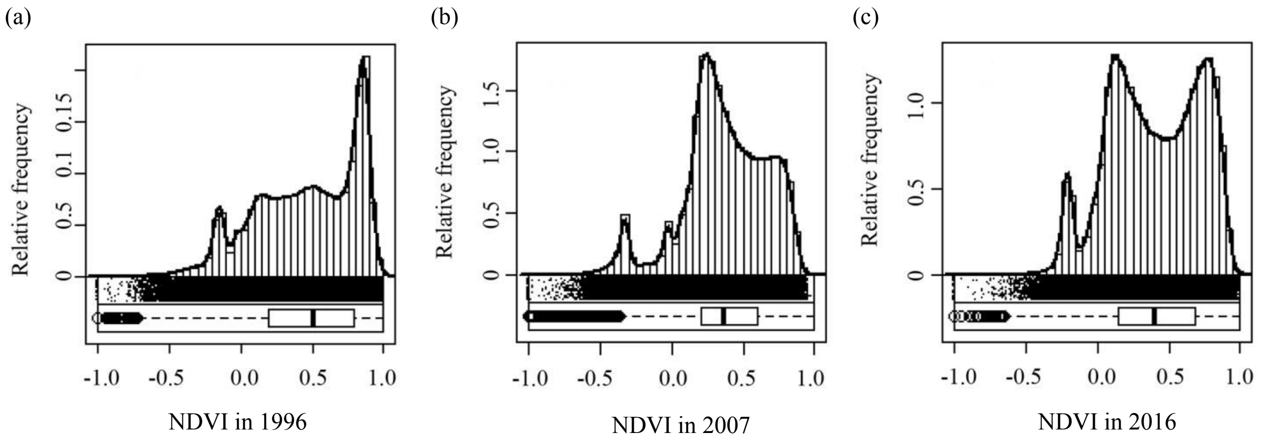

Figure 6. Histograms, density traces, 1-D scatter-plot and box-plots of the NDVI in 1996, 2007 and 2016

3.3 NDBI in 1996, 2007 and 2016

Data from Table 5 demonstrates that the extracted built-up land using NDBI from 2016 Landsat-8 images resulted in a overall accuracy of 89.3% with a kappa statistic of 0.79. The confusion matrix along with user's and producer's accuracies of more than 80% for built-up land map are also provided in Table 5. These accuracies meet the 80% accuracy standard of the United States National Vegetation Classification (Grossman et al., 1998). This result indicates that the combination of Landsat images and NDBI can be used reliably for the built-up land extraction and for the investigation of the effects of changes in vegetation and built-up land on land surface temperature in this study.

Table 5. Summary of accuracy assessment of the extracted built-up land.

Land cover types	Built-up land	Others	Classification overall	Producer's Accuracy	User's Accuracy	Overall accuracy	Kappa
Buil-up land	181	24	205	90.5	88.3	89.3	0.79
Others	19	176	195	88.0	90.3		
Trueth overall	200	200					

The distribution of NDBI values of the HMA obtained from Landsat images acquired in 1997, 2007 and 2017 are shown in Figure 7 and 8, and are statistically summarized in Table 6. Data from this table shows that the values of NDBI ranged from 0.77 to 0.56 in 1996, from -0.45 to 0.48 in 2007 and from -0.64 to 0.58 in 2016. Small areas of high NDBI values were detected in the core urban areas of the HMA in 1997 (Figure 7 (a)). But by 2007 and 2016, high NDBI areas had greatly expanded outside the HMA center, which expands towards the western, north-western and south-western parts of the core urban HMA, especially in the period of 1996-2007 (Figure 7 (b) and (c)). The rapid expansion of high NDBI areas during the period of 1996-2007 was due to the high rate of urbanization after the Doi Moi Policy started in 1986 (Logan, 2005). Data from histograms and boxplots in Figure 8 demonstrates that the distribution of the NDBI was similar to those of the LST shown in Figure 3. The NDBI was strongly right-skewed in 1996, quite balanced in 2007 and left-skewed in 2016. Similar to those reported by Nguyen et al. (2019), the NDBI had been increasing during this period, especially in the period of 1996-2007. The number of construction and rehabilitation of the city's infrastructure led to the rapid increase of 4870.5 thousand m^2 of new buildings in Hanoi during 1990-2013 reported by Nguyen et al. (2019) was the most important cause of the increasing of high NDBI areas. In addition, a drastic increase in population from 2685 thousand people in 1999 to 7328.4 thousand people in 2016 (Nguyen et al., 2019), and transformation from natural forests into urban built-up areas (Thanh Hoan et al., 2018) and an increase rate of electricity per capita (Nguyen et al., 2019) have also significantly contributed to those changes of NDBI areas.

Table 6. Descriptive statistics of the NDBI in the HMA.

Date	Time (GMT)	Minimum	Median	Mean	Maximum
1996-9-30	02:41:56.28	-0.77	-0.08	-0.07	0.56
2007-5-24	03:23:04.77	-0.45	-0.07	-0.07	0.48
2016-6-01	03:17:49.46	-0.64	0.02	0.02	0.58

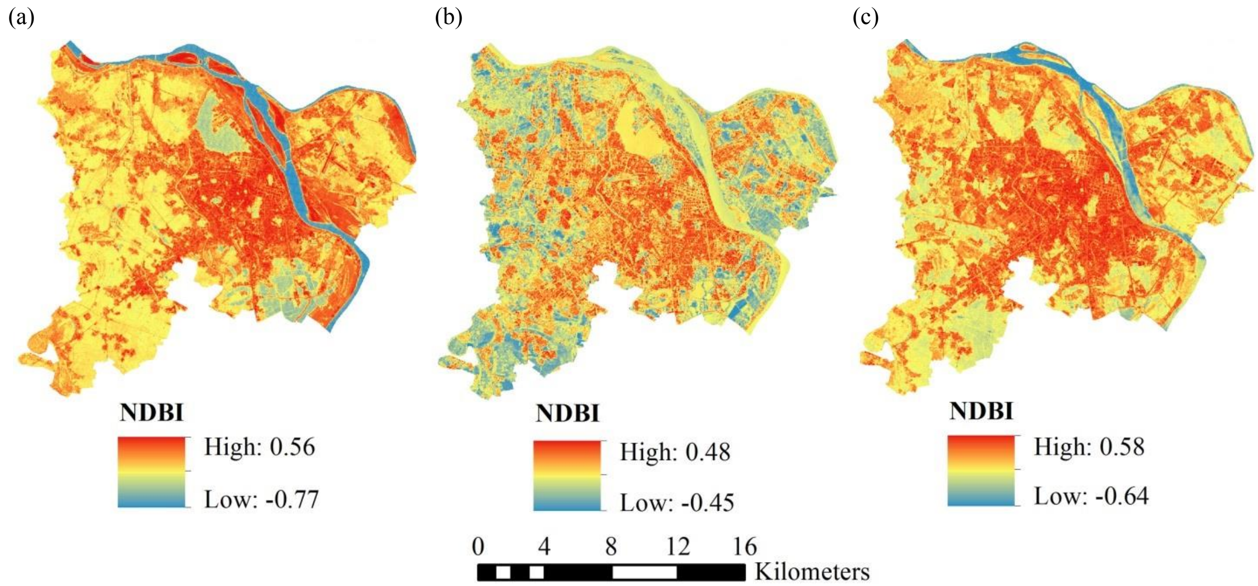

Figure 7. NDBI in 1996, 2007 and 2016

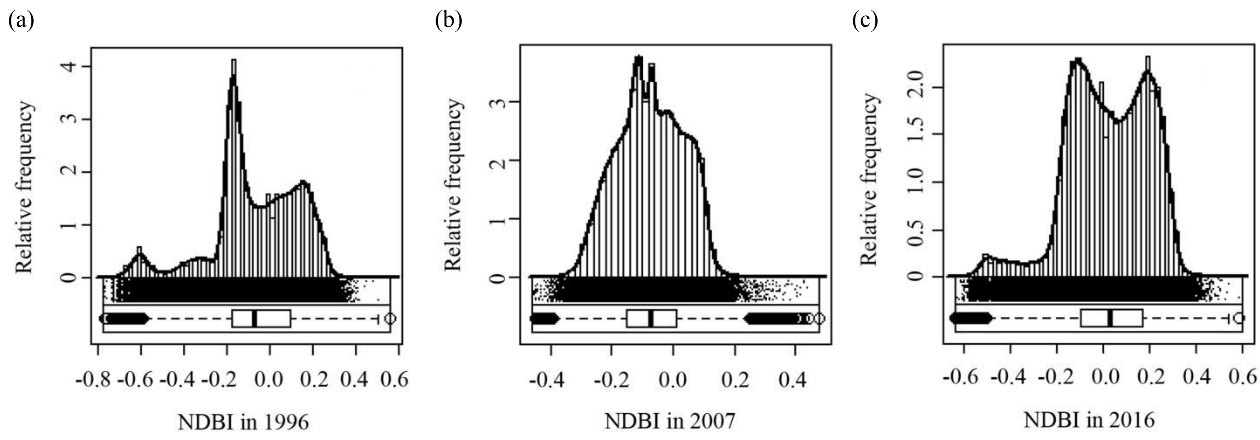

Figure 8. Histograms, density traces, 1-D scatter-plot and box-plots of the NDBI retrieved in 1996, 2007 and 2016

3.4 Spatio-temporal variation of relationship between LSTs, vegetation and built-up land

Data from scatter-plots in Figure 8 show that there were significant negative regression coefficients indicating negative correlations between LST and NVDI ($p<0.001$) with the values of -1.61 in 1996 and -3.98 in 2016 (Figure 9 (a) and (c)). This indicates LSTs were negatively correlated with vegetation cover. However, opposite to those reported in previous studies (Liu and Zhang, 2011; Ranagalage et al., 2017; Sanecharoen et al., 2019), a significant positive regression coefficient of 0.56 was estimated in 2007 (Figure 9 (b)). In addition, low values of coefficient of determination (R^2) of 0.076 in 1996, 0.001 in 2007 and 0.044 in 2016 indicate a relative bad goodness of fit for the observations. This is due to the existence of a large area of surface water (rivers and lakes) in the study area, which negatively affects the predictive accuracy of the ULRM. Therefore, surface water pixels were removed to re-estimate of the relationship between LST and NDVI. Data from Figure 9 (d), (e) and (f) shows that after the NDVI values of surface water were removed, all of coefficient of determinations had much improved with R^2 of 0.682 in 1996, 0.316 in 2007 and 0.524 in 2016. Although the R^2 values for the last two-time points were not as high as those of 1996, particularly in the year of 2016, they were all statistically significant at the 0.001 level. These regression coefficients were negative and statistically highly significant ($p<0.001$) at the three-time points showing the LST is strongly and negatively correlated with vegetation cover. Our finding is consistent with those reported in previous studies (Kumar and Shekhar, 2015; Nguyen et al., 2019; Sanecharoen et al., 2019).

It can be seen in Figure 9 that the NDBI spatial pattern of values shown in Figure 7 considerably mirrors those of LST as shown in Figure 3. This indicates a positive correlation between LST and NDBI. The significant positive regression coefficient between LST and NDBI was low in 1996 due to less urbanization in the HMA at the first time point. Nevertheless, like the correlation between LST and NDVI (vegetation), the correlation between LST and NDBI (built-up land) was also statistically significant at the 0.001 level ($p<0.001$) with high R^2 values of 0.676 in 1996 and 0.768 in 2016. Although the R^2 value of 0.163 in 2016 was not as high as those of 1996 and 2007, it was still statistically significant ($p<0.001$). The regression coefficient increases considerably as the area became more urbanized (Ranagalage et al., 2017). Therefore, the increasing of regression coefficients from 8.47 in 1996 to 18.29 in 2007, and to 30.2 in 2016 proves a rapid urbanization process in the HMA during 1996-2016. A significant increase in the area of building land occurred with the increases of 13.18% in the residential area and 2.66% in the industrial area indicated by Nguyen et al. (2019) can be account for this urbanization process. It can be concluded that there existed a very strong positive correlation and relationship between LST and built-up land during the period of 1996-2016. This finding is consistent with those reported in previous studies (Sanecharoen et al., 2019; Zhang et al., 2009), especially in the HMA (Nguyen et al., 2019).

The evaluation of the joint effect of both vegetation cover and built-up land on LST was carried out using the MLRM. Data from Table 7 shows that, in general, there existed a significant negative relationship (correlation) between LST and NDVI and a significant positive relationship between LST and NDBI at all three-time points, particularly in the case of surface water removed from predicting models. The high R^2 values of 0.742 in 1996 and 0.774 in 2016 proves that 74.2% and 77.4% of the LST were predicted by the NDVI and the NDBI. Although R^2 value of 0.394 in 2007 was not as high as those of the two previous time points, it was statistically significant at the 0.001 level. Generally, the absolute values of regression coefficients of NDBI were greater than those of NDVI indicating the relationship between the LST and the NDBI (Figure 9 (g), (h) and (i)) was stronger than that of between the LST and the NDVI (Figure 9 (d), (e) and (f)). This indicates that the explanatory power of built-up land with regards to the distribution of LST spatial pattern of in the HMA is much stronger than that of vegetation coverage.

Recent studies have shown that vegetation cover has dramatically decreased in urban districts and some areas of suburban districts because of the incessant urbanization process in the central urban areas and some sub-urban areas of the Hanoi city (Hoang, 2016; Hoang, 2017). Particularly, the Doi Moi Policy since 1986 has greatly contributed to the rapid urbanization process in Hanoi city (Tsunoda et al., 2014). Nguyen et al. (2019) also reported that the construction and rehabilitation of the city's infrastructure and the number of industrial establishments has increased by 4,870,500 m^2, equivalent to an increase rate of 211,760 m^2/year since 1990. In addition, high population density ranged from 21,000 people/km^2 to 40,000 people/km^2 in urban districts in 2016 and tends to increase in urban districts since 1990. Similar to those reported in previous studies (Hoang, 2016; Hoang, 2017; Nguyen et al., 2019), the rapid development in these urban areas has brought the replacement of land cover types, especially vegetation cover, with urban built-up land. It is apparent that transitions of land cover types, especially from vegetation and other types to built-up land were the main causes of the increase of LST in the HMA. In addition, the emergence of Hatay province, Vinhphuc province's Melinh district and four communes of Hoabinh province's Luongson district into the metropolitan area of Hanoi in August 2008 (Hiep, 2014) has led a two-fold jump in population with an increase of 3,153,300 people as compared with that of 2007 (Nguyen et al., 2019). A recent study by Nguyen et al. (2019) has also shown that Hanoi had experienced a remarkable change in the total population and population density during 1998-2016. The total population significantly increased from 2,685,000 people in 1999 to 7,328,400 people in 2016 with a rate of increase of 273,140 people per year (Nguyen et al., 2019). It is clear that the change in the total population and population density also accounted for the increase of LSTs. It can be concluded from the above discussion that the increase of built-up land and the decrease in vegetation cover are linked with the increase of LSTs. In addition, the relationship between LSTs and vegetation and built-up land was strongly correlated with continuous increases in population and socio-economic factors in the HMA.

Table 7. MRLMs for predicting LST of HMA

Date	Model	Coefficient of determination (R^2)	Significance level (p)
1996-9-30	LST = -1.498*NDVI + 8.410*NDBI + 27.710	0.742	0.001
	LST* = -3.219*NDVI + 6.060*NDBI + 27.710	0.774	0.001
2007-5-24	LST = 1.784*NDVI + 19.129*NDBI + 39.553	0.174	0.001
	LST* = -8.739*NDVI + 11.306*NDBI + 44.240	0.394	0.001
2016-6-01	LST = 0.944*NDVI + 30.699*NDBI + 41.90	0.770	0.001
	LST* = -0.116*NDVI + 29.906*NDBI + 42.514	0.729	0.001

Notes: *indicates multivariable linear regression models were predicted after surface water pixels were removed.

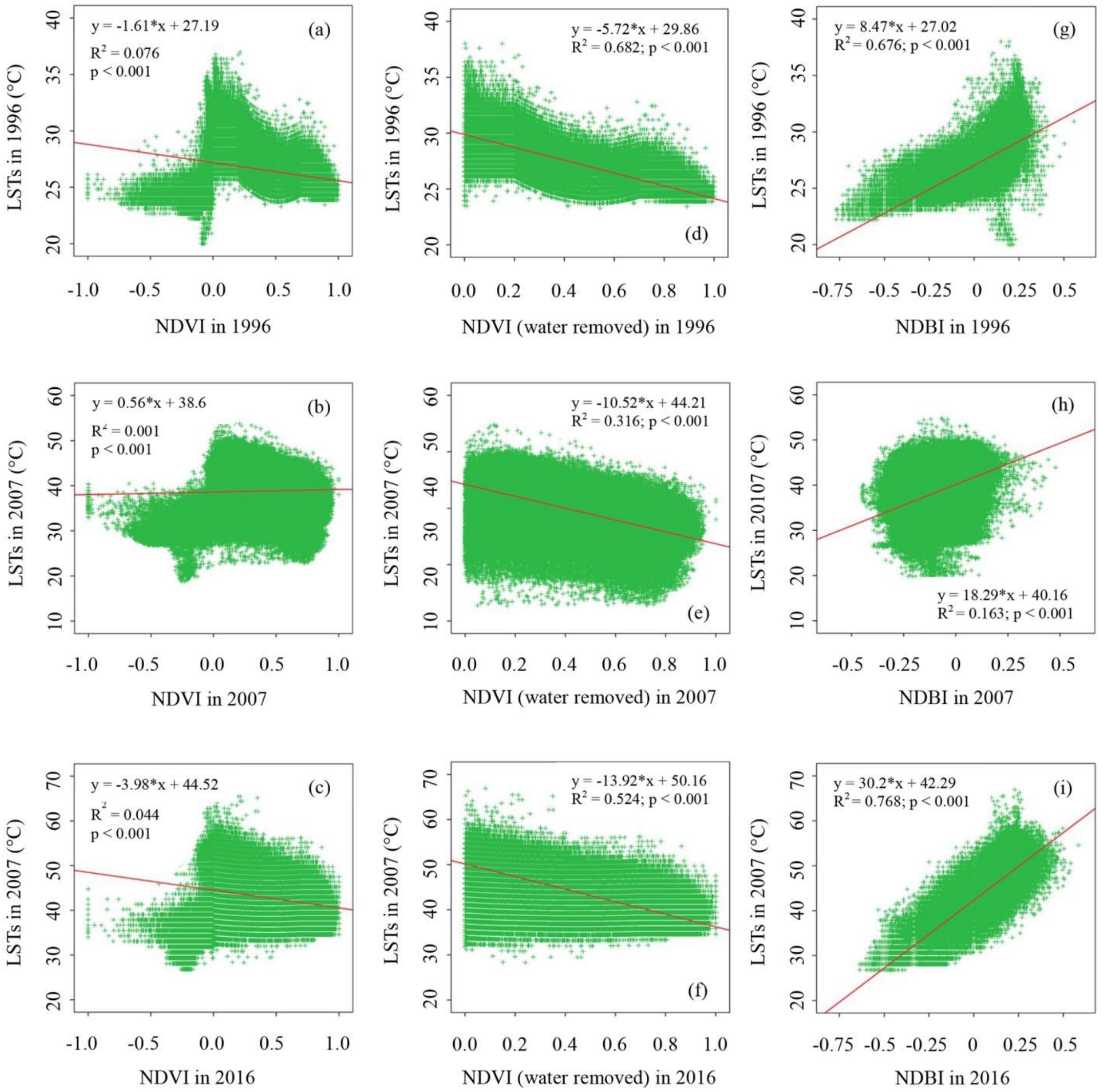

Figure 9. Scatter-plots of between LSTs and NDVI and NDBI

4. CONCLUSION

In this study, the effects of changes in vegetation and built-up land on LST was investigated based on multi-spectral Landsat-5 TM and Landsat-8 time-series images collected in summer in the HMA in the period of 1996-2016. LSTs were first retrieved by means of the RTM. Scatter-plots and the ULRM were then used to independently measure the influence of each NDVI and NDBI on LST, respectively. The MLRM was finally applied to improve the accuracy of the predicted model in the estimation of the joint effect of both of NDVI (vegetation) and NDBI (built-up land) on LST. It was found that (i) high LSTs and built-up land sprawl rate had been increasing along with the decrease of vegetation during 1996-2016 and tends to expand towards the western, north-western and south-western parts of the HMA; (ii) there exists a negative correlation between LST and vegetation, whereas, a very strong positive correlation between LST and built-up land was also identified. The effect of changes in vegetation and built-up land on LST tend to increase rapidly in recent years. This result also indicated vegetation weakens the effect of UHIs, whereas the built-up land greatly strengthens the effects of UHIs in urban areas. These findings suggest that (i) LST, NDVI, NDBI and their spatio-temporal variations can be effectively derived from Landsat TM and OLI/TIRS data; (ii) the MLRM allows for the effective investigation of the joint-effects of both NDVI (vegetation) and NDBI (built-up land) on LST. Although this study revealed promising findings, further research is still required as some problems and difficulties have not been resolved in this study. For instance, other types of remotely sensed data acquired in winter need to be used instead of Landsat images which are not available.

ACKNOWLEDGEMENTS

The author wishs to thank anonymous reviewers, editors for their valuable comments and insightful suggestions, U.S. Geological Survey (USGS) for the data support, and Msc. Van Sao Bui (Northeast Meteorological and Hydrological Observatory, Vietnam Meteorological and Hydrological Administration, Ministry of Natural Resources and Environment of the Socialist Republic of Vietnam) for providing meteorological air temperature data in this work.

REFERENCES

Adler-Golden S, Berk A, Bernstein L, Richtsmeier S, Acharya P, Matthew M, et al. FLAASH, a MODTRAN4 atmospheric correction package for hyperspectral data retrievals and simulations. Proceedings of the 7th Ann JPL Airborne Earth Science Workshop; 1998 Jan 12-16; CA: USA; 1998.

Adler-Golden SM, Matthew MW, Bernstein LS, Levine RY, Berk A, Richtsmeier SC, et al. Atmospheric correction for shortwave spectral imagery based on MODTRAN4. Imaging Spectrometry V: International Society for Optics and Photonics 1999;3753:61-70.

Ahmadian N, Demattê J, Xu D, Borg E, Zölitz R. A new concept of soil line retrieval from Landsat 8 images for estimating plant biophysical parameters. Remote Sensing 2016;8(9):738-61.

Balling R, Brazel SW. High-resolution surface temperature patterns in a complex urban terrain. Photogrammetric Engineering and Remote Sensing 1988;54(9):1289-93.

Barsi JA, Barker JL, Schott JR. An atmospheric correction parameter calculator for a single thermal band earth-sensing instrument. Proceedings of the IEEE International Geoscience and Remote Sensing Symposium (IGARSS 2003); 2003 July 21-25; Toulouse: France; 2003.

Bokaie M, Zarkesh MK, Arasteh PD, Hosseini A. Assessment of urban heat island based on the relationship between land surface temperature and land use/land cover in Tehran. Sustainable Cities and Society 2016;23:94-104.

Chan HP, Chang CP, Dao PD. Geothermal anomaly mapping using landsat etm+ data in ilan plain, northeasten Taiwan. Pure and Applied Geophysics 2018;175(1):303-23.

Chander G, Markham BL, Helder DL. Summary of current radiometric calibration coefficients for Landsat MSS, TM, ETM+, and EO-1 ALI sensors. Remote Sensing of Environment 2009;113(5):893-903.

Dousset B, Gourmelon F. Satellite multi-sensor data analysis of urban surface temperatures and landcover. ISPRS Journal of Photogrammetry and Remote Sensing 2003;58(1-2):43-54.

Estoque RC, Murayama Y, Myint SW. Effects of landscape composition and pattern on land surface temperature: An urban heat island study in the megacities of Southeast Asia. Science of the Total Environment 2017;577:349-59.

Gallo K, McNab A, Karl TR, Brown JF, Hood J, Tarpley J. The use of NOAA AVHRR data for assessment of the urban heat island effect. Journal of Applied Meteorology 1993;32(5): 899-908.

Garcia O, Hemme T, Nho LT, Tra HTH. The Economics of Milk Production in Hanoi, Viet Nam, with Particular Emphasis on Small-Scale Producers. PPLPI Working Paper No. 33; 2006.

Goward SN, Xue Y, Czajkowski KP. Evaluating land surface moisture conditions from the remotely sensed temperature/vegetation index measurements: An exploration with the simplified simple biosphere model. Remote Sensing of Environment 2002;79(2-3):225-42.

Grossman DH, Faber-Langendoen D, Weakley AS, Anderson M, Bourgeron P, Crawford R, et al. International Classification of Ecological Communities: Terrestrial Vegetation of the United States. Volume I: The National Vegetation Classification System: Development, Status, and Applications. Virginia, USA: The Nature Conservancy; 1998.

Hiep NT. Economic evaluation of transportation infrastructure. Science 2014;47:415-55.

Hoang AH. Fractional vegetation cover estimation in urban area of Hanoi City using Landsat 8 OLI Images. VNU Journal of Science: Earth and Environmental Sciences 2016;32(3S): 101-8.

Hoang AH. Assessment of fractional vegetation cover changes in some urban and sub-urban areas of Hanoi using multi-spectral and multi-temporal Landsat Images. VNU Journal of Science: Earth and Environmental Sciences 2017;33(2):40-7.

Jensen JR. Remote Sensing of the Environment: An Earth Resource Perspective. Bengaluru, India: Pearson Education India; 2009.

Kikon N, Singh P, Singh SK, Vyas A. Assessment of urban heat islands (UHI) of Noida City, India using multi-temporal satellite data. Sustainable Cities and Society 2016;22:19-28.

Kumar D, Shekhar S. Statistical analysis of land surface temperature-vegetation indexes relationship through thermal remote sensing. Ecotoxicology and Environmental Safety 2015;121:39-44.

Lasko K, Vadrevu KP, Nguyen TTN. Analysis of air pollution over Hanoi, Vietnam using multi-satellite and MERRA reanalysis datasets. PloS One 2018;13(5):e0196629.

Liu L, Zhang Y. Urban heat island analysis using the Landsat TM data and ASTER data: A case study in Hong Kong. Remote Sensing 2011;3(7):1535-52.

Logan WS. The cultural role of capital cities: Hanoi and Hue, Vietnam. Pacific Affairs 2005;78(4):559-75.

Lu Y, Feng X, Xiao P, Shen C, Sun J. Urban heat island in summer of Nanjing based on TM data. 2009 Joint Urban Remote Sensing Event; 2009 May 20-22; Shanghai: China; 2009.

Nguyen DQ, Yamasue E, Okumura H, Ishihara KN. Use and disposal of large home electronic appliances in Vietnam. Journal of Material Cycles and Waste Management 2009;11(4):358-66.

Nguyen TM, Lin T-H, Chan H-P. The environmental effects of urban development in Hanoi, Vietnam from satellite and meteorological observations from 1999-2016. Sustainability 2019;11(6):1768-92.

Nguyen TT, Vu TD. Use of hot spot analysis to detect underground coal fires from Landsat-8 TIRS data: A case study in the Khanh Hoa coal field, north-east of Vietnam. Environment and Natural Resources Journal 2019;17(3):1-10.

Oke TR. The energetic basis of the urban heat island. Quarterly Journal of the Royal Meteorological Society 1982; 108(455):1-24.

Ongsomwang S, Dasananda S, Prasomsup W. Spatio-temporal urban heat island phenomena assessment using Landsat Imagery: A case study of Bangkok metropolitan and its vicinity, Thailand. Environment and Natural Resources Journal 2018;16(2):29-44.

Orhan O, Ekercin S, Dadaser-Celik F. Use of Landsat land surface temperature and vegetation indices for monitoring drought in the Salt Lake Basin Area, Turkey. The Scientific World Journal 2014;2014:1-11.

Ranagalage M, Estoque RC, Murayama Y. An urban heat island study of the Colombo metropolitan area, Sri Lanka, based on Landsat data (1997-2017). ISPRS International Journal of Geo-Information 2017;6(7):189-206.

Rhee J, Im J. Estimating high spatial resolution air temperature for regions with limited in situ data using MODIS products. Remote Sensing 2014;6(8):7360-78

Sanecharoen W, Nakhapakorn K, Mutchimwong A, Jirakajohnkool S, Onchang R. Assessment of urban heat island patterns in Bangkok metropolitan area using time-series of LANDSAT thermal infrared data. Environment and Natural Resources Journal 2019;17(4):87-102.

Sobrino JA, Jiménez-Muñoz JC, Sòria G, Romaguera M, Guanter L, Moreno J, et al. Land surface emissivity retrieval from different VNIR and TIR sensors. IEEE Transactions on Geoscience and Remote Sensing 2008;46(2):316-27.

Star JL, Estes, JE, McGwire KC, Arvidson RE, Rycroft MJ. Integration of Geographic Information Systems and Remote Sensing. New York, USA: Cambridge University Press; 1997.

Sun Q, Tan J, Xu Y. An ERDAS image processing method for retrieving LST and describing urban heat evolution: A case study in the Pearl River Delta Region in South China. Environmental Earth Sciences 2010;59(5):1047-55.

Tan J, Zheng Y, Tang X, Guo C, Li L, Song G, et al. The urban heat island and its impact on heat waves and human health in Shanghai. International Journal of Biometeorology 2010; 54(1):75-84.

Thanh Hoan N, Liou YA, Nguyen KA, Sharma R, Tran DP, Liou CL, et al. Assessing the effects of land-use types in surface urban heat islands for developing comfortable living in Hanoi City. Remote Sensing 2018;10(12):1965.

Tsunoda T, Cuong TC, Dong TD, Yen NT, Le NH, Phong TV, et al. Winter refuge for *Aedes aegypti* and *Ae*. *albopictus* mosquitoes in Hanoi during winter. PloS One 2014; 9(4):e95606.

Tuan VA, Shimizu T. Modeling of household motorcycle ownership behaviour in Hanoi City. Journal of the Eastern Asia Society for Transportation Studies 2005;6:1751-65.

Vu TD, Nguyen TT. Remote sensing and GIS-based river bank accretion/erosion assessment in the confluence of Thao-Da-Lo Rivers, North-East of Vietnam. EnvironmentAsia 2018a; 11(3):27-44.

Vu TD, Nguyen TT. Spatio-temporal changes of underground coal fires during 2008-2016 in Khanh Hoa coal field (North-east of Vietnam) using Landsat time-series data. Journal of Mountain Science 2018b;15(12):2703-20.

Weng Q. A remote sensing - GIS evaluation of urban expansion and its impact on surface temperature in the Zhujiang Delta, China. International Journal of Remote Sensing 2001; 22(10):1999-2014.

Weng Q, Lu D, Schubring J. Estimation of land surface temperature-vegetation abundance relationship for urban heat island studies. Remote Sensing of Environment 2004; 89(4):467-83.

Zanter K. Landsat 8 (L8) Data Users Handbook. California, USA: CreateSpace Independent Publishing Platform; 2016.

Zha Y, Gao J, Ni S. Use of normalized difference built-up index in automatically mapping urban areas from TM imagery. International Journal of Remote Sensing 2003;24(3):583-94.

Zhang Y, Odeh IO, Han C. Bi-temporal characterization of land surface temperature in relation to impervious surface area, NDVI and NDBI, using a sub-pixel image analysis. International Journal of Applied Earth Observation and Geoinformation 2009;11(4):256-64.

Estuary Sediment Treatment for Reducing Sulfate in Acid Mine Water

Fahruddin Fahruddin[1*], As'adi Abdullah[1], Nurhaedar[1], and Nursiah La Nafie[2]

[1]*Department of Biology, Faculty of Mathematics and Natural Sciences, Hasanuddin University, Indonesia*
[2]*Department of Chemistry, Faculty of Mathematics and Natural Sciences, Hasanuddin University, Indonesia*

ARTICLE INFO

Received: 25 Aug 2019
Received in revised: 24 Dec 2019
Accepted: 15 Jan 2020
Published online: 18 Feb 2020
DOI: 10.32526/ennrj.18.2.2020.18

Keywords:
Acid mine water/ Bioremediation/ Estuary sediment/ Sulfate-reducing bacterial/ Sulfate

*** Corresponding author:**
E-mail: fahruddin65@gmail.com

ABSTRACT

Acid mine water causes environmental problems due to its high acidity caused by its high sulfate content which can disturb the life of organisms. This problem can be resolved by utilizing sulfate-reducing bacteria (SRB) abundantly found in sediments. The purpose of this research is to study the use of estuary sediments as a source of SRB inoculums to reduce sulfate in acid mine water. The bioremediation treatment of acid mine water is carried out in a column bioreactor, with treatment T1 comprising of sediment and compost, and then comparing it to treatments T2 of sediment, T3 of compost, and T4 as the control treatment of only acid mine water. Results show that treatment T1 was able to reduce sulfate concentrations by 78%, compared to T2 by 56%, T3 by 21% and T4 by 5%. The reduction of sulfate was followed by increases in pH where T1 reached a pH value of 7.1, compared to treatments T2 and T3 which had pH values less than 5.5, whereas treatment T4 had a pH of 2.2. The reduced sulfate and increased pH was also followed by an increase of SRB growth, especially in T1. Estuary sediments as a source of SRB inoculums can be used in the bioremediation of acid mine water by adding compost to maximize the process of sulfate reduction and pH increase.

1. INTRODUCTION

The mining industry in Indonesia has undergone rapid development due to it being one of the main industries in the national and regional economies (Widyati, 2007; Abfertiawan et al., 2016). However, problems have also emerged along with the increase of mining activities, especially in aquatic environments. These include types of mining waste such as mine water, overburden, residues from the mining process, tailings, residual ore and sludge (Gaikwad et al., 2011; Simate and Ndlovu, 2014).

The Lamuru coal mine is one of the mines operating in Indonesia. There have been studies conducted on the coal produced from this mine. Microscopic petrographic analysis results have shown that the coal contains 11.86% sulphur which may be categorized under super high sulphur (Widodo et al., 2016). Additional X-ray diffraction (XRD) analysis of the coal has also found a type of framboidal pyrite of very fine crystals (Widodo et al., 2019). This type of spirit is very sensitive and rapidly reacts with air and is categorized as PAF (Potentially Acid Forming) that will trigger the formation of acid mine water, causing environmental problems at mining locations (Dai et al., 2008). This is also the concern of the Lamuru Mine, Bone Regency, South Sulawesi, Indonesia and therefore must be prevented.

Acid mine water is harmful due to its low pH value of around 1.5-3.5 and presence of a number of toxic heavy metals such as Hg, Cd, Pb, Fe, Al, U and Mn. The type of metal depends on the type of mine (Meier et al., 2012; Simate and Ndlovu, 2014; Fahruddin et al., 2018). Acid mine water is formed through the oxidation of sulfur with oxygen, water or carbon dioxide in the form of sulfate ions forming into sulfuric acid. The high sulfuric acid content causes acid mine water to have a low pH that triggers the formation of metal ions - reactive metals (Matshusa-Masithi et al., 2009; Burgos et al., 2012).

Acid mine water will disrupt water biota if it enters a water source and will also disrupt life on land if it penetrates the soil, particularly vegetation

Citation: Fahruddin F, Abdullah A, Nurhaedar, Nafie NL. Estuary sediment treatment for reducing sulfate in acid mine water. Environ. Nat. Resour. J. 2020;18(2):191-199. DOI: 10.32526/ennrj.18.2.2020.18

(Afriyie-Debrah et al., 2010). Moreover, it can also dissolve heavy metals that can cause pollution in aquatic environments which can be indirectly harmful to humans (Saviour, 2012; Hedrich and Johnson, 2012). Acid mine water is difficult to treat if it has entered a waterway. The acidic environment triggers the growth of *Thiobacillus ferroxidans* bacteria that will catalyze the pyrite oxidation process (Mahmoud et al., 2005; Patel, 2010). Therefore, acid mine water needs to be well managed so that it is not harmful if it enters water environments.

To date, acid mine water has been treated through the use of chemical compounds by adding lime treatments to it; another method is the physical method of storing the acid mine water in a large hole and then tightly covering it; however these two methods have proven to be very inefficient, non-eco-friendly and very costly (Johnson and Hallberg, 2005).

Bioremediation is a good and environmentally friendly alternative for acid mine water waste treatment by utilizing microbes to reduce the sulfate in acid mine water (Luptakova and Kusnierova, 2005). Nowadays, bioremediation has continued to develop in its usage to treat acid mine water in the mining industry (Costa and Duarte, 2005). The microbes utilized in the bioremediation of acid mine water are the group of sulfate-reducing bacteria. In reducing sulfate, this type of bacteria produces hydrogen sulfide (H_2S) and hydroxyl ions (OH^-), thus an increase of pH occurs (Pester et al., 2012), then sulphide reacts with metal cations and forming metal sulfides that have a role as an electron donor and reduce metal cation into metal sulphide in acid mine water (Fahruddin et al., 2018).

Sulfate-reducing bacteria are abundantly found in muddy substrate such as wetland sediments. This is the reason why the sediments can be directly applied to the acid mine water treatment bioreactor without having to perform a bacteria isolate culture in the laboratory (Whitehead and Prior, 2005). It is not necessary to inoculate microbe culture and add nutrients because wetland sediments naturally contain an abundant number and many types of sulfate-reducing bacteria (Pester et al., 2012; Fahruddin et al., 2017). Therefore, research has been conducted regarding the application of wetland sediment as a source of sulfate-reducing bacterial inoculums in reducing sulfate in acid mine water.

Previous research results by Fahruddin and Abdullah (2015) have shown that the application of wetland sediment from mangroves and swamps on acid mine water is able to increase the pH of acid mine water, decrease sulfate levels and increase the growth of sulfate-reducing bacteria, which can be used to treat environmental pollution caused by acid mine water. In several studies, it was found that many types of groups of sulfate-reducing bacteria exist in estuary sediments, the distribution and amount of sulfate-reducing bacteria varies at each location depending on the organic content of sediment (Compeau and Bartha, 1985; Purdy et al., 2002; Colin et al., 2017). Based on these studies, estuary sediment was the wetland sediment chosen as the bacterial inoculum source to reduce sulfate in the acid mine water treatment for application in the bioreactor.

2. METHODOLOGY

2.1 Sampling

The acid mine water sample were obtained from the Lamuru Mine located at Masserengpulu Subdistrict, Bone Regency (Figure 1). The estuary sediment was gathered from the Tallo estuary, Makassar (Figure 2), and the compost was farmyard manure obtained from commercial plant sellers in Panaikang, Makassar. The characteristics of this compost was a decomposed mixture of dung and urine of farm animals and urine along with litter and leftover organic material from domestic waste.

2.2 Acid mine water and sediment characterization

The characterization of estuary sediments involves the measurement of total organic carbon using the TOC method, total nitrogen using the Micro Kjehdahl method, as well as total phosphorous with the Stannous Chloride method (Greenberg et al., 1992). The characterization of acid mine water included measuring sulfate content using a spectrophotometer with a length wave of 420 nm, while pH was measured using a pH meter (Greenberg et al., 1992).

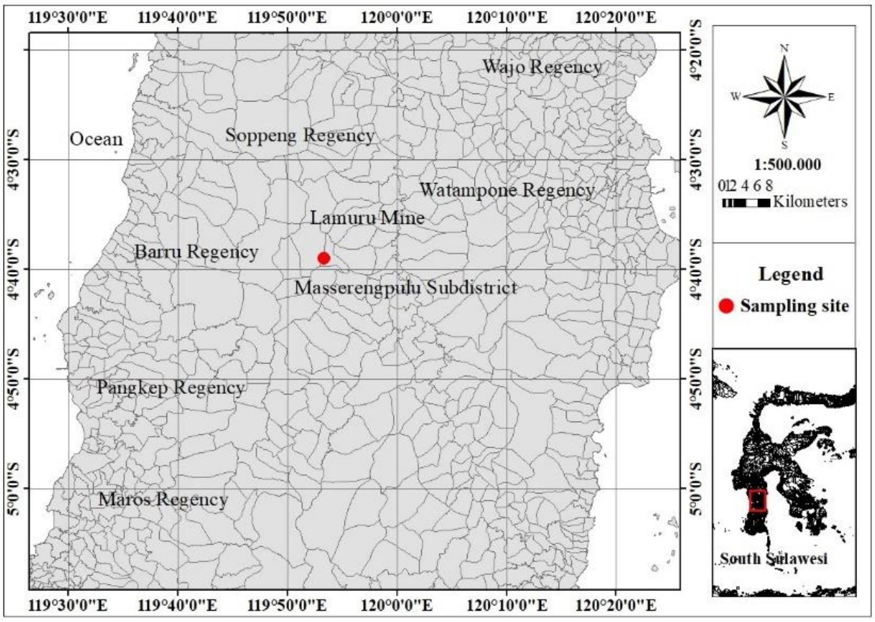

Figure 1. Map of the sampling site of acid mine water on the Lamuru Mine, Masserengpulu Subdistrict, Bone Regency, South Sulawesi, Indonesia.

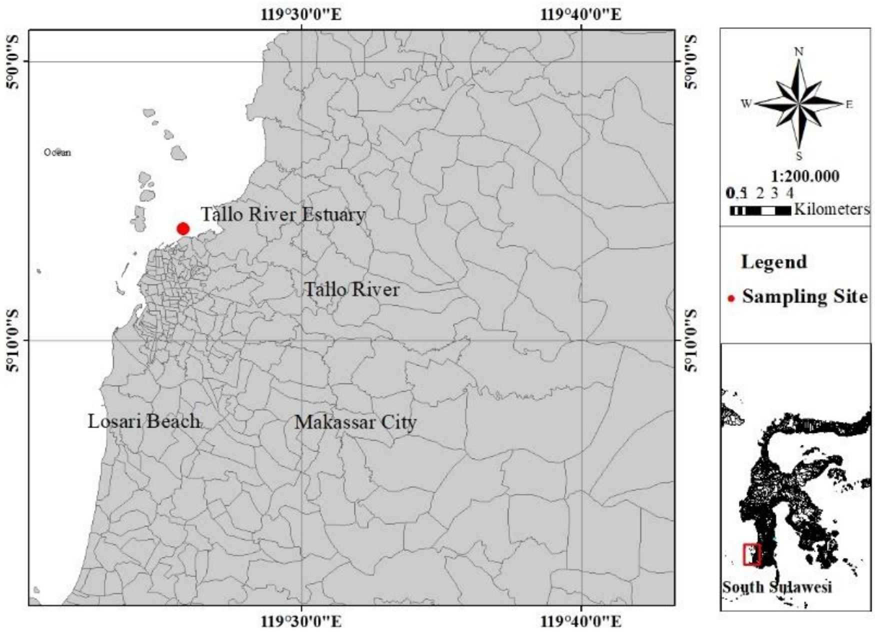

Figure 2. Map of the sampling site of the estuary sediment on the Tallo estuary, Makassar, South Sulawesi, Indonesia

2.3 Treatments and experiments

The treatments were made in a bioreactor column made from a modified container with a laboratory-scale anaerobic chamber with an inner diameter of 15 cm and length of 35 cm (Figure 3). The bioreactor column is filled with 800 mL of acid mine water along with 10% sediment and 5% compost, the best ratio based on previous research by Fahruddin and Abdullah (2015) in various sized volumes. In this study, the sediment is the source of sulfate-reducing bacteria, while the compost is rich with nutrients and becomes the simple carbon source for bacterial growth. All treatments were performed in duplicate and incubated for 30 days at room temperature (27 ^{o}C). The four treatments were as follows:

- Treatment T1 was 10% sediment and 5% compost
- Treatment T2 was 10% sediment
- Treatment T3 was 5% compost
- Treatment T4 was the control treatment without any added sediment and compost

The treatments were left alone for 30 days and sampled on days 0, 5, 10, 15, 20, 25 and 30 to observe sulfate concentration, change in pH and the amount of sulfate-reducing bacteria.

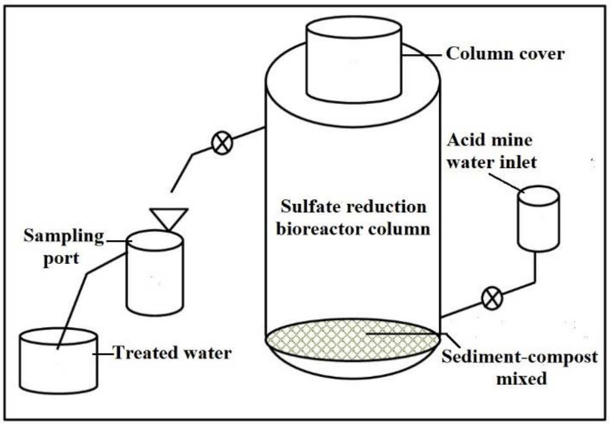

Figure 3. Schematic of the bioreactor for sulfate reduction

2.4 Measurement of sulfate concentration

The measurement of the sulfate concentration of the acid mine water treatments was performed by using a spectronic-20 spectrophotometer, where a sulfate concentration calibration curve was made beforehand. $BaCl_2$ crystals and buffer acid salt were added to the acid mine water samples to form a colloid suspension through the presence of turbidity, then absorbency was measured using a spectrophotometer with a wave length of 420 nm and the measurements recorded (Greenberg et al., 1992).

2.5 Measurement of pH

pH was measured using a pH meter that had been calibrated using a buffer of pH 4 and pH 7 with a stabilization time of 15 min. The electrodes were rinsed with distilled water and dried, and then dipped into the acid mine water treatment solutions (Greenberg et al., 1992).

2.6 Enumeration of the sulfate-reduction bacteria

The suspensions from the acid mine water treatment samples were made into serial dilutions by taking 1 mL from each sample, inoculating it in a reaction tube filled with 9 mL of sterile physiological salt solution (0.85%), and then homogenized using a vortex mixer. Then, 1 mL of suspension was placed into a petri dish containing Postgate medium and incubated at 37 °C for 48 h. Sodium lactate was used as a carbon source in the anaerobic chamber. Sulfate-reduction bacteria growth is marked by the formation of a dark brown or blackish colony due to the formation of iron sulfides. The Post gate standard medium contained per L: KH_2PO_4 0.5 g; NH_4Cl 1.0 g; $CaSO_4 \cdot 2H_2O$ 1.26 g; $MgSO_4 \cdot 7H_2O$ 2.0 g; Sodium lactate 3.5; Yeast extract 1.0 g; Ascorbic acid 0.1; Thioglycolic acid 0.1; $FeSO_4 \cdot 7H_2O$ 0.5 g (Atlas, 1993).

3. RESULTS AND DISCUSSION

3.1 The characterization of estuary sediment and acid mine water

The chemical characterization of estuary sediment and compost comprised of analyses of organic carbon, total phosphorus and total nitrogen; while the characterization of acid mine water comprised of sulfate concentration and pH analyses (Table 1). Results from X-ray Fluorescence (XRF) analysis of the mine water showed there was not much organic carbon, nitrogen and phosphorus, but had particularly higher concentrations of Fe, Mn, K, and sulfate. Therefore, mine water bioremediation required compost as a source of organic carbon. According to Hu et al. (2018), the availability of carbon sources is the critical limiting factor for sulfate-reducing bacteria reaction. In acid mine water, the carbon source is limited and requires additional or external carbon sources for successful treatment.

Table 1. Chemical characterization of estuary sediment, compost, and acid mine water

Estuary sediment	Value
Organic carbon	327,000 mg/L
Nitrogen	19,200 mg/L
Phosphor	8300 mg/L
Compost	Value
Organic carbon	386,000 mg/L
Nitrogen	32,300 mg/L
Phosphor	18,000 mg/L
Acid mine water	Value
Sulfate	1.18 mg/L
pH	3.2

Characterization of the sediment, compost and acid mine water was conducted to determine the initial condition of all acid mine water bioremediation treatment samples. The addition of 5% compost to the acid mine water bioremediation treatment was done due to the compost having a simple carbon content. The compost serves as nutrients for microbes for their growth and development during the reduction process in the acid mine water treatment. The donor electron is a molecular hydrogen sourced from organic compounds in compost and is required to enhance microbial activity for reduction of sulfate to hydrogen sulfide (Fukui and Takii, 1996; Zhao et al., 2010; Pester et al., 2012), while the reduction occurs by the presence of organic carbon as an electron donor (Sánchez-Andrea et al., 2014). The sulfur-reducing bacteria obtain energy through the reaction of organic compounds oxidation from compost to the reduction of sulfate or other sulfur compounds to sulphide (Matshusa-Masithi et al., 2009).

3.2 Sulfate concentration

The sulfate concentration measurement results of the acid mine water bioremediation treatments for treatment T1 containing estuary sediment and compost showed the treatment was able to reduce the sulfate concentration to 0.39 ppm on the 30th day, from an initial concentration of 0.92 ppm. Treatment T2 which contained sediment experienced a slight gradual decrease up to the 30th day with a sulfate concentration of 0.58, compared to the initial concentration of 1 ppm. Treatment T3 which only contained compost showed a small reduction in sulfate concentration on the 30th day at 0.67 ppm from an initial concentration of 0.92 ppm. Meanwhile, treatment T4, as the control, experienced the lowest reduction of sulfate concentration on the 30th day at 0.79 ppm compared to the initial concentration of 1.03 ppm (Figure 4).

The reduction of sulfate content in the treatments was caused by the activities of the sulfate-reducing bacteria from the estuary sediment. This caused a large reduction of sulfate concentration in treatment T1 and was also the case in T2 although not as large as the T1 treatment with compost. The reason for this is because the two treatments comprised of sediments act as an inoculating source of sulfate-reducing bacteria.

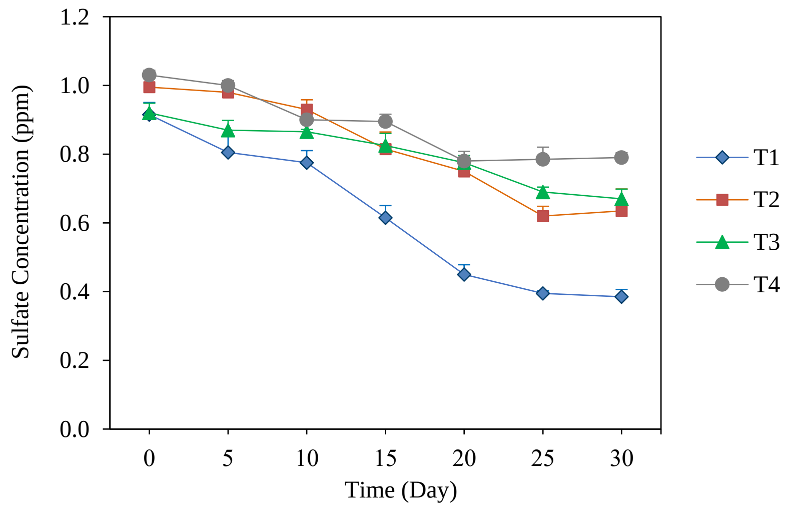

Figure 4. Sulfate concentration in acid mine water with treatments: 10% sediment and 5% compost (T1), 10% sediment (T2), 5% compost (T3) and without added sediment and compost (T4)

The estuary sediment is a wetland sediment with anaerobic environmental conditions that support the growth of anaerobic bacteria (Colin et al., 2017). Therefore, the sediment is rich in sulfate-reducing bacterial species (Fahruddin et al., 2018). However, the growth of these bacteria requires simple carbon and nutrients that can be obtained from compost that is rich with organic matter. The compost becomes the carbon sources for triggering sulfate-reducing bacteria to reduce sulfate producing sulfide and bicarbonate that affects the rise in pH (Dong et al., 2019). When only using sediment in the treatment, the sulfate-reducing bacteria do not get the energy of the oxidation of organic compounds as an electron donor to generate hydrogen sulfide under anaerobic conditions (Hu et al., 2018). Conversely, if only compost alone is present, there is no sulfate-reducing bacteria to reduce sulfate in acid mine water (Zhang and Wang, 2014).

Meanwhile, treatment T3 encountered a low reduction of sulfate-reducing bacteria from the compost. In the case of treatment T4 as the control, according to Fahruddin and Abdullah (2015), the lowest reduction of sulfate concentration was due to loss caused by the abiotic loss factor.

Wetland sediment contains a large amount of sulfate-reducing bacteria due to its high organic content that provides an ideal environment for its population (Fukui and Takii, 1996; Fichtel et al., 2012; Sánchez-Andrea et al., 2012). A simpler carbon source with a low molecule weight can be naturally found in the sediment which can act as an electron donor for the sulfate-reducing bacteria (Whitehead and Prior, 2005). This bacteria utilizes the sulfate contained in the acid mine water for its metabolic activities by transferring hydrogen to sulfate as an electron acceptor under anaerobic conditions using organic matter contained in sediments or compost as the electron source (Elliott et al., 1998). Therefore, sulfate is reduced to hydrogen sulfide, so the sulfate concentration will be reduced in the acid mine water. The molecular H_2S, formed from sulfate reduction, dissolves in acid mine water, as shown by the following reaction:

$$SO_4^{2-} + \text{organic matter} \xrightarrow[\text{anaerobic}]{\text{sulfate-reducing bacteria}} S^{2-} + H_2O + CO_2 \quad (1)$$

$$S^{2-} + 2H^+ \longrightarrow H_2S \quad (2)$$

The sulfate reduction process occurs during an anaerobic condition which is similar to respiration that uses oxygen as an electron acceptor on the aerobic condition, hence is called sulfate respiration or disimilatory sulfate reduction (Jansen et al., 1985; Bradley et al., 2011; Qian et al., 2018).

3.3 Change in pH values

The pH measurement results of the acid mine water bioremediation treatments are: Treatment T1 which contained estuary sediment and added compost showed a significant change in pH, from an initial value of pH 3.7 to pH 7.1 on the 30th day of observation. Treatment T2 which contained sediment showed a small change of pH value, from pH 3 to pH 5.4 on the 30th day of observation. Treatment T3 containing compost showed a very slight increase in pH, from pH 3.2 to pH 4.2 on the 30th day, while T4 as the control treatment did not see much of a change in pH value (Figure 5).

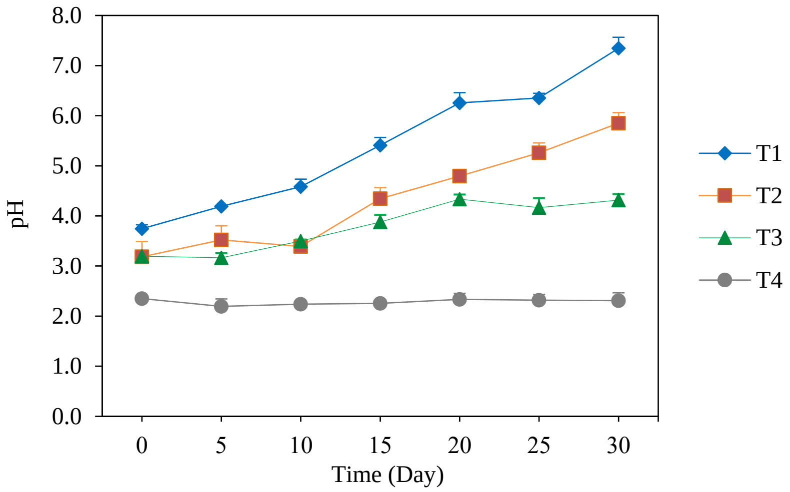

Figure 5. Changes of pH in acid mine water with treatments: 10% sediment and 5% compost (T1), 10% sediment (T2), 5% compost (T3) and without added sediment and compost (T4)

A change in pH is related to the decrease of sulfate concentration, which proves that the estuary sediment contains bacteria that are able to reduce sulfate into sulfide in acid mine water treatments (Luptakova and Kusnierova, 2005). This was the case for treatments T1 and T2; while there was not a significant change in pH for treatment T3 at only pH 4.2 and was similar to T4 because neither contained sediment as an inoculum source of sulfate-reducing bacteria (Whitehead and Prior, 2005).

The sulfate reduction process by the group of sulfate-reducing bacteria produces sulfide and bicarbonate that causes an increase in pH, the sulfide will react with the dissolved metal ions to create insoluble metal sulfides (Wu et al., 2017).

The reaction of sulfide minerals and water releases hydrogen ions that cause the pH value to decrease in acid mine water and is a conducive environment for the growth of *Thiobacillus ferooxidans* bacteria. This bacteria will accelerate the pyrite oxidation rate which will then form sulfuric acid. On the other hand, sulfate-reducing bacteria can increase pH or restore it to neutral pH through the reduction of sulfate into sulfide (H_2S) and releasing hydroxyl ions (OH^-) (Patel, 2010; Fahruddin and Abdullah, 2015).

3.4 Number of sulfate-reducing bacteria

The number of sulfate-reducing bacteria in the acid mine water bioremediation treatment was determined by the Standard Plate Count (SPC) method by using Postgate medium. The growth of blackish-brown colored bacterial colonies is the indicator of the presence of sulfate-reducing bacteria. The results showed that treatment T1 containing estuary sediment and added compost increased in the number of sulfate-reducing bacteria from initially 16×10^4 CFU/mL to 53×10^4 CFU/mL after 30 days. Treatment T2 containing sediment shows a reduction in the number of sulfate-reducing bacteria from 12×10^4 CFU/mL at the beginning to 11×10^4 CFU/mL on day 10, however their numbers increased to 53×10^4 CFU/mL on the 30th day. Treatment T3 which only comprised of compost showed a decrease in the number of sulfate-reducing bacteria until the 20th day, from initially 6×10^4 CFU/mL to 3×10^4 CFU/mL. However, their numbers slightly increased on the 30th day of observation to 8×10^4 CFU/mL. Meanwhile treatment T4 as the control shows the existence of sulfate-reducing bacteria in pure acid mine water which experienced a decrease from 5.7×10^4 CFU/mL at the beginning to 2×10^4 CFU/mL on the 30th day of observation (Figure 6).

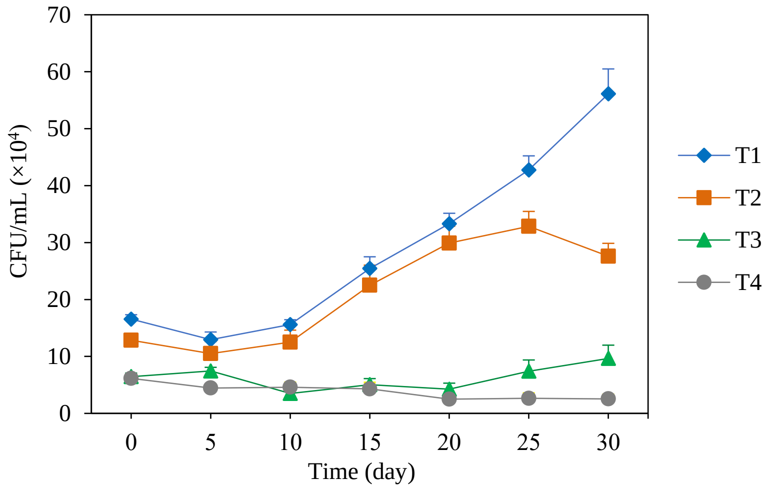

Figure 6. Number of sulfate-reducing bacteria in acid mine water with treatments: 10% sediment and 5% compost (T1), 10% sediment (T2), 5% compost (T3) and without added sediment and compost (T4).

There was a reduction in the number of sulfate-reducing bacteria up to the 10th day in all treatments; this was because some sulfate-reducing bacteria from the sediment and compost were unable to survive the very acidic conditions (Costa and Duarte, 2005; Whitehead and Prior, 2005; Pester et al., 2012). This is called the lag phase, where microbes in this condition will try to adapt to survive and those that do not will die. However, on the 15th day of treatments T1 and T2 saw a sharp increase in the number of sulfate-reducing bacteria up to the 30th day. This is called the log phase, where the bacterial cells that are able to survive low pH will increase in number (Kushkevych et al., 2017). On the other hand, the sulfate-reducing bacteria in treatment T3 saw almost no increase; this was also the case with treatment T4 as the control treatment where there was even a reduction in the number of cells. This is called the stationary phase and is followed by the death phase that is caused by an unsupportive environment, such as a very acidic environment, low pH, exhausted nutrients or toxic substances produced by the microbes themselves that can inhibit their growth (Meier et al., 2012; Kushkevych et al., 2017).

If we compare the treatments, we can see that the main source of the sulfate-reducing bacteria came from the sediment. There was more sulfate-reducing bacteria growth in treatments T1 and T2, whereas treatments T3 and T4 contained a very small number of sulfate-reducing bacteria. Hence, an increase in sulfate-inducing bacteria numbers can lower the concentration of sulfate, which follows an increase of pH value. Thus, estuary sediment as an inoculum source of sulfate-reducing bacteria is effective in lowering sulfate levels in acid mine water.

The results of this study were more successful in reducing sulfate of acid mine water using the estuary sediment as a source of sulfate-reducing bacteria inoculums with the addition of compost as source of nutrients, when compared to previous studies. Dong et al. (2019) recently reported that the removal percentages of sulfate in a column were

52.94%, and the effluent pH value was 6.56 with treatment of acid mine water by modified corncob fixed SRB sludge particles in the column test models. Yim et al. (2015) reported that passive treatment systems utilizing mushroom compost indicated a sulfate treatment efficiency of 63% within 120 days with a neutral pH value. Another monitoring study indicated a mushroom compost-based SAPS in Korea had sulfate removal efficiency of 7.8-20.3% (Cheong et al., 2010). Bai et al. (2013) reported that more than 61% of sulfate was removed and the effluent pH was improved from 2.75 to 6.20 during the operation. Furthermore, laboratory scale test with sawdust bioreactor gave removal efficiency of 50.27% on 35th day (Medírcio et al., 2007).

4. CONCLUSION

The use of sediment on the bioremediation of acid mine water has an effect on its sulfate content and pH value. Acid mine water treated with estuary sediments as a bacterial inoculum source has proven successful in reducing sulfate concentration and increasing pH value in acid mine water. This study utilized four types of treatments; the one with the best results was treatment T1 with added sediment and compost that was able to reduce sulfate by 78% as well as increasing pH to 7.1. In the case of treatment T2 with only added sediment, sulfate content decreased by 56% and pH was measured at 5.4, whereas treatment T3 with only added compost saw a reduction of 21% in sulfate content and a pH value of 4.2. It can be concluded that the application of estuary sediment on the treatment of acid mine water will be more effective in reducing sulfate if compost is also added. The sulfur-reducing bacteria obtain energy by oxidation of organic compounds from compost as an electron donor reacting with elemental sulfur in the acid mine water under anaerobic condition that utilizes sulfate as a terminal electron acceptor to generate hydrogen sulfide.

ACKNOWLEDGEMENTS

The researchers appreciate the efforts of the to Directorate General of Higher Education (DGHE), Indonesia for funds as Grants Research Program and appreciate the efforts of the Dean of Faculty of Mathematics and Natural Sciences, Hasanuddin University, Makassar, Indonesia on the implementation of this study.

REFERENCES

Abfertiawan MS, Gautama RS, Kusuma SB, Notosiswoyo S. Hydrology simulation of Ukud River in Lati Coal Mine. Journal of Novel Carbon Resource Sciences and Green Asia Strategy 2016;3(1):21-31.

Afriyie-Debrah C, Obiri-Danso K, Ephraim JH. Effect of acid mine drainage on creeks or streams in a mining community in Ghana and treatment options. International Journal of Environmental Science and Development 2010;1(5):399-403.

Atlas RM. Hand Book of Microbiologycal Media. Boca Raton, Florida, United States of America: CRC Press; 1993.

Bai H, Kang Y, Quan H, Han Y, Sun J, Feng Y. Treatment of acid mine drainage by sulfate reducing bacteria with iron in bench scale runs. Bioresource 2013;128:818-22.

Bradley AS, Leavitt WD, Johnston DT. Revisiting the dissimilatory sulfate reduction pathway. Geobiology 2011;9(5):446-57.

Burgos WD, Borch T, Troyer LD, Luan F, Larson LN, Brown JF, Lambson J, Shimizu M. Schwertmannite and Fe oxides formed by biological low-pH Fe(II) oxidation versus abiotic neutralization: Impact on trace metal sequestration. Geochimica et Cosmochimica Acta 2012;76:29-44.

Cheong YW, Bidus KD, Arup R, Jayanta B. Performance of a SAPS-based chemo-bioreactor treating acid mine drainage using low-DOC spent mushroom compost, and limestone as substrate. Mine Water and the Environment 2010;29:217-24

Colin Y, Goñi-Urriza M, Gassie C, Carlier E, Monperrus M, Guyoneaud R. Distribution of sulfate-reducing communities from estuarine to marine bay waters. Microbial Ecology 2017;73(1):39-49.

Compeau GC, Bartha R. Sulfate-reducing bacteria: Principal methylators of mercury in anoxic estuarine sediment. Applied and Environmental Microbiology 1985;5(2):498-502.

Costa MC, Duarte JC. Bioremediation of acid mine drainage using acidic soil and organic wastes for promoting sulphate-reducing bacteria activity on a column reactor. Water, Air, and Soil Pollution 2005;165(1-4):325-45.

Dai S, Ren D, ZhouY, Chou CL, Wang X, Zhao L, Zhu X. Mineralogy and geochemistry of a superhigh-organic-sulfur coal, Yanshan Coalfield, Yunnan, China: Evidence for a volcanic ash component and influence by submarine exhalation. Chemical Geology 2008;255(1-2):182-94.

Dong YR, Di JZ, Wang MX, Ren YD. Experimental study on the treatment of acid mine drainage by modified corncob fixed SRB sludge particles. Royal Society of Chemistry Advances 2019;9:19016-30.

Elliott P, Ragusa S, Catcheside D. Growth of sulfate-reducing bacteria under acidic conditions in an upflow anaerobic bioreactor as a treatment system for acid mine drainage. Water Research 1998;32(12):3724-30.

Fahruddin, Abdullah A. Use of organic materials wetland for improving the capacity of sulfate reduction bacteria (SRB) in reducing sulfate in acid mine water (AMW). Asian Journal of Microbiology, Biotechnology and Environmental Sciences Paper 2015;17(2):321-4.

Fahruddin, Abdullah A, Nafie NL. Sediment treatment for increasing pH and reducing heavy metal cadmium (Cd) in acid mine drainage. Applied Microbiology 2017;3(2):1-4.

Fahruddin F, Abdullah A, Nafie NL. Treatment of acid mine drainage waste using sediment as source of sulfate-reducing bacteria to reduce sulfates. Pollution Research Paper 2018;37(4):903-7.

Fichtel K, Falko M, Martin K, Heribert C, Bert E. Isolation of sulfate-reducing bacteria from sediments above the deep-sub sea floor aquifer. Frontiers in Microbiology 2012;3:65.

Fukui M, Takii S. Microdistribution of sulfate-reducing bacteria in sediments of a hypertrophic lake and their response to the addition of organic matter. Ecological Research 1996; 11(3):257-67.

Gaikwad RW, Sapkal VS, Sapkal RS. Acid mine drainage: A water pollution issue in mining industry. International Journal of Advanced Engineering Technology 2011;2(4):257-62.

Greenberg AE, Clesceri LS, Eaton AD. Standard Methods for the Examination of Water and Waste Water. Washington DC, United States of America: Public Health Association; 1992.

Hedrich S, Johnson DB. A Modular continuous flow reactor system for the selective bio-oxidation of iron and precipitation of schwertmannite from mine-impacted waters. Bioresource Technology 2012;106:44-9.

Hu X, Sobotka D, Czerwionka K, Zhou Q, Xie L, Makinia J. Effects of different external carbon sources and electron acceptors on interactions between denitrification and phosphorus removal in biological nutrient removal processes. Journal of Zhejiang University-SCIENCE B 2018;19(4):305-16.

Jansen KG, Fuchs, Thauer RK. Autotrophic CO_2 fixation by *Desulfovibrio baarsii*: Demonstration of enzyme activities characteristic for the acetyl-CoA pathway. FEMS Microbiology Letter 1985;28(3):311-5.

Johnson DB, Hallberg KB. Acid mine drainage remediation options: A review. Science of the Total Environment 2005;338(1-2):3-14.

Kushkevych I, Vítězová M, Fedrová P, Vochyanová Z, Paráková L, Hošek J. Kinetic properties of growth of intestinal sulphate-reducing bacteria isolated from healthy mice and mice with ulcerative colitis. Acta Veterinaria Brno 2017;86(4):405-11.

Luptakova A, Kusnierova M. Bioremediation of acid mine drainage contaminated by SRB. Hydrometallurgy 2005;77(1-2):97-102.

Mahmoud KK, Leduc LG, Ferroni GD. Detection of *Acidithiobacillus ferrooxidans* in acid mine drainage environments using fluorescent in situ hybridization (FISH). Journal of Microbiological Methods 2005:61(1):33-45.

Matshusa-Masithi MP, Ogola JS, Chimuka L. Use of compost bacteria to degrade cellulose from grass cuttings in biological removal of sulphate from acid mine drainage. Water SA 2009;35(1):111-6.

Medírcio SN, Leão VA, Teixeira MC. Specific growth rate of sulfate reducing bacteria in the presence of manganese and cadmium. Journal of Hazardous Materials 2007;143(1-2): 593-6.

Meier J, Piva A, Fortin D. Enrichment of sulfate-reducing bacteria and resulting mineral formation in media mimicking pore water metal ion concentrations and pH conditions of acidic pit lakes. FEMS Microbiology Ecology 2012;79(1):69-84.

Patel AK. Isolation and characterization of *Thiobacillus ferrooxidans* from coal acid mine drainage. International Journal of Applied Agricultural Research 2010;5(1):73-85.

Pester M, Knorr KH, Friedrich MW, Wagner M, Loy A. Sulfate-reducing microorganisms in wetlands-fameless actors in carbon cycling and climate change. Frontiers in Microbiology 2012;3:1-19.

Purdy KJ, Embley TM, Nedwell DB. The distribution and activity of sulphate reducing bacteria in estuarine and coastal marine sediments. Antonie van Leeuwenhoek 2002;81(1-4):181-7.

Qian Z, Tianwei H, Mackey HR, Loosdrecht MCMV, Guanghao C. Recent advances in dissimilatory sulfate reduction: From metabolic study to application. Water Research 2018;150:162-81.

Sánchez-Andrea I, Triana D, Sanz JL. Bioremediation of acid mine drainage coupled with domestic wastewater treatment. Water Science and Technology 2012;66(11):2425-31.

Saviour MN. Environmental impact of soil and sand mining: A review. International Journal of Science, Environment and Technology 2012;1(3):125-34.

Simate GS, Ndlovu, S. Acid mine drainage: Challenges and opportunities. Journal of Environmental Chemical Engineering 2014;2(3):1785-803.

Whitehead PG, Prior H. Bioremediation of acid mine drainage: An introduction to the Wheal Jane wetlands project. Science of The Total Environment 2005;338(1-2):15-21.

Widodo S, Sufriadin, Ansyariah, Budiman AA, Asmiani N, Jafar N, Babay MF. Characterization of the mineral pyrite on coal based on results of microscopy, proximate, sulfur total analysis, and x-ray diffraction: Potential for the existence of acid mine water. Jurnal Geosapta 2019;5(2):121- 6.

Widodo S, Sufriadin, Imai A, Anggayana K. Characterization of some coal deposits quality by use of proximate and sulfur analysis in the Southern Arm Sulawesi. Indonesia International Journal of Engineering and Science Applications 2016;3(2):137-44.

Widyati E. The use of sulphate-reducing bacteria in bioremediation of ex-coal mining soil. Biodiversitas 2007;8(4):283-6.

Wu J, Liu H, Wang P, Zhang D, Sun Y, Li E. Oxygen reduction reaction affected by sulfate-reducing bacteria: Different roles of bacterial cells and metabolites. Indian Journal of Microbiology 2017;57(3):344-50.

Yim G, Ji S, Cheong Y, Neculita CM, Song H. The influences of the amount of organic substrate on the performance of pilot-scale passive bioreactors for acid mine drainage treatment. Environmental Earth Sciences 2015;73(8):4717-27.

Zhang M, Wang H. Organic wastes as carbon sources to promote sulfate reducing bacterial activity for biological remediation of acid mine drainage. Minerals Engineering 2014;69:81-90.

Zhao YG, Wang AJ, Ren NQ. Effect of carbon sources on sulfidogenic bacterial communities during the starting-up of acidogenic sulfate-reducing bioreactors. Bioresource Technology 2010;101(9):2952-9.

Responses to Flooding of Two Riparian Tree Species in the Lowland Tropical Forests of Thailand

Boontida Moungsrimuangdee*, Panya Waiboonya, Prapatsorn Yodsa-nga, and Panadda Larpkern

Bodhivijjalaya College, Srinakharinwirot University, Nakhon Nayok 26120, Thailand

ARTICLE INFO

Received: 24 Sep 2019
Received in revised: 13 Jan 2020
Accepted: 21 Jan 2020
Published online: 27 Feb 2020
DOI: 10.32526/ennrj.18.2.2020.19

Keywords:
Flood-tolerant species/ *Hydnocarpus anthelminthicus*/ Riparian Forest/ Stress/ Waterlogging/ *Xanthophyllum lanceatum*

*** Corresponding author:**
E-mail: boonthida@g.swu.ac.th

ABSTRACT

Responses of riparian woody species, especially in the tropical forests of Thailand, under flooding condition remain unknown. The effects of flooding on growth of the native species, *Hydnocarpus anthelminthicus* and *Xanthophyllum lanceatum*, which dominate in the lowland tropical forests in the East of Thailand, were observed during 16 weeks. The growth and morphological responses were determined in one-year-old seedlings, which stems were submerged at a level of 3 cm above the soil surface (flooded). They were compared to the control (unflooded) at every 2, 4, 8, 12, and 16 weeks. Flooding did not suppress shoot elongation in *H. anthelminthicus* and *X. lanceatum* over the study period. In general, leaf, stem, and root biomass were not significantly different between flooded and unflooded seedlings in both species. Adventitious roots were found in flooding seedlings of both species, while hypertrophied lenticels were not formed during the submergences. In addition, senescence, necrosis, abscission, or mortality were not observed in the flooded seedlings in this study. Preliminarily, *H. anthelminthicus* and *X. lanceatum* could be considered as potential species for restoring the riparian forest, especially in the studied region.

1. INTRODUCTION

Flooding negatively affects growth and development of many woody plants (Kozlowski, 1997). Numerous reports have demonstrated the effects of flooding on morphological and physiological responses in both gymnosperms and angiosperms (Yamamoto and Kozlowski, 1986; Yamamoto, 1992; Lopez and Kursar, 1999; Sakio, 2005; Higa et al., 2012). Vegetative and reproductive growth suppression, alternation of plant anatomy, and promotion of senescence and mortality usually occur in most terrestrial plants under flooding condition. Plants that tolerate waterlogged conditions can survive by using the complexity of interactions of morphological, anatomical, and physiological adaptations, such as formation of hypertrophic stem growth, aerenchyma tissue and adventitious roots (Kozlowski and Pallardy, 1979; Yamamoto et al., 1995; Wang and Cao, 2012; Oliveira et al., 2015). Such various reactions to tolerate flooding depend on plant species and genotype, age, properties of the floodwater, and time or duration of flooding (Kozlowski, 1984).

Riparian forests occur along bodies of water, such as streams, lakes, and rivers, and they play an important role by providing environmental services to both aquatic and terrestrial ecosystems (Broadmeadow and Nisbet, 2004; Gunderson et al., 2010). Particularly, riparian vegetation is crucial for freshwater landscape by regulating flow of sediment and nutrients (Luke et al., 2007; Mayer et al., 2007), moderating light and temperature for aquatic life (Broadmeadow and Nisbet, 2004), filtering the heavy metals from agricultural land (Zhang et al., 2010; Pavlovic et al., 2016), providing habitat for forest species (Waiboonya et al., 2016; Moungsrimuangdee et al., 2017a) and reducing soil erosion and stabilizing the stream banks (USDA National Agroforestry Center, 1997).

Phra Prong River, the origin of Bang Pakong River, is one of the most important rivers in the East of Thailand. It represents a freshwater ecosystem for

Citation: Moungsrimuangdee B, Waiboonya P, Yodsa-nga P, Larpkern P. Responses to flooding of two riparian tree species in the lowland tropical forests of Thailand. Environ. Nat. Resour. J. 2020;18(2):200-208. DOI: 10.32526/ennrj.18.2.2020.19

biodiversity conservation and supplying foods and water use for the local people livelihood (Moungsrimuangdee et al., 2017b; Yodsanga et al., 2017). Riparian forests along Phra Prong River have dramatically declined in the last decades due to an expansion of agricultural land and irrigation management practices. Consequently, the distribution and regeneration of native tree species have been severely affected (Moungsrimuangdee et al., 2015).

Regular and irregular flooding are considered to be major factors influencing riparian species diversity and habitat (Uowolo et al., 2005). Few studies have focused on the effects of flooding on riparian species composition and abundance, especially in the tropical forests of Thailand. In addition, the flood-tolerant trees of the tropical forests in this region have also rarely been investigated. Therefore, in this study, we focused on the responses of *Hydnocarpus anthelminthicus* and *Xanthophyllum lanceatum*, the native and dominant tree species of Phra Prong riparian forest of the Eastern Thailand, to flooded condition. Currently, constitutive defense responses to cope with the stress of these species are still not known. Flooded responses of the native species could explain the habitat and ecological characteristics of these species and provide more insight into riparian restoration efforts which are highly required in this area.

2. METHODOLOGY

2.1 Study site and study species

Hydnocarpus anthelminthicus Pierre ex Laness. (Achariaceae) and *Xanthophyllum lanceatum* J. J. Sm. (Polygalaceae) were selected in this study. They are commonly found, and classified as dominant trees in the riparian forests of Phra Prong River according to our previous studies (Moungsrimuangdee et al., 2015; Nawajongpan and Moungsrimuangdee, 2016; Moungsrimuangdee et al., 2017a). In addition, both species often grow in the freshwater swamp forest of Thailand (Santisuk, 2012). On July 2015, seeds of these species were collected from the mature trees growing naturally in the riparian forest found along the Phra Prong River, located in Watthana Nakhon District, Sa Kaeo Province. Seeds were sown in plastic trays containing sandy soils. Seedlings with at least two pairs of true leaves were transplanted into plastic bags containing a forest soil collected form the riparian forest of Phra Prong River. The plants were raised at the nursery of the Bodhivijjalaya College, Srinakharinwirot University, Sa Kaeo, located close to the river. One-year-old seedlings were transplanted into plastic pots (15 cm × 15 cm × 18 cm), containing the forest soils mentioned above. They were left to grow in the nursery under the same conditions with watering, pesticides and fertilizations for three months. Climatic data (2006-2015) at the study site showed 28.5 ^{o}C mean annual air temperature with 73% mean annual relative air humidity and 1,200 mm annual sum of precipitation (Meteorological Department, 2016).

2.2 Experimental design

On November 2016, seedlings of each species were selected for uniform size and development. The selected seedlings were divided into two treatments, unflooded and flooded, with three replications (35 seedlings per replication). For each treatment, another five seedlings of each species were randomly harvested for biomass analysis at the beginning of the experiment. The average height and stem diameter at ground level of each species at the initial stage were measured. The size of seedlings at the starting time did not differ significantly between the unflooded and flooded seedlings ($p<0.05$, t-test) as shown in Table 1.

Table 1. Size of the seedlings at the initial stage. Data are given as mean±standard error. D0 means stem diameter at ground level.

Species	Unflooded		Flooded	
	Height (cm)	D0 (mm)	Height (cm)	D0 (mm)
Hydnocarpus anthelminthicus	42.37±1.05	4.85±0.12	42.31±1.01	4.43±0.12
Xanthophyllum lanceatum	35.36±0.77	5.52±0.16	35.58±0.84	4.83±0.17

The treatments with flooding were applied by placing the seedling pots in the water-filled containers providing water received from the Phra Prong River at a level of 3 cm above the soil surface (roots and the basal part of the stems flooded). Water was added periodically to keep the water level steadily without changing the water throughout the experiment. The unflooded seedlings were daily watering to prevent soil desiccation. All seedlings were grown in the nursery under the shading net giving 40% of full sunlight.

2.3 Data collection and analysis

Shoot elongation or shoot height, number of leaves, leaf area, biomass, and total nitrogen in leaves were determined after 2, 4, 8, 12, and 16 weeks. Seedling mortality, adventitious roots, hypertrophied lenticels, and leaf chlorosis or necrosis were also observed until the end of the study period. Seven seedlings in each replication of all treatments were harvested at each data collection. All fresh leaves of the harvested seedlings were scanned into JPEG image format using a scanner (Canon Scan MF4800; Canon Inc., Tokyo, Japan). Then leaf area was calculated by using free online software (ImageJ) (https://imagej.nih.gov/ij/index.html) (Moungsrimuangdee et al., 2011). For biomass analysis, all harvested seedlings were separated into leaves, stems and roots. All portions were then separately dried at 70 °C, 48-72 h until samples reached a constant dry weight (University of Idaho, 2009). Composite samples of leaves from each individual replication within the treatment were taken from the dry material for a total nitrogen analysis according to the Kjeldahl method (1883). The differences in the mean values between the treatments were analyzed by using a t-test ($p<0.05$). Statistical analyses were performed with PAST version 3.22 (Hammer et al., 2001).

3. RESULTS

3.1 Shoot elongation

Flooding did not reduce the shoot elongation of *H. anthelminthicus* and *X. lanceatum* throughout the experiment. Besides, the shoot growth of the flooded plants was higher than those unflooded seedlings in all submerged periods (Figure 1 and 2). In *X. lanceatum*, shoots of flooded seedlings distinctly increased in comparison with unflooded seedlings after 12 weeks of the experiment (Figure 2). However, there were no significant differences among the treatments in both species (Figure 1 and 2).

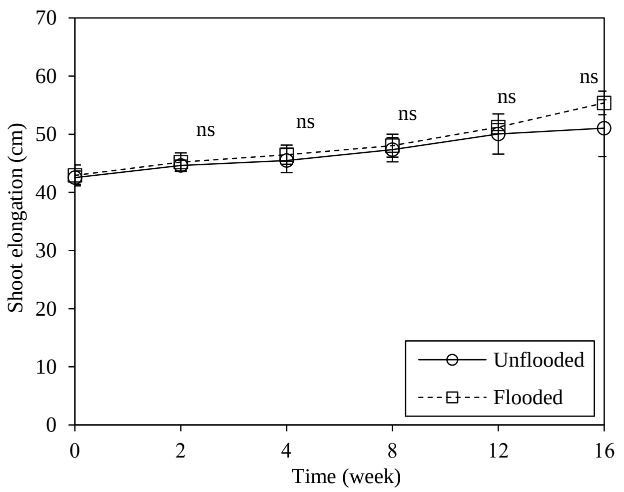

Figure 1. Shoot elongation in flooded and unflooded seedlings of *H. anthelminthicus*. Data are given as mean±standard error (ns represents the non-significant difference between the unflooded and flooded seedlings within the same submerged period at $p<0.05$ by t-test).

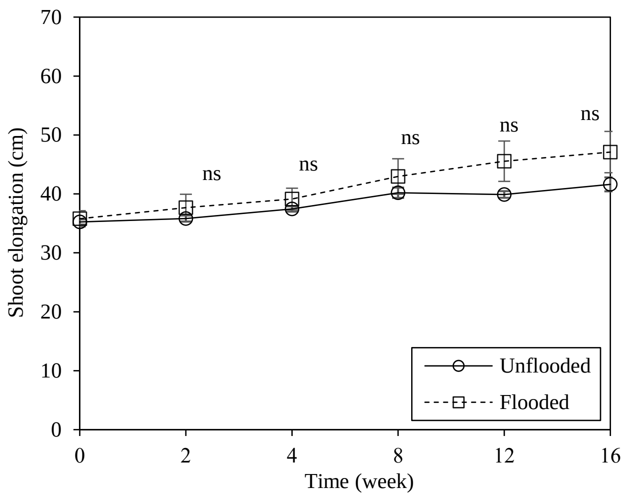

Figure 2. Shoot elongation in flooded and unflooded seedlings of *X. lanceatum*. Data are given as mean±standard error (ns represents the non-significant difference between the unflooded and flooded seedlings within the same submerged period at $p<0.05$ by t-test).

3.2 Number of leaves and leaf area

Leaves slightly decreased in flooded seedlings of *H. anthelminthicus* after 2 weeks of the submergence and gradually increased after 4 weeks until the end of the experiment (Figure 3). The number of leaves was lower in flooded than in unflooded seedlings in all time periods (Figure 3). In *X. lanceatum*, flooded seedlings had almost the same number of leaves as unflooded seedlings in all time periods, except in weeks 8 and 16 in which the flooded were lower than in unflooded (Figure 4). However, *H. anthelminthicus* and *X. lanceatum* leaf numbers did not significantly differ between treatments and periods. Pattern of leaf area was similar in the flooded and unflooded *H. anthelminthicus*. Leaf area decreased after 2 weeks, then slightly increased after 4 weeks of the experiment in both treatments (Figure 5). Flooded *X. lanceatum* reached the highest leaf area after 12 weeks (Figure 6).

3.3 Biomass

Leaf, stem, and root biomass of *H. anthelminthicus* seedlings were not significantly different among the flooded and unflooded treatments within studied periods (Table 2). In general, flooded seedlings of *H. anthelminthicus* showed higher dry weight of leaves, stems, and roots than unflooded, except seedlings after 12 weeks and 16 weeks (Table 2). A similar trend was found in *X. lanceatum*, in which dry weight did not differ significantly among treatments, except in week 4 and week 12, where flooded plants' stem biomass were significantly higher than unflooded (t-test, $p<0.05$, Table 3).

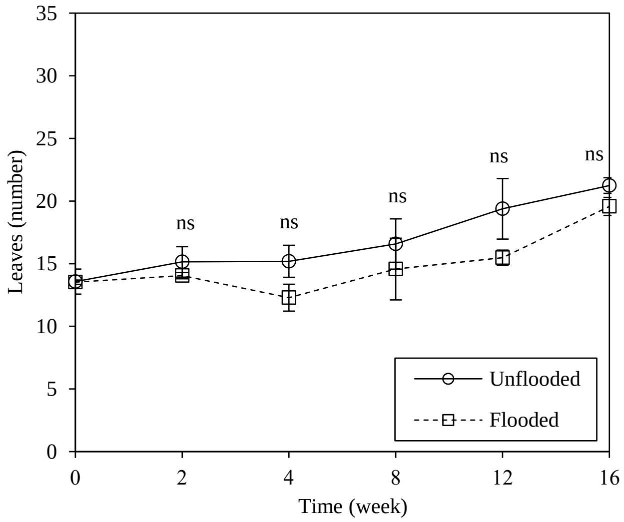

Figure 3. Number of leaves in flooded and unflooded seedlings of *H. anthelminthicus*. Data are given as mean±standard error (ns represents the non-significant difference between the unflooded and flooded seedlings within the same submerged period at p<0.05 by t-test).

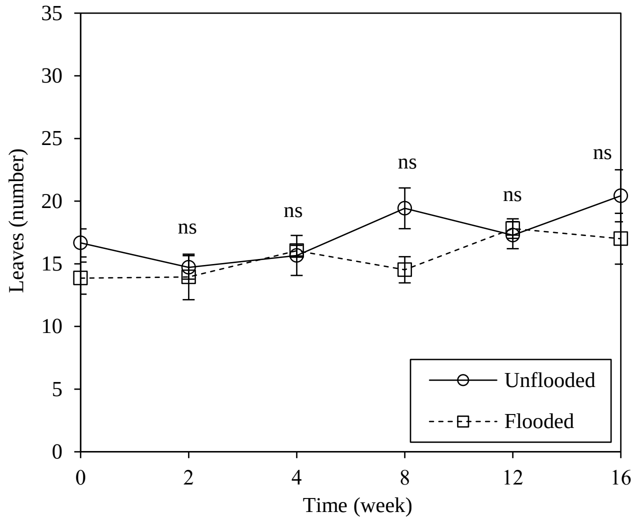

Figure 4. Number of leaves in flooded and unflooded seedlings of *X. lanceatum*. Data are given as mean±standard error (ns represents the non-significant difference between the unflooded and flooded seedlings within the same submerged period at p<0.05 by t-test).

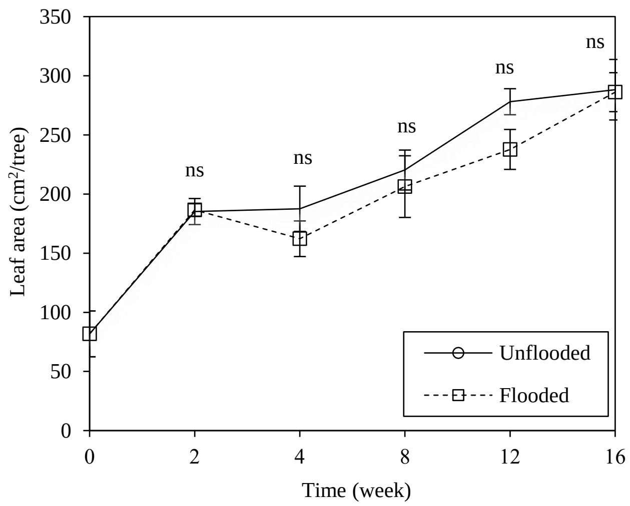

Figure 5. Leaf area in flooded and unflooded seedlings of *H. anthelminthicus.* Data are given as mean±standard error (ns represents the non-significant difference between the unflooded and flooded seedlings within the same submerged period at p<0.05 by t-test).

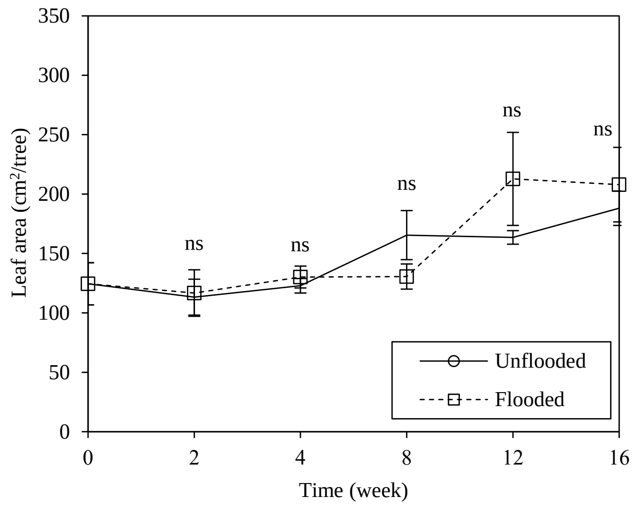

Figure 6. Leaf area in flooded and unflooded seedlings of *X. lanceatum*. Data are given as mean±standard error (ns represents the non-significant difference between the unflooded and flooded seedlings within the same submerged period at p<0.05 by t-test).

Table 2. Leaf, stem, and root biomass of *H. anthelminthicus*. Data are given as mean±standard error (ns represents the non-significant difference between the unflooded and flooded seedlings within the same submerged period at $p<0.05$ by t-test).

Biomass	Submerged period (week)					
	0	2	4	8	12	16
Leaves (g)						
Unflooded	1.20 ± 0.25^{ns}	3.67 ± 0.09^{ns}	4.36 ± 0.23^{ns}	3.68 ± 0.42^{ns}	5.36 ± 0.40^{ns}	4.04 ± 0.28^{ns}
Flooded	0.69±0.09	3.89±0.08	4.44±0.19	3.92±0.62	5.50±0.31	3.96±0.16
Stems (g)						
Unflooded	1.66 ± 0.58^{ns}	3.49 ± 0.19^{ns}	4.19 ± 0.44^{ns}	4.89 ± 0.51^{ns}	5.77 ± 0.27^{ns}	4.97 ± 1.06^{ns}
Flooded	0.95±0.24	3.94±0.06	4.44±0.17	5.20±0.58	5.84±0.07	6.00±0.48
Roots (g)						
Unflooded	1.44 ± 0.44^{ns}	4.66 ± 0.15^{ns}	5.53 ± 1.09^{ns}	4.35 ± 0.67^{ns}	5.73 ± 0.35^{ns}	6.13 ± 0.74^{ns}
Flooded	0.73±0.18	4.82±0.24	5.95±0.24	4.37±0.52	5.12±0.18	5.20±0.56
Total (g)						
Unflooded	4.30 ± 1.17^{ns}	11.82 ± 0.13^{ns}	14.08 ± 1.69^{ns}	12.92 ± 1.41^{ns}	16.86 ± 0.53^{ns}	15.14 ± 1.40^{ns}
Flooded	2.37±0.47	12.64±0.34	14.82±0.30	13.49±1.65	16.46±0.22	15.16±1.17

Table 3. Leaf, stem, and root biomass of *X. lanceatum*. Data are given as mean±standard error (* represents the significant difference between the unflooded and flooded seedlings within the same submerged period at $p<0.05$ by t-test, ns represents the non-significant difference).

Biomass	Submerged period (week)					
	0	2	4	8	12	16
Leaves (g)						
Unflooded	1.47 ± 0.38^{ns}	2.96 ± 0.08^{ns}	3.76 ± 0.12^{ns}	3.32 ± 0.13^{ns}	4.37 ± 0.34^{ns}	3.36 ± 0.32^{ns}
Flooded	1.31±0.32	3.09±0.14	4.93±0.42	2.90±0.31	6.18±0.64	3.62±0.25
Stems (g)						
Unflooded	2.42 ± 0.49^{ns}	3.94 ± 0.31^{ns}	$2.95 \pm 0.07^{*}$	4.14 ± 0.08^{ns}	$4.83 \pm 0.06^{*}$	4.11 ± 0.21^{ns}
Flooded	2.47±0.50	4.27±0.43	3.82±0.20	3.93±0.21	6.16±0.46	4.98±0.62
Roots (g)						
Unflooded	2.16 ± 0.55^{ns}	2.59 ± 0.29^{ns}	4.11 ± 0.47^{ns}	4.49 ± 0.45^{ns}	5.04 ± 0.16^{ns}	5.68 ± 0.28^{ns}
Flooded	2.08±0.39	3.02±0.33	4.57±0.86	3.68±0.18	5.41±0.36	4.55±0.41
Total (g)						
Unflooded	6.05 ± 1.21^{ns}	9.49 ± 0.65^{ns}	10.82 ± 0.45^{ns}	11.96 ± 0.59^{ns}	14.25 ± 0.48^{ns}	13.15 ± 0.45^{ns}
Flooded	5.88±0.74	10.39±0.88	13.32±1.31	10.51±0.30	17.75±1.27	13.16±1.04

3.4 Root:shoot ratio

Changes of root:shoot ratio were analyzed to better understanding the effect of flooding on biomass allocation of the submerged seedlings. The root:shoot ratio of the flooded plants was less than in the unflooded in the *H. anthelminthicus* seedlings, without statistically significant differences over the studied periods (Figure 7). In contrast, flooding was found to significantly reduced root:shoot ratio of *X. lanceatum* at week 12 (t-test, $p<0.01$) and week 16 (t-test, $p<0.05$), compared to the unflooded seedlings (Figure 8).

3.5 Total nitrogen

The total nitrogen of *H. anthelminthicus* was significantly less in flooded than in unflooded seedlings at week 2, 4, and 8, but it was slightly increased, almost at the same rate as unflooded, as shown in week 12 and 16 (Figure 9). The differences of total nitrogen among treatments were not found significant in *X. lanceatum* (Figure 10).

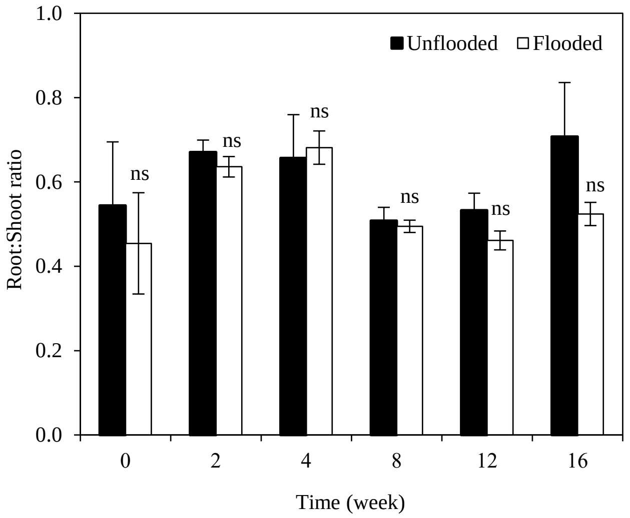

Figure 7. Root:shoot ratio in flooded and unflooded seedlings of *H. anthelminthicus*. Data are given as mean±standard error (ns represents the non-significant difference between the unflooded and flooded seedlings within the same submerged period at p<0.05 by t-test).

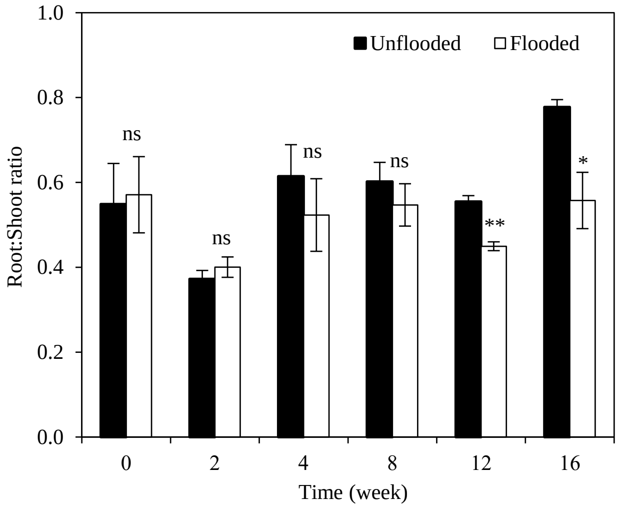

Figure 8. Root:shoot ratio in flooded and unflooded seedlings of *X. lanceatum*. Data are given as mean±standard error (** and * represent the significant difference between the flooded and unflooded seedlings within the same submerged period at p<0.01 and 0.05 by t-test, respectively, ns represents the non-significant difference).

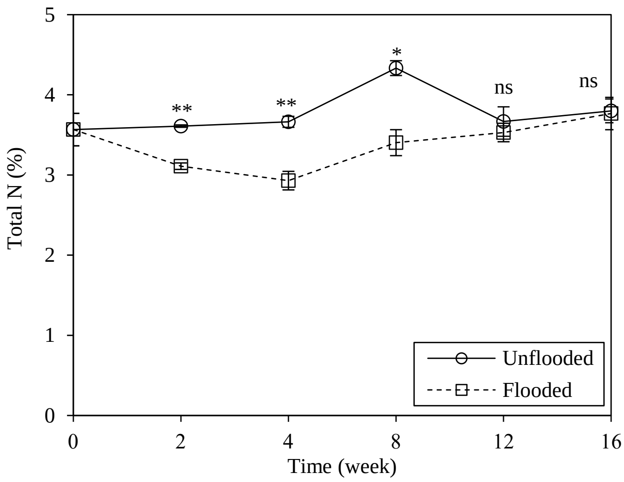

Figure 9. Total N in flooded and unflooded seedlings of *H. anthelminthicus*. Data are given as mean±standard error (** and * represent the significant difference between the unflooded and flooded seedlings within the same submerged period at p<0.01 and 0.05 by t-test, respectively, ns represents the non-significant difference).

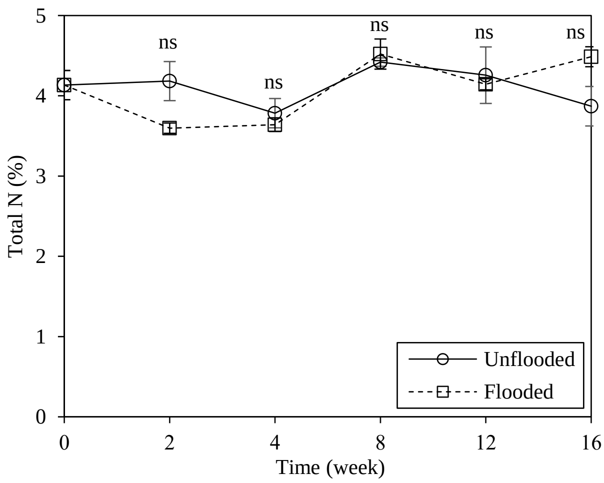

Figure 10. Total N in flooded and unflooded seedlings of *X. lanceatum*. Data are given as mean±standard error (ns represents the non-significant difference between the unflooded and flooded seedlings within the same submerged period at p<0.05 by t-test).

3.6 Adventitious roots

No adventitious roots were found in the unflooded seedlings of both species. The formation of adventitious roots, which were found only in flooded treatments, developed faster in *H. anthelminthicus* than in *X. lanceatum* seedlings. Adventitious roots were formed at week 4 in *H. anthelminthicus*, while adventitious roots of *X. lanceatum* developed later, in week 16 (Figure 11). In addition, the hypertrophied lenticels, an enlarged pore through which gases are exchanged between plant and air, were looked for during the study. These types of lenticels were not found in any of the species.

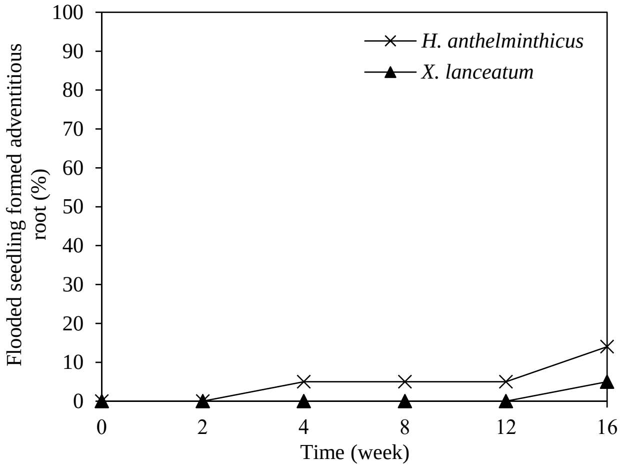

Figure 11. Percentage of flooded seedlings that formed adventitious roots.

4. DISCUSSION

Flooding has been shown to have various effects on riparian species. Shoot growth was found to be inhibited during flooding in several species, such as *Taxodium distichum* (Yamamoto, 1992), *Lepidium latifolium* (Chen et al., 2002), *Alnus japonica* (Iwanaga and Yamamoto, 2008), *Populus euphratica* (Yu et al., 2015) , *Pinus elliottii* (Yang and Li, 2016), and *Alternanthera philoxeroides* (Luo et al., 2018). In contrast, flooding promoted shoot growth and biomass of some riparian species such as *Nyssa aquatica* (McKevlin et al., 1995), *Pterocarya stenoptera* (Yang and Li, 2016), and *Fraxinus excelsior* and *Quercus robur* (Heklau et al., 2019). Plants have responded by adjusting the combination of morphology, physiology, and biochemistry for surviving under the flooding condition such as the recovery of photosynthetic rate and stomatal conductance, enhancement of ethylene production, induction of hypertrophy of lenticels, and formation of adventitious roots containing aerenchyma tissue. In this study, leaf senescence, necrosis, abscission, and mortality were not observed in *H. anthelminthicus* and *X. lanceatum* under the flooding condition. These signs typically occur when plants are under flooding stress. The studied species, therefore, are flood-tolerant species.

Flooding did not affect shoot growth in the two species during 16 weeks of submergence. *X. lanceatum* exhibited a high tolerance to soil flooding by stimulating stem growth and the same rate of leaf growth (number of leaves and leaf area) as the control. *H. anthelminthicus* showed a reduction of leaf growth at week 4, but it gradually increased to an equal number as the control at the end of the experiment. Root growth of flooded *H. anthelminthicus* and *X. lanceatum* was lower than stem growth. This symptom was expressed in the decrease of root:shoot ratio. In woody species, the root typically grows slower than the shoot because the flooding leads to the decay of the root system (Kozlowski, 1997).

Flooding also induces certain morphological changes of wetland species. For example, the formation of adventitious roots, initiation of hypertrophied lenticels, and enhancement of aerenchyma tissue formation (Pezeshki, 2001). In this study, *H. anthelminthicus* developed adventitious roots at the beginning of the period, at week 4, while, *X. lanceatum* produced them later, at week 16. Hypertrophied lenticels, pores for exchange of gas, were not found in this study. The delay of adventitious root formation and lack of hypertrophied lenticels may affect growth and development of root and shoot in the flooded woody species. Many reports describe the importance of adventitious roots as the shoot growth supporter during prolonged flooding, especially in flood-tolerant species (Jackson, 1985; Armstrong et al., 1994; Islam and MacDonald, 2004; Pernot et al., 2019). Iwanaga and Yamamoto (2008) indicate the coincidental relationship between adventitious root formation and recovery of reduced photosynthetic rate in *Alnus japonica* under the water stress. Tsukahara and Kozlowski (1985) also report that height and diameter growth in flooded *Platanus occidentalis* seedlings decreased after removing adventitious roots from submerged portions of stem.

The current study showed that flooded *H. anthelminthicus* and *X. lanceatum* seedlings produced few adventitious roots with no effects on shoot growth. The function of adventitious roots in these species may play an important role in the growth and vitality of flooded seedlings. This could be investigated in future experiments of these two species by expanding study periods of flooding and various levels of submergences. Hypertrophied lenticels were not found in *H. anthelminthicus* and *X. lanceatum* seedlings under flooding condition during the study period. These lenticels were slowly developed in *Calophyllum longifolium* and *Virola surinamensis* during a flooding experiment, which resulted in root death and blocked the root growth (Lopez and Kursar, 1999). This indicates that the existence of adventitious roots and hypertrophied lenticels in response to flooding stress may present various effects depending on the species.

Extended flooding more than 12 weeks increased aboveground biomass and greatly decreased root:shoot ratio observed in *X. lanceatum* seedlings. It is possible that *X. lanceatum* seedlings escape the excessive water condition by elongating the stem length to obtain more oxygen and accumulate leaf biomass to enhance the photosynthetic efficiency to survive under flooding stress, an adaptive mechanism described by Yang and Li (2016) found in *Ptercarya stenoptera* and *Pinus elliottii* seedlings and Pires et al. (2018) found in *Genipa americana* from the dryland of Central Brazil. In addition, a decrease in biomass allocation to roots diminishes the metabolic requirement and stressed roots for oxygen, water and nutrient uptake (Naidoo and Naidoo, 1992).

5. CONCLUSIONS

Despite finding that flooding had negligible effects on growth in both *H. anthelminthicus* and *X. lanceatum*, further studies should focus on physiological and biochemical responses, which are easily induced through short-term soil flooding conditions, to provide more insights into constitutive adaptations of these species. In overall, our results indicated that *H. anthelminthicus* and *X. lanceatum* are considered to be flood-tolerant species because none of the seedlings had died by the end of the study. Therefore, both native species are promising candidates for the riparian restoration in this region.

ACKNOWLEDGEMENTS

This research was funded by a grant of Strategic Wisdom and Research Institute, Srinakharinwirot University (No. 564/2559). We thank Maliwan Saeyang for field work assistance. We also thank Marit Eriksen for her valuable advices for improving our manuscript.

REFERENCES

Armstrong W, Brandle R, Jackson MB. Mechanism of flood tolerance in plants. Acta Botanicz Neerlandica 1994;43:307-58.

Broadmeadow S, Nisbet TR. The effects of riparian forest management on the freshwater environment: A literature review of best management practice. Hydrology and Earth System Sciences Discussions 2004;8:286-305.

Chen H, Qualls RG, Miller GC. Adaptive responses of *Lepidium latifolium* to soil flooding: Biomass allocation, adventitious rooting, aerenchyma formation and ethylene production. Environmental and Experimental Botany 2002;48:119-28.

Gunderson P, Lauren A, Finer L, Ring E, Koivusalo H, Saeersdal M, Weslien J, et al. Environmental services provided from riparian forests in the Nordic countries. AMBIO 2010; 39:555-66.

Hammer Ø, Harper DAT, Ryan PD. PAST: Paleontological statistics software package for education and data analysis. Palaeontologia Electronica 2001;4:4-9.

Heklau H, Jetschke G, Bruelheide H, Seidler G, Haider S. Species-specific responses of wood growth to flooding and climate in floodplain forests in Central Germany. iForest 2019;12:226-36.

Higa M, Moriyama T, Ishikawa S. Effects of complete submergence on seedling growth and survival of five riparian tree species in the warm-temperate regions of Japan. Journal of Forest Research 2012;17:129-36.

Islam MA, MacDonald SE. Ecophysiological adaptations of black spruce (*Picea mariana*) and tamarack (*Larix laricina*) seedlings to flooding. Trees 2004;18:35-42.

Iwanaga F, Yamamoto F. Effects of flooding depth on growth, morphology and photosynthesis in *Alnus japonica* species. New Forests 2008;35:1-14.

Jackson MB. Ethylene and responses of plants to soil waterlogging and submergence. Annual Review of Plant Physiology 1985;36:145-74.

Kjeldahl J. A new method for the determination of nitrogen in organic matter. Zeitschrift für Analytische Chemie 1883;22:366-82.

Kozlowski TT. Responses of woody plants to flooding. In: Kozlowski TT, editor. Flooding and Plant Growth. Orlando, FL: Academic Press; 1984. p. 129-63.

Kozlowski TT, Pallardy SG. Stomatal responses of *Fraxinus pennsylvanica* seedlings during and after flooding. Physiologia Plantarum 1979;46:155-8.

Kozlowski TT. Responses of woody plants to flooding and salinity. Tree Physiology Monograph No.1 1997:1-29.

Lopez OR, Kursar TA. Flood tolerance of four tropical tree species. Tree Physiology 1999;19:925-32.

Luke SH, Luckai NJ, Burke JM, Prepas EE. Riparian areas in the Canadian Boreal Forest and linkages with water quality in streams. Environmental Reviews 2007;15:79-97.

Luo FL, Matsubara S, Chen Y, Wei GW, Dong BC, Zhang MX, Yu FH. Consecutive submergence and de-submergence both impede growth of a riparian plant during water level fluctuations with different frequencies. Environmental and Experimental Botany 2018;155:641-9.

Mayer PM, Reynolds SK, McMutchen MD, Canfield TJ. Metaanalysis of nitrogen removal in riparian buffers. Journal of Environment Quality 2007;36:1172-80.

McKevlin MR, Hook DD, Mckee WH. Growth and nutrient use efficiency of water tupelo seedlings in flooded and well-drained soil. Tree Physiology 1995;15:753-8.

Meteorological Department. Meteorological Data Year 2006-2015 from Aranyaprathet Weather Station. Bangkok: Meteorological Department; 2016.

Moungsrimuangdee B, Moriwaki H, Nakayama M, Nishigaki S, Yamamoto F. Effects of injection of ethrel, methyl jasmonate, and salicylates and *Raffaelea quercivora* inoculation on sapwood discoloration in *Quercus serrata*. International Association of Wood Anatomists 2011;32:41-53.

Moungsrimuangdee B, Kanin W, Larpkern P, Kosuwan S. Species diversity and forest cover changes of Khlong Phra Prong, Sa Kaeo Province. Proceedings of the 4th Thai Forest Ecological Research Network (T-Fern), Ecological Knowledge for Sustainable Management Conference; 2015 Jan 22-23; Faculty of Agriculture Natural Resources and Environment, Phitsanulok: Thailand; 2015.

Moungsrimuangdee B, Waiboonya P, Larpkern P, Yodsa-nga P, Saeyang M. Reproductive ecology and growth of riparian species along Phra Prong River, Sa Kaeo Province, Eastern Thailand. Journal of Landscape Ecology 2017a;10:5-18.

Moungsrimuangdee B, Boonsri H, Larpkern P. Utilization of forest product in the riparian forest along Phra Prong Canal, Watthana Nakhon District, Sa Kaeo Province. Journal of Humanities and Social Sciences 2017b;18:84-95.

Naidoo G, Naidoo S. Waterlogging responses of *Sporobolus virginicus* (L.) Kunth. Oecologia 1992;90:445-50.

Nawajongpan T, Moungsrimuangdee B. A survey of riparian species in the Bodhivijjalaya College's Forest, Srinakharinwirot University, Sa Kaeo. Thai Journal of Forestry 2016;35:15-29.

Oliveira AS, Ferreira CS, Graciano-Ribeiro D, Franco AC. Anatomical and morphological modifications in response to flooding by six Cerrado tree species. Acta Botanica Brasilica 2015;29:478-88.

Pavlovic P, Mitrovic M, Dordevic D, Sakan S, Slobodnik J, Liska I, et al. Assessment of the contamination of riparian soil and vegetation by trace metals-A Danube River case study. Science of the Total Environment 2016;540:396-409.

Pezeshki SR. Wetland plant responses to soil flooding. Environmental and Experimental Botany 2001;46:299-312.

Pires HRA, Franco AC, Piedade MTF, Scudeller VV, Kruijt B, Ferreira CS. Flood tolerance in two tree species that inhabit both the Amazonian floodplain and the dry Cerrado savanna of Brazil. AoB Plants 2018;10:ply065.

Pernot C, Thiffault N, DesRoschers A. Influence of root system characteristics on Black Spruce seedlings responses to limiting conditions. Plants 2019;8(3):70.

Sakio H. Effects of flooding on growth of seedlings of woody riparian species. Journal of Forest Research 2005;10:341-6.

Santisuk T. Forest of Thailand. Bangkok, Thailand: Office of the Forest Herbarium, Department of National Parks, Wildlife and Plant Conservation; 2012.

Tsukahara H, Kozlowski TT. Importance of adventitious root to growth of flooded *Platanus occidentalis* seedling. Plant and Soil 1985;88:123-32.

University of Idaho. Principles of vegetation measurement, assessment, ecological monitoring and analysis: Direct measures of biomass [Internet]. 2009 [cited 2019 Oct 10]. Available from: https://www.webpages.uidaho.edu/veg_measure/Modules/Lessons/Module%207(Biomass&Utilization)/7_3_Direct%20Methods.htm.

Uowolo AL, Binkley D, Adair EC. Plant diversity in riparian forests in northwest Colorado: Effects of time and river regulation. Forest Ecology and Management 2005;218:107-14.

USDA National Agroforestry Center. Agroforestry notes: riparian buffer for agricultural land [Internet]. 1997 [cited 2018 Oct 15] Available from: https://www.fs.usda.gov/nac/assets/documents/agroforestrynotes/an03rfb02.pdf.

Waiboonya P, Meesena J, Larpkern P, Yodsa-nga P, Moungsrimuangdee B. Diversity of birds during winter in the riparian forest along Phra Prong Canal, Watthana Nakhon District, Sa Kaeo Province. Proceeding of the 3rd National Meeting on Biodiversity Management in Thailand; 2016 Jun 15-17; The Empress hotel, Nan: Thailand; 2016.

Wang GB, Cao FL. Formation and function of aerenchyma in baldcypress (*Taxodium distichum* (L.) Rich.) and Chinese tallow tree (*Sapium sebiferum* (L.) Roxb.) under flooding. South African Journal of Botany 2012;81:71-8.

Yamamoto F. Effects of depth of flooding on growth and anatomy of stems and knee roots of *Taxodium distichum*. IAWA Bulletin 1992;13:93-104.

Yamamoto F, Kozlowski TT. Effect of flooding of soil on growth, stem anatomy, and ethylene production of *Thuja orientalis* seedlings. IAWA Bulletin New Series 1986;8:21-9.

Yamamoto F, Sakata S, Terazawa K. Physiological, morphological and anatomical responses of *Fraxinus mandshurica* seedlings to flooding. Tree Physiology 1995;15:713-9.

Yang Y, Li C. Photosynthesis and growth adaptation of *Pterocarya stenoptera* and *Pinus elliottii* seedlings to submergence and drought. Photosynthetica 2016;54:120-9.

Yodsanga P, Moungsrimuangdee B, Waiboonya P, Larpkern P. Water yields in the Phra Prong Basin: Water quality and flow timings. Srinakharinwirot Science Journal 2017;33:87-102.

Yu B, Zhao CY, Li J, Li JY, Peng G. Morphological, physiological, and biochemical responses of *Populus euphratica* to soil flooding. Photosynthetica 2015;53:110-7.

Zhang H, Cui B, Xiao R, Zhao H. Heavy metals in water, soils and plants in riparian wetlands in the Pearl River Estuary, South China. Procedia Environmental Sciences 2010;2:1344-54.

Hydrodynamic Simulation of Suspended Solids Concentration in Isahaya Regulating Reservoir

Cong Khiem Ta[1], Seiji Suzuki[1], and Nhat Huy Nguyen[2*]

[1]Department of Advanced Engineering, Graduate School of Engineering, Nagasaki University, 1-14 Bunkyo, Nagasaki, 852-8521 Japan

[2]Faculty of Environment and Natural Resources, Ho Chi Minh City University of Technology, VNU-HCM, 268 Ly Thuong Kiet St., Dist. 10, Ho Chi Minh City, Vietnam

ARTICLE INFO

Received: 3 Sep 2019
Received in revised: 16 Jan 2020
Accepted: 13 Feb 2020
Published online: 11 Mar 2020
DOI: 10.32526/ennrj.18.2.2020.20

Keywords:
Suspended solids (SS)/ Isahaya regulating reservoir/ Osaka daigaku estuary model (ODEM)/ Unmanned Aerial Vehicle (UAV)

*** Corresponding author:**
E-mail: nnhuy@hcmut.edu.vn

ABSTRACT

In this study, Osaka daigaku estuary model (ODEM) was applied for hydrodynamic simulation of suspended solids (SS) concentration in the Isahaya regulating reservoir. Water samples were collected every hour from 9:00 to 15:00 at nine sampling points inside the observation area of the reservoir. Parameters used for the model included initial conditions (i.e., SS concentration, water depth, temperature, and salinity) and boundary conditions (i.e., wind speed and direction, atmospheric temperature, solar irradiation, and cloud cover). The calculated results of SS in the reservoir and its concentration fluctuation from the model were compared with those estimated from the image analysis of unmanned aerial vehicle (UAV) and observed results. The SS simulated from ODEM distributed in high concentration, whereas that estimated from UAV distributed in low concentration although in both data they spread across a wide range at most investigated times. Although there was a big difference between the accuracy of ODEM and UAV, the SS concentration values described by them were closed to the observed values. Between them, the ODEM model showed its advantages in simulating the SS concentration and achieved more accuracy than UAV, showing a potential for using ODEM model in monitoring of SS in water.

1. INTRODUCTION

There have been hydraulic, ecological, and biological changes to water quality in Isahaya regulating reservoir since the Isahaya Bay witnessed the erection of a sea dike in 1997. Among these changes, it is notable that SS is one of the main factors that has a great influence on water quality and have been investigated by scientists over the years (Bilotta and Brazier, 2008; Chebbo and Bachoc, 1992; Gartner, 2004). Methods for observing SS in water environment are primarily based on conventional methods (e.g., field sampling and then analysis in laboratory). These methods are often time-consuming, labor-intensive, and costly but not well representative of the large observing area, which are unlikely to meet the long-term observing requirements and can result in failure to realize the quick fluctuations of water quality over time (Schaeffer et al., 2013). On the contrary, together with the strong development of information technology and electrical telecommunications in recent years, many programs and computer software have been developed and widely applied in many fields of study, such as Fortran programming language. Osaka daigaku estuary model (ODEM) based on Fortran 90 program statements was built and can be considered as a means of remote simulation of SS. This model is composed of elements of a numerical model regarding the process of fluid dynamics described by basic hydrodynamic equations such as the three-dimensional partial differential equations of flow motion, flow continuity, heat, salt transport, and water density. In addition, it can be used to observe water environment through simulating SS besides other water quality parameters in different places on a large scale of a target area and over a long period of time thanks to its ease of operation and portability. ODEM have been used to simulate seasonal tidal residual

Citation: Ta CK, Suzuki S, Nguyen NH. Hydrodynamic simulation of suspended solids concentration in Isahaya regulating reservoir. Environ. Nat. Resour. J. 2020; 18(2): 209-223. DOI: 10.32526/ennrj.18.2.2020.20

current in Bohai Sea and the modelled tidal residual current was discovered to be weak in most parts of the Bohai Sea but much more powerful in the inshore parts. Similarly, it was apparent from the central part of the Bohai Sea that seasonal wind had a considerable influence on the tidal residual current, though it had insignificant effect on the tidal residual current in the inshore part of the Bohai Sea (Liang et al., 2003a; Liang et al., 2003b). The model was also applied for converting model parameters, in which the temporal-spatial conversion approach was revealed to be better than others (i.e., temporal, spatial, and non-temporal and non-spatial) (Li et al., 2012). However, SS concentration was not considered in those studies.

The interaction between SS and water quality parameters such as biochemical oxygen demand (BOD), salinity, and phosphorus has been studied and analyzed, while there have been a lack of specific SS observing methods. For example, several studies have been done on the effect of SS on the reservoir water quality due to salinity reduction (Sasaki, 2017) and the effect of SS changes on BOD after construction of a sea dike in Isahaya bay (Nishida et al., 1997). There were also works on the analysis of SS behavior according to the increase of seawater from the Ariake Sea (Nagase et al., 2014), the resuspension of SS caused by the coagulation of phosphorus in Isahaya reservoir (Mitsugi et al., 2013), and the settling velocity of SS affected by seawater from Ariake Sea flowing to Isahaya reservoir (Koga et al., 2003). Furthermore, SS concentration has been estimated by using other methods such as Acoustic Doppler Current Profiler (ADCP, using echo intensity backscattered from SS) (Dwinovantyo et al., 2017), Landsat 7 (using Landsat 7 as remote sensing) (Shahzad et al., 2018), and online auto sensors (using high frequency observation with online auto sensors) (Valkama and Ruth, 2017). Although it is worthy to investigate, up to the present, there have not been any works on the usage of ODEM for simulation of SS in Isahaya regulating reservoir.

In this work, we aimed to apply computational simulation through the ODEM model to predicting the SS concentration which dominates water quality and ecosystem in Isahaya regulating reservoir. The simulated results were then compared with those estimated from unmanned aerial vehicle (UAV) and field sampling to elucidate the capability of ODEM model in simulating SS in the reservoir. Besides, consideration of crucial relationships between biomass development of microorganism and pollutant concentration was also discussed in this work.

2. METHODOLOGY

2.1 Instruments and equipment for field sampling, measuring, and analyzing

Items required for field sampling, measuring, and analyzing include a van, inflatable pontoon, plastic bottle, wash bottle, DR/2010 portable datalogging spectrophotometer, laboratory tissue, AAQ1183-H multi-parameter water quality meter, Neo pyranometer, and WJ-24 hand anemoscope/ anemometer. The detailed technical specifications of DR/2010 portable datalogging spectrophotometer are described in Table S2.

2.2 Study area

A large-scale sea dike project with a length of 7 km (Yamaguchi and Hayami, 2018) along with a reclamation project were constructed in 1997 (Mitsugi et al., 2013) to protect Isahaya city from saline intrusion and high tidal waves (Figure 1). Therefore, the sea dike has incidentally created a large regulating reservoir situated between the residential area and the dike to the southwest of the Ariake Sea. The reservoir covers an area of 2,600 ha, comprising 13 rivers starting from the first class Honmyo River, which has a depth of 3.5 m at the deepest part and an average depth of about 1.1 m (Yamaguchi and Hayami, 2018). This regulating reservoir, therefore, has a relatively shallow area of water and the bottom sludge is easily disturbed by wind. Besides, the hydraulic, ecological, and biological characteristics of the reservoir have been changed, such as eutrophication due to increase of phosphorus from contaminant loads in the flood influent (Niki et al., 1999), tidal current high, decline in salinity, increase in suspended solids (SS), and oxygen depletion on account of the discharge of rainwater and domestic wastewater. Particularly, the outbreak of red tide has become a phenomenon expressing degradation of water quality in the reservoir during the winter between 2000 and 2001 (Tada et al., 2010).

2.3 Sampling points

The position of sampling points is shown in Figure 2 whereby the sampling points were marked on the picture according to the actual coordinates. These points were chosen in the observation area near the bank beside the north floodgate of the sea dike.

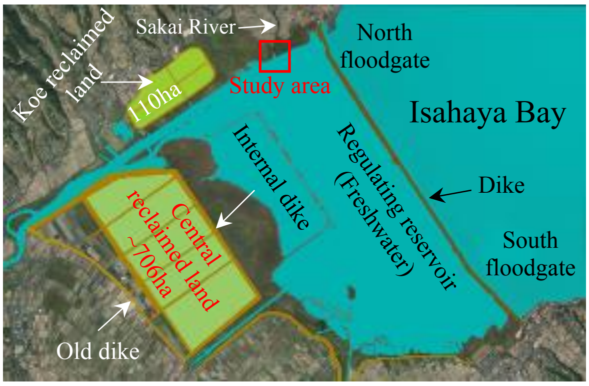

Figure 1. Study area in Isahaya regulating reservoir

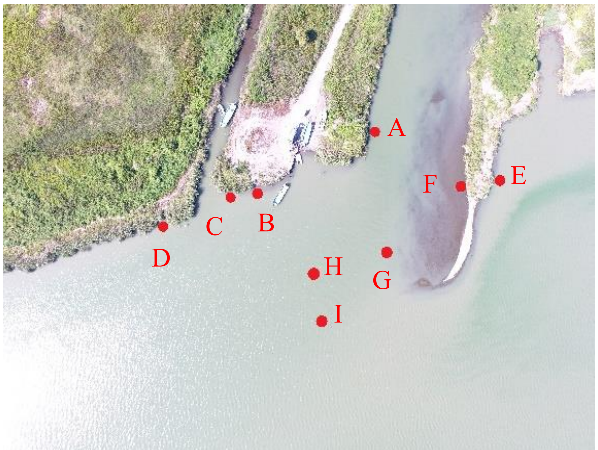

Figure 2. Positions of sampling points in study area

2.4 Sampling and measurement procedures

Sampling is one of the important steps in the operation of the model and the results from the analysis and measurement are the important database for the model. The values of the SS analysis results by the spectrophotometer at the first measurement are the baseline in which the simulation results of the model at the next measurement are based on. The principle of this method is to measure the transmittance of light passing through a solution containing SS. On the other hand, this transmittance is proportional to the absorbance in relation: A=-logT, and the absorbance is proportional to the concentration of SS absorbed (Harris, 2007). According to Krawczyk and Gonglewski (1959), SS concentration in the sewage samples after being diluted with city water was directly proportional to the transmittance. Further, this method was consistent with the law of colorimetry and can be applied for measuring SS concentration.

2.5 Assigning the initial values of SS concentration

Assuming that the sequence number of cells on the horizontal and vertical direction are known, two lines are drawn through the two cells. If the intersection of the two lines coincides with one of the sampling points (e.g., point A Figure 2), the initial value of the SS concentration at that point is the initial value of the SS concentration at the point A. Otherwise, it is the initial value of the SS concentration at adjacent sampling point (e.g., point B in Figure 2).

2.6 Assigning the initial values of water depth, water temperature, and salinity

The values of water depth, water temperature, and salinity were constant at different sampling points where the water temperature and salinity were taken as 10 m and 0 ‰, respectively, and the water depths at all points were 0.5 m.

2.7 Entering meteorological data as input parameters into the model

Meteorological parameters were also measured during sampling including wind speed, wind direction, air temperature, radiation, total solar radiation, and cloud cover as shown in Table 1.

Table 1. Meteorological data used as input parameters for the model

Time	Air temperature (°C)	Wind		Total solar radiation (MJ/m^2)	Cloud cover
		Speed (m/s)	Direction (degree)		
09:00	22.9	0.1	135	1.49	0+
10:00	24.0	0.0	0	1.82	
11:00	26.5	1.0	135	2.11	
12:00	27.1	3.1	90	2.65	6
13:00	28.2	3.1	135	2.93	
14:00	28.3	2.3	90	2.73	
15:00	28.5	2.8	90	2.03	7

2.8 Mass balance formula of SS

The sediment particles can be supplied directly into the flowing water from the sweeping layer or bottom. In the actual watershed, the transition process is complicated because sediment is not a single-sized particle and the flow is locally changing. As a method for evaluating the rolling up flux of sediment particles, sediment is considered as one of continuous and granular particles. In this study, it is assumed that the size of sediment particles in Isahaya regulating reservoir is 4 μm (Nishida et al., 2014) and after leaving the bottom it immediately transits to a floating state. Furthermore, if the sweeping force exceeds its limit, rolling up occurs and it is evaluated by Equation 1. The sweeping force is displayed in a dimensionless manner as $\left(\frac{\tau_b}{\sigma-\rho} g \cdot d\right)$.

$$\begin{cases} \tau_{*f} \leq \tau_{*cf} & F_c = 0 \\ \tau_{*f} > \tau_{*cf} & F_c = \sigma v_s P_s / a_s \end{cases} \tag{1}$$

Where; τ_{*cf} and τ_{*f} are dimensionless sweeping force and its value at the movement limit, respectively; ρ is density of water (kg/m^3); σ and v_s are density (kg/m^3) and volume (m^3) of the sediment particle, respectively; a_s is orthogonal projection area of the sediment particle (m^2); and p_s is pick-up rate.

The pick-up rate is evaluated by the following equation (Murakami et al., 1992):

$$\frac{\sqrt{P_S}}{\sqrt{\left(\frac{\sigma}{\rho-1}\right)\frac{g}{d}}} = F_P \cdot \tau_{*f} \cdot \left(1 - k_2 \frac{\tau_{*cf}}{\tau_{*f}}\right)^2 \tag{2}$$

In addition, τ_{*cf} is calculated from the equation below:

$$\tau_{*f} = \frac{\mu}{1+k_L\mu} \cdot \frac{1}{\varepsilon \cdot A_*^2 \cdot C_D A_2 / 2A_3} \tag{3}$$

Where; d is diameter of the sediment particle (m); g is gravitational acceleration (m/s^2); k_L is drag/lift ratio (0.85); μ is static friction coefficient (1.0); A_2 and A_3 are shape factors of the sediment particle; C_D is drag coefficient when the Reynolds number is large enough, C_D=0.4, F_p=0.03, k_2=0.7, m=2.89.

Sediment flux is amount corresponding to the settling velocity to the bottom (kg/ (m^2·s)):

$$Fd = SS \cdot w_0 \tag{4}$$

Where; W_0 is the settling velocity of SS in freshwater (m/s). Settling velocity is evaluated by Rubey's equation shown in the following equation:

$$\frac{w_0}{\sqrt{\left(\frac{\sigma}{\rho}-1\right)gd}} = \sqrt{\frac{2}{3} + \frac{36v^2}{\left(\frac{\sigma}{\rho}-1\right)gd^3}} - \sqrt{\frac{36v^2}{\left(\frac{\sigma}{\rho}-1\right)gd^3}} \tag{5}$$

2.9 Calculation conditions of model

The model uses the target calculation area as shown in Figure 2. The spatial difference interval is Δx=Δy=10 m in horizontal direction and 10 layers divided into four kinds of thickness Δz in vertical direction including 5 layers of 0.5 m, 1 layer of 0.4 m, 1 layer of 0.3 m, and 3 layers of 0.1 m from bottom to surface. The time difference interval was Δt=0.1 s. The boundary conditions (i.e., wind speed, wind direction, air temperature, radiation, and cloud cover) were taken from field sampling in Table 1. The initial conditions such as SS concentration, water depth, water temperature, and salinity at each sampling point were applied to the reservoir (Sections 2.5-2.7).

3. RESULTS AND DISCUSSION

3.1 Analysis results of SS concentration

Figure 3 plots the changes in SS concentration from 9:00 to 15:00 as sampled and analyzed on September 28, 2018. In general, the SS concentration at sampling points decreased with time except at points F and H. During the period from 9:00 to 15:00, SS concentration at points E and I increased significantly from 9:00 to 12:00 and followed by a considerable fluctuation from 12:00 to 15:00. To be more precise, SS concentration at these points E and I declined dramatically from 124 and 155 mg/L at 12:00 to 40 and 114 mg/L at 13:00, respectively, but later went up sharply by 67 and 34 mg/L, respectively, at 14:00. This could come from anthropogenic activities that occurred between two periods of time before and after 13:00 in the area. At the same time, SS concentration at points A, F, G, and H went up marginally and always lower in comparison with that at points E and I. During the same period, there was an opposite tendency of SS concentration at points B, C, and D. The period starting from 12:00 onwards experienced a downward trend of SS concentration at most points except F and H. However, most of the SS concentration at the sampling points was very high, in which the SS concentrations at points E and I were the highest ones. In other words, p value (0.001) in Table 2 was less than 0.05 (significant level), i.e., variances between observed SS at 9 points were heterogeneous. It was not surprising, therefore, that ANOVA cannot be used on this account. Despite this, a post-hoc test (Table 3) needs to be used to identify further which pairs of points are statistically higher or lower. The mean observed SS at points A and B was statistically different because p equal to 0.001 was less than 0.05. The mean observed SS at point A was less than that at point B because the mean difference in observed SS between these two points was negative when the mean observed SS at point B was subtracted from mean observed SS at point A. Similarly, the mean observed SS between the following pairs also were statistically significant, including A:C, A:D, A:E, A:G, A:H, A:I, B:F, B:I, C:F, C:I, D:F, E:F, E:G, F:H, F:I, G:H, G:I, and H:I in which the mean differences with negative values were found in the following pairs: A:C, A:D, A:E, A:G, A:H, A:I, B:I, C:I, F:H, F:I, G:H, G:I, and H:I. Pairs with p values less than 0.05 that are not listed above were those whose mean differences had values with the sign inverse to that of the mean differences in the above pairs, including B:A, C:A, D:A, E:A, G:A, H:A, I:A, F:B, I:B, F:C, I:C, F:D, F:E, G:E, H:E, I:F, H:G, I:G, and I:H. Among the pairs whose mean differences had statistically significant values of negative and positive signs, pairs E:G and G:E had the highest statistically significant mean differences with p values equal to 0.027 compared to those of the others. Pairs A:H, A:I, F:H, F:I, H:A, H:F, I:A, and I:F, meanwhile, were those whose mean differences were the lowest statistically significant because their p values were equal to 0.000. The very high SS concentration at most sampling points suggests that water quality at reservoir is low due to high turbidity, water layers disturbed by wind, and development of microbiological biomass (Mitsugi et al., 2013). This was contrast to the lowest SS concentration at point A where the water was clearest due to its lowest turbidity. Indeed, from the correlation coefficient in Table 4, it is apparent that three water quality parameters, consisting of turbidity, temperature, and chlorophyll in which chlorophyll is representative of microbiological biomass, exerted a certain influence on observed SS, especially at point G for turbidity, F for temperature, and points C and G for chlorophyll where relative correlations with observed SS were seen clearly. Besides having good correlations with observed SS at the above points, turbidity and temperature were also correlated with observed SS with moderate correlation coefficients of over 0.5 to just below 0.8 which could be taken into account such as 0.64 at point B and 0.57 at point C for turbidity; and 0.53 at point C, 0.74 at point D, and 0.58 at point H for temperature. Also, despite of having no moderate correlation coefficients with observed SS, chlorophyll had two correlation coefficients of over 0.8 compared to the other two parameters. Therefore, it can be said that high turbidity, temperature, and chlorophyll were associated with high SS concentration.

Table 2. Test of homogeneity of variances between observed SS concentrations at sampling points

Levene statistic	df1	df2	Sig.
3.772	8	54	0.001

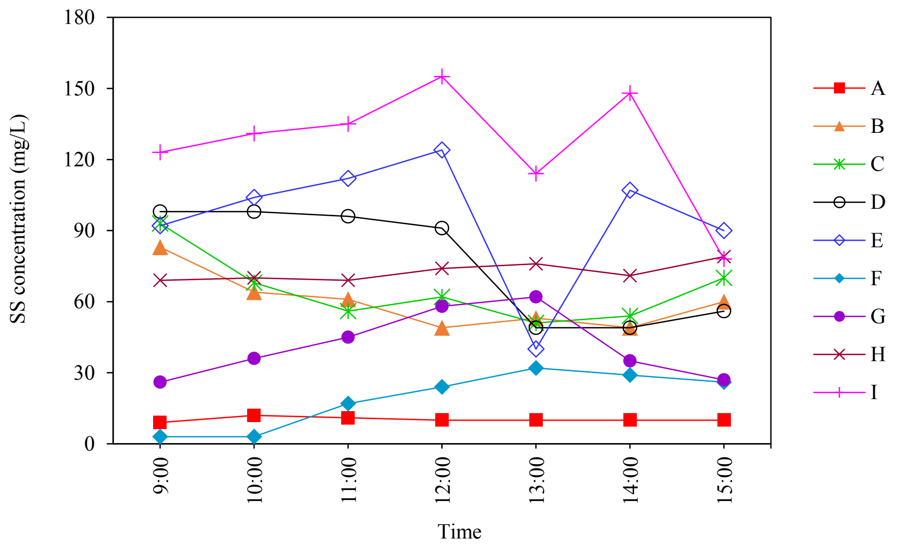

Figure 3. SS concentration fluctuation at sampling points

Table 3. Dunnett T3 test for multiple comparisons between observed SS of point pairs

(I) Point	(J) Point	Mean difference (I-J)	Std. error	Sig.	95% Confidence interval	
					Lower bound	Upper bound
A	B	-49.57143*	4.47822	**0.001**	-71.1067	-28.0362
	C	-54.57143*	5.41226	**0.001**	-80.6400	-28.5028
	D	-66.42857*	9.06702	**0.006**	-110.1987	-22.6584
	E	-85.28571*	10.25525	**0.003**	-134.8054	-35.7661
	F	-8.85714	4.53632	0.771	-30.6746	12.9604
	G	-31.00000*	5.41791	**0.022**	-57.0960	-4.9040
	H	-62.28571*	1.50509	**0.000**	-69.2554	-55.3160
	I	-116.00000*	9.62741	**0.000**	-162.4819	-69.5181
B	A	49.57143*	4.47822	**0.001**	28.0362	71.1067
	C	-5.00000	7.00631	1.000	-32.8827	22.8827
	D	-16.85714	10.09984	0.909	-59.9003	26.1860
	E	-35.71429	11.17882	0.215	-84.2552	12.8266
	F	40.71429*	6.35407	**0.001**	15.6102	65.8184
	G	18.57143	7.01068	0.383	-9.3309	46.4737
	H	-12.71429	4.69694	0.397	-33.8872	8.4587
	I	-66.42857*	10.60580	**0.005**	-112.0471	-20.8101
C	A	54.57143*	5.41226	**0.001**	28.5028	80.6400
	B	5.00000	7.00631	1.000	-22.8827	32.8827
	D	-11.85714	10.54727	0.998	-55.5035	31.7892
	E	-30.71429	11.58465	0.401	-79.5718	18.1432
	F	45.71429*	7.04360	**0.001**	17.7095	73.7191
	G	23.57143	7.64119	0.203	-6.6169	53.7597
	H	-7.71429	5.59458	0.973	-33.4197	17.9911
	I	-61.42857*	11.03273	**0.008**	-107.5034	-15.3537
D	A	66.42857*	9.06702	**0.006**	22.6584	110.1987
	B	16.85714	10.09984	0.909	-26.1860	59.9003
	C	11.85714	10.54727	0.998	-31.7892	55.5035
	E	-18.85714	13.67927	0.985	-73.0682	35.3539
	F	57.57143*	10.12574	**0.008**	14.5047	100.6381
	G	35.42857	10.55017	0.154	-8.2230	79.0801
	H	4.14286	9.17702	1.000	-39.3502	47.6359
	I	-49.57143	13.21512	0.070	-101.8196	2.6768
E	A	85.28571*	10.25525	**0.003**	35.7661	134.8054
	B	35.71429	11.17882	0.215	-12.8266	84.2552
	C	30.71429	11.58465	0.401	-18.1432	79.5718
	D	18.85714	13.67927	0.985	-35.3539	73.0682
	F	76.42857*	11.20222	**0.003**	27.8792	124.9779
	G	54.28571*	11.58729	**0.027**	5.4251	103.1464
	H	23.00000	10.35263	0.636	-26.2676	72.2676
	I	-30.71429	14.05698	0.651	-86.2954	24.8668
F	A	8.85714	4.53632	0.771	-12.9604	30.6746
	B	-40.71429*	6.35407	**0.001**	-65.8184	-15.6102
	C	-45.71429*	7.04360	**0.001**	-73.7191	-17.7095
	D	-57.57143*	10.12574	**0.008**	-100.6381	-14.5047
	E	-76.42857*	11.20222	**0.003**	-124.9779	-27.8792
	G	-22.14286	7.04794	0.189	-50.1670	5.8812

Table 3. Dunnett T3 test for multiple comparisons between observed SS of point pairs (cont.)

(I) Point	(J) Point	Mean difference (I-J)	Std. error	Sig.	95% Confidence interval	
					Lower bound	Upper bound
	H	-53.42857*	4.75237	**0.000**	-74.8826	-31.9746
	I	-107.14286*	10.63047	**0.000**	-152.7771	-61.5086
G	A	31.00000*	5.41791	**0.022**	4.9040	57.0960
	B	-18.57143	7.01068	0.383	-46.4737	9.3309
	C	-23.57143	7.64119	0.203	-53.7597	6.6169
	D	-35.42857	10.55017	0.154	-79.0801	8.2230
	E	-54.28571*	11.58729	**0.027**	-103.1464	-5.4251
	F	22.14286	7.04794	0.189	-5.8812	50.1670
	H	-31.28571*	5.60005	**0.018**	-57.0186	-5.5528
	I	-85.00000*	11.03550	**0.001**	-131.0790	-38.9210
H	A	62.28571*	1.50509	**0.000**	55.3160	69.2554
	B	12.71429	4.69694	0.397	-8.4587	33.8872
	C	7.71429	5.59458	0.973	-17.9911	33.4197
	D	-4.14286	9.17702	1.000	-47.6359	39.3502
	E	-23.00000	10.35263	0.636	-72.2676	26.2676
	F	53.42857*	4.75237	**0.000**	31.9746	74.8826
	G	31.28571*	5.60005	**0.018**	5.5528	57.0186
	I	-53.71429*	9.73108	**0.024**	-99.9314	-7.4972
I	A	116.00000*	9.62741	**0.000**	69.5181	162.4819
	B	66.42857*	10.60580	**0.005**	20.8101	112.0471
	C	61.42857*	11.03273	**0.008**	15.3537	107.5034
	D	49.57143	13.21512	0.070	-2.6768	101.8196
	E	30.71429	14.05698	0.651	-24.8668	86.2954
	F	107.14286*	10.63047	**0.000**	61.5086	152.7771
	G	85.00000*	11.03550	**0.001**	38.9210	131.0790
	H	53.71429*	9.73108	**0.024**	7.4972	99.9314

* The mean difference is significant at the 0.05 level.

Table 4. Correlation coefficient of water quality parameters with observed SS (R^2)

Point	Turbidity	pH	DO	Temperature	Chlorophyll	Salinity
A	0.0125	0.3410	0.0509	0.0282	0.0918	0.7091
B	0.6352	0.0771	0.3185	0.4691	0.4897	0.6326
C	0.5701	0.0617	0.0654	0.5300	**0.8311**	**0.9297**
D	0.2897	0.2417	0.6365	0.7420	0.4528	0.1528
E	0.1268	0.0257	0.0779	0.0713	0.0237	0.0176
F	0.1458	0.0295	0.3183	**0.8579**	0.4590	0.0000
G	**0.9722**	0.0281	0.3108	0.0715	**0.8973**	0.6108
H	0.3199	0.5444	0.6181	0.5849	0.2804	0.0000
I	0.3963	0.1651	0.0085	0.1673	0.0042	0.6798

3.2 Distribution of SS concentration and flow structure in observation area

In a previous study of Dohi in our group (unpublished results), SS concentration in Isahaya Bay was also observed and estimated from photos taken by UAV. Therefore, in order to understand objectively hydrodynamic simulation of SS concentration utilizing the model, the results in this study were compared with those in the above study. The ODEM model was operated according to the initial conditions and boundary conditions described in Sections 2.5-2.7. The obtained results were exported as plots showing the distribution of SS concentration and flow structure.

As displayed in Figure 4, it is obvious that SS distributed in low concentration through the vicinity of Sakai River (Figure 1). SS distributed in high concentration in the remote area of the estuary where E and I points were situated. Thus, this result conformed to the field analysis results at points E and I as shown in Section 3.1. However, there was little difference between results estimated from the UAV and those simulated from ODEM. Whereas simulated SS (on the left) distributed in high concentration, the estimated SS (on the right) distributed in slightly low concentration although both of them spread across a large range at most hours from 9:00 to 15:00. In particular, the results obtained from image analysis on the right in the area around the estuary from 12:00 onwards showed that SS distributed in low concentration. It is explained that the low concentration of SS in surroundings of the estuary is due to clear water flowing from the Sakai River into the reservoir with low flowrate as well as the low wind speed in this area.

In contrast, SS distributed in high concentration in the remote area of the estuary at most investigated times could be because of (i) low salinity in the reservoir (Table S3), (ii) large reservoir area, (iii) increase in wind speed over time, and (iv) increase in stratification. Regarding salinity, there are always two types of ions (Na^+ and Cl^-) of the sodium chloride compound in seawater. Once these two types of ions encounter solid particles such as clay particles, suspended solids, and suspended sediments, the phenomenon of combining ions to form molecules (also called combination reaction) will take place thereafter. At that point, the negative ions of the particles will be neutralized by positive ions of salt in the seawater then the particles will be combined together and form larger particles (Sasaki, 2017). Once formed large enough, these particles will overcome the repulsive force of water and sink into the reservoir. By this way, the more seawater there is, the less suspended solids there are and vice versa. Also, the vertical diffusion will decrease with the higher salinity (Kim et al., 2018), and the suspended particles will be easier to settle. Moreover, with a large area of 2,600 ha, Isahaya regulating reservoir has a high wind disturbance resulting from its large surface momentum (Magee and Wu, 2017) combined with low water depths, the bottom sludge or sediment is easily disturbed by wind. Furthermore, the increase in wind speed over time (Table 1) could also have a significant effect. Bottom sludge or sediment disturbed by high wind speed will make water turbid. Finally, an increase in water temperature (Table S3) leads to increased stratification. Once stratification takes place, the water convection of internal and external parts in the reservoir will occur simultaneously. Water of the internal part flows outward in the upper layer in contrast to that in the lower layer (Sasaki, 2017). Therefore, the water layers will be disturbed along with the circulation of water in the reservoir. Since the sea dike was built, areas, containing water in the reservoir, have become closed areas and can undergo eutrophication under hypoxic conditions (Hodoki and Murakami, 2006). Water quality in such areas is then deteriorated due to increased amount of bottom sludge or sediment generated from algae and aquatic plants, which results in increased concentration of SS. In theoretical terms, this result could be explained in this way, but the fact (Table 5) remains that salinity and water temperature had statistically significant linear relationships with observed SS ($p<0.01$) as against correlation between wind speed and observed SS. Moreover, water temperature and observed SS was negatively correlated ($r=-0.33$), meaning that greater water temperature related to smaller amount of observed SS or vice versa. This could be attributed to the sample size of salinity was different to that of the other two parameters because of missing measured values of salinity at point F. Considering only 56 observations at point F, salinity was closely correlated with observed SS, but the direction of relationship was negative. However, if a full 63 (7 times × 9 points) observations had been made, the correlation would have remained the same, but the direction of the relationship would have been positive. In addition, it was the first attempt to apply ODEM for modelling SS concentration and the analysis of SS was mistakenly not repeated, which contributed to the limitation of this study. Briefly, the results obtained from ODEM, from which SS distributed in low concentration around the estuary, were closer to the field analysis results than that from UAV.

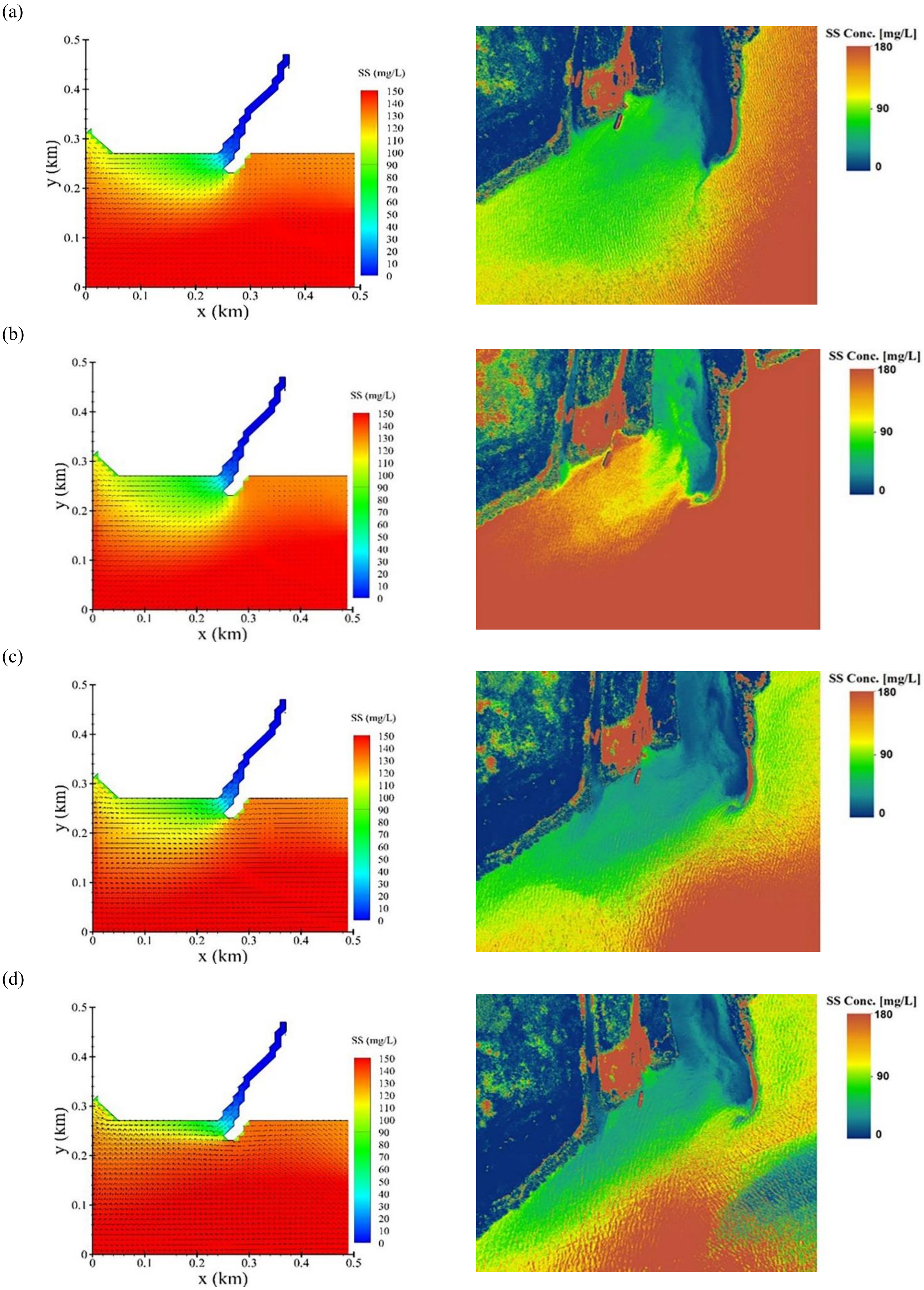

Figure 4. Distribution of SS concentration and flow structure obtained from ODEM (left) and UAV (right) at (a) 9:00, (b) 10:00, (c) 11:00, (d) 12:00, (e) 13:00, 14:00, and (g) 15:00

(e)

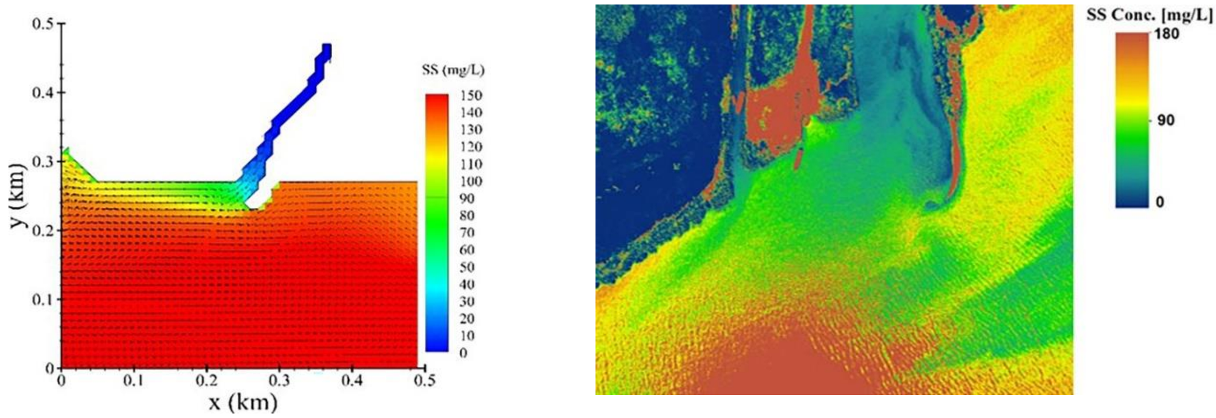

(f)

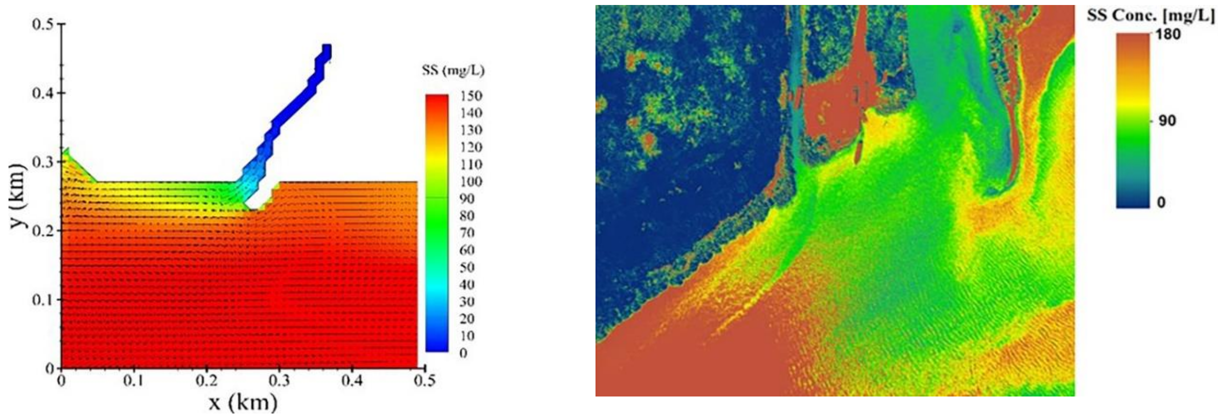

(g)

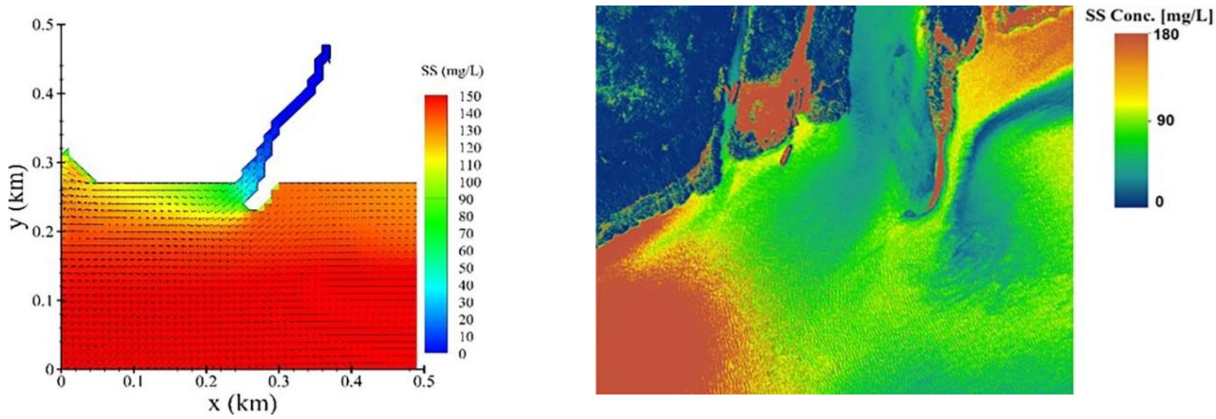

Figure 4. Distribution of SS concentration and flow structure obtained from ODEM (left) and UAV (right) at (a) 9:00, (b) 10:00, (c) 11:00, (d) 12:00, (e) 13:00, 14:00, and (g) 15:00 (cont.)

Table 5. Correlation matrix of water quality parameters and meteorological parameters with observed SS

		Observed SS	Salinity	Wind speed	Water temperature
Observed SS	Pearson Correlation	1	0.412**	-0.063	-0.330**
	Sig. (2-tailed)	-	0.002	0.626	0.008
	N	63	56	63	63
Salinity	Pearson Correlation	0.412**	1	-0.220	-0.149
	Sig. (2-tailed)	0.002	-	0.103	0.273
	N	56	56	56	56

Table 5. Correlation matrix of water quality parameters and meteorological parameters with observed SS (cont.)

		Observed SS	Salinity	Wind speed	Water temperature
Wind speed	Pearson correlation	-0.063	-0.220	1	0.719**
	Sig. (2-tailed)	0.626	0.103		0.000
	N	63	56	63	63
Water temperature	Pearson Correlation	-0.330**	-0.149	0.719**	1
	Sig. (2-tailed)0	0.008	0.273	0.000	
	N	63	56	63	63

** Correlation is significant at the 0.01 level (2-tailed).

3.3 Comparison of SS concentration simulated from ODEM and estimated from UAV with observed values

The comparison of simulated values from ODEM, the estimated values from the UAV, and the observed values from field sampling are presented in Table 6 (processed from detailed data of Table S4) and Figure 5. In short, Table 6 summarizes the errors between the SS concentration values from ODEM and UAV and the observed results. It can be seen that the errors at point F of both ODEM and UAV were very high as opposed to other points. These high errors could have resulted from differences in water depth between this point and other points. During the sampling period, water parameters were analyzed manually in situ, consisting of turbidity, pH, DO, temperature, chlorophyll, and salinity in which water temperature and salinity were the main factors directly affecting results of the model because these two parameters were two of three parameters (water depth, water temperature, and salinity) used as the initial values of the model (Section 2.6). Therefore, errors were unavoidable because the sampling depth of each point at different times along with movement of hands could have been different. Based on the study of Dwinovantyo et al. (2017), only an error of 5% between SS concentrations from ADCP and field analysis was detected. By comparison, this (high error at point F) declared that the ODEM and UAV did not have a high level of ability to simulate and estimate SS concentration, respectively.

Table 6. Error between the SS concentration values from ODEM and UAV and the observed results

Time	Error between SS concentration values from ODEM and observed results (%)								
	A	B	C	D	E	F	G	H	I
09:00	34	45	36	24	44	393	0	14	19
10:00	13	25	11	24	26	483	20	12	27
11:00	42	9	23	15	17	45	22	3	16
12:00	93	11	7	12	7	23	29	27	12
13:00	102	14	43	73	236	11	35	9	21
14:00	135	36	49	90	26	14	28	20	9
15:00	174	12	16	69	50	26	70	3	63
Time	Error between SS concentration values from UAV and observed results (%)								
09:00	52	12	43	56	3	15	55	20	11
10:00	6	5	12	34	14	390	13	15	26
11:00	25	1	12	58	6	49	14	10	39
12:00	25	8	19	55	38	43	33	19	4
13:00	2	27	36	79	151	26	23	18	23
14:00	20	110	2	99	50	83	1	5	30
15:00	24	60	18	90	37	18	31	27	9

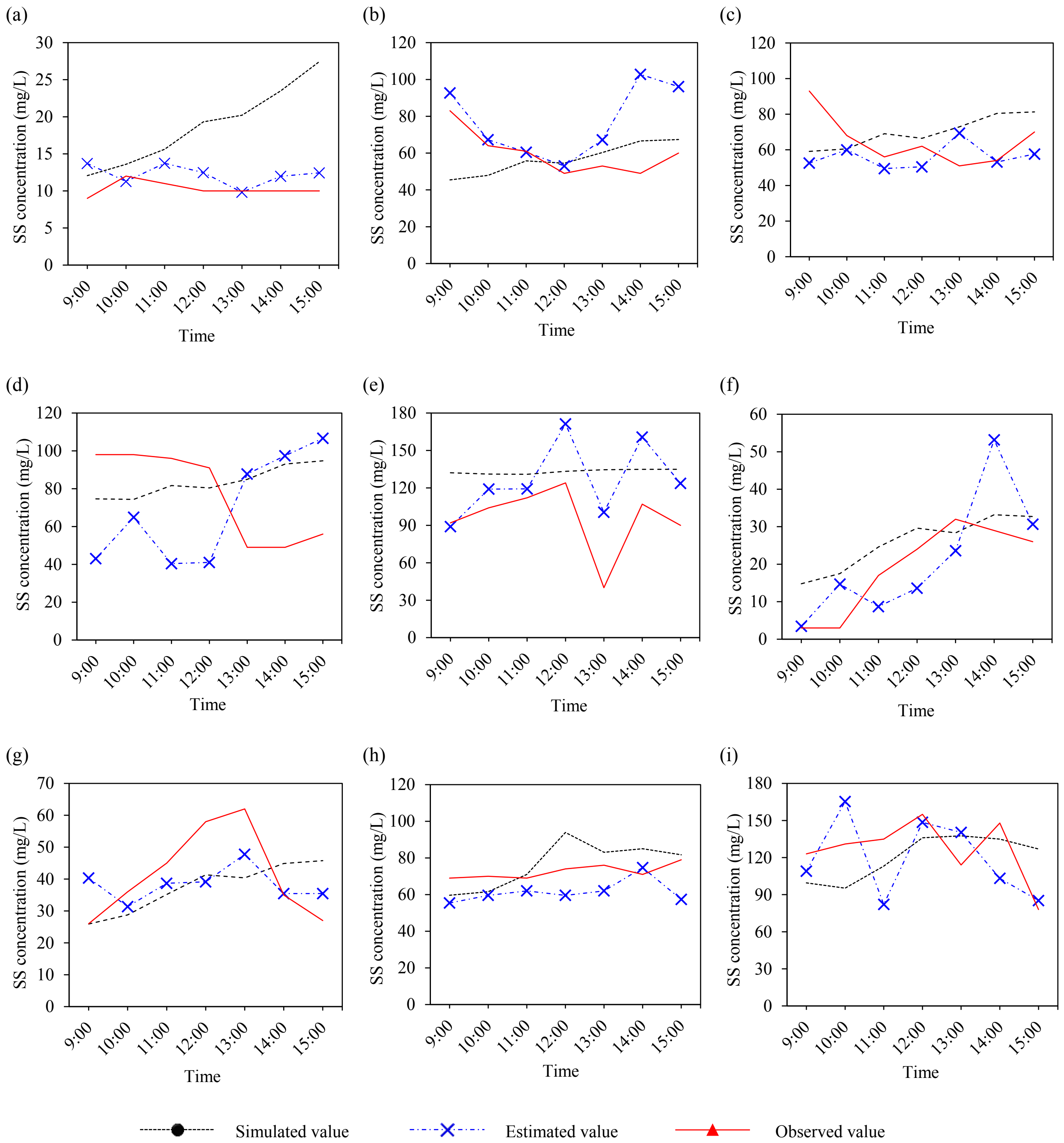

Figure 5. Changes in simulated values, estimated values, and observed values of SS concentration over time at point: a) A, b) B, c) C, d) D, e) E, f) F, g) G, h) H, and i) I

However, it was difficult to recognize the correlation of values from ODEM and UAV with observed values in Figure 5. Therefore, it was simply that their correlation with the observed values was expressed by the difference in concentration between them and the observed values, in which the concentration difference was taken absolutely. Table 7 highlights a number of p-values that differences in SS concentration have at each sampling point. It is known that if p-value is greater than or equal to 0.05 (significance level), there is no statistically significant difference in SS concentration between simulated values (SS1) and observed values (SS3), estimated values (SS2) and observed values (SS3). On the contrary, if p-value is less than 0.05, there is a statistically significant difference in SS concentration between SS1 and SS3, SS2 and SS3. In this regard, p-values at A and D, standing at 0.03 and 0.00, respectively, were less than 0.05. Therefore, it is considered that statistically significant differences were seen at these two points. By comparison, there is no statistically significant difference in SS concentration between SS1 and SS3, SS2 and SS3 at the remaining points (B, C, E, F, G, H, and I). This declared clearly that although there was a big difference between the accuracy of ODEM and UAV (Figure S2), their results could accurately describe the observed values. In terms of considering correlation, Ganti (2019) argued that the correlation between the two variables was significant only if it had a value of greater than 0.8. Accordingly, the correlation of values from them with the observed values at different points was different, in which the correlation was distinctly shown at points F and D (Table 8). Consequently, it can be concluded that while a total of 9 points were observed, there were 2 points whose values described by ODEM and UAV were close to the observed values.

Table 7. Independent samples test of difference in SS concentration

Point	Difference	N	Mean	Std. deviation	Std. error mean	t	p-value
A	|SS1-SS3|	7	8.53	5.78	2.19	2.82	0.03
	|SS2-SS3|	7	2.17	1.47	0.56		
B	|SS1-SS3|	7	13.80	11.61	4.39	-0.41	**0.69**
	|SS2-SS3|	7	17.36	20.03	7.57		
C	|SS1-SS3|	7	16.93	10.76	4.07	0.46	**0.65**
	|SS2-SS3|	7	14.00	12.86	4.86		
D	|SS1-SS3|	7	27.24	12.66	4.79	-3.51	0.00
	|SS2-SS3|	7	47.36	8.38	3.17		
E	|SS1-SS3|	7	37.52	27.87	10.53	0.44	**0.67**
	|SS2-SS3|	7	31.47	23.28	8.80		
F	|SS1-SS3|	7	7.72	4.02	1.52	-0.63	**0.54**
	|SS2-SS3|	7	9.72	7.40	2.80		
G	|SS1-SS3|	7	12.02	7.47	2.82	0.65	**0.53**
	|SS2-SS3|	7	9.61	6.46	2.44		
H	|SS1-SS3|	7	9.06	6.27	2.37	-0.94	**0.36**
	|SS2-SS3|	7	12.11	5.80	2.19		
I	|SS1-SS3|	7	26.52	12.02	4.54	-0.01	**0.99**
	|SS2-SS3|	7	26.58	18.34	6.93		

SS1=Simulated SS, SS2=Estimated SS, SS3=Observed SS

The linear relationships between simulated values from ODEM and observed values, estimated values from UAV and observed values at all points are demonstrated in Figure 6. Detailed results of SS concentration from ODEM and UAV are provided in Table S4. The results in Table 8 showed that the correlation coefficients of simulated values with observed values and estimated values with observed values at most of the points were not too high (except for point F and D, respectively), especially at point A where the correlation coefficient of simulated values with observed values was not even greater than 0.1. That of estimated values with observed values, meanwhile, was found to be less than 0.1 at points A, B, C, and H. These denoted that both ODEM and UAV were not very good in concord with observed values in comparison with other studies. Typically, Dwinovantyo et al. (2017) reported that estimated SS concentration from ADCP closely correlated with that from field analysis. ADCP is a method of estimating SS concentration based on converting backscatter (echo) intensity measured from it into SS concentration using sonar equation. According to their study, ADCP could be used as a good technique in observing SS concentration, which was more comparatively viable than conventional method. As Shahzad et al. (2018) stated, results of SS concentration estimated by Landsat 7 and field analyses were not substantially different, and the Landsat 7 could be used as an effective means of daily water quality observation. Moreover, it was ascertained that high frequency observation with online auto sensors could be a coherent method of measuring SS presented by Valkama and Ruth

(2017). In our study, even though the linearity was quite low, the correlation coefficient for all points was not too low, as can be seen in Figure 6. Nevertheless, it was found that this was exactly dissimilar from results of suspended sediment concentration from the study by Thanh et al. (2017). The suspended sediment concentration simulated from Delft3D-4 model and Delft3D FM model proved to be in harmony with observed data (Thanh et al., 2017). On the other hand, if the accuracy between ODEM and UAV is taken into account, the ODEM showed its advantages in simulating the SS concentration and achieved more accurately than UAV because a correlation coefficient of simulated SS with observed SS was seen to be 0.8727 at point F which was greater than 0.8064 between estimated SS and observed SS at point D (Table 8). In addition, the correlation coefficient for all points between simulated SS and observed SS was also greater than that between estimated SS and observed SS (Figure 6).

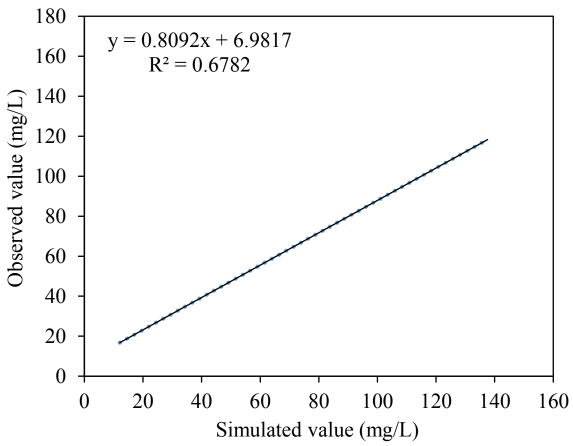

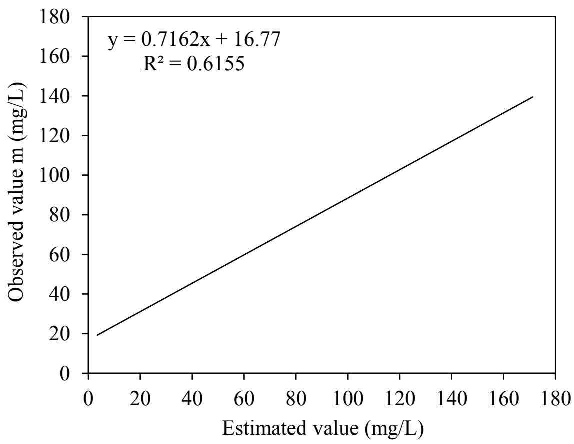

Figure 6. Linear relationship between simulated values and observed values, estimated values and observed values at all points

Table 8. Correlation of simulated values with observed values and estimated values with observed values

Point	Correlation coefficient with observed value		Correlation with observed value	
	Simulated value	Estimated value	Simulated value	Estimated value
A	0.0485	0.0536	Insig.	Insig.
B	0.4508	0.0650	Insig.	Insig.
C	0.2988	0.0691	Insig.	Insig.
D	0.7339	**0.8064**	Insig.	**Sig.**
E	0.1679	0.3992	Insig.	Insig.
F	**0.8727**	0.4329	**Sig.**	Insig.
G	0.3898	0.3898	Insig.	Insig.
H	0.3910	0.0261	Insig.	Insig.
I	0.1321	0.1321	Insig.	Insig.

Sig.=Significant, Insig.=Insignificant

4. CONCLUSIONS

The research into suspended solids has been carried out initially in this study to simulate the hydrodynamics of SS in Isahaya regulating reservoir as well as to review and evaluate simulation capability and accuracy of the ODEM model in comparison with UAV. As a result, the SS concentrations obtained from them were in relative accord with filed observed data. Therefore, this study has shown that the ODEM and UAV in the initial stage was quite good at monitoring SS concentration. As regards accuracy in monitoring SS, ODEM was better than UAV. Manipulation of the ODEM model was inexpensive, easy to operate and highly portable, which was very potential as an appropriate alternative for expensive observation of SS by manual methods. Apart from the favorable results achieved, some disadvantages remained. In this study, data were collected only once at each sampling point at each time. Some errors may have occurred, and the observed data may not have been fully representative of actual values of parameter concentrations observed at each sampling point during the investigated time. Thus, future work should focus on multiple repetitions of sampling and analysis with long-term monitoring to bring about better results of hydrodynamic simulation SS concentration in the future.

ACKNOWLEDGEMENTS

The instruments and equipment in this study were supported by Department of Advanced Engineering, Nagasaki University. The most grateful thanks to Mr. Dohi for data from his study using UAV method for SS estimation and to all members in the laboratory of Water and Environmental Engineering, Nagasaki University for their cooperation during sampling process.

REFERENCES

Bilotta G, Brazier R. Understanding the influence of suspended solids on water quality and aquatic biota. Water Research 2008;42(12):2849-61.

Chebbo G, Bachoc A. Characterization of suspended solids in urban wet weather discharges. Water Science and Technology 1992;25(8):171-9.

Dwinovantyo A, Manik HM, Prartono T, Ilahude D. Estimation of suspended sediment concentration from Acoustic Doppler Current Profiler (Adcp) instrument: A case study of Lembeh Strait, North Sulawesi. IOP Conference Series: Earth and Environmental Science 2017;54(1):012082

Ganti A. Correlation coefficient [Internet]. 2019 [cited 2020 Jan 20] Available from: https://www.investopedia.com/terms/c/correlationcoefficient.asp.

Gartner JW. Estimating suspended solids concentrations from backscatter intensity measured by acoustic doppler current profiler in San Francisco Bay, California. Marine Geology 2004;211(3-4):169-87.

Harris DC. Quantitative Chemical Analysis. USA: Craig Bleyer; 2007.

Hodoki Y, Murakami T. Effects of tidal flat reclamation on sediment quality and hypoxia in Isahaya Bay. Aquatic Conservation: Marine and Freshwater Ecosystems 2006;16(6):555-67.

Kim S, Hayami Y, Tai A, Tada A. The Mechanism of bottom water variation in summer at the northern mouth of Isahaya Bay, Japan. Journal of Oceanography 2018;74(6):595-605.

Koga K, Vongthanasunthorn N, Araki H, Yamanishi H, Kawabe M, Ohwa N. Study on water quality analysis in the reservoir of Isahaya Bay land reclamation project. Environmental Engineering Research 2003;40:541-50.

Krawczyk D, Gonglewski N. Determining suspended solids using a spectrophotometer. Sewage and Industrial Wastes 1959;31(10):1159-64.

Li M-C, Liang S-X, Sun Z-C, Zhang G-Y. Optimal dynamic temporal-spatial parameter inversion methods for the marine integrated element water quality model using a data-driven neural network. Journal of Marine Science and Technology 2012;20(5):575-83.

Liang S, Nakatsuji K, Sun Z, Yamanaka R, Dalian P. Residual circulation system and its driving mechanism in the Bohai Sea. International Conference on Estuaries and Coasts; 2003 Nov 9-11; Hangzhou: China; 2003.

Liang S, Yamanaka R, Nakatsuji K. Typical seasonal circulation in the Bohai Sea. Proceedings of the Thirteenth (2003) International Offshore and Polar Engineering Conference; 2003 May 25-30; Honolulu, Hawaii: USA; 2003.

Magee MR, Wu CH. Response of water temperatures and stratification to changing climate in three lakes with different morphometry. Hydrology and Earth System Sciences 2017;21(12):6253-74.

Mitsugi Y, Vongthanasunthorn N, Mishima Y, Koga K, Araki H, Ittisukananth P. Long-term change of water quality in the reservoir of the Isahaya Bay reclamation project. Lowland Technology International 2013;15(1):21-8.

Murakami S, Tsujimoto T, Nakagawa H. Pick-up rate of sand and gravels. Japan Society of Civil Engineers 1992;(443):9-16.

Nagase S, Mishima Y, Mitsugi Y, Araki H, Yamanishi H, Koga K. Study on behavior of suspended solids under seawater in the reservoir of the Isahaya Bay reclamation project. Japan Society of Civil Engineers 2014;70(6): II_167-II_73.

Niki M, Nishida W, Noguchi M, Hashimoto A. Study on prediction and evaluation of water quality change in Isahaya regulating reservoir. Proceedings of Hydraulic Engineering 1999;43:1007-12.

Nishida W, Noguchi M, Yanamoto S. Prediction of the water quality change under a construction of sea dyke. Proceedings of Hydraulic Engineering 1997;41:457-62.

Nishida W, Suzuki S, Uehara Y, Shige R, Nozoe Y. Spatial and temporal changes of suspended solids in the northern waters of Isahaya Bay reclamation reservoir. Japan Society of Civil Engineers 2014;70(7):III_341-III_47.

Sasaki K. Changes in water quality of the regulating reservoir and impacts of Isahaya Bay reclamation project on Isahaya Bay and the Ariake Sea. Environment and Fisheries in the Ariake Sea 2017;4:13-5.

Schaeffer BA, Schaeffer KG, Keith D, Lunetta RS, Conmy R, Gould RW. Barriers to adopting satellite remote sensing for water quality management. International Journal of Remote Sensing 2013;34(21):7534-44.

Shahzad MI, Meraj M, Nazeer M, Zia I, Inam A, Mehmood K, Zafar H. Empirical estimation of suspended solids concentration in the indus delta region using Landsat-7 Etm+ imagery. Journal of Environmental Management 2018;209:254-61.

Tada A, Nakamura T, Sakai SI, Mizunuma M, Takenouchi K. Study on the characteristics of surface layer's currents around the mouth of Isahaya Bay. Coastal Environmental and Ecosystem Issues of the East China Sea 2010:13-27.

Thanh VQ, Reyns J, Wackerman C, Eidam EF, Roelvink D. Modelling suspended sediment dynamics on the subaqueous delta of the Mekong River. Continental Shelf Research 2017;147:213-30.

Valkama P, Ruth O. Impact of calculation method, sampling frequency and hysteresis on suspended solids and total phosphorus load estimations in cold climate. Hydrology Research 2017;48(6):1594-610.

Yamaguchi S, Hayami Y. Impact of Isahaya dike construction on concentration in the Ariake Sea. Journal of Oceanography 2018;74(6):565-86.

GUIDE FOR AUTHORS

Publication and Peer-reviewing processes of Environment and Natural Resources Journal

Environment and Natural Resources Journal is a peer reviewed and open access journal that is published twice a year (January-June and July-December). Manuscripts should be submitted online at https://www.tci-thaijo.org/index.php/ennrj/ by registering and logging into this website. Submitted manuscripts should not have been published previously, nor be under consideration for publication elsewhere (except conference proceedings papers). A guide for authors and relevant information for the submission of manuscripts are provided in this section and also online at: www.tci-thaijo.org/index.php/ennrj/navigationMenu/view/author. All manuscripts are refereed through a **double-blind peer-review** process.

Submitted manuscripts are reviewed by outside experts or editorial board members of **Environment and Natural Resources Journal**. This journal uses double-blind review, which means that both the reviewer and author identities are concealed from the reviewers, and vice versa, throughout the review process. Steps in the process are as follows:

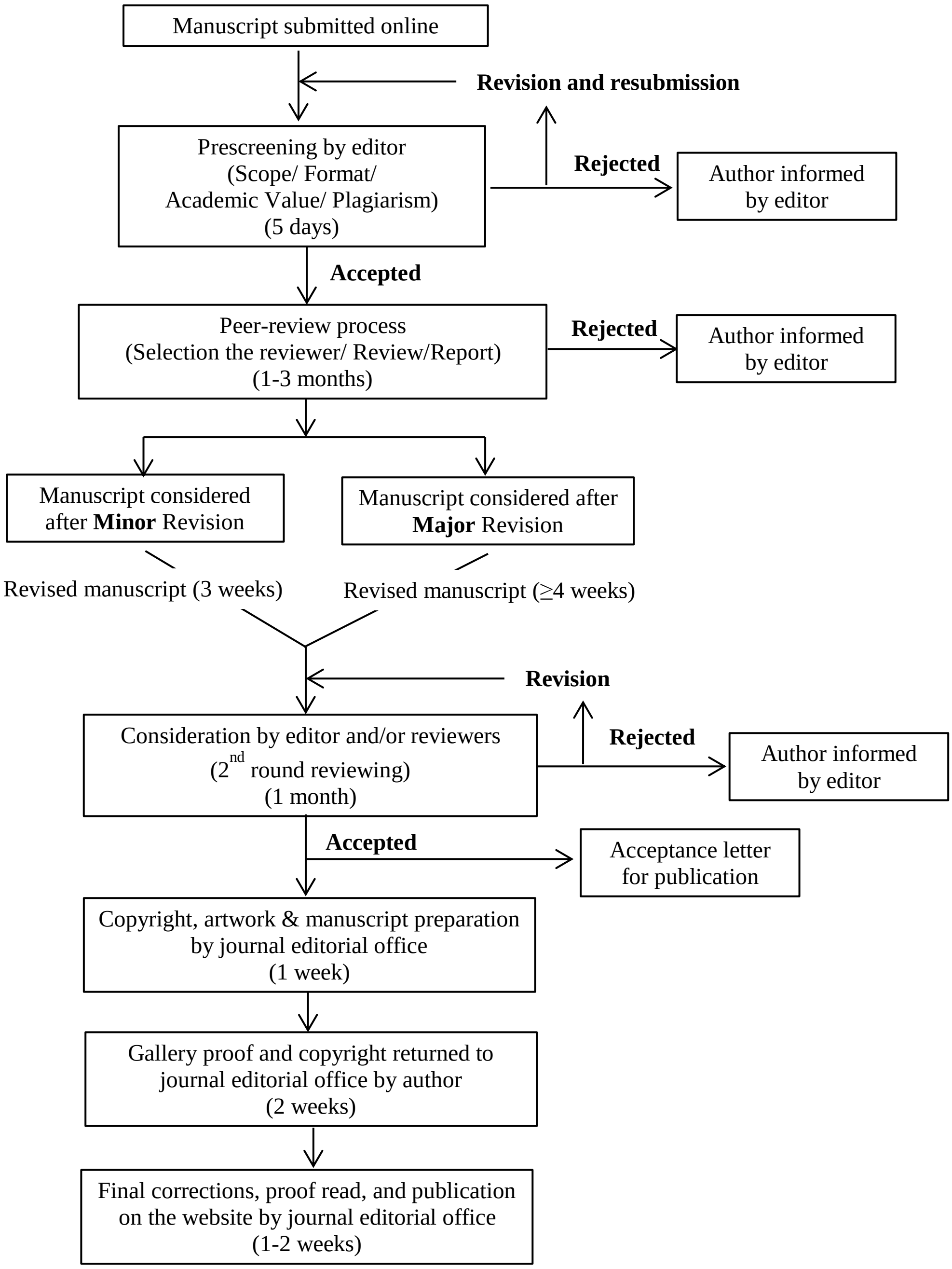

The Environment and Natural Resources Journal (EnNRJ) accepts 2 types of articles for consideration of publication as follows:

- *Original Research Article:* Manuscripts should not exceed 3,500 words (excluding references).
- *Review Article (by invitation):* This type of article focuses on the in-depth critical review of a special aspect in the environment and also provides a synthesis and critical evaluation of the state of the knowledge of the subject. Manuscripts should not exceed 6000 words (excluding references).

Preparation of Manuscripts

Manuscript should be prepared strictly as per guidelines given below. The manuscript (A4 size page) should be submitted in Microsoft Word (.doc or .docx) with Times New Roman 12 point font and a line spacing of 1.5. *The manuscript that is not in the correct format will be returned and the corresponding author may have to resubmit*. The submitted manuscript must have the following parts:

Title should be concise and no longer than necessary. Capitalize first letters of all important words, in Times New Roman 12 point bold.

Author(s) name and affiliation must be given, especially the first and last names of all authors, in Times New Roman 11 point bold.

Affiliation of all author(s) must be given in Times New Roman 11 point italic.

Abstract should indicate the significant findings with data. A good abstract should have only one paragraph and be limited to 200 words. Do not include a table, figure or reference.

Keywords should adequately index the subject matter and up to six keywords are allowed.

Text body normally includes the following sections: 1. Introduction 2. Methodology 3. Results and Discussion 4. Conclusions 5. Acknowledgements 6. References

Reference style must be given in Vancouver style. Please follow the format of the sample references and citations as shown in this Guide below.

Format and Style

Paper Margins must be 2.54 cm on the left and the right. The bottom and the top margin of each page must be 1.9 cm.

Introduction is critically important. It should include precisely the aims of the study. It should be as concise as possible with no sub headings. The significance of problem and the essential background should be given.

Methodology should be sufficiently detailed to enable the experiments to be reproduced. The techniques and methodology adopted should be supported with standard references.

Headings in Methodology section and Results and Discussion section, no more than three levels of headings should be used. Main headings should be typed (in bold letters) and secondary headings (in bold and italic letters). Third level headings should be typed in normal and no bold, for example;

2. Methodology
2.1 Sub-heading
2.1.1 Sub-sub-heading

Results and Discussion can be either combined or separated. This section is simply to present the key points of your findings in figures and tables, and explain additional findings in the text; no interpretation of findings is required. The results section is purely descriptive.

Tables Tables look best if all the cells are not bordered; place horizontal borders only under the legend, the column headings and the bottom.

Figures The journal does not normally use color for figures. Figures should be submitted in black and white; make sure that they are clear and understandable. Photographs converted from color to black and white format usually need to have their contrast adjusted. Regardless of the application used, when your electronic artwork is finalized, please 'save as' or convert the images to TIFF (or JPG) and separately send them to EnNRJ. Do not directly cut and paste them from MS Excel. The images require a resolution of at least 300 dpi (dots per inch). The lettering used in the artwork should be consistent in size and type.

Conclusions should include the summary of the key findings, and key take-home message. This should not be too long or repetitive, but is worth having so that your argument is not left unfinished. Importantly, don’t start any new thoughts in your conclusion.

Acknowledgements should include the names of those who contributed substantially to the work described in the manuscript but do not fulfill the requirements for authorship. It should also include any sponsor or funding agency that supported the work.

References should be cited in the text by the surname of the author(s), and the year. This journal uses the author-date method of citation: the last name of the author and date of publication are inserted in the text in the appropriate place. If there are more than two authors, "et al." after the first author' name must be added. Examples: (Frits, 1976; Pandey and Shukla, 2003; Kungsuwas et al., 1996). If the author's name is part of the sentence, only the date is placed in parentheses: "Frits (1976) argued that . . ."

In the list of references at the end of the manuscript, full and complete references must be given in the following style and punctuation, arranged alphabetically by first author's surname. Examples of references as listed in the References section are given below.

Book

Tyree MT, Zimmermann MH. Xylem Structure and the Ascent of Sap. Heidelberg, Germany: Springer; 2002.

Chapter in a book

Kungsuwan A, Ittipong B, Chandrkrachang S. Preservative effect of chitosan on fish products. In: Steven WF, Rao MS, Chandrkachang S, editors. Chitin and Chitosan: Environmental and Friendly and Versatile Biomaterials. Bangkok: Asian Institute of Technology; 1996. p. 193-9.

Journal article

Muenmee S, Chiemchaisri W, Chiemchaisri C. Microbial consortium involving biological methane oxidation in relation to the biodegradation of waste plastics in a solid waste disposal open dump site. International Biodeterioration and Biodegradation 2015;102:172-81.

Published in conference proceedings

Wiwattanakantang P, To-im J. Tourist satisfaction on sustainable tourism development, amphawa floating marketSamut songkhram, Thailand. Proceedings of the 1st Environment and Natural Resources International Conference; 2014 Nov 6-7; The Sukosol hotel, Bangkok: Thailand; 2014.

Ph.D. thesis

Shrestha MK. Relative Ungulate Abundance in a Fragmented Landscape: Implications for Tiger Conservation [dissertation]. Saint Paul, University of Minnesota; 2004.

Website

Orzel C. Wind and temperature: why doesn't windy equal hot? [Internet]. 2010 [cited 2016 Jun 20]. Available from: http://scienceblogs.com/principles/2010/08/17/wind-and-temperature-why-doesn/.

Remark

** Please be note that manuscripts should usually contain at least 15 references and some of them must be up-to-date research articles.*

** Please strictly check all references cited in text, they should be added in the list of references. Our Journal does not publish papers with incomplete citations.*

Copyright transfer

The copyright to the published article is transferred to Environment and Natural Resources Journal (EnNRJ) which is organized by Faculty of Environment and Resource Studies, Mahidol University. The accepted article cannot be published until the Journal Editorial Officer has received the appropriate signed copyright transfer.

Online First Articles

The article will be published online after receipt of the corrected proofs. This is the official first publication citable with the Digital Object Identifier (DOI). After release of the printed version, the paper can also be cited by issue and page numbers. DOI may be used to cite and link to electronic documents. The DOI consists of a unique alpha-numeric character string which is assigned to a document by the publisher upon the initial electronic publication. The assigned DOI never changes.

Mahidol University

Wisdom of the Land

Research and Academic Service Section, Faculty of Environment and Resource Studies, Mahidol University
999 Phutthamonthon 4 Rd, Salaya, Nakhon Pathom 73170, Phone +662 441-5000 ext. 2108 Fax. +662 441 9509-10
E-mail: ennrjournal@gmail.com Website: https://www.tci-thaijo.org/index.php/ennrj